

INFORMATION TO USERS

This reproduction was made from a copy of a document sent to us for microfilming. While the most advanced technology has been used to photograph and reproduce this document, the quality of the reproduction is heavily dependent upon the quality of the material submitted.

The following explanation of techniques is provided to help clarify markings or notations which may appear on this reproduction.

1. The sign or "target" for pages apparently lacking from the document photographed is "Missing Page(s)". If it was possible to obtain the missing page(s) or section, they are spliced into the film along with adjacent pages. This may have necessitated cutting through an image and duplicating adjacent pages to assure complete continuity.
2. When an image on the film is obliterated with a round black mark, it is an indication of either blurred copy because of movement during exposure, duplicate copy, or copyrighted materials that should not have been filmed. For blurred pages, a good image of the page can be found in the adjacent frame. If copyrighted materials were deleted, a target note will appear listing the pages in the adjacent frame.
3. When a map, drawing or chart, etc., is part of the material being photographed, a definite method of "sectioning" the material has been followed. It is customary to begin filming at the upper left hand corner of a large sheet and to continue from left to right in equal sections with small overlaps. If necessary, sectioning is continued again—beginning below the first row and continuing on until complete.
4. For illustrations that cannot be satisfactorily reproduced by xerographic means, photographic prints can be purchased at additional cost and inserted into your xerographic copy. These prints are available upon request from the Dissertations Customer Services Department.
5. Some pages in any document may have indistinct print. In all cases the best available copy has been filmed.

**University
Microfilms
International**
300 N. Zeeb Road
Ann Arbor, MI 48106

8420494

Borja, Ronaldo Israel

FINITE ELEMENT ANALYSIS OF THE TIME-DEPENDENT BEHAVIOR OF
SOFT CLAYS

Stanford University

PH.D. 1984

University
Microfilms
International 300 N. Zeeb Road, Ann Arbor, MI 48106

Copyright 1984

by

Borja, Ronaldo Israel

All Rights Reserved

PLEASE NOTE:

In all cases this material has been filmed in the best possible way from the available copy.
Problems encountered with this document have been identified here with a check mark .

1. Glossy photographs or pages _____
2. Colored illustrations, paper or print _____
3. Photographs with dark background _____
4. Illustrations are poor copy _____
5. Pages with black marks, not original copy _____
6. Print shows through as there is text on both sides of page _____
7. Indistinct, broken or small print on several pages
8. Print exceeds margin requirements _____
9. Tightly bound copy with print lost in spine _____
10. Computer printout pages with indistinct print _____
11. Page(s) _____ lacking when material received, and not available from school or author.
12. Page(s) _____ seem to be missing in numbering only as text follows.
13. Two pages numbered _____. Text follows.
14. Curling and wrinkled pages _____
15. Other _____

**University
Microfilms
International**

**FINITE ELEMENT ANALYSIS
OF THE TIME-DEPENDENT BEHAVIOR
OF SOFT CLAYS**

**A DISSERTATION
SUBMITTED TO THE DEPARTMENT OF CIVIL ENGINEERING
AND THE COMMITTEE ON GRADUATE STUDIES
OF STANFORD UNIVERSITY
IN PARTIAL FULFILLMENT OF THE REQUIREMENTS
FOR THE DEGREE OF
DOCTOR OF PHILOSOPHY**

**By
Ronaldo Israel Borja
April 1984**

I certify that I have read this thesis and that in my opinion
it is fully adequate, in scope and quality, as a dissertation
for the degree of DOCTOR OF PHILOSOPHY.

Edward Karayanyan, Ph.D.
Principal Advisor

I certify that I have read this thesis and that in my opinion
it is fully adequate, in scope and quality, as a dissertation
for the degree of DOCTOR OF PHILOSOPHY.

Thomas J. Doherty

I certify that I have read this thesis and that in my opinion
it is fully adequate, in scope and quality, as a dissertation
for the degree of DOCTOR OF PHILOSOPHY.

James K. Mitchell

Approved for the University Committee
on Graduate Studies:

Gerald J. Lieberman
Dean of Graduate Studies and Research

© Copyright 1984
by
Ronaldo Israel Borja

*To
My Mother
and Father*

ABSTRACT

A major consideration in the design and analysis of structures founded on soft clays is the foundation deformation that develops with time. This deformation is due to both consolidation and creep effects. At the present time, numerical analyses of time-dependent foundation deformation are restricted to either consolidation effects or undrained creep individually, without considering the combined effect of both. The objective of this thesis is to develop a numerical method that accounts for both consolidation and creep effects.

To provide solutions to boundary-value problems of axisymmetric (torsionless) and plane strain configurations, a finite element program SPIN 2D was developed. SPIN 2D is a quasi-static program that has the capability to solve combined consolidation and creep problems. It also has the capability to analyze undrained problems by mixed and penalty methods and to treat incompressibility by selective reduced integration. This program requires soil parameters that can easily be obtained from conventional laboratory tests.

The time-independent constitutive model used in SPIN 2D is a modified Cam clay elasto-plastic strain hardening model. The yield surface is a family of ellipsoids, which also serves as the plastic potential by the associative flow rule. Creep contributions are incorporated using the associative flow rule on the same yield surface as in the time-independent model.

To investigate the validity of the constitutive model, the program was used to perform parametric studies on San Francisco Bay Mud. Soil properties and test results were taken from published information on Bay Mud. The numerical experiments included drained, undrained, and consolidation tests, creep and stress relaxation tests, and combined stress relaxation and creep tests in 'triaxial' and plane strain stress conditions. Comparison of the numerical results with the test results showed excellent agreement and affirmed the validity of the constitutive model.

To further verify the model, SPIN 2D was used to predict the long-term field behavior of the I-95 test embankment founded on a Boston Blue Clay deposit. Results of the numerical predictions showed that creep-induced deformations constitute a major fraction of the overall deformation in this problem.

Recommendations are made for further improvement of the constitutive model.

ACKNOWLEDGMENTS

I am most grateful to my academic and thesis advisor, Prof. Edward Kavazanjian, Jr., who first convinced me to delve on the subjects of solid mechanics and constitutive models in geotechnical engineering in lieu of earthquake engineering for my research topic. His guidance, patience, support, and warm friendship are sincerely appreciated.

My gratitude also goes to Prof. Thomas J. R. Hughes for his many stimulating discussions, helpful suggestions, and invaluable lectures on finite elements.

I would like to thank Prof. James K. Mitchell of U. C. Berkeley for his comments and suggestions during the preparation of the final draft of my thesis.

My gratitude also goes to my colleagues in geotechnical engineering for the many fruitful discussions during the course of this research. My special thanks to Mr. Hsing-Lian Jong for performing the numerical experiments on the I-95 test embankment during the time that I was preparing for my thesis defense.

Finally, I would like to thank my Filipino friends within and around the Stanford campus for their company and for making my stay in the Bay Area a pleasant and memorable one.

Academic funding was provided by a UNESCO fellowship. Funding for the research work was provided by a grant from the National Science Foundation.

CONTENTS

1. INTRODUCTION	1
Statement of purpose	1
Methodology	1
Structure of presentation	2
2. BACKGROUND LITERATURE	4
2.1 Introduction	4
2.2 Preliminaries	4
2.3 Cam clay Theory and the Critical State Concept	6
- The critical state	6
- Definition of 'wet' clay	8
- State boundary surface and yielding	8
- Work equation and flow rule	10
- Original Cam clay model	10
- Modified Cam clay model	13
- Plastic shear distortion beneath the state boundary surface	14
- Evaluation of M and K_o	16
- Pender's model for overconsolidated clay	18
- Remarks	20
2.4 Effect of Time	20
- Volumetric creep	20
Notations	20
Primary/secondary consolidation	21
Immediate/delayed compression	23
Development of a quasi-preconsolidation	23
On the secondary compression coefficient C_α	25
- Deviatoric creep	26
Rate process theory	26
Singh-Mitchell creep equation	28
Kondner's hyperbolic stress-strain model	31
2.5 Phenomenological Stress-Strain-Time Models	32
- Preliminaries	32
- Kavazanjian model	33
General volumetric model	34
General deviatoric model	34
Remarks	38
- Kavazanjian-Bonaparte-Mitchell Model	38
General volumetric model	41
General deviatoric model	41
Remarks	42

3. DEVELOPMENT OF THE CONSTITUTIVE EQUATION	43
3.1 Preliminaries	43
– Definitions	43
– Abstract of the constitutive model	44
– Yield surface and hardening rule	46
– Growth of preconsolidation pressure	46
3.2 Formulation of the Constitutive Equation	49
– Evaluation of derivatives	51
– Contraction of indices	51
– Elastic stress-strain matrix	53
3.3 Creep Strain Rate	54
– Volumetric scaling	56
Volumetric age	56
– Deviatoric scaling	57
Deviatoric stress level and failure strength	58
Deviatoric age	59
– Nonassociative flow rule for plane strain	60
3.4 Summary	61
4. DEVELOPMENT OF A FINITE ELEMENT PROGRAM	63
4.1 Introduction	63
4.2 Finite Element Formulation	63
– Strong form	65
– Weak form	66
– Galerkin approximations	68
– Matrix form	69
4.3 Time Integration	73
– The parameter β	73
– The parameter α	75
4.4 Large Deformation Problems	75
– Kinematics	75
– Rate of deformation, spin, and natural strain increments	77
– Objectivity	78
– Modified constitutive equation	78
– Initial stress stiffness	79
4.5 Analysis Options	80
– Drained analysis	83
– Undrained analysis	83
Mixed formulation	83
Penalty formulation	84
– Consolidation analysis	88
– Creep options	89
4.6 Computer Implementation	90

- Input phase	91
Floating point data generation	91
Integer data generation	92
Load-time functions	95
- Solution phase	99
Element calculations	101
Constitutive routines	101
Equation solving routine	104
4.7 Illustrations (Examples)	106
- 1. Drained test on Weald clay	106
- 2. Undrained test on UBM, no creep	108
- 3. Isotropic undrained test with volumetric creep	111
- 4. Terzaghi's one-dimensional consolidation theory	112
- 5. Radial consolidation, free strain	116
- 6. Rigid body rotation using finite deformation	118
- 7. Uniaxial compression, Lagrangian strains	118
- 8. Combined compression and simple shear	120
4.8 Summary	122
5. EVALUATION OF THE CONSTITUTIVE MODEL	125
<i>Part A. Parametric Studies on San Francisco Bay Mud</i>	
5.1 Introduction	125
5.2 Soil Parameters for Bay Mud	126
5.3 Drained 'Triaxial' Tests on Undisturbed Bay Mud	128
5.4 Undrained Tests on Undisturbed Bay Mud	131
- Choice of finite element	132
- Undrained creep tests	135
- Creep tests at different strain rates	137
- Combined creep and stress-relaxation test	140
- Undrained plane strain test	142
5.5 Consolidation Tests on Remolded Bay Mud	145
- Isotropic consolidation tests	145
- One-dimensional consolidation tests	147
5.6 Dependence of C_o on \bar{D}	154
5.7 On the Lateral Pressure Coefficient K_o	158
- Values of K_o obtained from time-independent analyses	158
- Values of K_o obtained from creep-inclusive analyses	160
- Remark	164
<i>Part B. Long-Term Field Behavior of the I-95 Test Embankment</i>	
5.8 Background	165
5.9 Soil Parameters for Boston Blue Clay	165
5.10 Problem Geometry	167
5.11 Discussion of Results	170
5.12 Summary of Main Points	173

6. CONCLUSIONS AND RECOMMENDATIONS	174
Conclusions	174
Recommendations	175
- On the constitutive model	175
- On the finite element program	176
REFERENCES	178
APPENDICES	183
1.1 Development of Weak Form	183
1.2 Modified Constitutive Equation	
Accounting for Finite Deformation	184
2.1 Flow Charts of Constitutive Routines	187
2.2 Program Listing	191
3.1 SPIN 2D User's Manual	198
3.2 Solved Problem	213
4 Notations	220

LIST OF FIGURES

CHAPTER 2

2.1 The state boundary surface	7
2.2 Strain hardening, state path, and stress path	9
2.3 Consolidation curves in the natural p and $\ln p$ scales	11
2.4 Horizontal yield loci beneath the state boundary surface	15
2.5 Development of plastic shear distortion beneath the state boundary surface	17
2.6 Pender's yield loci for overconsolidated and K_o -consolidated soils	19
2.7 Definitions of primary-secondary and immediate-delayed compressions	22
2.8 Bjerrum's model for one-dimensional compression	24
2.9 Mesri-Godlewski's representation of consolidation in e - $\ln \sigma$ - $\ln t$ space	27
2.10 Representation of Singh-Mitchell's creep equation	30
2.11 Kavazanjian's general volumetric model	35
2.12 Illustration of Kavazanjian's general volumetric model	36

CHAPTER 3

3.1 Development of quasi-preconsolidation	46
3.2 Evaluation of volumetric and deviatoric ages	55

CHAPTER 4

4.1 Problem domain and boundaries	64
4.2 Elements of matrices B , C^* , S , and T	81
4.3 Element library in SPIN 2D	82
4.4 Comparison between the normal quadrature rule and selective reduced integration rule	86
4.5 Isoparametric floating point data generation along a line	93
4.6 Isoparametric floating point data generation over a surface	94
4.7 Element nodal data generation	96
4.8 Load-time function for load case i	97
4.9 Flow chart of a typical quasi-static finite element program	99
4.10 Flow chart of stiffness assembly routine	100
4.11 Sketch of the shape function routine	102
4.12 Flow chart of stress-strain matrix assembly routine	103
4.13 Storage scheme for a typical stiffness matrix	105
4.14 Drained test on Weald clay	107
4.15 Hyperbolic stress-strain diagram, undisturbed Bay Mud	109
4.16 Hyperbolic pore pressure-strain diagram, UBM	110
4.17 Isotropic undrained stress relaxation $\lambda = 0.0065$, $\kappa = 0.045$	113
4.18 Isochrones for one-dimensional consolidation	114

4.19 One-dimensional consolidation	115
4.20 Radial consolidation, free strain	117
4.21 Stresses during rigid body rotation	119
4.22 Normal strain in uniaxial compression; strain 11 in combined compression and simple shear	121
4.23 Strains in combined compression and simple shear	123
CHAPTER 5	
5.1 Sensitivity of the stress-strain and pore pressure-strain diagram to values of e_a	129
5.2 Drained test on undisturbed San Francisco Bay Mud	130
5.3 Undrained test on San Francisco Bay Mud: (a)undeformed mesh, (b) deformed mesh, (c) rotation of principal axes, (d)pore pressure distribution	133
5.4 Influence of the top cap on the behavior of soil in a 'triaxial' test	134
5.5 Undrained creep tests on undisturbed Bay Mud	136
5.6 Undrained 'triaxial' tests on undisturbed Bay Mud performed at different strain rates	139
5.7 Combined creep and stress relaxation test on undisturbed Bay Mud	141
5.8 Stress-strain diagram for a plane strain test on UBM	143
5.9 Pore pressure-strain diagram for a plane strain undrained test on UBM	144
5.10 Consolidation test on remolded Bay Mud showing the influence of secondary compression	146
5.11 Pore pressure distribution during isotropic consolidation	148
5.12 Volumetric age profile during isotropic consolidation	148
5.13 One-dimensional consolidation curves with creep	151
5.14 Isochrones for one-dimensional consolidation with creep	152
5.15 Compression versus log-time plots for specimens of different heights	159
5.16 Relationship between secondary compression coefficient ψ and deviator stress level \bar{D}	156
5.17 Contour of constant ψ on the $\log \dot{\epsilon}_{22} - \bar{D}$ plane	157
5.18 Drained K_o -test on undisturbed Bay Mud	159
5.19 Dependence of K_o on effective friction angle	161
5.20 Variation of K_o with time	162
5.21 Plot of K_o with time showing influence of permeability	163
5.22 Soil profile at the I-95 embankment test site	168
5.23 Finite element mesh for the I-95 embankment problem	169
5.24 Surface centerline settlement versus time for the I-95 embankment problem	171
5.25 Pore pressure head versus time at points <i>A</i> and <i>B</i> within the Boston Blue Clay layer	172

**FINITE ELEMENT ANALYSIS
OF THE TIME-DEPENDENT BEHAVIOR
OF SOFT CLAYS**

Chapter 1

INTRODUCTION

Statement of purpose

The time-dependent behavior of cohesive soils is an important consideration in the design and analysis of geotechnical structures such as embankments, tunnels, and excavations. Time-dependent deformations are due to both hydrodynamic lag and creep effects. At the present time, numerical analyses of time-dependent foundation deformations are restricted to either consolidation effects or undrained creep considered separately. It is the objective of this dissertation to develop a numerical approach of solving the combined effects of hydrodynamic lag and creep in the framework of a finite element formulation.

Methodology

Development of a constitutive equation for cohesive soils is necessary in order to mathematically represent the material response to applied loads. To incorporate creep effects in the constitutive model, it is assumed that the total deformation can be separated into time-independent and time-dependent parts.

The classical theory of plasticity is employed to characterize the time-independent stress-strain behavior of cohesive soils using the realistic, simple, and self-consistent modified Cam clay model. The yield surface is a family of ellipsoids which also serves as the plastic potential by the associative flow rule.

The time-dependent (creep) component of the total strain is evaluated by employing (a) the associative flow rule on the same yield surface as in the time-independent model, and (b) the consistency requirement which requires that the magnitude of the creep strain rate tensor reduce to phenomenological creep expressions whenever this tensor degenerates to either drained isotropic, or undrained

'triaxial' stress tensors. (1)

The finite element method is used as the numerical approach for obtaining approximate solutions to boundary-value problems. The finite element formulation consists of the classical statement of the model problem and the development of the matrix form using variational concepts. An incremental approach of numerical analysis is adopted to account for the history-dependency inherent in all plasticity problems.

To incorporate the influence of hydrodynamic lag, a "mixed" type of formulation is employed, in which the displacement and the pore pressure degrees of freedom are coupled by the equilibrium and continuity requirements. Whereas effective stresses and strains are governed by the rate-constitutive equation, the influence of hydrodynamic lag is treated using Darcy's law for transient pore pressure dissipation.

To provide approximate solutions to boundary-value problems of axisymmetric (torsionless) and plane strain configurations, a quasi-static finite element computer program SPIN 2D is developed. This program is capable of analyzing drained, undrained, consolidation, and creep problems.

To investigate the validity of the constitutive model, SPIN 2D is used to perform parametric studies on San Francisco Bay Mud. The long-term field behavior of an embankment founded on a Boston Blue Clay deposit is also predicted to evaluate the performance of both the constitutive model and the finite element program in predicting the time-dependent behavior of a full-scale earth structure.

Structure of presentation

Chapter 2 presents a comprehensive review of previous work on the Cam clay models as well as a summary of phenomenological creep equations used in the

(1) Throughout, apostrophes will enclose the word "triaxial" whenever it is used to refer to the conventional axisymmetric test stress condition; apostrophes will be omitted whenever "triaxial" is used to refer to the more general case where the three principal stresses can be independently varied.

subsequent formulation.

Chapter 3 presents a general formulation of the constitutive equation in both tensor and matrix forms.

Chapter 4 presents the development of the finite element program SPIN 2D and discusses numerical aspects such as time-discretization, the large-deformation formulation, and computer implementation. This chapter concludes by showing several simple example problems as a prelude to more detailed numerical studies in the following chapter.

Chapter 5 deals with verification of the program. Part A of this chapter is concerned with parametric studies on San Francisco Bay Mud. The ability of the constitutive model to predict results of laboratory tests is evaluated by performing numerical experiments to simulate drained, undrained, and consolidation tests, creep and stress relaxation tests, and combined stress relaxation and creep tests in 'triaxial' and plane strain stress conditions. Part B of this chapter presents numerical analyses of the I-95 test embankment founded on a compressible Boston Blue Clay deposit. Results of the numerical predictions are compared with the field behavior. These results show the significance of determining the combined effects of hydrodynamic lag and creep on the time-dependent settlement and pore pressure behavior of compressible soils.

Chapter 6 summarizes the work done. Recommendations are made for improvement of both the constitutive model and the finite element program.

Chapter 2

BACKGROUND LITERATURE

2.1 INTRODUCTION

Constitutive equations are mathematical relationships characterizing the behavior of a material with respect to its reaction to applied loads. These relationships usually involve quantities such as stress, strain, temperature, and time.

Constitutive equations for soils can be derived using a *microscopic* approach, or a *macroscopic* approach. The *rate process theory* described in Sec. 2.4 was developed on the microscopic level, while *continuum mechanics* is an example of a macroscopic approach.

The objective of this chapter is to present existing stress-strain and stress-strain-time relationships for cohesive soils which will be utilized in the development of a general creep-inclusive constitutive equation in Chapter 3 using a macroscopic approach. A major consideration is that the soil parameters required for material characterization be few and obtainable from conventional laboratory tests to facilitate applications in engineering practice.

2.2 PRELIMINARIES

The general constitutive relationships for soils can be written symbolically as [58]:

$$\sigma_{ij}(\mathbf{x}, t) = F_{ijkl}(\epsilon_{kl}(\mathbf{x}, t), T(\mathbf{x}, t), \gamma(\mathbf{x}, t), w(\mathbf{x}, t), \dots; \mathbf{x}, t), \quad (2.1)$$

where σ_{ij} and ϵ_{kl} are the (i, j) and the (k, l) components of the effective stress ⁽¹⁾ and strain tensors, respectively; F_{ijkl} is the (i, j, k, l) general nonlinear constitutive

⁽¹⁾ To simplify notation, effective stresses will be written unprimed.

function; (\mathbf{x}, t) are the space geometry ⁽¹⁾ and time, respectively; T is temperature, γ is unit weight, and w is water content. The symbol '...' refers to other variables that need to be accounted for, based on the principle of equipresence [39], which requires that all variables that could possibly influence the response of the soil be incorporated in F_{ijkl} .

If all variables, except ϵ_{kl} , are ignored (2.1) becomes

$$\sigma_{ij} = F_{ijkl}(\epsilon_{kl}(\mathbf{x}, t)) . \quad (2.2)$$

The problem in this formulation is the evaluation of the F_{ijkl} 's.

If the F_{ijkl} 's are linear functions, a linear rate-dependent material such as a viscoelastic material may be obtained. If the material is rate-independent and the strains are small ⁽²⁾,

$$\sigma_{ij} = c_{ijkl}\epsilon_{kl} , \quad (2.3)$$

where c_{ijkl} is a fourth order stiffness tensor consisting of 81 elements. By invoking symmetry, homogeneity, and isotropy, the number of independent elements in c_{ijkl} may be reduced down to 2. For example, in terms of the Lamé elastic constants $\bar{\lambda}$ and $\bar{\mu}$ (summation implied on repeated subscripts),

$$\sigma_{ij} = \bar{\lambda}\epsilon_{kk}\delta_{ij} + 2\bar{\mu}\epsilon_{ij} , \quad (2.4)$$

where δ_{ij} is the Kronecker delta.

Equation (2.4) is an oversimplification of the problem in that soils are not, in general, homogeneous and isotropic. A convenient approach is to adopt an heuristic procedure for describing the behavior of the material. For example, Newmark [47] proposed a set of equations

$$\left\{ \begin{array}{l} \sigma_{oct} = f_1(\epsilon_{oct}) + f_2(\gamma_{oct}/2) + f_3(\varphi) \\ \tau_{oct} = f_4(\epsilon_{oct}) + f_5(\gamma_{oct}/2) + f_6(\varphi) \\ \vartheta = f_7(\epsilon_{oct}) + f_8(\gamma_{oct}/2) + f_9(\varphi) \end{array} \right\} , \quad (2.5)$$

⁽¹⁾ Tensors and vectors will be written either in boldface as "x", or with a top tilde as " $\tilde{\sigma}$ ".

⁽²⁾ Large strain problems are dealt with in Section 4.4.

with nonlinear functions f_1, f_2, \dots, f_9 . The normal and the shear octahedral stresses and strains $\sigma_{\text{oct}}, \tau_{\text{oct}}, \epsilon_{\text{oct}}$, and γ_{oct} are invariants, i.e., they do not change with the orientation of the reference axes; the parameters ϑ and φ are functions of the third stress and strain invariants, respectively. The heuristic procedure allows the definition of quasi-elastic constants such as the shear modulus $G = \tau_{\text{oct}}/(2\gamma_{\text{oct}})$ and the bulk modulus $K = \sigma_{\text{oct}}/(3\epsilon_{\text{oct}})$ which also become invariants.

In conducting an experimental testing procedure, the heuristic approach imposes less severe demands because only the principal stresses σ_1, σ_2 , and σ_3 need be varied. It also permits the use of a rigid platen cubical triaxial apparatus to measure the principal strains ϵ_1, ϵ_2 , and ϵ_3 without having to measure shear strains.

2.3 CAM CLAY THEORY AND THE CRITICAL STATE CONCEPT

Critical state soil mechanics was developed at Cambridge University to describe the behavior of an isotropic, continuous, elasto-plastic, strain-hardening 'wet' clay. It evolved from the observation that 'wet' soils continuously deform as a frictional fluid when subjected to large external stresses [54].

The critical state

The critical state is defined by the two equations

$$q = Mp \quad (2.6)$$

$$\epsilon = e_c - \lambda \ln p . \quad (2.7)$$

The first equation is the *critical state line* relating the deviator stress q to the volumetric stress p , through the (constant) slope M . Any state point on this line will be in a state of plastic shear deformation instability characterized by frictional flow without volume change.

The second equation defines a *consolidation curve* and involves void ratio ϵ , stress p , and the constants e_c and λ . Simultaneous satisfaction of (2.6) and (2.7) defines an arc in the ϵ - p - q space (Fig. 2.1).

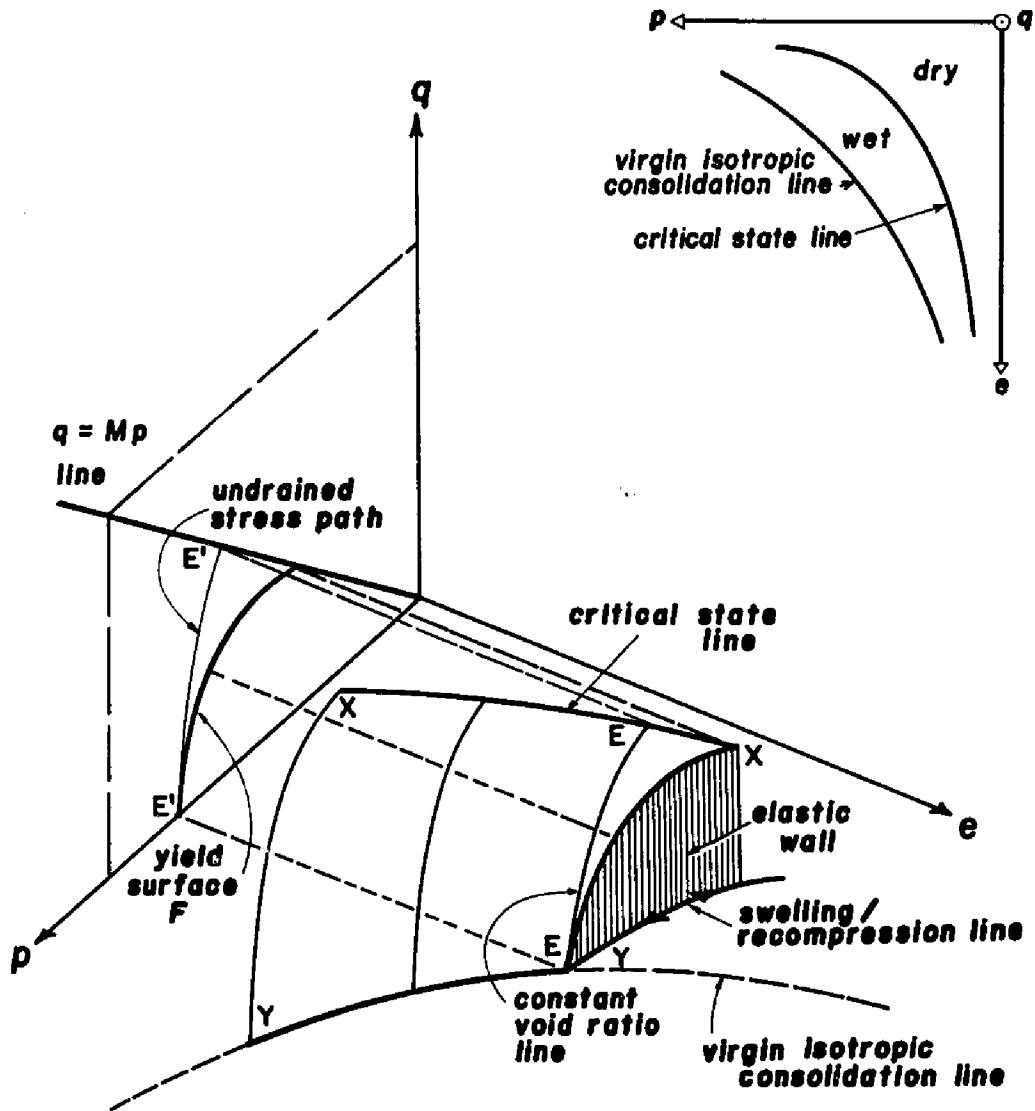


FIG. 2.1. THE STATE BOUNDARY SURFACE.

Definition of 'wet' clay

By definition, the soil is 'wet' if it contracts when sheared and increases in strength when drainage is allowed; otherwise, the soil is 'dry' [54]. Using the three parameters p , q , and e , the critical state line may be projected on the $e-p$ plane as shown in Fig. 2.1. This projection separates the 'wet' region from the 'dry' region.

State boundary surface and yielding

The Cam clay theory postulates the existence of a unique state boundary surface, $XXYY$, in Figs. 2.1 and 2.2, representing the limit of all possible states of a 'wet' soil in the $e-p-q$ space.

This surface intersects the $e-p$ plane along the *virgin isotropic consolidation line* $YY-$ a line which can be obtained from isotropic consolidation tests. The surface also intersects the critical state line XX in the $e-p-q$ space.

The state of the soil at any point a in Fig. 2.2 is defined by the (e, p, q) coordinates of that point. The state point at a may shift to another state point, say at b , via state path ab , with stress path $a'b'$ as its projection on the $p-q$ plane. For example, the undrained effective stress path $E'E'$ in Fig. 2.1 is the projection of the state path EE on the state boundary surface of constant void ratio.

A virgin consolidation curve in the natural $e-p$ scale transforms into a straight line when plotted on the $e-\ln p$ scale (Figs. 2.3a,b). The slope of this line λ is the *virgin compression index* which is commonly assumed constant in the range of engineering interest for many 'wet' clays.

If the soil is allowed to swell from a preconsolidation pressure p_c on the isotropic virgin curve, a small fraction of the total deformation will be recovered. This recoverable deformation represents the *elastic* part of the total deformation, and is typically many times smaller than the irrecoverable *plastic* part.

When the soil is reloaded, the state of the soil follows a *recompression* curve until it reaches p_c . This curve is often assumed to trace the swelling curve because the "hysteresis" that develops is usually small and can be ignored for most soils. When plotted on the $e-\ln p$ plane, the swelling-recompression curve traces a straight

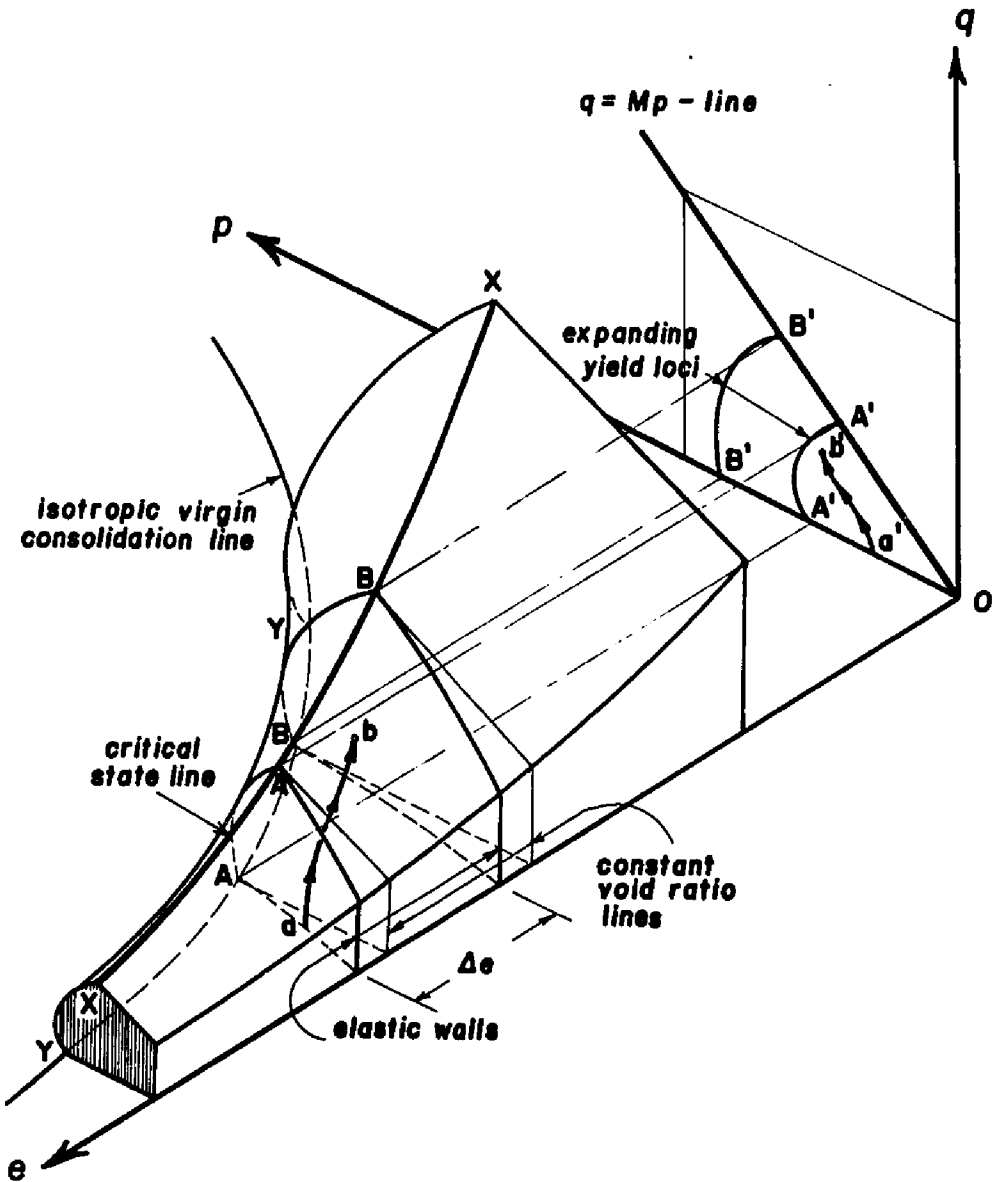


FIG. 2.2. STRAIN HARDENING, STATE PATH,
AND STRESS PATH.

line of slope κ ; hence, the recompression/swelling index κ is an elastic property (refer to Figs. 2.3a, b).

In the $e-p-q$ space, the swelling-recompression curve forms a cylindrical *elastic wall*. This wall is a surface within which the behavior of the soil is purely elastic. The elastic wall intersects the state boundary surface in space. Two such intersections are indicated by arcs AA and BB in Fig. 2.2; their projections $A'A'$ and $B'B'$ on the $p-q$ plane define their corresponding *yield loci*.

When the yield locus expands from $A'A'$ to $B'B'$ in Fig. 2.2, the soil is said to *strain harden*. This expansion is an irreversible process if the soil can only compress (and not swell) plastically. During this expansion, the soil is brought to a state of higher preconsolidation pressure, p_c .

Work equation and flow rule

A set of many possible values of $\Delta\sigma_{ij}$ can cause the current yield locus F to expand, strain-harden, and bring it to F' . The stress increment should have an outward direction with respect to F , otherwise no expansion of F would take place.

The only possible direction of the associated plastic strain increment $\Delta\epsilon_{ij}^p$, which produces a positive incremental plastic work ΔW^p , defined by

$$\Delta W^p = \Delta\sigma_{ij}\Delta\epsilon_{ij}^p \geq 0, \quad (2.8)$$

is the normal to F . This normality requirement is called the *associative flow rule*.

Original Cam clay model

The original Cam clay model was developed by Roscoe, Schofield, and Thuraiyah [51] using an energy method of formulation from 'triaxial' test data. They defined the stress parameters p and q as follows:

$$p = \frac{1}{3}(\sigma_1 + \sigma_2 + \sigma_3) \quad (2.9a)$$

$$q = (\sigma_1 - \sigma_3), \quad (2.9b)$$

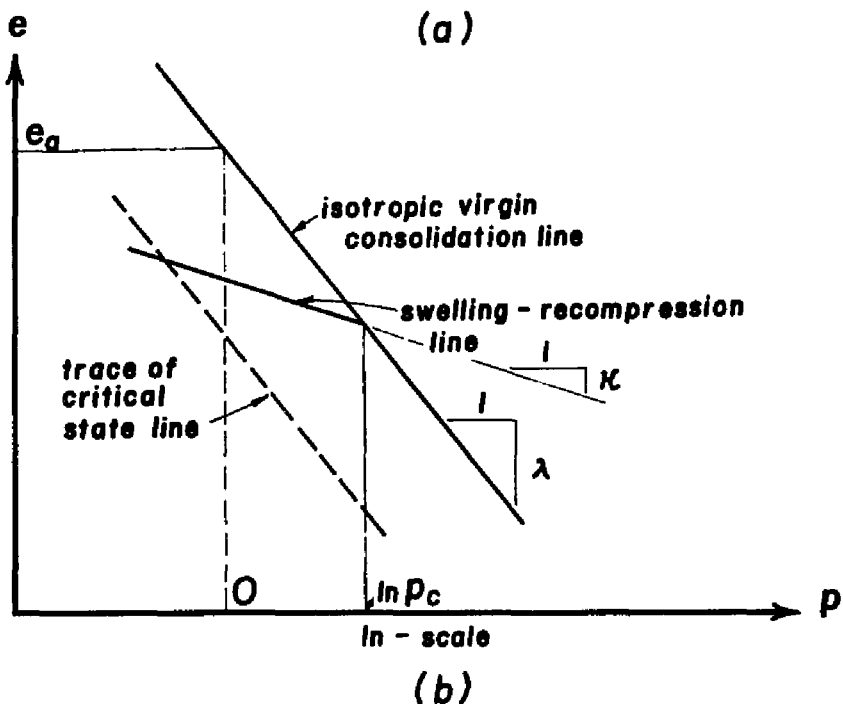
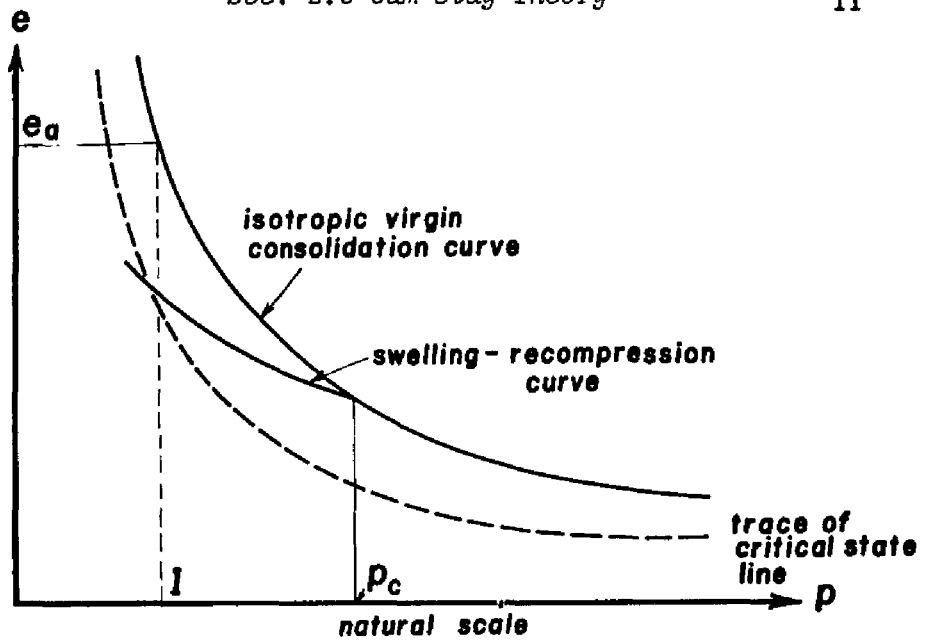


FIG. 2.3. CONSOLIDATION CURVES IN (a) NATURAL p -SCALE; (b) $\ln p$ -SCALE.

where σ_1 and σ_3 are the *major* and *minor* principal effective stresses, respectively (compression, positive); $\sigma_2 = \sigma_3$ for 'triaxial' compression and $\sigma_2 = \sigma_1$ for 'triaxial' extension.

For this condition, the differential total strains $d\epsilon_v$ and $d\epsilon_d$ become

$$d\epsilon_v = d\epsilon_1 + d\epsilon_2 + d\epsilon_3 = d\epsilon_1 + 2d\epsilon_3 \quad (2.10a)$$

$$d\epsilon_d = d\epsilon_1 - \frac{1}{3}d\epsilon_v = \frac{2}{3}(d\epsilon_1 - d\epsilon_3), \quad (2.10b)$$

where $d\epsilon_1$ is the differential axial strain and $d\epsilon_3$ is the differential radial strain.

By assuming that the *dissipated energy* dW_d transmitted across the boundary in the critical state condition is given by

$$dW_d = q \cdot d\epsilon_d = Mp \cdot d\epsilon_d, \quad (2.11)$$

the following expressions were derived [51]:

The equation of the state boundary surface in the e - p - q space is

$$q \doteq \frac{Mp}{\lambda - \kappa} (e_a - e - \lambda \ln p), \quad (2.12)$$

where e_a is the void ratio when $p = 1$.

The yield locus on the p - q plane has the equation

$$q = Mp \ln \left(\frac{p_o}{p} \right), \quad (2.13)$$

where p_o is the volumetric stress when $q = 0$. This yield surface has the shape of a bullet. At $p = p_o$ (the isotropic compression line), the associative flow rule becomes inapplicable because the normal to the yield surface is not parallel to the volumetric axis.

The undrained stress path is given by the expression

$$q = \frac{Mp}{1 - \kappa/\lambda} \ln \left(\frac{p_o}{p} \right), \quad (2.14)$$

which reduces to (2.13) when $\kappa = 0$. If $\kappa = 0$, the elastic wall through p_o is also a constant-void-ratio plane.

Differential stresses dp and dq will produce differential deviatoric strain given by

$$d\epsilon_d = d\epsilon_d^p = \frac{\lambda - \kappa}{Mp(1 + e)} \left[dp + \frac{dq}{M - \eta} \right], \quad (2.15)$$

where $\eta = \text{stress ratio } q/p$. The elastic component of the volumetric strain $d\epsilon_v^e$ is given by

$$d\epsilon_v^e = \frac{\kappa}{1 + e} \cdot \frac{dp}{p}. \quad (2.16)$$

Using associative flow rule to obtain $d\epsilon_v^p$,

$$d\epsilon_v = d\epsilon_v^e + d\epsilon_v^p = \frac{1}{1 + e} \left[\frac{\lambda - \kappa}{Mp} (dq - \eta dp) + \frac{\lambda dp}{p} \right]. \quad (2.17)$$

It can be seen from (2.15) and (2.17) that, whereas $d\epsilon_v$ consists of elastic and plastic parts, the Cam clay model assumes that $d\epsilon_d$ is purely plastic.

The foregoing development requires only 4 material constants, namely, κ , λ , M , and e_a . This model, however, overpredicts the strain increments due to $d\eta$ for small values of η . This model also tends to overpredict the at-rest lateral pressure coefficient K_o .

Modified Cam clay model

Roscoe and Burland [52] proposed a modified Cam clay theory by using a different dissipated energy equation having the form

$$dW_d = p \sqrt{(d\epsilon_v^p)^2 + (M d\epsilon_d^p)^2}. \quad (2.18)$$

This work equation changes the form of the state boundary surface to

$$\frac{p}{p_e} = \frac{e_a - e}{\lambda \ln p} = \left(\frac{M^2}{M^2 + \eta^2} \right)^{(1-\kappa/\lambda)}, \quad (2.19)$$

where

$$p_e = \exp \left(\frac{e_a - e}{\lambda} \right). \quad (2.20)$$

The equation of the yield locus on the $p-q$ plane changes to

$$p = p_o \left(\frac{M^2}{M^2 + \eta^2} \right), \quad (2.21)$$

which has the shape of an ellipse with center at $p_o/2$.

The undrained stress path through p_o is

$$p = p_o \left(\frac{M^2}{M^2 + \eta^2} \right)^{(1-\kappa/\lambda)}, \quad (2.22)$$

which also reduces to (2.21) when $\kappa = 0$.

The differential deviatoric strain due to dp and $d\eta$ becomes

$$d\epsilon_d = d\epsilon_d^p = \frac{\lambda - \kappa}{1 + e} \left(\frac{2\eta}{M^2 - \eta^2} \right) \left(\frac{2\eta d\eta}{M^2 + \eta^2} + \frac{dp}{p} \right), \quad (2.23)$$

and using the associative flow rule,

$$d\epsilon_v = d\epsilon_v^e + d\epsilon_v^p = \frac{1}{1 + e} \left[(\lambda - \kappa) \cdot \frac{2\eta d\eta}{M^2 + \eta^2} + \lambda \left(\frac{dp}{p} \right) \right]. \quad (2.24)$$

Although the modified theory is in better agreement with 'triaxial' test results, it underpredicts $d\epsilon_v$ and (more particularly) $d\epsilon_d$ in undrained tests.

Plastic shear distortion beneath the state boundary surface

To allow the retention of the associative flow rule while improving the prediction for $d\epsilon_d$, Roscoe and Burland [52] postulated that horizontal deviatoric yield loci exist beneath the state boundary surface, and that deviatoric yielding may also take place on or within the elastic wall even with no plastic volume change.

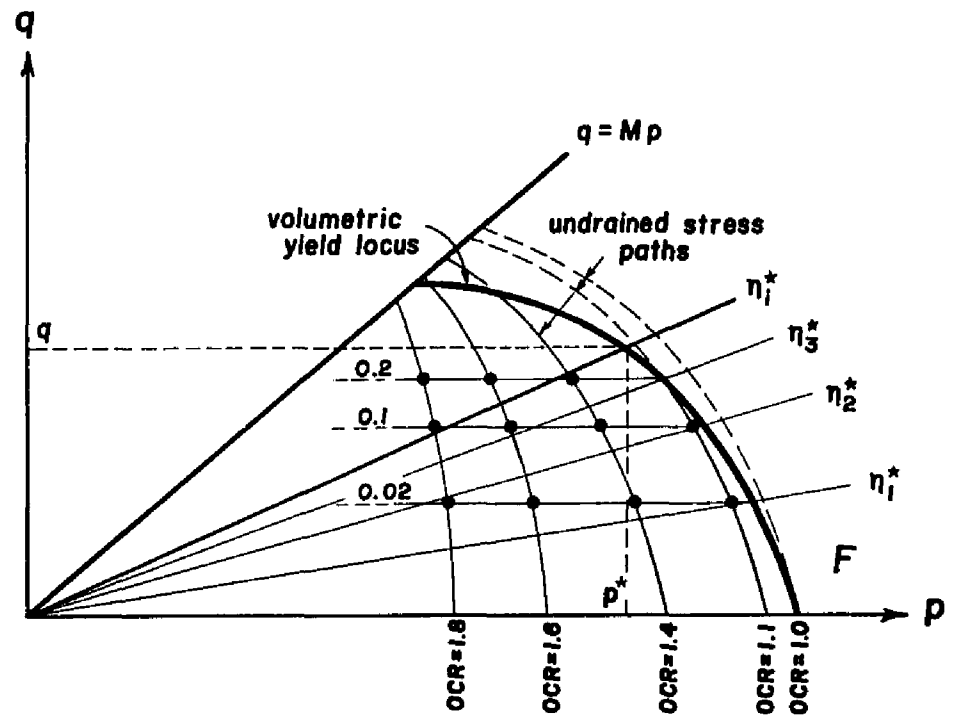
This shear distortion is assumed to be proportional to q and is superimposable with the plastic strain components that develop when the state point moves to another elastic wall. This additional plastic shear distortion $d\epsilon_d^p$ is represented by the strain contour of Fig. 2.4 which has the following characteristics:

Let p^* be the p -coordinate of the point on F corresponding to a given q . For example, assuming that the yield surface is given by the ellipse (2.21), then

$$p^* = \frac{p_e}{2} \left[1 + \sqrt{1 - (2q/Mp_e)^2} \right]. \quad (2.25)$$

Also, let

$$\eta^* = q/p^*. \quad (2.26)$$



• to be determined from experimental data

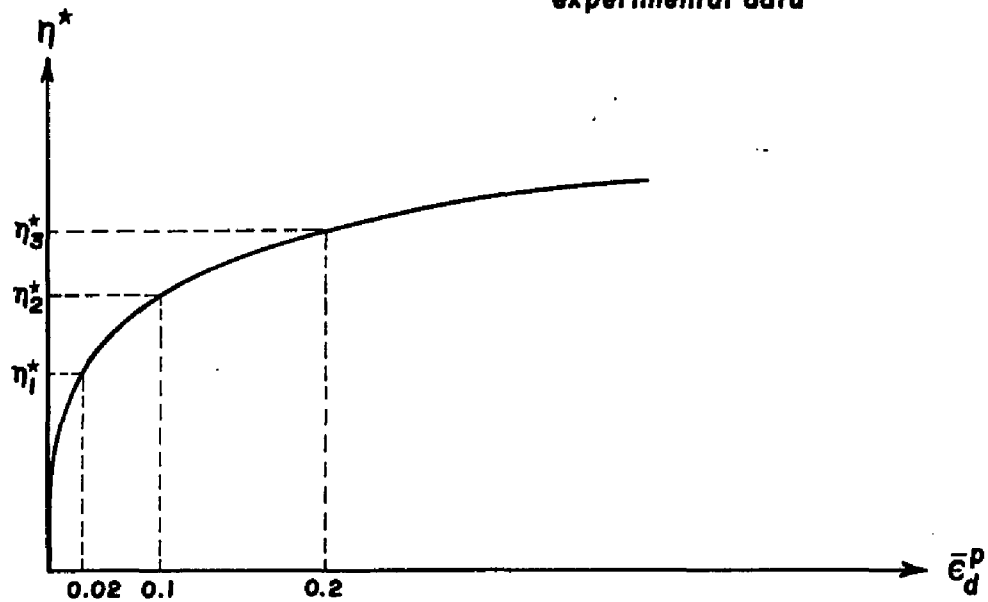


FIG. 2.4. HORIZONTAL YIELD LOCI BENEATH THE STATE BOUNDARY SURFACE.

Note that η^* is not the same as $\eta = q/p$, but they will be equal when the stress point in question is on the yield surface.

The additional plastic shear distortion is obtained by reading off from the strain-contour of Fig. 2.4 the incremental plastic strain obtained when dp and dq cause η^* to increase by $d\eta^*$, i.e.,

$$d\bar{\epsilon}_d^p = \frac{d\bar{\epsilon}_d^p}{d\eta^*} \cdot d\eta^*, \quad d\eta^* \geq 0. \quad (2.27)$$

The plastic-strain contour of Fig. 2.4 has to be determined from experimental data, requiring an experimental relationship between η^* and $\bar{\epsilon}_d^p$ for stress paths on which ϵ_0^p is held constant. Another possible procedure for determining this relationship involves performing undrained 'triaxial' tests on a normally consolidated clay and a lightly overconsolidated clay which has been isotropically overconsolidated from the same p_c [52].

Figure 2.5 illustrates how this plastic shear distortion is developed for various possible stress probes. The horizontal yield loci beneath F is denoted as G . Expansion of the yield locus is shown as a dashed line.

Stress probes (a) and (b) do not cause expansion in either F or G . In these cases, $d\eta^* = 0$ and no strain hardening can take place.

In cases (c) and (d), plastic shear distortion causes G to expand without producing plastic volumetric strains. In case (e), strain hardening causes F to expand without producing additional plastic shear distortion.

Finally, stress probe (f) causes both F and G to expand. In this situation, the resulting plastic strain increment is neither normal to F nor to G (Fig. 2.5g).

Evaluation of M and K_o .

The special case of a zero lateral strain condition may be obtained by setting $d\epsilon_3 = 0$. This leads to an expression for the geostatic lateral earth pressure coefficient K_o as follows:

$$K_o = \frac{3 - \eta_o}{2\eta_o + 3}, \quad (2.28)$$

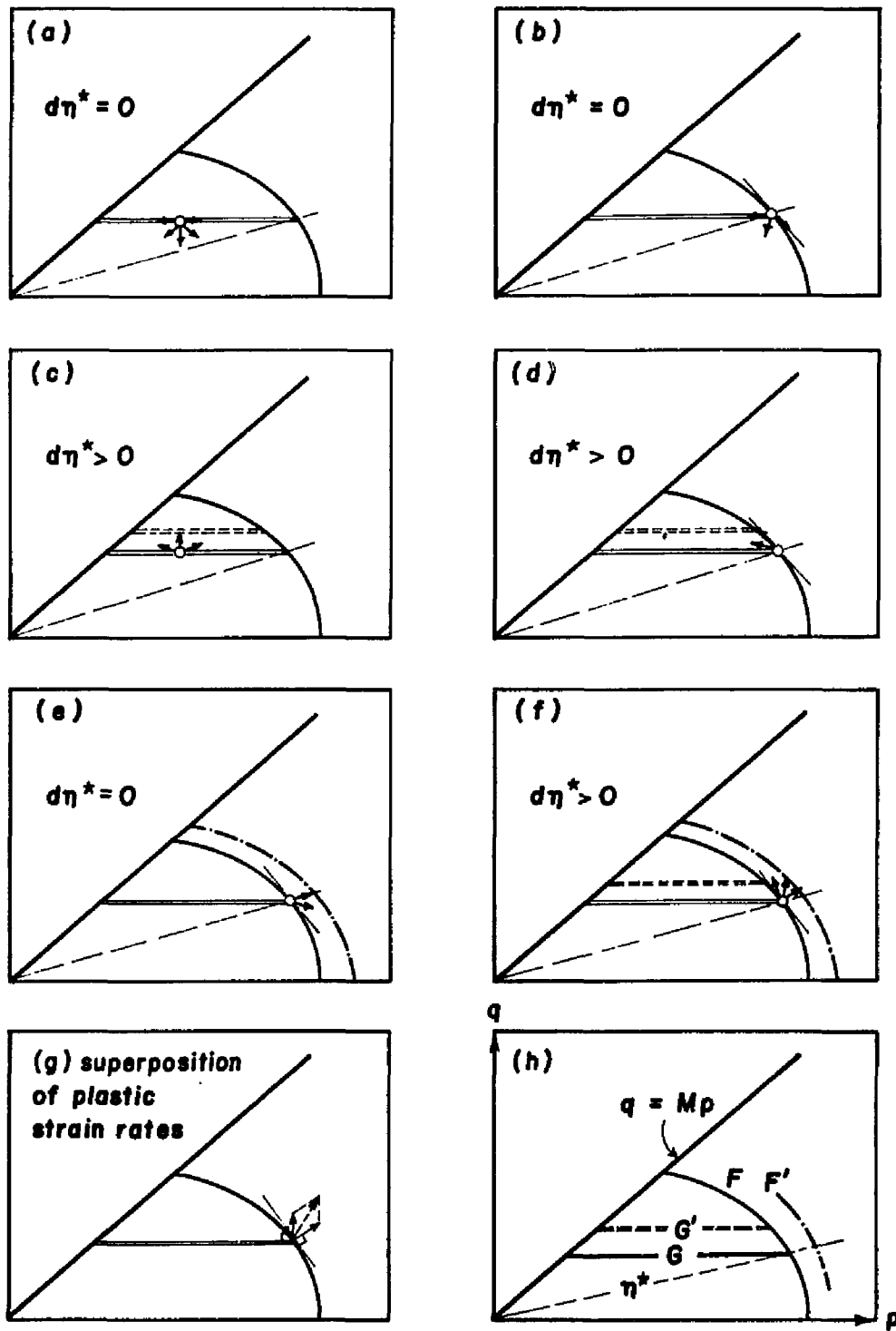


FIG. 2.5. DEVELOPMENT OF PLASTIC SHEAR DISTORTION BENEATH THE STATE BOUNDARY SURFACE.

where η_o is evaluated from the quadratic equation

$$\eta_o^2 + 3(1 - \kappa/\lambda)\eta_o - M^2 = 0 . \quad (2.29)$$

The parameter M may be deduced from the slope of the conventional Mohr-Coulomb rupture envelope. If ϕ' is the Mohr-Coulomb effective friction angle, then

$$M = \frac{6 \sin \phi'}{3 - \sin \phi'} . \quad (2.30)$$

Pender's model for overconsolidated clay

Pender [49] postulated that an overconsolidated yield locus given by

$$q = \eta p \quad (2.31)$$

exists. This overconsolidated yield locus is a radial line emanating from the origin of the p - q axes. If an associative flow rule is assumed, an overconsolidated soil would yield plastically in the direction normal to the conical surface generated by (2.31) about the p -axis.

He further postulated that the shape of the normally consolidated yield locus is not unique but depends primarily on the stress history experienced by the soil. Two such yield loci are drawn in Fig. 2.6 for a soil initially consolidated to an isotropic stress ($\eta_i = 0$), and for a soil initially consolidated to a K_o -condition ($\eta_i = \eta_o$).

At point A , where a linear overconsolidated yield locus intersects a normally isotropically consolidated yield locus, the plastic strain rate tensor lies somewhere within "angle ϑ " and is obtained by superposing the components of plastic volumetric and plastic deviatoric strain rates.

By setting $d\epsilon_2 = d\epsilon_3 = 0$ and assuming that σ_h/σ_u is constant, Pender obtained an expression for K_o as follows:

$$K_o = \frac{15 - 9\kappa/\lambda - 2M}{15 - 9\kappa/\lambda + 4M} . \quad (2.32)$$

Pender asserted that (2.32) predicts K_o "better" than does the Cam-clay model because it uses a yield locus appropriate for a K_o -consolidated sample.

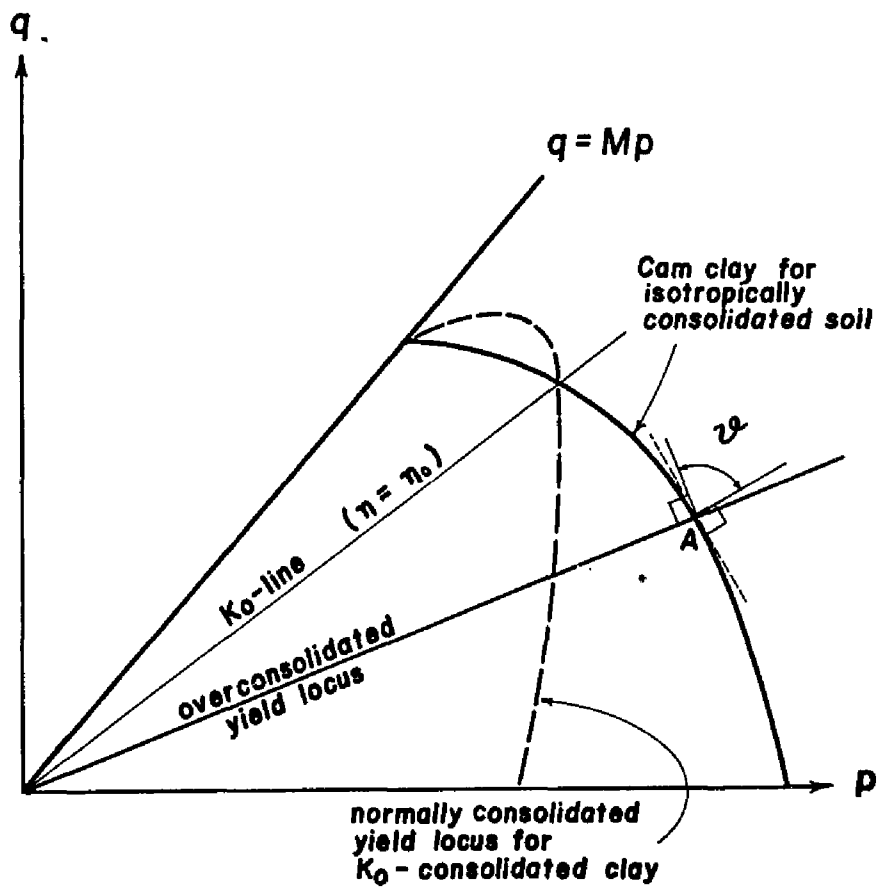


FIG. 2.6. PENDER'S YIELD LOCI FOR OVERCONSOLIDATED AND K_0 -CONSOLIDATED SOILS.

This model provides an interpretation of preconsolidation effects for stresses other than isotropic or K_o -conditions. Pender suggested a different value of M for materials under extension rather than compression.

Remarks

Several other derivatives of the Cam clay model have been proposed to account for preconsolidation effects for stresses other than isotropic or K_o -conditions. For example, Sekiguchi and Ohta [57] observed that the yield loci for most soils are not generally symmetric about the p -axis, and they attributed this lack of symmetry to anisotropy. Tavenas and Leroueil [62] noted that the yield surface for "destructured" Champlain clays are somewhat rotated about the K_o -line.

It should be noted, however, that these models are *time-independent* plasticity models and do not generally account for creep effects which develop with time.

2.4 EFFECT OF TIME

The Cam clay equations presented in Sec. 2.3 involve effective stress quantities and do not account for excess pore pressures that develop due to *hydrodynamic lag*. Furthermore, Cam clay is a *time-independent* plasticity model and does not include *time-dependent* or *creep* contributions.

This section treats time-dependency in terms of separate but interdependent volumetric and deviatoric components.

VOLUMETRIC CREEP

Notations

The following symbols for material properties will be used interchangeably:

$$C_c = \ln 10 \cdot \lambda \quad : \text{virgin compression index} \quad (2.33a)$$

$$C_r = \ln 10 \cdot \kappa \text{ :swelling/recompression index} \quad (2.33b)$$

$$C_\alpha = \ln 10 \cdot \psi \text{ :secondary compression coefficient .} \quad (2.33c)$$

Dual symbols are adopted because the natural logarithm-based quantities λ , κ , and ψ are simpler to deal with analytically, whereas the common logarithm-based quantities C_c , C_r , and C_α are more conveniently obtained graphically and are the standard parameters used in practice.

Primary/secondary consolidation

A typical plot of void ratio e versus common logarithm of time t in a one-dimensional consolidation test is shown in Fig. 2.7a. Taylor [64] identified the curve to consist of two phases: a *primary consolidation phase* for $t \leq t_p$ in which excess pore pressures dissipate, and a *secondary compression phase* for $t \geq t_p$ in which the soil continues to deform beyond the primary phase at a constant effective stress.

Casagrande suggested that the time $t_p = t_{100}$ at 100 percent consolidation can be empirically evaluated as the time-coordinate of the intersection point A of the tangent drawn at the point of inflection on the consolidation curve and the sloping line AB (which would be horizontal without the effect of creep).

Assuming that line AB in Fig. 2.7a is straight, the slope of this line in a common logarithm scale is defined as the *secondary compression coefficient* C_α and is given by

$$C_\alpha = \frac{-\Delta e}{\Delta \log t} = \frac{-\Delta e}{\log(t_2/t_1)}, \quad (2.34)$$

where $-\Delta e$ is the change in void ratio between times t_1 and t_2 in the secondary compression region. It should be noted that the values of C_α obtained from one-dimensional, and not isotropic, consolidation tests are not a true index of pure volumetric creep. However, Ladd and Preston [35] concluded that C_α is not significantly affected by the stress ratio σ_h/σ_v if the stress condition is not close to failure, as discussed subsequently. Thus the error involved in using C_α from one-dimensional tests should be small.

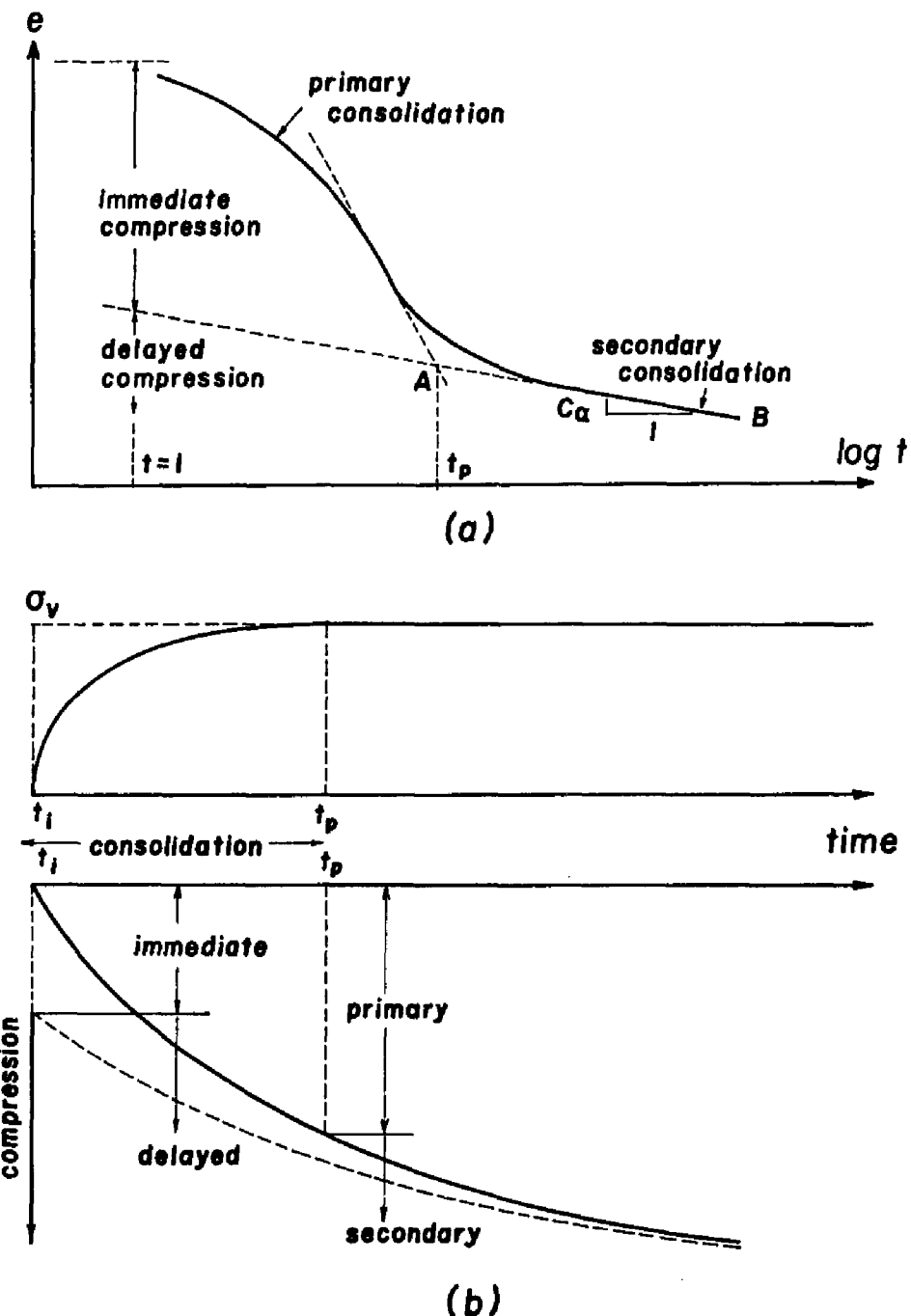


FIG. 2.7. DEFINITIONS OF PRIMARY/SECONDARY AND IMMEDIATE/DELAYED COMPRESSIONS.

Immediate/delayed compression

The total deformation may also be decomposed into an *immediate compression* part which occurs at the same instant the external load is applied, and a *delayed compression* part that persists indefinitely. This decomposition scheme was proposed by Bjerrum [8] and does not consider the effect of hydrodynamic lag.

These definitions of primary, secondary, immediate and delayed compressions are unified in Fig. 2.7b.

Development of a quasi-preconsolidation pressure

Bjerrum's graphical representation of the effect of delayed compression on the void ratio-vertical effective stress diagram for a one-dimensional vertical consolidation test is shown in Fig. 2.8. The diagram consists of contours of constant-time, each contour representing deformation after an equal duration of sustained loading. The diagram presented by Bjerrum showed these constant-time lines equally spaced, implying that the secondary compression coefficient C_s is constant.

The soil element portrayed in Fig. 2.8 is subjected to a sustained effective stress σ_o for a period of four log-cycles of time relative to t_i . During this time, volumetric creep occurs. Upon subsequent increase of vertical pressure, the soil exhibits apparent stiffening until a quasi-preconsolidation pressure σ_c is reached. Beyond σ_c , further immediate compression takes place along the virgin curve at which $t = t_i$.

At the end of virgin loading, the soil element creeps under the sustained vertical stress of $\sigma_o + \Delta\sigma$; thus, the previous apparent gain in stiffness with age is offset by deformation during the aging process. For example, after another period of four log-cycles of time relative to t_i , the stiffness previously gained is completely lost as the state point returns to the same time-contour it was on prior to application of $\Delta\sigma$.

If the undrained strength q_u varies linearly with the effective confining pressure (or with σ_v for a one-dimensional compression model), then the void ratio versus $\log q_u$ curve will also define a straight line parallel to the e - $\log \sigma_v$ plots in Fig. 2.8.

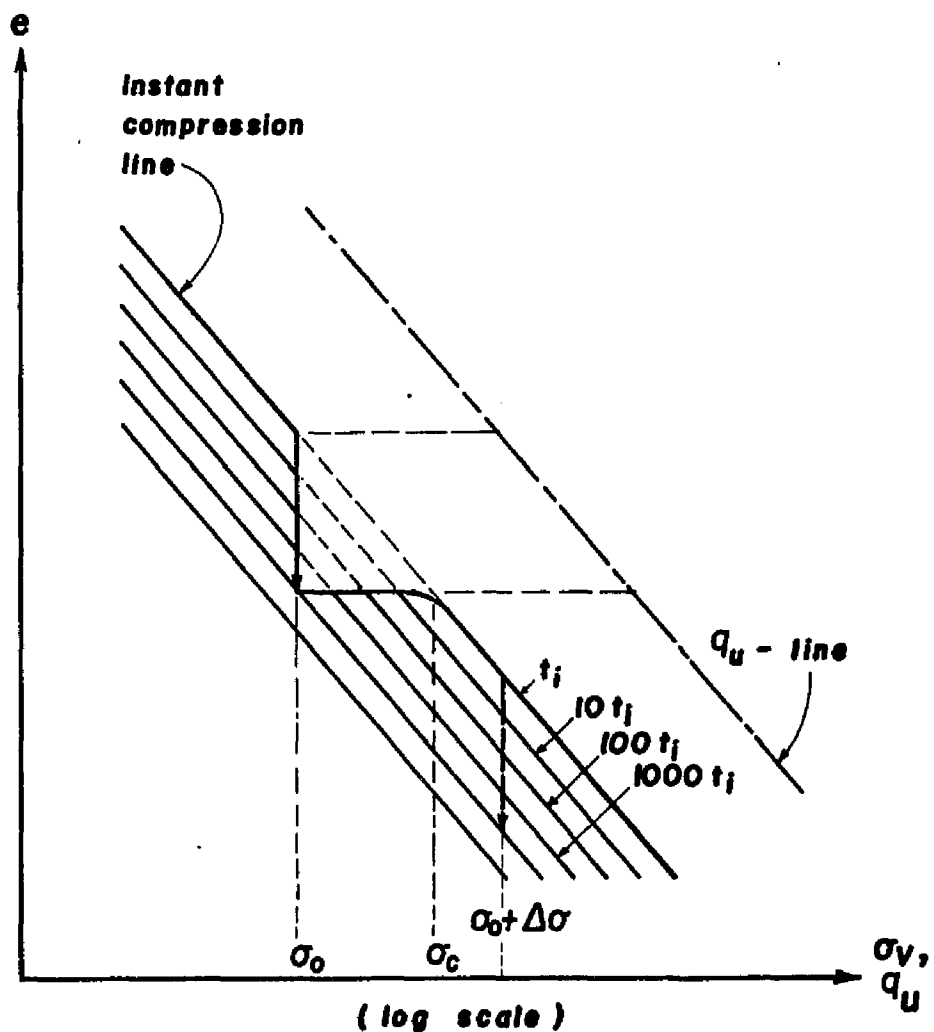


FIG. 2.8. BJERRUM'S MODEL FOR ONE-DIMENSIONAL COMPRESSION.

Hence, the effect of delayed compression is to increase the undrained shear strength from $(q_u)_o$ to $(q_u)_c$, such that

$$(q_u)_c = (q_u)_o \left(\frac{\sigma_c}{\sigma_o} \right) . \quad (2.35)$$

On the secondary compression coefficient C_α

Ladd and Preston [35] investigated the characteristics of C_α for Boston Blue Clay (BBC) and Vicksburg Buckshot Clay (VBC) from 'triaxial' and oedometer test results. From their test results, they concluded that C_α

- decreases with increasing overconsolidation ratio; they suggested that preloading with an overload can reduce the effects of secondary compression.
- increases with the compression index C_c .
- does not seem to depend on the thickness of the sample; the thickness of the sample affects only the time for primary consolidation to be complete; the slope of the straight-line portion of the curve appears to be constant.
- tends to increase at higher temperatures, although the data are limited.
- does not appreciably change with the stress ratio $K_h = \sigma_h/\sigma_v$, for $K_o < K_h < 1.0$; however, C_α increases as K_h approaches the stress ratio at failure, i.e., $K_o > K_h \rightarrow K_f$.
- affects the location of the void ratio versus $\log \sigma_c$ -curve.

From a compilation of different field records of long-term settlements and results for three types of clay tested, Mesri and Godlewski [44] indicated that the values of C_α are not a function of the load-increment ratio $\Delta\sigma/\sigma$, and that the ratio

$$R = C_\alpha / \left(\frac{-\partial e}{\partial(\log \sigma_v)} \right) \quad (2.36)$$

is constant for most cohesive soils. They reported values of R to lie within a narrow range of 0.025 to 0.10.

A three-dimensional representation of (2.36) in the e - $\log \sigma_v$ - $\log t$ space is shown in Fig. 2.9. The derivative $-\partial e/\partial(\log \sigma_v)$ is a general expression for slope which

takes the value C_r in the overconsolidated region and gradually increases to C_c in the normally consolidated region. Thus, C_α is smaller in the overconsolidated region than in the normally consolidated region.

In the region where $-\partial e/\partial(\log \sigma_v) = C_c$ is constant, C_α is also constant. Thus, the secondary consolidation curve beyond the end of primary compression is given by a straight line; the projection on the e - $\log \sigma_v$ plane of any locus of points on the surface of Fig. 2.9 representing equal duration of sustained load forms a contour similar to that in Fig. 2.8 proposed by Bjerrum.

DEVIATORIC CREEP

Rate process theory

The theory of rate processes was developed to describe the absolute reaction rates of various natural phenomena. This theory is based on the concept that atoms, molecules, and particles participate in a time-dependent flow or deformation process in flow units to overcome the constraint from relative movement imposed by energy barriers separating each equilibrium position [46].

Any displacement to the next equilibrium position is an activation process. The activation frequency v is given by

$$v = \frac{kT}{h} \exp\left(\frac{-\Delta F}{NkT}\right), \quad (2.37)$$

where ΔF is the potential energy barrier, k is the Boltzmann's constant (1.38×10^{-16} erg/ $^{\circ}$ K), T is the absolute temperature in $^{\circ}$ K, h is the Planck's constant (6.624×10^{-27} erg/sec), and N is the Avogadro number (6.02×10^{23}). This frequency has no preferred direction if the applied potential is randomly oriented; the barriers will be crossed with equal frequency in all directions.

An activation energy acquired from thermal or applied stress potential must be of sufficient magnitude to surmount the energy barriers. A directed shear force \vec{r} is a directional potential that distorts the energy barrier distribution.

The strain rate $\dot{\epsilon}$ in the direction of \vec{r} is the product of the net activation

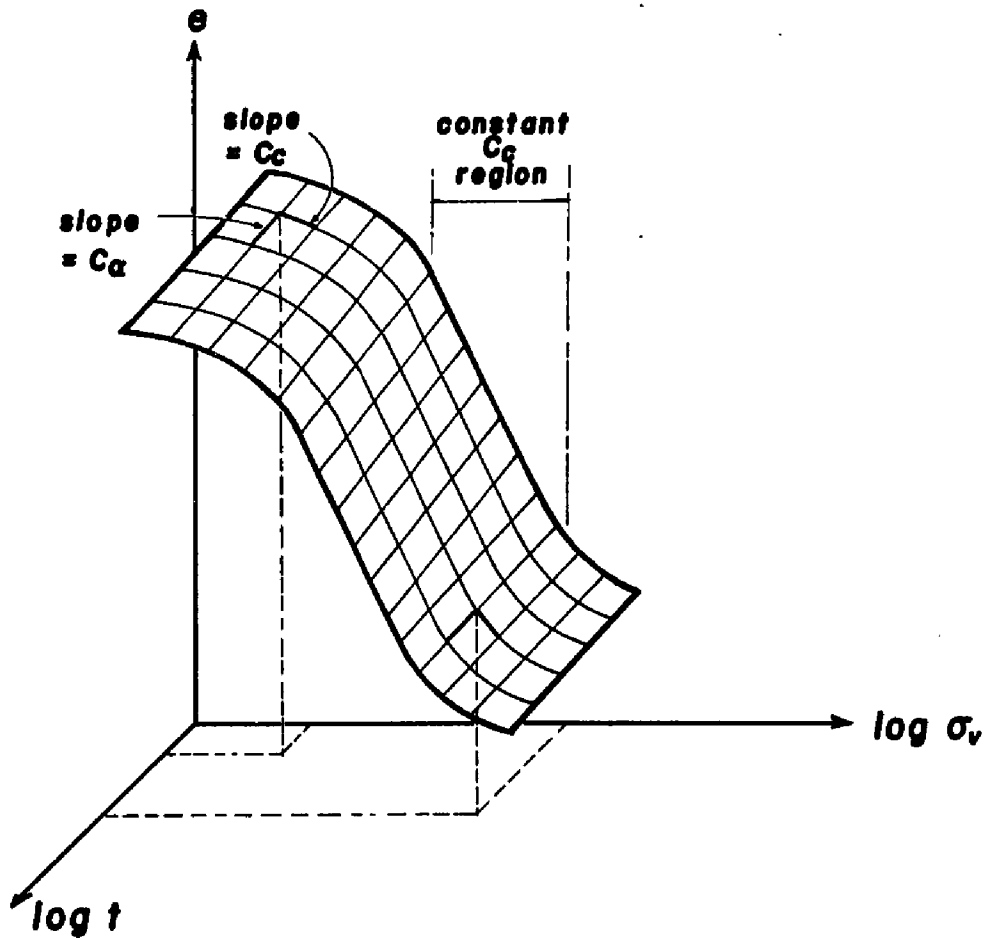


FIG. 2.9. MESRI/GODLEWSKI'S REPRESENTATION OF CONSOLIDATION IN $e-\ln \sigma_v - \ln t$ SPACE.

frequency and the proportion χ of the number of "successful jumps" of the activated flow units crossing the potential barrier, i.e.,

$$\dot{\epsilon} = 2\chi \frac{kT}{h} \exp\left(\frac{-\Delta F}{RT}\right) \sinh\left(\frac{\vec{r}\lambda_o}{2kT}\right), \quad (2.38)$$

where R is the gas constant (1.98 cal/ $^{\circ}$ K-mole) and λ_o is the distance between equilibrium positions.

Equation (2.38) can be approximated by the following expressions [46]:

$$\dot{\epsilon} \approx \frac{\vec{r}}{h} \exp\left(\frac{-\Delta F}{RT}\right), \text{ if } (\vec{r}\lambda_o/2kT) < 1; \quad (2.39a)$$

$$\approx \chi \frac{kT}{h} \exp\left(\frac{-\Delta F}{RT}\right) \exp\left(\frac{\vec{r}\lambda_o N}{2RT}\right), \text{ if } (\vec{r}\lambda_o/2kT) > 1. \quad (2.39b)$$

Taking the natural logarithm of both sides of (2.39b),

$$\ln \dot{\epsilon} = \left[\ln \left(\chi \frac{kT}{h} \right) - \frac{\Delta F}{RT} \right] + \left(\frac{\lambda_o N}{2RT} \right) \vec{r}. \quad (2.40)$$

Thus a straight line variation of $\ln \dot{\epsilon}$ versus shear stress \vec{r} is obtained using this approximation. It will be shown subsequently that the form of (2.40) also describes soil behavior on a macroscopic basis; thus rate process theory provides a good example of how phenomenological soil models may be interpreted on the microscopic level.

On the soil particle level, the activation energy may be interpreted as the shear stress required to break the individual soil particle contact points. The displacement, failure, slippage, or large abrupt movement that result from the contact point rupture are equivalent to "successful jumps" made over the potential energy barriers [41].

Singh-Mitchell creep equation

Singh and Mitchell [59] developed a phenomenological relationship for the time-dependent shear deformation behavior of clays from a collection of strain rate-time and strain-time 'triaxial' test data for clays subjected to a constant stress loading.

Irrespective of whether the clay is undisturbed or remolded, wet or dry, normally consolidated or overconsolidated, or tested drained or undrained, they observed that the plot of log strain rate versus log time for any specimen under a sustained deviator stress level \bar{D} ($=$ deviator stress/deviator stress at failure) in a 'triaxial' test is a straight line (see Fig. 2.10). There also exists a contour of parallel straight lines on the log strain-log time plane for different values of \bar{D} , tending to give higher strain rates for larger \bar{D} .

For values of \bar{D} in the range of about 30 to 90 percent, the logarithm of strain rate is approximately linear with \bar{D} , (Fig. 2.10). From the geometric properties of the curve shown in Fig. 2.10, the deviatoric creep equation is written

$$\dot{\epsilon}_a = A e^{\alpha \bar{D}} \left(\frac{t_i}{t} \right)^m , \quad (2.41)$$

where t_i is the reference time (usually 1.0), A is the strain rate at time t_i extrapolated to $\bar{D} = 0$, α is the slope of $\ln \dot{\epsilon}_a$ against \bar{D} , and $-m$ is the slope of $\ln \dot{\epsilon}_a$ versus $\ln t$ at any given \bar{D} .

Taking the natural logarithm of both sides of (2.41),

$$\ln \dot{\epsilon} = \left[\ln A + m \ln \left(\frac{t_i}{t} \right) \right] + \alpha \bar{D} , \quad (2.42)$$

which is seen to have a form very similar to (2.40) for a strain rate that results from an activation process.

It should be noted that (2.41) does not hold for values of \bar{D} outside of about 30 to 90 percent. It should also be pointed out that (2.41) was derived from 'triaxial' test data. Plane strain creep tests may exhibit a similar form of variation but the values of the creep parameters obtained from these tests are generally different.

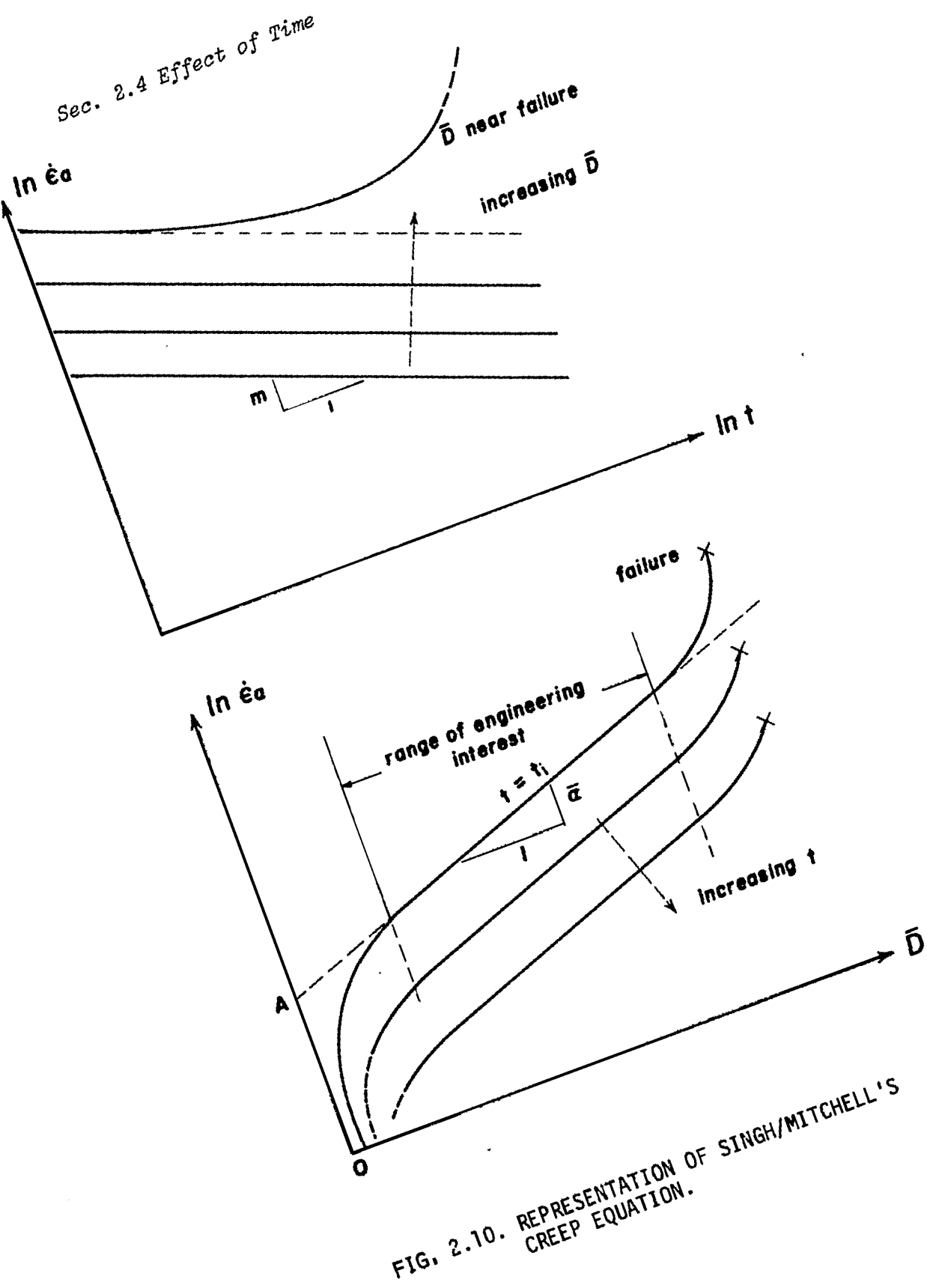
The axial strain ϵ_a may be obtained upon integration of (2.41) as follows:

$$\epsilon_a = \epsilon_i + \frac{A}{(1-m)} e^{\alpha \bar{D}} t_i^m t^{(1-m)} ; \text{ for } m \neq 1 \quad (2.43a)$$

$$= \epsilon_i + A e^{\alpha \bar{D}} \ln \left(\frac{t}{t_i} \right) ; \text{ for } m = 1 , \quad (2.43b)$$

where ϵ_i is the axial strain at reference time t_i .

30



Kondner's hyperbolic stress-strain model

The hyperbolic stress-strain equation for 'triaxial' stress states was proposed by Kondner [33] to model the deviator stress-axial strain curves for soils subjected to a constant rate of axial deformation. The hyperbola has the form

$$\sigma_1 - \sigma_3 = \frac{\epsilon_a}{a' + b'\epsilon_a}, \quad (2.44)$$

where $(\sigma_1 - \sigma_3)$ is the deviator stress and ϵ_a is the axial strain.

The *initial tangent modulus* of (2.44) is

$$E_i = \frac{d(\sigma_1 - \sigma_3)}{d\epsilon_a} \Big|_{\epsilon_a=0} = \frac{1}{a'}, \quad (2.45)$$

while the *ultimate value of the deviator stress* $(\sigma_1 - \sigma_3)$ is the asymptote

$$(\sigma_1 - \sigma_3)_{ult} = \lim_{\epsilon_a \rightarrow \infty} \left(\frac{\epsilon_a}{a' + b'\epsilon_a} \right) = \frac{1}{b'}. \quad (2.46)$$

Equation (2.44) can be rewritten as

$$\frac{\epsilon_a}{\sigma_1 - \sigma_3} = a' + b'\epsilon_a \quad (2.47)$$

which indicates that a plot of $\epsilon_a/(\sigma_1 - \sigma_3)$ versus ϵ_a is a straight line with intercept a' and slope b' .

Kondner pointed out that the ultimate strength and the initial tangent modulus of the hyperbola depend on the imposed strain rate. Hence, it may be postulated that each hyperbola corresponding to a particular imposed strain rate has an associated "deviatoric age". If this age is taken as the reference time t_i introduced in (2.41), then the hyperbola will give the the reference axial strain ϵ_i in (2.43a, b) at a given stress level \bar{D} .

2.5 PHENOMENOLOGICAL STRESS-STRAIN-TIME MODELS

Generalization of the time-independent and time-dependent constitutive equations applicable to 'triaxial' stress conditions has been developed by Kavazanjian [30], and later extended to plane strain by Bonaparte [11] and to three-dimensional principal-stress conditions by Kavazanjian, Bonaparte and Mitchell [32]. This section outlines the main features of their work and demonstrates, through their models, how the concepts of Secs. 2.3 and 2.4 may be unified in the solution of actual problems having simple geometrical configurations.

Preliminaries

Tensor formulation is a convenient means of representing stresses and strains in a general three-dimensional problem. It is implied throughout, unless otherwise stated, that "stresses" are Cauchy and "strains" are infinitesimal. Repeated subscripts are used to imply summation and the same tensor notations defined in Sec. 2.2 are adopted.

The general stress tensor consists of nine elements six of which are independent by symmetry:

$$\tilde{\sigma} = \begin{bmatrix} \sigma_{11} & \sigma_{12} & \sigma_{13} \\ \sigma_{21} & \sigma_{22} & \sigma_{23} \\ \sigma_{31} & \sigma_{32} & \sigma_{33} \end{bmatrix} = \sigma_{ij} = \sigma_{ji} . \quad (2.48)$$

Part of this tensor represents the spherical or volumetric component and the remainder represents the deviatoric component:

$$(\sigma_v)_{ij} = \frac{1}{3}\sigma_{kk}\delta_{ij} \quad (2.49)$$

$$(\sigma_d)_{ij} = \sigma_{ij} - (\sigma_v)_{ij} , \quad (2.50)$$

where $\frac{1}{3}\sigma_{kk}$ is the invariant octahedral normal stress.

Along the principal stress axes 1, 2, and 3, the off-diagonal terms of σ_{ij} will drop out. Thus, equations (2.49) and (2.50) reduce to

$$\tilde{\sigma}_v = \frac{\sigma_1 + \sigma_2 + \sigma_3}{3} \begin{bmatrix} 1 & 0 & 0 \\ 0 & 1 & 0 \\ 0 & 0 & 1 \end{bmatrix} \quad (2.51)$$

$$\tilde{\sigma}_d = \frac{1}{3} \begin{bmatrix} (2\sigma_1 - \sigma_2 - \sigma_3) & 0 & 0 \\ 0 & (-\sigma_1 + 2\sigma_2 - \sigma_3) & 0 \\ 0 & 0 & (-\sigma_1 - \sigma_2 + 2\sigma_3) \end{bmatrix}, \quad (2.52)$$

where σ_1 , σ_2 , and σ_3 are the principal stresses.

Similarly, the symmetric strain tensor

$$\tilde{\epsilon} = \begin{bmatrix} \epsilon_{11} & \epsilon_{12} & \epsilon_{13} \\ \epsilon_{21} & \epsilon_{22} & \epsilon_{23} \\ \epsilon_{31} & \epsilon_{32} & \epsilon_{33} \end{bmatrix} = \epsilon_{ij} = \epsilon_{ji} \quad (2.53)$$

may be separated into volumetric and deviatoric components

$$(\epsilon_v)_{ij} = \frac{1}{3} \epsilon_{kk} \delta_{ij} \quad (2.54)$$

$$(\epsilon_d)_{ij} = \epsilon_{ij} - (\epsilon_v)_{ij}, \quad (2.55)$$

where $\frac{1}{3}(\epsilon_{11} + \epsilon_{22} + \epsilon_{33})$ is the invariant octahedral normal strain.

Along the principal strain axes 1, 2, and 3

$$\tilde{\epsilon}_v = \frac{\epsilon_1 + \epsilon_2 + \epsilon_3}{3} \begin{bmatrix} 1 & 0 & 0 \\ 0 & 1 & 0 \\ 0 & 0 & 1 \end{bmatrix} \quad (2.56)$$

$$\tilde{\epsilon}_d = \frac{1}{3} \begin{bmatrix} (2\epsilon_1 - \epsilon_2 - \epsilon_3) & 0 & 0 \\ 0 & (-\epsilon_1 + 2\epsilon_2 - \epsilon_3) & 0 \\ 0 & 0 & (-\epsilon_1 - \epsilon_2 + 2\epsilon_3) \end{bmatrix}, \quad (2.57)$$

in which ϵ_1 , ϵ_2 , and ϵ_3 are the principal strains. The principal axes for strains do not generally coincide with the principal axes for stresses.

Kavazanjian model

Kavazanjian and Mitchell [31] postulated that both strain components (2.56) and (2.57) consist of immediate and delayed components analogous to immediate and delayed compression discussed in Sec. 2.4. Letting the roman superscripts I and D denote the immediate and delayed parts, respectively,

$$\tilde{\epsilon}_v = \tilde{\epsilon}_v^I + \tilde{\epsilon}_v^D \quad (2.58)$$

$$\tilde{\epsilon}_d = \tilde{\epsilon}_d^I + \tilde{\epsilon}_d^D. \quad (2.59)$$

■ **General volumetric model.** Kavazanjian's [30] general volumetric model shown in Fig. 2.11 consists of a series of parallel planes in the e - $\log \sigma_{\text{oct}}$ - $\log t$ space for different values of the stress level

$$\bar{D} = \frac{\sigma_1 - \sigma_3}{(\sigma_1 - \sigma_3)_f}, \quad (2.60)$$

in which σ_1 and σ_3 are the major and the minor principal stresses, respectively, and $(\sigma_1 - \sigma_3)_f$ is the deviator stress at failure which is assumed to be uniquely related to void ratio. The use of planes rather than curved surfaces implies that C_a and C_c are both constant, and that the planes represent a unique relationship among void ratio, effective stress, and time under sustained loading.

To illustrate how these parallel planes work, consider a typical plane corresponding to an arbitrary stress level \bar{D} in Fig. 2.12. During the period $\Delta \log t$ under a sustained load of $(\sigma_{\text{oct}})_1$, the soil experiences a time-dependent incremental compression as the state point moves from a to b on the \bar{D} -plane at the rate of C_a with respect to time. If σ_{oct} is increased while maintaining the stress level at \bar{D} , the state point moves at the rate of C_r (the recompression index) with respect to σ_{oct} until it reaches the quasi-preconsolidation pressure $(\sigma_{\text{oct}})_2$ at c ; further loading would cause it to move down the virgin curve at the rate of C_v .

The problem created by hydrodynamic lag in determining the model parameters was treated by extrapolating the secondary compression line to immediate time t_i in order to backfigure the immediate compression from the results of consolidation tests. This method is illustrated in Fig. 2.7 except that the octahedral stress σ_{oct} is replaced by the vertical stress σ_v for the one-dimensional compression case.

■ **General deviatoric model.** The general deviatoric model adopted by Kavazanjian [30] consists of Kondner's [33] hyperbolic stress-strain curve representing the immediate deviatoric behavior ⁽¹⁾, and the creep equation proposed by Singh and Mitchell [59] representing the delayed part.

⁽¹⁾ It will be shown in Chapter 5 that the "hyperbola" obtained from conventional undrained tests representing the "immediate" behavior also contains "time-dependent" components.

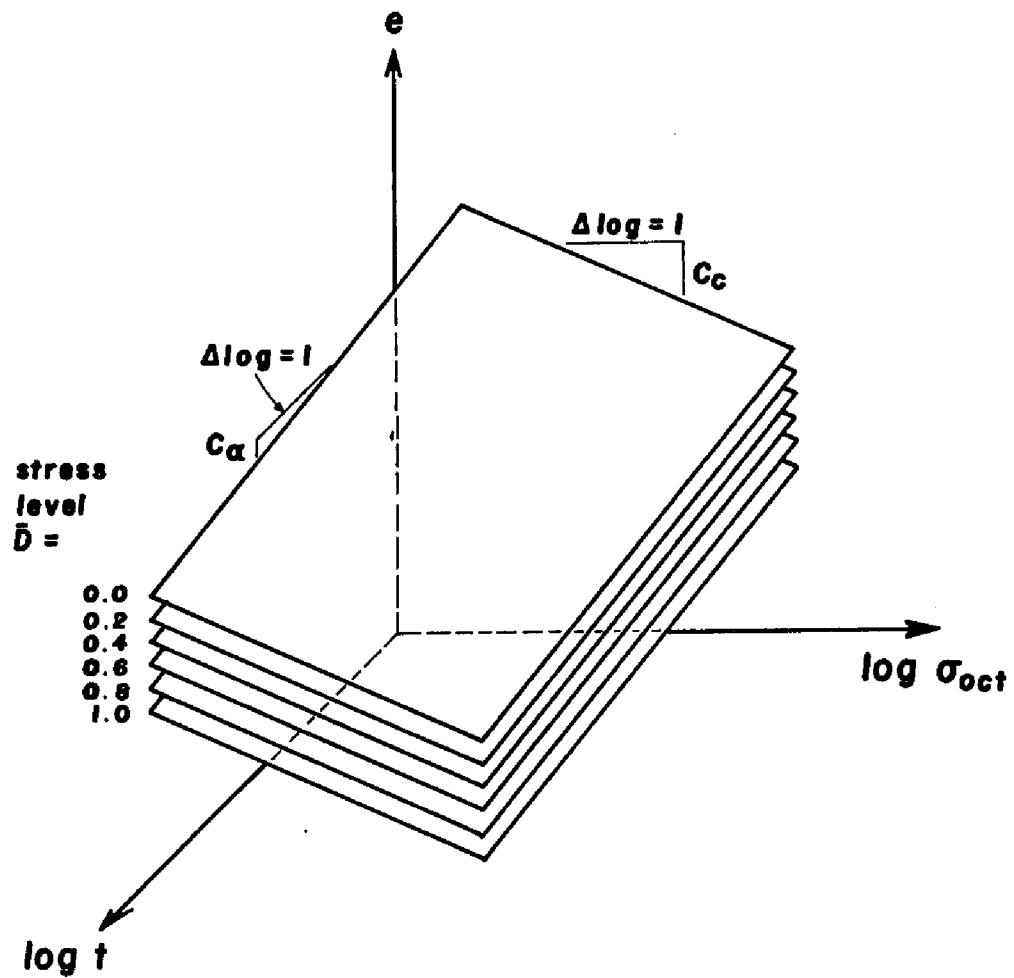


FIG. 2.11. KAVAZANJIAN'S GENERAL VOLUMETRIC MODEL.

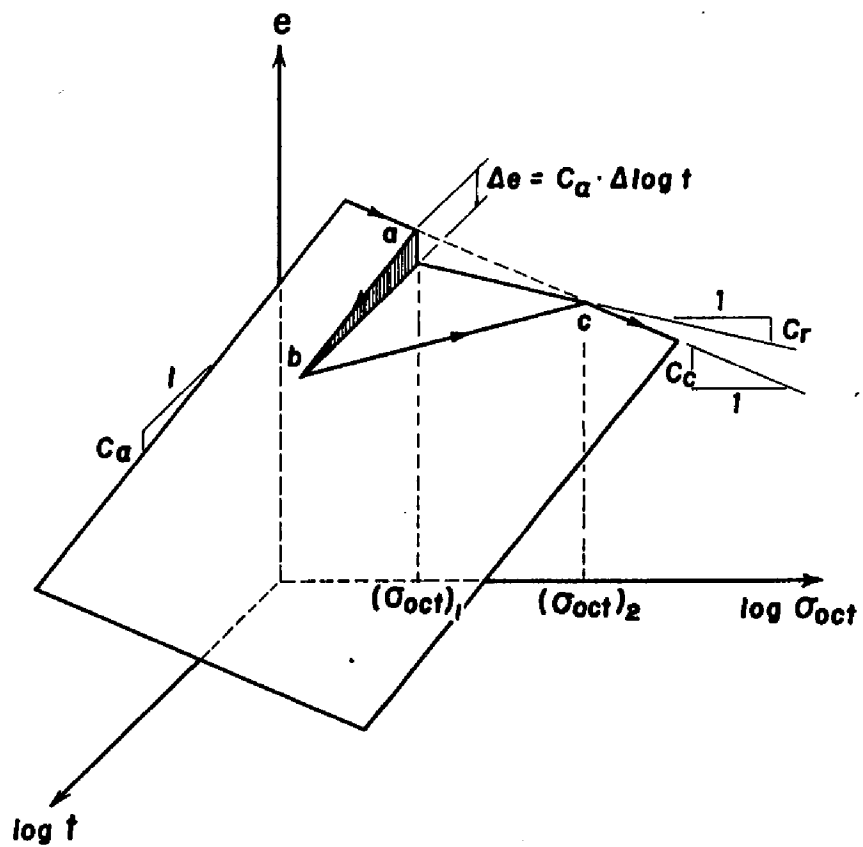


FIG. 2.12. ILLUSTRATION OF KAVAZANJIAN'S GENERAL VOLUMETRIC MODEL.

The hyperbola is defined by the parameters a and b , and R_f . A unique hyperbola encompassing all effective confining pressures is assumed, following Ladd and Foott's [36] postulate that in isotropically consolidated undrained triaxial tests, the deviator stress-strain diagram for a normally consolidated clay can be normalized by dividing the deviator stress by the effective confining pressure, i.e.,

$$\sigma_1 - \sigma_3 = \frac{\epsilon_a \sigma_e}{a + b\epsilon_a}, \quad (2.61)$$

where σ_e is the effective confining pressure. If the clay is lightly overconsolidated, the effective confining pressure is taken as the equivalent isotropic consolidation pressure that would characterize the soil if it were normally consolidated at its present void ratio.

Comparing (2.61) with Kondner's hyperbola (2.44), it can be seen that the hyperbolic parameters $a = a'\sigma_e$ and $b = b'\sigma_e$. Since the ultimate strength in (2.61) is obtained at an infinite strain, the multiplier R_f , termed the failure ratio by Duncan and Chang [17], is introduced to force the hyperbolic curve to pass through the failure point at an actual finite strain. Thus, equation (2.61) changes to

$$\sigma_1 - \sigma_3 = \frac{\epsilon_a \sigma_e}{a + b\epsilon_a} R_f. \quad (2.62)$$

A consequence of shearing is the development of excess pore pressure with axial strain. Kavazanjian [30] assumed a normalized hyperbolic plot of $\Delta u/\Delta u_f$ versus axial strain as follows:

$$\Delta u = \frac{\epsilon_a \Delta u_f}{a_p + b_p \epsilon_a}, \quad (2.63)$$

where a_p and b_p are pore pressure hyperbolic parameters (cf. (2.61)), Δu is the shear-induced excess pore pressure, and Δu_f is the excess pore pressure at failure, evaluated on the basis of the unique relationship between void ratio and deviator stress at failure in the volumetric model.

Figure 2.13 shows the general deviatoric model with the hyperbolic curve representing the immediate deviatoric behavior. As the soil is initially loaded, it shows an initial stiffness of E_i . Under a sustained deviatoric load, it creeps according to

(2.43a) or (2.43b), gradually diminishing in rate due to the deviatoric aging process simultaneously taking place. When the soil is unloaded or reloaded below the immediate curve, it behaves like a linear elastic solid with a modulus equal to E_i . Thus E_i is an elastic soil property.

It may be inferred from the foregoing that the hyperbolic curve representing the immediate behavior is, conceptually, a result of time-independent deviatoric yielding in the context of the theory of plasticity.

■ **Remarks.** The general volumetric model proposed by Kavazanjian and the volumetric Cam clay model have similarities. Kavazanjian's contour of parallel consolidation lines on the e -log p plane representing different values of \bar{D} is equivalent to the contour derived from the Cam clay model for different values of η . The limits $\bar{D} = (0, 1)$ correspond to the conditions $\eta = (0, M)$.

Kavazanjian's three-dimensional representation of the state point in the e -log σ_{oct} -log t space, however, does not describe the spacing of the parallel planes for different stress levels. If the original Cam-clay equations are to be used, in which η is linear in $\ln p$ for the case when e is constant, a four-dimensional representation of Kavazanjian's model in the e - σ_{oct} - η - t space such as that shown in Fig. 2.14 can be obtained.

Kavazanjian-Bonaparte-Mitchell Model

Bonaparte [11] adopted a modified strain tensor decomposition following Taylor's concept of primary and secondary consolidation as follows:

$$\tilde{\epsilon}_v = \tilde{\epsilon}_v^P + \langle \tilde{\epsilon}_v^S \rangle \quad (2.64)$$

$$\tilde{\epsilon}_d = \tilde{\epsilon}_d^I + \tilde{\epsilon}_d^D, \quad (2.65)$$

where the symbol $\langle \tilde{\epsilon}_v^S \rangle$ implies that the quantity is zero during the primary consolidation phase and $\tilde{\epsilon}_v^S$ when pore pressure dissipation is complete, while the roman superscripts P, S, I, and D denote the primary, secondary, immediate, and delayed components, respectively.

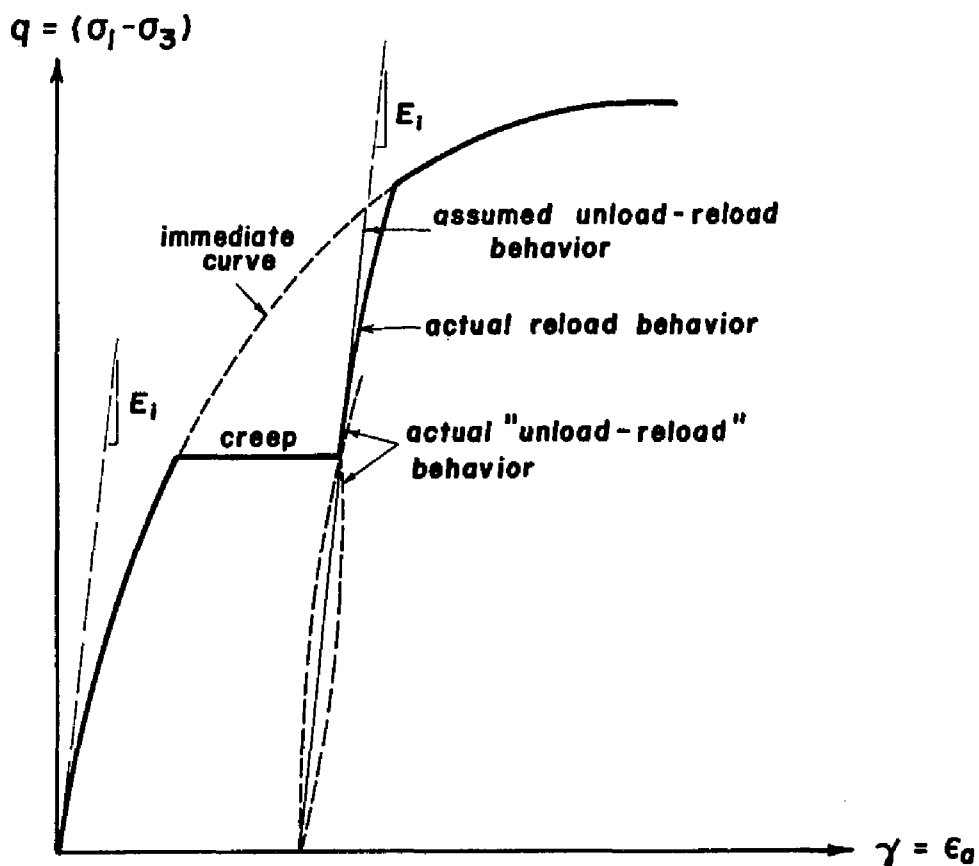


FIG. 2.13. KAVAZANJIAN'S GENERAL DEVIATORIC MODEL.

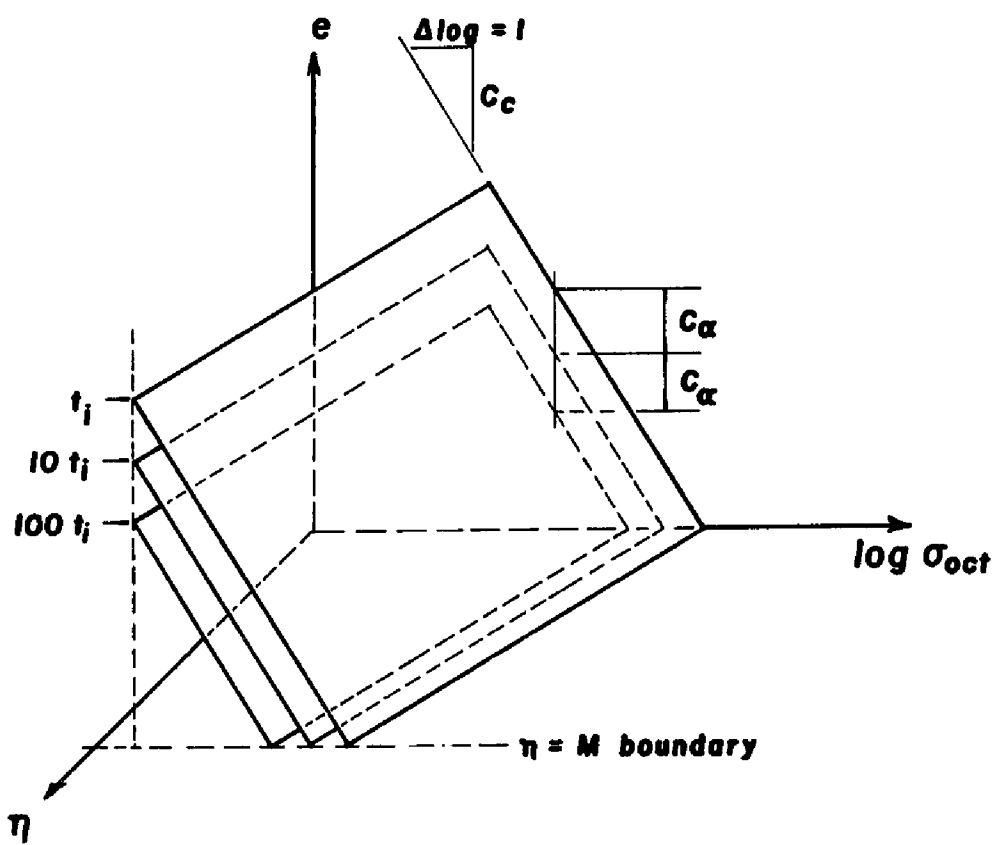


FIG. 2.14. UNIFICATION OF KAVAZANJIAN'S GENERAL VOLUMETRIC MODEL AND CAM CLAY MODEL.

■ **General volumetric model.** Bonaparte's choice of primary and secondary consolidation for the volumetric model is based on the assumption that the C_α -volumetric creep effect takes place only after all excess pore pressures have been completely dissipated.

The volumetric strain during primary consolidation consists of a component due to isotropic virgin loading and a component that accounts for the non-zero value of the stress ratio $\eta = q/p = (\sigma_1 - \sigma_3)/\sigma_{oct}$ obtained from the modified Cam clay yield surface. The incremental volumetric strain for a soil in virgin compression loading is given by

$$\Delta\epsilon_v^P = \frac{C_c}{1+e_o} \log \left(\frac{\sigma_{oct} + \Delta\sigma_{oct}}{\sigma_{oct}} \right) + \frac{C_c - C_r}{1+e_o} \log \left(\frac{M^2 + (\eta + \Delta\eta)^2}{M^2 + \eta^2} \right), \quad (2.66)$$

which is derived from the modified Cam clay theory.

Volumetric strains due to secondary consolidation of a soil with volumetric age t_v is obtained from the equation

$$\Delta\epsilon_v^S = \frac{C_\alpha}{1+e_o} \log \left(\frac{t_v + \Delta t}{t_v} \right), \quad (2.67)$$

which does not begin until primary consolidation is essentially complete. Bonaparte [11] defined the end of primary consolidation as the time at which excess pore pressure had dissipated to 95 percent of its initial value.

For stress states other than isotropic, Bonaparte [11] assumed that the volumetric creep strain induces a deviatoric creep component obtained upon application of the normality rule on the yield surface of the modified (time-independent) Cam clay theory.

■ **General Deviatoric model.** Kavazanjian, Bonaparte and Mitchell [32] postulated that deviatoric deformation consists of immediate and time-dependent components, represented by Kondner's hyperbolic curves for deviator stress/pore pressures and the Singh-Mitchell creep equation, respectively. They generalized the concept to three dimensions by defining the stress level \bar{D} as

$$\bar{D} = \frac{\tau_{oct}}{(\tau_{oct})_f}, \quad (2.68)$$

where τ_{oct} is the invariant octahedral shear stress and $(\tau_{\text{oct}})_f$ is the octahedral shear stress at failure, a quantity which is uniquely related to void ratio.

Along the principal stress axes, the value of $(\tau_{\text{oct}})_f$ alone does not completely define the principal stresses σ_1 , σ_2 , and σ_3 at failure. By assuming that the shear stress ratio

$$n = \frac{\sigma_2 - \sigma_3}{\sigma_1 - \sigma_3}, \quad \sigma_3 \leq \sigma_2 \leq \sigma_1 \quad (2.69)$$

remains constant, they used the three-dimensional failure criterion proposed by Lade and Duncan [37] for cohesionless soils

$$\frac{I_\sigma^3}{III_\sigma} = \text{constant}, \quad (2.70)$$

where $I_\sigma = \sigma_1 + \sigma_2 + \sigma_3$ and $III_\sigma = \sigma_1 \sigma_2 \sigma_3$ are the first and third effective principal stress invariants, respectively, to completely define the principal stresses at failure.

The effect of time-dependent deviatoric yielding has been considered by Bonaparte [11] by superimposing this deviatoric component with the creep strain increment obtained from the volumetric model. Since the latter component obeys the normality rule, the direction of the resulting creep strain increment deviates from the normal to the yield surface, resulting in nonassociative flow rule for creep strain, overall.

Remarks

The above works of Kavazanjian, Bonaparte, and Mitchell are phenomenological. Explicit relationships involving stresses, strains, and pore pressures need to be established to carry out a numerical solution to boundary-value problems using these results.

In Chapter 3 of this thesis, a constitutive model for the time-dependent behavior of soft clay will be formally developed. In Chapter 4, this model will be implemented within the framework of a finite element formulation. The model centers on Cam clay theory to model time-independent plasticity, and uses some of the explicit relationships presented in this section for the time-dependent aspects.

Chapter 3

**DEVELOPMENT
OF THE
CONSTITUTIVE EQUATION**

3.1 PRELIMINARIES

The objective of this chapter is to formally develop a creep-inclusive constitutive equation for cohesive soils, in a form suitable for finite element implementation, using continuum mechanics and the phenomenological relationships presented in Chapter 2. In order to represent the general three-dimensional state of stress, appropriate definitions of stress and strain terms are necessary.

Definitions

The volumetric effective stress p is defined as⁽¹⁾

$$p = \sigma_{\text{oct}} = \frac{1}{3}\sigma_{kk} = \frac{1}{3}I_{\sigma}, \quad (3.1)$$

where I_{σ} is the first invariant of the stress tensor σ_{ij} .

The deviatoric stress q is defined as

$$q = \frac{3}{\sqrt{2}}\tau_{\text{oct}} = \sqrt{\frac{3}{2}(\sigma_d)_{ij}(\sigma_d)_{ij}} = \sqrt{3\Pi_{\sigma_d}}, \quad (3.2)$$

where Π_{σ_d} is the second invariant of the deviatoric stress tensor $(\sigma_d)_{ij}$. In the 'triaxial' stress condition, the above definition for q reduces to $(\sigma_1 - \sigma_3)$, where σ_1 and σ_3 are the major (axial) and the minor (confining) principal stresses, respectively

⁽¹⁾ All stress terms considered henceforth are effective stresses (no pore pressure contribution). To simplify notation, these stresses will be written unprimed.

(cf. (2.9b)). In the undrained plane strain condition where $\sigma_2 = \frac{1}{2}(\sigma_1 + \sigma_3)$, the above definition for q reduces to $\frac{\sqrt{3}}{2}(\sigma_1 - \sigma_3)$.

The volumetric strain is defined as

$$\epsilon_v = 3\epsilon_{oct} = \epsilon_{kk} = I_\epsilon , \quad (3.3)$$

where I_ϵ is the first invariant of the strain tensor ϵ_{ij} .

The deviatoric strain γ is defined as

$$\gamma = \sqrt{2}\gamma_{oct} = \sqrt{\frac{2}{3}(\epsilon_d)_{ij}(\epsilon_d)_{ij}} = \sqrt{\frac{4}{3}\Pi_{\epsilon_d}} \quad (3.4)$$

where Π_{ϵ_d} is the second invariant of the deviatoric part of ϵ_{ij} . In the undrained 'triaxial' stress condition where the principal strains are $(\epsilon_a, -\frac{1}{2}\epsilon_a, -\frac{1}{2}\epsilon_a)$, the above definition for γ reduces to ϵ_a . In the undrained plane strain condition where $\epsilon_3 = -\epsilon_1$ and $\epsilon_2 = 0$, the above definition for γ reduces to $\frac{2}{\sqrt{3}}\epsilon_1$.

Abstract of the constitutive model

It is assumed in the model that the deformation behavior of 'wet' clays can be separated into a time-independent part and a time-dependent part.

The time-independent model is an elasto-plastic strain-hardening model whose yield surface, F , is the ellipsoid of the modified Cam clay model. This yield surface also serves as the plastic potential by the associative flow rule.

Time-independent volumetric strains consist of an elastic component whose magnitude is governed by the recompression index κ , and a plastic volumetric component obtained from the associative flow rule and consistency requirement on the yield surface F . Time-independent deviatoric strains contain an elastic component governed by the elastic shear modulus μ^e , and a plastic deviatoric component scaled from the normal to the yield surface based upon the plastic volumetric strain. ⁽¹⁾

⁽¹⁾ Note that this model slightly differs from the modified Cam clay model which assumes that deviatoric strains are purely plastic and do not contain any elastic part (refer to Sec. 2.3).

A three-dimensional generalization of the model is made by defining the state parameters with invariants p , q , ϵ_v , and γ to encompass all the components of the tensors σ_{ij} and ϵ_{kl} . Although the validity of this generalization is yet to be verified in three-dimensional applications, it has been shown [52] that this scheme accurately predicts the stress-strain behavior of ‘wet’ clays not only in the ‘triaxial’ (axisymmetric) compression case but under plane strain conditions as well.

It is further assumed (and later verified in Sec. 4.7) that the trace of the Cam clay model on the q - γ plane is a hyperbola of the form (2.61) representing the time-independent deviatoric behavior. The rules for loading, unloading, and reloading on this hyperbola follow those described by Kavazanjian [30]. However, only the hyperbolic parameters a (which gives the elastic shear modulus μ^*) and R_f are directly input. The remaining hyperbolic parameter b is backfigured from the volumetric Cam clay model.

Time-dependency is incorporated by allowing creep strains and quasi-preconsolidation to develop. The effect of quasi-preconsolidation is to make the size p_c of the yield surface grow with time.

To obtain the direction of the creep strain rate tensor $\dot{\epsilon}_{kl}^t$, the same normality rule is employed on the equivalent yield surface associated with the current stress state (p, q) if the soil were normally consolidated. To completely define $\dot{\epsilon}_{kl}^t$, the tensor normal to the yield surface is “scaled” either by prescribing the creep strain component along the volumetric axis according to the coefficient of secondary compression C_α (volumetric or C_α -scaling), or along the deviatoric axis according to the Singh-Mitchell creep function (deviatoric or Singh-Mitchell scaling). The coefficient of secondary compression also describes the rate at which the stiffness and strength increase with time due to quasi-preconsolidation effects.

The prescribed creep strain components are evaluated by defining “age variables” t_v and t_d . The volumetric age t_v is evaluated by measuring the e -distance of the state point (e, p, q) from the state boundary surface. The deviatoric age t_d is obtained by measuring the γ -distance of the state point (q, γ) from the hyperbolic curve.

Yield surface and hardening rule

The ellipsoidal yield surface of the modified Cam clay model given by

$$F = F(\sigma_{ij}, p_c) = \frac{q^2}{M^2} + p(p - p_c) = 0 \quad (3.5)$$

is used in this model. The size of this ellipsoid is represented by the current value of the preconsolidation pressure p_c . This yield surface also serves as the *plastic potential* by the associative flow rule; thus the normal to F defines the direction of the incremental plastic strain when the soil is yielding.

The “trace” of F on the q - γ plane is assumed to be given by the hyperbola

$$q = \frac{\gamma p_c}{a + b\gamma} R_f, \quad (3.6)$$

where a , b , and R_f are the hyperbolic parameters of (2.61). The validity of this assumption will be verified in Sec. 4.7.

The *strain-hardening rule* for F is defined by the isotropic consolidation curve. This is obtained from (2.19) by setting $\eta = 0$ and $p = p_c$, resulting in:

$$e_a - e - \lambda \ln p_c = 0, \quad (3.7)$$

where $e_a = e|_{p_c=1}$ on the isotropic consolidation curve.

Growth of preconsolidation pressure

Assume that the size p_c of the yield surface is given by the function

$$p_c = p_c(e_v^p, t_v). \quad (3.8)$$

Equation (3.8) states that the preconsolidation pressure p_c does not only grow because of time-independent strain-hardening but also expands with time, resulting in the development of a state of quasi-preconsolidation.

Consider the consolidation curve of Fig. 3.1. If a soil element at a state point at A , with volumetric age t_v , volumetrically creeps in time period $\Delta t = \Delta t_v$ at a constant effective stress, the soil linearly ages with natural time t in this time interval. Consequently, the soil would shrink by an amount

$$\Delta e = \psi \ln \left(1 + \frac{\Delta t_v}{t_v} \right) = (\lambda - \kappa) \ln \left(1 + \frac{\Delta p_c}{p_c} \right), \quad (3.9)$$

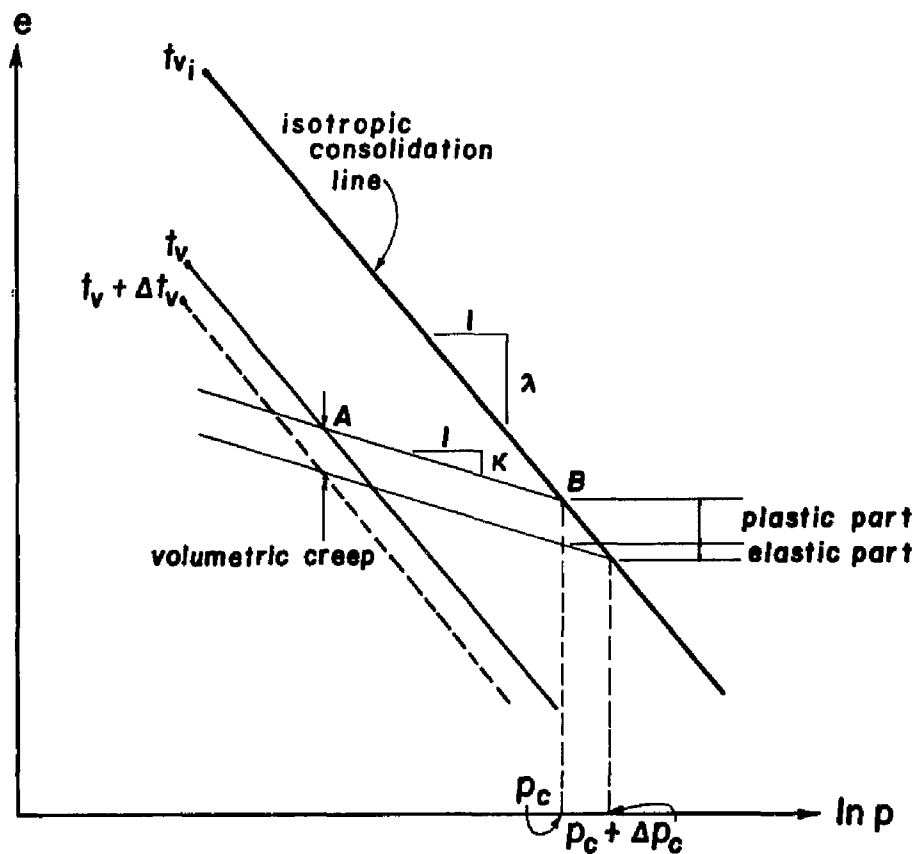


FIG. 3.1. DEVELOPMENT OF QUASI-PRECONSOLIDATION.

where the second term of (3.9) is deduced from geometrical construction in Fig. 3.1.

Solving for $\Delta p_c/p_c$,

$$\frac{\Delta p_c}{p_c} = \left[\left(1 + \frac{\Delta t_v}{t_v} \right)^{\psi/(\lambda-\kappa)} - 1 \right] \quad (3.10a)$$

$$= \frac{\psi}{\lambda - \kappa} \left(\frac{\Delta t_v}{t_v} \right) + \frac{1}{2!} \frac{\psi}{\lambda - \kappa} \left(\frac{\psi}{\lambda - \kappa} - 1 \right) \left(\frac{\Delta t_v}{t_v} \right)^2 + \dots \quad (3.10b)$$

where ψ is the secondary compression coefficient, while (3.10b) is the binomial series expansion of (3.10a). Taking the limit of $(\Delta p_c/\Delta t_v)$ as $\Delta t_v \rightarrow 0$,

$$\frac{\partial p_c}{\partial t_v} = \frac{\psi}{\lambda - \kappa} \frac{p_c}{t_v}. \quad (3.11)$$

Hence, the rate of growth of p_c decreases as the soil ages.

Again, consider the consolidation curve of Fig. 3.1. Along any line of constant t_v , say at $t_v = (t_v)_i$,

$$-\Delta e^e = \kappa \ln \left(1 + \frac{\Delta p_c}{p_c} \right) \quad (3.12)$$

$$-\Delta e^p = (\lambda - \kappa) \ln \left(1 + \frac{\Delta p_c}{p_c} \right), \quad (3.13)$$

so that $\Delta e = \Delta e^e + \Delta e^p$.

The plastic volumetric strain increment is obtained thus:

$$\Delta \epsilon_v^p = \frac{-\Delta e^p}{1+e} = \frac{\lambda - \kappa}{1+e} \ln \left(1 + \frac{\Delta p_c}{p_c} \right) \quad (3.14a)$$

$$= \frac{\lambda - \kappa}{1+e} \left[\left(\frac{\Delta p_c}{p_c} \right) - \frac{1}{2} \left(\frac{\Delta p_c}{p_c} \right)^2 + \dots \right], \quad (3.14b)$$

in which (3.14b) is the Taylor's series expansion of (3.14a). Taking the limit of $(\Delta p_c/\Delta \epsilon_v^p)$ as $\Delta \epsilon_v^p \rightarrow 0$,

$$\frac{\partial p_c}{\partial \epsilon_v^p} = \frac{1+e}{\lambda - \kappa} p_c. \quad (3.15)$$

Equations (3.15) and (3.11) are the hardening rules that describe the time-independent and the time-dependent components of the rate of growth of the size p_c of the yield surface, respectively.

3.2 FORMULATION OF THE CONSTITUTIVE EQUATION

In this section, a constitutive equation incorporating creep effects will be formulated in a rate form, leading to an incremental type of plasticity analysis after time discretization.

The strain rate tensor $\dot{\epsilon}_{kl}$ is decomposed, viz.:

$$\dot{\epsilon}_{kl} = (\dot{\epsilon}_{kl}^e + \dot{\epsilon}_{kl}^p) + \dot{\epsilon}_{kl}^t, \quad (3.16)$$

where the superscripts e and p denote the *time-independent* elastic and plastic parts, respectively, while the superscript t denotes the *time-dependent* (creep) plastic part. In principle, the above decomposition employs Bjerrum's [8] scheme of separating the total strains into immediate and delayed components.

Applying the associative flow rule on $\dot{\epsilon}_{kl}^p$,

$$\dot{\epsilon}_{kl}^p = \phi \frac{\partial F}{\partial \sigma_{kl}}, \quad (3.17)$$

and setting $l = k$,

$$\dot{\epsilon}_{kk}^p = \phi \frac{\partial F}{\partial \sigma_{kk}} \quad \text{or} \quad \dot{\epsilon}_v^p = \phi \frac{\partial F}{\partial p}, \quad (3.18)$$

where ϕ is a proportionality factor.

Rewriting (3.16) explicitly,

$$\dot{\epsilon}_{kl} = \left[(c_{ijkl}^e)^{-1} \dot{\sigma}_{ij} + \phi \frac{\partial F}{\partial \sigma_{kl}} \right] + \dot{\epsilon}_{kl}^t \quad (3.19)$$

or,

$$\dot{\sigma}_{ij} = c_{ijkl}^e \cdot \left(\dot{\epsilon}_{kl} - \phi \frac{\partial F}{\partial \sigma_{kl}} - \dot{\epsilon}_{kl}^t \right), \quad (3.20)$$

where c_{ijkl}^e is the rank-four elastic stress-strain tensor.

Consider the plastic potential $F = F(p, q, p_e) = F(\sigma_{ij}, p_e)$ given by (3.5).

Consistency requirement on F demands that the time rate of change

$$\dot{F} = \frac{\partial F}{\partial \sigma_{ij}} \dot{\sigma}_{ij} + \frac{\partial F}{\partial p_e} \dot{p}_e = 0, \quad (3.21)$$

where

$$\dot{p}_e = \dot{\epsilon}_v^p \frac{\partial p_e}{\partial \epsilon_v^p} \Big|_{t_v} + \frac{\partial p}{\partial t_v} \Big|_{\epsilon_v^p} \quad (3.22a)$$

$$= \frac{1+e}{\lambda-\kappa} p_e \dot{\epsilon}_v^p + \frac{\psi}{\lambda-\kappa} \frac{p_e}{t_v}, \quad (3.22b)$$

in which the symbol “ $|_()$ ” implies differentiation with the quantity inside the parentheses held fixed, while the terms in (3.22b) are obtained upon substitution of (3.11) and (3.15) in (3.22a).

Substituting (3.20) and (3.22b) in (3.21) and solving for ϕ ,

$$\phi = \chi \left[\frac{\partial F}{\partial \sigma_{ij}} c_{ijkl}^e (\dot{\epsilon}_{kl} - \dot{\epsilon}_{kl}^t) + \frac{\partial F}{\partial p_e} \frac{p_e}{t_v} \frac{\psi}{\lambda-\kappa} \right], \quad (3.23)$$

where

$$\frac{1}{\chi} = \frac{\partial F}{\partial \sigma_{ij}} c_{ijkl}^e \frac{\partial F}{\partial \sigma_{kl}} - \frac{\partial F}{\partial p_e} \frac{\partial F}{\partial p} \frac{1+e}{\lambda-\kappa} p_e. \quad (3.24)$$

Substituting ϕ in (3.20) and simplifying,

$$\dot{\sigma}_{ij} = c_{ijkl}^{ep} \dot{\epsilon}_{kl} - \dot{\sigma}_{ij}^t, \quad (3.25)$$

where c_{ijkl}^{ep} is the rank-four elasto-plastic stress strain tensor and $\dot{\sigma}_{ij}^t$ is the stress relaxation rate given, respectively, by:

$$c_{ijkl}^{ep} = c_{ijkl}^e - \chi \left(c_{ijpq}^e \frac{\partial F}{\partial \sigma_{pq}} \frac{\partial F}{\partial \sigma_{rs}} c_{rskl}^e \right) \quad (3.26)$$

and

$$\dot{\sigma}_{ij}^t = c_{ijkl}^{ep} \dot{\epsilon}_{kl}^t + \chi \left(\frac{\partial F}{\partial p_e} \frac{p_e}{t_v} \frac{\psi}{\lambda-\kappa} \right) c_{ijkl}^e \frac{\partial F}{\partial \sigma_{kl}}. \quad (3.27)$$

It can be seen that c_{ijkl}^{ep} has the major symmetry if and only if c_{ijkl}^e has the major symmetry.

When creep is ignored, $\dot{\epsilon}_{kl}^t = 0$, $\psi = 0$, and hence, $\dot{\sigma}_{ij}^t = 0$. If the response of the soil is perfectly elastic,

$$\dot{\sigma}_{ij} = c_{ijkl}^e \dot{\epsilon}_{kl} - \dot{\sigma}_{ij}^t, \quad (3.28)$$

where

$$\dot{\sigma}_{ij}^t = c_{ijkl}^e \dot{\epsilon}_{kl}^t . \quad (3.29)$$

Thus, the general creep-inclusive constitutive equation for 'wet' clay can be written in the rate form

$$\dot{\sigma}_{ij} = c_{ijkl} \dot{\epsilon}_{kl} - \dot{\sigma}_{ij}^t \quad (3.30)$$

by defining the tensors c_{ijkl} and $\dot{\sigma}_{ij}^t$ appropriately.

Evaluation of derivatives

The following are the derivatives of F (refer to (3.5)):

$$\frac{\partial F}{\partial p} = 2p - p_c \quad (3.31)$$

$$\frac{\partial F}{\partial q} = \frac{2q}{M^2} \quad (3.32)$$

$$\frac{\partial F}{\partial p_c} = -p . \quad (3.33)$$

By definitions (3.2) and (3.3) for p and q , respectively,

$$\frac{\partial p}{\partial \sigma_{ij}} = \frac{1}{3} \delta_{ij} \quad (3.34)$$

$$\frac{\partial q}{\partial \sigma_{ij}} = \frac{3}{2q} (\sigma_{ij} - \frac{1}{3} \sigma_{kk} \delta_{ij}) . \quad (3.35)$$

Thus, the normal at any point on F is given by:

$$\frac{\partial F}{\partial \sigma_{ij}} = \frac{\partial F}{\partial p} \frac{\partial p}{\partial \sigma_{ij}} + \frac{\partial F}{\partial q} \frac{\partial q}{\partial \sigma_{ij}} \quad (3.36a)$$

$$= \frac{1}{3} \left[\left(2 - \frac{9}{M^2} \right) p - p_c \right] \delta_{ij} + \frac{3}{M^2} \sigma_{ij} . \quad (3.36b)$$

Contraction of indices

Assuming that the tensor c_{ijkl} has the major symmetry (i.e., $c_{ijkl} = c_{klji}$), then the minor symmetries in ij and kl may likewise be established by observing that both $\dot{\sigma}_{ij}$ and $\dot{\epsilon}_{kl}$ are symmetric. Higher order tensors may then be reduced to lower order matrices by collapsing the indices according to the element ordering scheme shown below.

Table 3.1

I / J	i / k	j / l
1	1	1
2	2	2
3	3	3
4	1	2
4	2	1
5	2	3
5	3	2
6	1	3
6	3	1

The tensors $\dot{\sigma}_{ij}$ and $\dot{\epsilon}_{kl}$ are vectorized in the following form:

$$\{\dot{\sigma}_I\} = \begin{Bmatrix} \dot{\sigma}_{11} \\ \dot{\sigma}_{22} \\ \dot{\sigma}_{33} \\ \dot{\sigma}_{12} \\ \dot{\sigma}_{23} \\ \dot{\sigma}_{13} \end{Bmatrix}; \quad \{\dot{\epsilon}_J\} = \begin{Bmatrix} \dot{u}_{1,1} \\ \dot{u}_{2,2} \\ \dot{u}_{3,3} \\ \dot{u}_{1,2} + \dot{u}_{2,1} \\ \dot{u}_{2,3} + \dot{u}_{3,2} \\ \dot{u}_{1,3} + \dot{u}_{3,1} \end{Bmatrix} \quad (3.37a)$$

in three-dimensional analyses, and

$$\{\dot{\sigma}_I\} = \begin{Bmatrix} \dot{\sigma}_{11} \\ \dot{\sigma}_{22} \\ \dot{\sigma}_{33} \\ \dot{\sigma}_{12} \end{Bmatrix}; \quad \{\dot{\epsilon}_J\} = \begin{Bmatrix} \dot{u}_{1,1} \\ \dot{u}_{2,2} \\ \dot{u}_{3,3} \\ \dot{u}_{1,2} + \dot{u}_{2,1} \end{Bmatrix} \quad (3.37b)$$

in plane strain and axisymmetric (torsionless) analyses. Note that engineering definitions for $\{\dot{\epsilon}_J\}$ are employed, in which engineering shear strains are twice the tensorial shear strains.

The general creep-inclusive constitutive equation for 'wet' clay is then written in the matrix form

$$\{\dot{\sigma}_I\} = [C_{IJ}]\{\dot{\epsilon}_J\} - \{\dot{\sigma}_I^e\}, \quad (3.38)$$

where the matrix subscripts I and J are obtained by contracting the tensor indices i, j, k , and l for three-dimensional problems in the manner shown in Table 3.1. As an example, element c_{1112} in which $(i, j, k, l) = (1, 1, 1, 2)$, is re-labeled C_{14} where $(I, J) = (1, 4)$. The first five rows in Table 3.1 also apply to axisymmetric/plane strain cases.

The expression for the elasto-plastic c_{ijkl}^{ep} in matrix form becomes

$$[C_{IJ}^{ep}] = [C_{IJ}^e] - \chi [C_{IJ}^e] \left\{ \frac{\partial F}{\partial \sigma_K} \right\} \cdot \left\{ \frac{\partial F}{\partial \sigma_L} \right\}^T [C_{LJ}^e] \quad (3.39)$$

where

$$\frac{1}{\chi} = \left\{ \frac{\partial F}{\partial \sigma_1} \right\} [C_{IJ}^e] \left\{ \frac{\partial F}{\partial \sigma_J} \right\} + p p_c (2p - p_c) \frac{1+e}{\lambda - \kappa}, \quad (3.40)$$

while the normal at any point on F becomes

$$\left\{ \frac{\partial F}{\partial \sigma_1} \right\} = \begin{Bmatrix} \bar{p} + 3\sigma_{11}/M^2 \\ \bar{p} + 3\sigma_{22}/M^2 \\ \bar{p} + 3\sigma_{33}/M^2 \\ 6\sigma_{12}/M^2 \\ 6\sigma_{23}/M^2 \\ 6\sigma_{13}/M^2 \end{Bmatrix}, \quad \bar{p} = \frac{1}{3} \left[\left(2 - \frac{9}{M^2} \right) p - p_c \right]. \quad (3.41)$$

Elastic stress-strain matrix

The stress-strain matrix $[C_{IJ}^e]$ requires at least two independent elastic material properties for complete definition. Two properties are adequate by assuming homogeneity, material isotropy, and major/minor symmetries in c_{ijkl}^e .

A combination of elastic bulk modulus K^e and elastic shear modulus μ^e completely defines $[C^e]$ as follows:

$$[C_{IJ}^e] = \begin{bmatrix} C_1 & C_2 & C_2 & 0 & 0 & 0 \\ C_2 & C_1 & C_2 & 0 & 0 & 0 \\ C_2 & C_2 & C_1 & 0 & 0 & 0 \\ 0 & 0 & 0 & \mu^e & 0 & 0 \\ 0 & 0 & 0 & 0 & \mu^e & 0 \\ 0 & 0 & 0 & 0 & 0 & \mu^e \end{bmatrix}, \quad (3.42)$$

where $C_1 = K^e + \frac{4}{3}\mu^e$ and $C_2 = K^e - \frac{2}{3}\mu^e$.

The elastic bulk modulus is obtained from the volumetric Cam clay model by rewriting (2.16) as follows:

$$dp = \left(\frac{1+e}{\kappa} p \right) d\epsilon_v^e, \quad (3.43a)$$

or,

$$K^e = \frac{1+e}{\kappa} p. \quad (3.43b)$$

Thus the bulk modulus increases linearly with the volumetric stress p , necessitating a positive (non-zero) value of p at any stage of the solution.

The elastic shear modulus is backfigured from the initial tangent modulus of the hyperbolic curve (3.6) as follows:

$$\left. \frac{dq}{d\gamma} \right|_{\gamma=0} = \frac{p_c R_f}{a} = \frac{3}{2} \frac{d\tau_{oct}}{d\gamma_{oct}} = 3\mu^e \quad (3.44a)$$

or,

$$\mu^e = \frac{p_c R_f}{3a} . \quad (3.44b)$$

Thus, the shear modulus increases linearly with the size p_c of the yield surface, necessitating that the soil be initially preconsolidated to develop a non-zero elastic shear stiffness.

3.3 CREEP STRAIN RATE

The quantities in (3.27) that remain to be evaluated are the volumetric age t_v and the components of the creep strain rate tensor $\dot{\epsilon}_{kl}^t$. The latter components are insignificant for clays that have undergone unloading or long period of natural aging. For 'young' clays, however, creep effects can constitute a relatively large fraction of the total deformation.

The direction of $\dot{\epsilon}_{kl}^t$ is obtained from the normality rule applied to the equivalent yield surface associated with the stress state (p, q) as follows:

$$\dot{\epsilon}_{kl}^t = \varphi \frac{\partial F}{\partial \sigma_{kl}} , \quad (3.45)$$

where φ is a proportionality factor and F is the equivalent yield surface evaluated using (3.5), whose size is given by

$$p_o = p + \frac{q^2}{M^2 p} \leq p_c \quad (3.46)$$

which equals p_c for normally consolidated soils (refer to Fig. 3.2).

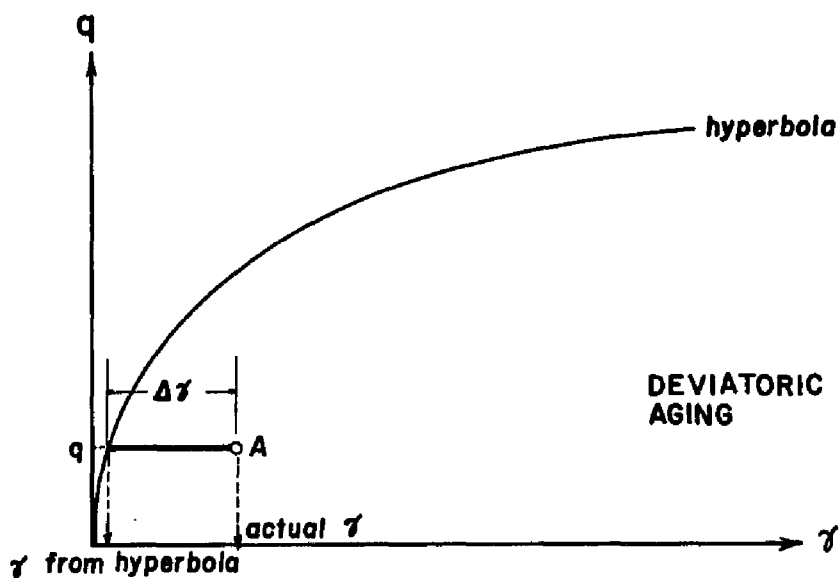
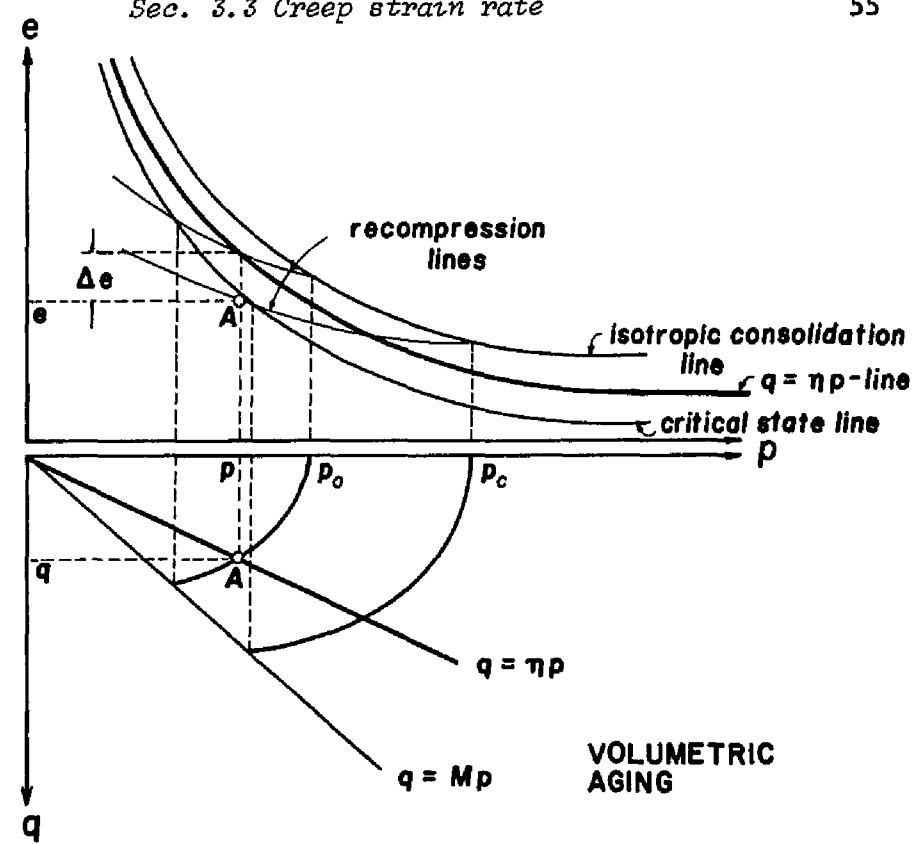


FIG. 3.2. EVALUATION OF VOLUMETRIC AND DEVIATORIC AGES.

The magnitude of $\dot{\epsilon}_{kl}^t$ is obtained by degenerating this tensor either to an isotropic tensor or a 'triaxial' tensor and appropriately scaling $\varphi (\partial F / \partial \sigma_{kl})$ using either the C_α - creep law for the isotropic condition, or the Singh-Mitchell creep equation for the 'triaxial' stress condition. These two methods are herein called *volumetric scaling* and *deviatoric scaling*, respectively.

Volumetric scaling

The magnitude of the trace of $\dot{\epsilon}_{kl}^t$ along the volumetric axis p is a measure of the *volumetric creep rate* for the soil. The volumetric part of $\dot{\epsilon}_{kl}^t$ is

$$(\dot{\epsilon}_v^t)_{kl} = \frac{1}{3} \dot{\epsilon}_v^t \delta_{kl} = \frac{1}{3} \varphi \frac{\partial F}{\partial \sigma_{ii}} \delta_{kl}. \quad (3.47)$$

Recalling that the rate of secondary compression is given by the index C_α (ψ in the natural log scale),

$$\dot{\epsilon}_v^t = \varphi \frac{\partial F}{\partial \sigma_{ii}} = \frac{\psi}{(1+e)t_v} \quad (3.48)$$

or,

$$\varphi = \frac{\psi}{(1+e)t_v} \left(\frac{\partial F}{\partial \sigma_{ii}} \right)^{-1}. \quad (3.49)$$

Upon substitution of φ in (3.45), the creep strain tensor is obtained as

$$\dot{\epsilon}_{kl}^t = \left[\frac{\psi}{(1+e)(2p-p_o)t_v} \right] \frac{\partial F}{\partial \sigma_{kl}}. \quad (3.50)$$

The above expression for $\dot{\epsilon}_{kl}^t$ is singular when $p = p_o/2$ (i.e., when the point is on the critical state line) because the normal to F at this point is vertical and can not be scaled in the (horizontal) p -direction. If ψ is assumed constant, (3.50) will predict higher deviatoric creep strain rates at higher deviatoric stress levels.

■ **Volumetric age.** The volumetric age of the soil is obtained by examining its location in the $e-p-q$ space relative to the position it would occupy if it were normally consolidated. The volumetric age is back-calculated based upon the secondary compression coefficient C_α and the void ratio-distance of the state point from the state boundary surface.

Figure 3.2 shows an overconsolidated soil element A with coordinates (e_1, p, q) beneath the state boundary surface. This soil element somehow developed a pre-consolidation p_c , either by unloading or by natural aging. In this situation, the quantities e_1 , p , q , and p_c are not all independent, but satisfy the relationship

$$e_1 = e_a - (\lambda - \kappa) \ln p_c - \kappa \ln p . \quad (3.51)$$

The location of soil element A on the void ratio axis would be given by

$$e_2 = e_a - (\lambda - \kappa) \ln p_o - \kappa \ln p , \quad (3.52)$$

if it were normally consolidated.

Thus the *volumetric age* of the soil is computed from (2.34) to be

$$t_v = (t_v)_i \exp \left(\frac{e_2 - e_1}{\psi} \right) \quad (3.53a)$$

$$= (t_v)_i \text{antilog} \left(\frac{e_2 - e_1}{C_\alpha} \right) , \quad (3.53b)$$

where $(t_v)_i$ is the *instant volumetric time* (usually taken as 1.0) associated with the virgin consolidation curve.

Deviatoric scaling

Consider the deviatoric component of $\dot{\epsilon}_{kl}^t$ given by:

$$(\dot{\epsilon}_d^t)_{kl} = \varphi \left(\frac{\partial F}{\partial \sigma_{kl}} - \frac{1}{3} \frac{\partial F}{\partial \sigma_{ii}} \delta_{kl} \right) . \quad (3.54)$$

The magnitude of this deviatoric tensor is evaluated as

$$\begin{aligned} |(\dot{\epsilon}_d^t)_{kl}| &= \sqrt{(\dot{\epsilon}_d^t)_{kl} (\dot{\epsilon}_d^t)_{kl}} \\ &= \varphi \left[\frac{\partial F}{\partial \sigma_{kl}} \frac{\partial F}{\partial \sigma_{kl}} - \frac{1}{3} \left(\frac{\partial F}{\partial p} \right)^2 \right]^{1/2} . \end{aligned} \quad (3.55)$$

In undrained 'triaxial' creep tests, the tensor $\dot{\epsilon}_{kl}^t$ would simplify to

$$\dot{\epsilon}_{kl}^t = (\dot{\epsilon}_d^t)_{kl} = \begin{bmatrix} \dot{\epsilon}_a^t & 0 & 0 \\ 0 & -\frac{1}{2}\dot{\epsilon}_a^t & 0 \\ 0 & 0 & -\frac{1}{2}\dot{\epsilon}_a^t \end{bmatrix} , \quad (3.56)$$

which is purely deviatoric because drainage is suppressed. The magnitude of this tensor is obtained from the Singh-Mitchell equation to be

$$|(\dot{\epsilon}_d^t)_{kl}| = \sqrt{\frac{3}{2}} \dot{\epsilon}_a^t = \sqrt{\frac{3}{2}} A e^{\alpha \bar{D}} \left[\frac{(t_d)_i}{t_d} \right]^m, \quad (3.57)$$

where t_d is the deviatoric age of the soil and $(t_d)_i$ is the immediate deviatoric time (usually taken as 1.0) associated with the immediate hyperbolic stress-strain curve (3.6).

Comparing (3.55) and (3.57) and solving for φ ,

$$\varphi = \sqrt{\frac{3}{2}} A e^{\alpha \bar{D}} \left[\frac{(t_d)_i}{t_d} \right]^m \left[\frac{\partial F}{\partial \sigma_{kl}} \frac{\partial F}{\partial \sigma_{kl}} - \frac{1}{3} \left(\frac{\partial F}{\partial p} \right)^2 \right]^{-1/2}. \quad (3.58)$$

Substituting φ in (3.45),

$$\dot{\epsilon}_{kl}^t = \sqrt{\frac{3}{2}} A e^{\alpha \bar{D}} \left[\frac{(t_d)_i}{t_d} \right]^m \left[\frac{\partial F}{\partial \sigma_{pq}} \frac{\partial F}{\partial \sigma_{pq}} - \frac{1}{3} \left(\frac{\partial F}{\partial p} \right)^2 \right]^{-1/2} \cdot \frac{\partial F}{\partial \sigma_{kl}}. \quad (3.59)$$

The above expression for $\dot{\epsilon}_{kl}^t$ is singular when $p = p_o$ (the isotropic condition) because the normal to F at this point is horizontal and can not be scaled in the (vertical) q -direction. Further, (3.59) strictly holds only for values of \bar{D} of about 30 to 90 percent, the same restriction that governs the validity of the Singh-Mitchell equation. For values of \bar{D} close to zero (the isotropic condition), (3.59) would over-predict the creep strain rate; for values of \bar{D} close to unity (the failure condition), (3.59) would underpredict the creep strain rate (consult Fig. 2.10).

■ **Deviatoric stress level and failure strength.** The deviatoric stress level \bar{D} that appears in (3.57) is defined as

$$\bar{D} = \frac{q}{q_{ult}}, \quad (3.60)$$

where q is given by (3.2) and q_{ult} is the ultimate or failure strength which is assumed to be uniquely related to void ratio. This is equivalent to Kavazanjian, Bonaparte, and Mitchell's [32] definition (2.68) except that they used τ_{oct} instead of q , and to Kavazanjian's [30] definition (2.60) for the 'triaxial' stress condition.

The ultimate strength of the soil preconsolidated to a pressure p_c and allowed to trace the swelling curve (or the elastic wall) is

$$q_{ult} = \frac{1}{2} M p_c . \quad (3.61)$$

This ultimate strength is the q -coordinate of the intersection point of the elliptical yield surface F and the critical state line (2.6).

If the condition is undrained ($e = \text{constant}$), the ultimate strength of the soil is given by

$$q_{ult} = \left(\frac{1}{2}\right)^{(1-\kappa/\lambda)} M p_c . \quad (3.62)$$

This strength is the q -coordinate of the intersection point of the undrained stress path (2.22) through p_c and the critical state line (refer to Fig. 2.1).

The ultimate strength obtained from (3.62) is higher than that obtained from (3.61). If $\kappa = 0$ (i.e., no swelling during volumetric unloading), these two equations would give identical strengths. Since the Singh-Mitchell creep parameters are usually obtained from undrained 'triaxial' creep tests, (3.62) will be used to define the ultimate strength.

To be compatible with (3.62), the hyperbolic curve (3.6) should yield the same failure strength at an infinite deviatoric strain, i.e., $q_{ult} = q |_{\gamma \rightarrow \infty}$. This requisite condition can be used to backfigure the relationship between the stress-strain parameters b and R_f as follows:

$$\frac{b}{R_f} = \frac{2^{(1-\kappa/\lambda)}}{M} , \quad (3.63)$$

where κ , λ , and M are the Cam clay parameters.

■ **Deviatoric age.** Consider the same point A in Fig. 3.2 which is now given by the coordinates (q, γ_1) on the q - γ plane. If the soil is normally consolidated, the stress q would locate A on the hyperbolic curve (3.6) at

$$\gamma_2 = \frac{qa}{p_c R_f - qb} . \quad (3.64)$$

The deviatoric age t_d is computed from (2.62a) and (2.62b) based on γ_2 as

$$t_d = \left[\frac{(\gamma_1 - \gamma_2)(1-m)}{A e^{\alpha D} (t_d)_i^m} \right]^{\frac{1}{1-m}}, \quad \text{if } m \neq 1 \quad (3.65a)$$

$$= (t_d)_i \exp \left(\frac{\gamma_1 - \gamma_2}{A e^{\alpha D}} \right), \quad \text{if } m = 1. \quad (3.65b)$$

Nonassociative flow rule for plane strain

If ψ is constant, the volumetric and the deviatoric scaling procedures cannot give identical results because (3.50) would never equal (3.59). On the other hand, forcing the tensor $\dot{\epsilon}_{kl}^t$ to satisfy both the prescribed volumetric and deviatoric creep rates would be violating the normality rule requirement.

A creep strain formulation resulting in simultaneous satisfaction of volumetric and deviatoric creep requirements is presented herein for plane strain problems under the strict assumption that the off-plane creep component is zero.

Consider the two-dimensional plane strain condition in the 1-2 plane. Assuming that the off-plane creep strain component $\dot{\epsilon}_{33}^t = 0$, the tensor $\dot{\epsilon}_{kl}^t$ may be written in the compacted form

$$\dot{\epsilon}_{kl}^t = \begin{bmatrix} \dot{\epsilon}_{11}^t & \dot{\epsilon}_{12}^t \\ \dot{\epsilon}_{21}^t & \dot{\epsilon}_{22}^t \end{bmatrix}. \quad (3.66)$$

Let this tensor be decomposed into two parts

$$\dot{\epsilon}_{kl}^t = (\dot{\epsilon}_1^t)_{kl} + (\dot{\epsilon}_2^t)_{kl}, \quad (3.67)$$

where

$$(\dot{\epsilon}_1^t)_{kl} = \frac{1}{2} \dot{\epsilon}_v^t \begin{bmatrix} 1 & 0 \\ 0 & 1 \end{bmatrix} \quad (3.68)$$

$$(\dot{\epsilon}_2^t)_{kl} = \begin{bmatrix} \dot{\epsilon}_{11}^t - \frac{1}{2} \dot{\epsilon}_v^t & \dot{\epsilon}_{12}^t \\ \dot{\epsilon}_{21}^t & \dot{\epsilon}_{22}^t - \frac{1}{2} \dot{\epsilon}_v^t \end{bmatrix}, \quad (3.69)$$

in which $\dot{\epsilon}_v^t = \dot{\epsilon}_{11}^t + \dot{\epsilon}_{22}^t$ is the volumetric creep rate. The above decomposition is equivalent to separating the tensor $\dot{\epsilon}_{kl}^t$ into a volumetric part given by (3.68) and a deviatoric part given by (3.69), although $(\dot{\epsilon}_1^t)_{kl}$ is strictly not the general volumetric part of (3.47) in three dimensions.

Assume further that the principal directions of the deviatoric tensor $(\dot{\epsilon}_2^t)_{kl}$ and the stress tensor σ_{ij} are coincident. The elements of $\dot{\epsilon}_{kl}^t$ are obtained as follows:

$$\begin{Bmatrix} \dot{\epsilon}_{11}^t \\ \dot{\epsilon}_{22}^t \\ \dot{\epsilon}_{12}^t \end{Bmatrix} = \frac{1}{2} \begin{Bmatrix} \dot{\epsilon}_v^t + \sqrt{3} \dot{\epsilon}_a^t \cos 2\theta \\ \dot{\epsilon}_v^t - \sqrt{3} \dot{\epsilon}_a^t \cos 2\theta \\ 2\sqrt{3} \dot{\epsilon}_a^t \sin 2\theta \end{Bmatrix}, \quad (3.70)$$

where θ is the orientation of the major principal stress direction relative to the 1-2 axes evaluated as:

$$\theta = \frac{1}{2} \tan^{-1} \frac{2\sigma_{21}}{\sigma_{11} - \sigma_{22}}, \quad \sigma_{11} \neq \sigma_{22} \quad (3.71a)$$

$$= \frac{\pi}{4}, \quad \sigma_{11} = \sigma_{22}, \quad (3.71b)$$

while $\frac{\sqrt{3}}{2} \dot{\epsilon}_a^t$ which appears in (3.70) is the major principal component of the deviatoric tensor $(\dot{\epsilon}_2^t)_{kl}$ ⁽¹⁾.

The above approach does not satisfy the normality rule on F . However, (3.70) contains $\dot{\epsilon}_v^t$ and $\dot{\epsilon}_a^t$ which can be made to satisfy both prescribed volumetric and deviatoric creep rates, respectively.

3.4 SUMMARY

A constitutive equation incorporating the effects of creep has been developed for cohesive soils. The formulation involves superposition of time-independent and time-dependent deformation components.

The time-independent constitutive model is an elasto-plastic strain hardening model whose yield surface is a family of ellipsoids derived from the modified Cam clay equation. This yield surface also serves as the plastic potential surface by the associative flow rule.

Creep contributions were incorporated using the associative flow rule and the same yield surface as in the time-independent plasticity model. The creep strain rate tensor can be evaluated either by volumetric scaling in which the C_α -creep

⁽¹⁾ Recall that γ reduces to ϵ_a in 'triaxial' stress state and to $\frac{2}{\sqrt{3}}\epsilon_1$ in plane strain.

law is employed, or by deviatoric scaling in which the tensor normal to the yield surface is reduced into a 'triaxial' creep tensor which is subsequently scaled using the Singh-Mitchell creep equation. A third scheme was presented for the plane strain case where the creep strain tensor can be made to satisfy both the volumetric and the deviatoric requirements, but without employing the normality rule.

It was shown that the general constitutive equation can always be written in the rate form

$$\dot{\sigma}_{ij} = c_{ijkl}\dot{\epsilon}_{kl} - \dot{\sigma}_{ij}^t.$$

The term " $\dot{\sigma}_{ij}^t$ " representing the stress relaxation contribution can always be explicitly evaluated and "brought to the right-hand side" of the finite element matrix equations, leaving the term " $c_{ijkl}\dot{\epsilon}_{kl}$ " which is the "standard" form used in the framework of a finite element formulation.

Chapter 4

DEVELOPMENT OF A FINITE ELEMENT PROGRAM

4.1 INTRODUCTION

The finite element method is a numerical technique for obtaining solutions to boundary-value problems. It involves dividing the domain of the problem into a finite number of subdomains or elements and using variational concepts to approximate the solution. This method is most useful in solving complex two- or three-dimensional boundary-value problems when efficiently implemented.

This chapter presents a general finite element "mixed" formulation involving displacements and pore pressures in the solution of two- and three-dimensional consolidation/creep problems. A finite element computer program **SPIN 2D** is developed for analyzing geotechnical structures of axisymmetric (torsionless) or plane strain configurations.

4.2 FINITE ELEMENT FORMULATION

Consider a soil continuum in domain Ω and bounded by surface Γ . Part of its surface Γ_{g_i} is subjected to a prescribed displacement function g_i , while the remainder of its surface Γ_{h_i} is subjected to a traction h_i . The same total surface Γ may also be divided into a portion Γ_r subjected to a prescribed pressure function r , and the remainder Γ_s under an input hydraulic flux of s . In symbolic form, assume that the following set relations hold (see Fig. 4.1):

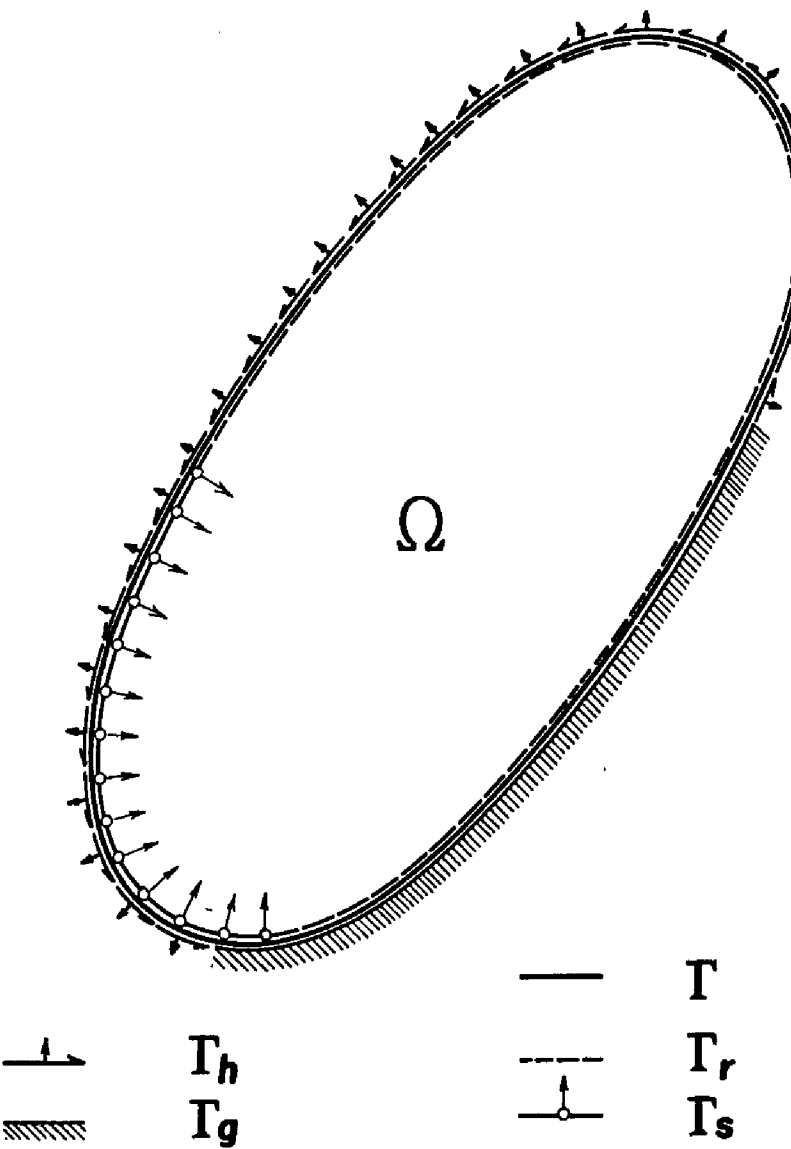


FIG. 4.1.
PROBLEM DOMAIN AND BOUNDARIES.

$$\left\{ \begin{array}{l} \Gamma = \Gamma_{g_i} \cup \Gamma_{h_i} = \Gamma_r \cup \Gamma_s \\ \emptyset = \Gamma_{g_i} \cap \Gamma_{h_i} = \Gamma_r \cap \Gamma_s \end{array} \right\}, \quad (4.1)$$

for $i = 1, \dots, n_{sd}$, where n_{sd} = number of spatial dimensions, \emptyset = null set, and the symbols \cup and \cap represent set union and intersection, respectively.

Strong Form

The strong form (S), or the classical statement of the model problem is presented mathematically in rate form as follows (summation implied on repeated subscripts):

Given f_i , g_i , h_i , r , and s , find the functions u_i and ρ such that

$$\dot{\sigma}_{ij,j} + f_i = 0 \quad \text{in } \Omega \quad (\text{Equilibrium}) \quad (4.2a)$$

$$\dot{u}_{i,i} - \dot{\epsilon}_v = 0 \quad \text{in } \Omega \quad (\text{Continuity}) \quad (4.2b)$$

$$\dot{u}_i = g_i \quad \text{on } \Gamma_{g_i} \quad (4.3a)$$

$$\dot{\sigma}_{ij}n_j = h_i \quad \text{on } \Gamma_{h_i} \quad (4.3b)$$

$$\dot{\rho} = r \quad \text{on } \Gamma_r \quad (4.4a)$$

$$\dot{u}_i n_i = s \quad \text{on } \Gamma_s, \quad (4.4b)$$

where

u_i = i th (Cartesian) component of the displacement
field function \mathbf{u}

ρ = pressure field function

σ_{ij} = (i, j) component of the symmetric (Cauchy) effective
stress tensor $\tilde{\sigma}$, compression positive

f_i = i th component of the effective body force \mathbf{f}

- ϵ_v = volumetric strain, compression positive
 g_i = i th component of the prescribed displacement \mathbf{g}
 h_i = i th component of the prescribed traction \mathbf{h}
 r = prescribed pressure function
 s = prescribed velocity flux
 n_i = direction cosine of the angle between
the (Cartesian) axis i and the surface normal.

Equations (4.2a) and (4.2b) are quasi-static rate equations involving effective stresses in a fully saturated soil mass. Consequently, a two-phase water-soil structure is implied. Since water is relatively incompressible compared with the soil skeleton, (4.2b) states that the rate of volume change equals the rate at which water is squeezed out of the soil mass (see Biot, 1941).

Weak Form

The weak form (W) or the variational counterpart of (S) involves the determination of functions u_i and ρ and the satisfaction of both the differential equations (4.2a,b) and the boundary conditions (4.3) and (4.4) on the basis of weighted averages.

As a prelude to the statement of (W), consider a set of *trial solutions*

$$\left\{ \begin{array}{l} \mathbf{T}_i = \{ u_i \mid u_i \in H^1, \dot{u}_i = \dot{g}_i \text{ on } \Gamma_{g_i} \} \\ \Phi = \{ \rho \mid \rho \in H^1, \dot{\rho} = \dot{r} \text{ on } \Gamma_r \} \end{array} \right\}, \quad (4.5)$$

and a set of *weighting functions*

$$\left\{ \begin{array}{l} \Theta_i = \{ w_i \mid w_i \in H^1, \dot{w}_i = 0 \text{ on } \Gamma_{g_i} \} \\ \Psi = \{ q \mid q \in H^1, \dot{q} = 0 \text{ on } \Gamma_r \} \end{array} \right\}, \quad (4.6)$$

where H^1 is a set of functions with square-integrable first derivatives ⁽¹⁾, and w_i and q are any possible "virtual displacements" and "virtual pressures", respectively,

⁽¹⁾ In general, H^n is a set of functions smooth enough to possess square-integrable n th derivatives.

in the context of a virtual work formulation. The set symbol \in means "belongs in" or "is an element of".

The statement of the weak form (W) is as follows (consult Appendix 1.1 for development):

Given f_i , g_i , h_i , r , and s as in (S), find $u_i \in T_i$ and $\rho \in \Phi$ such that for all $w_i \in \Theta_i$ and $q \in \Psi$,

$$\begin{aligned} & \int_{\Omega} w_{(i,j)} c_{ijkl} \dot{u}_{(k,l)} d\Omega + \int_{\Omega} w_{i,i} \dot{\rho} d\Omega \\ & - \int_{\Omega} q_{,i} \frac{k_{ij}}{\gamma_w} \rho_{,j} d\Omega + \int_{\Omega} q \dot{u}_{i,i} d\Omega \\ & = \int_{\Omega} w_i f_i d\Omega + \int_{\Omega} w_{i,j} \dot{\sigma}_{ij}^t d\Omega \\ & + \int_{\Gamma_s} q s d\Gamma_s + \sum_{n=1}^{n_{\text{nd}}} \left(\int_{\Gamma_{h_n}} w_i h_i d\Gamma_{h_n} \right), \end{aligned} \quad (4.7)$$

where $w_{(i,j)}$ and $\dot{u}_{(k,l)}$ are the symmetric parts of the tensor gradients $w_{i,j}$ and $\dot{u}_{k,l}$, respectively.

Equation (4.7) assumes that a creep-inclusive constitutive equation of the form

$$\dot{\sigma}_{ij} = c_{ijkl} \dot{\epsilon}_{ij} - \dot{\sigma}_{ij}^t \quad (3.30)$$

exists (see Sec. 3.2) and that the transient pore pressure dissipation is given by Darcy's law as follows:

$$\dot{u}_i = - \frac{k_{ij}}{\gamma_w} \rho_{,j}, \quad (4.8)$$

where γ_w = unit weight of water and k_{ij} = (i,j) component of the permeability tensor \mathbf{k} (the negative sign implies that the flow goes in the direction of decreasing gradient).

The weak statement (4.7) of the model problem parallels that of physical modeling in which stress and strain measurements are obtained on the basis of their

average values over a finite region, and not at any single point as suggested by the point-wise satisfaction of (4.2a, b) [2].

In abstract form, (4.7) is rewritten thus:

$$\begin{aligned} \mathbf{A}(\mathbf{w}, \dot{\mathbf{u}}) + (\operatorname{div} \mathbf{w}, \dot{\rho}) - \bar{\mathbf{A}}(q, \rho) + (q, \operatorname{div} \dot{\mathbf{u}}) \\ = (\mathbf{w}, \dot{\mathbf{f}}) + (\partial \mathbf{w}, \dot{\sigma}^t) + (q, s)_\Gamma + (\mathbf{w}, \dot{\mathbf{h}})_\Gamma , \end{aligned} \quad (4.9)$$

where $\mathbf{A}(\cdot, \cdot)$ and $\bar{\mathbf{A}}(\cdot, \cdot)$ are *symmetric bilinear operators* defined by

$$\mathbf{A}(\mathbf{w}, \dot{\mathbf{u}}) = \int_{\Omega} w_{(i,j)} c_{ijkl} \dot{u}_{(k,l)} d\Omega \quad (4.10a)$$

$$\bar{\mathbf{A}}(q, \rho) = \int_{\Omega} q_{,i} \frac{k_{ij}}{\gamma_w} \rho_{,j} d\Omega , \quad (4.10b)$$

and (\circ, \bullet) is an operator defined by

$$(\circ, \bullet) = \int_{\Omega} (\circ \bullet) d\Omega \quad (4.10c)$$

$$(\circ, \bullet)_\Gamma = \int_{\Gamma} (\circ \bullet) d\Gamma . \quad (4.10d)$$

Galerkin Approximations

The Galerkin formulation provides the *link* between the weak form (4.7) and its finite element counterpart by introducing the following approximations:

Let Υ^h , Θ^h , Φ^h , and Ψ^h be the *finite dimensional approximations* of Υ , Θ , Φ , and Ψ , respectively; i.e., $\Upsilon^h \subset \Upsilon$, $\Theta^h \subset \Theta$, $\Phi^h \subset \Phi$, and $\Psi^h \subset \Psi$, where the symbol \subset means "is a subset of", and the superscript h suggests that these approximations are associated with the discretization of domain Ω into a *mesh* of subdomains Ω^e .

The Galerkin form (G) of the model problem is stated as follows:

Given \mathbf{f} , \mathbf{g} , \mathbf{h} , \mathbf{r} , and \mathbf{s} as in (S), find

$$\left\{ \begin{array}{l} \mathbf{u}^h = \mathbf{v}^h + \boldsymbol{\varrho}^h \in \mathbf{T}^h \\ \boldsymbol{\varrho}^h = \boldsymbol{\varrho}^h + \mathbf{r}^h \in \Phi^h \end{array} \right\} \quad (4.11)$$

such that for all $\mathbf{w}^h \in \Theta^h$ and $\mathbf{q}^h \in \Psi^h$,

$$\begin{aligned} & \mathbf{A}(\mathbf{w}^h, \dot{\mathbf{v}}^h) + (\operatorname{div} \mathbf{w}^h, \dot{\boldsymbol{\varrho}}^h) - \bar{\mathbf{A}}(\mathbf{q}^h, \boldsymbol{\varrho}^h) + (\mathbf{q}^h, \operatorname{div} \dot{\mathbf{v}}^h) \\ &= (\mathbf{w}^h, \dot{\mathbf{f}}) + (\partial \mathbf{w}^h, \dot{\boldsymbol{\sigma}}^t) + (\mathbf{q}^h, \mathbf{s})_\Gamma + (\mathbf{w}^h, \mathbf{h})_\Gamma \\ & \quad - [\mathbf{A}(\mathbf{w}^h, \dot{\mathbf{g}}^h) + (\operatorname{div} \mathbf{w}^h, \dot{\mathbf{r}}^h) - \bar{\mathbf{A}}(\mathbf{q}^h, \mathbf{r}^h) + (\mathbf{q}^h, \operatorname{div} \dot{\mathbf{g}}^h)] , \end{aligned} \quad (4.12)$$

where $\mathbf{v}^h \in \Theta^h$ and $\boldsymbol{\varrho}^h \in \Psi^h$.

As an illustration, note that since $\mathbf{v}^h \in \Theta^h \subset \Theta$ and $\boldsymbol{\varrho}^h \in \Psi^h \subset \Psi$, $\dot{v}_i^h = 0$ on Γ_{g_i} and $\dot{\boldsymbol{\varrho}}^h = 0$ on Γ_r . Hence, $\dot{u}_i^h = 0 + g_i^h$ on Γ_{g_i} and $\dot{\boldsymbol{\varrho}}^h = 0 + \mathbf{r}^h$ on Γ_r , satisfying (4.11).

Matrix Form

Introducing interpolatory expansions for \mathbf{v}^h and $\boldsymbol{\varrho}^h$ and using parallel interpolations for \mathbf{w}^h and \mathbf{q}^h ,

$$\mathbf{v}^h(\mathbf{x}) = \sum_{a \in \eta - \eta_s} N_a(\mathbf{x}) \mathbf{d}_a \quad (4.13a)$$

$$\mathbf{w}^h(\mathbf{x}) = \sum_{a \in \eta - \eta_s} N_a(\mathbf{x}) \tilde{\mathbf{w}}_a \quad (4.13b)$$

$$\boldsymbol{\varrho}^h(\mathbf{x}) = \sum_{b \in \varsigma - \varsigma_r} \hat{N}_b(\mathbf{x}) p_b \quad (4.14a)$$

$$\mathbf{q}^h(\mathbf{x}) = \sum_{b \in \varsigma - \varsigma_r} \hat{N}_b(\mathbf{x}) \bar{q}_b , \quad (4.14b)$$

where N_a are the displacement shape functions associated with displacement node a and \hat{N}_b are the pressure shape functions associated with pressure node b ; \mathbf{d}_a is the nodal displacement vector with elements $\{d_1, \dots, d_{n_{sd}}\}_a$ at a , p_b is the nodal

Table 4.1

GLOBAL ARRAY	TERMS IN GALERKIN EQUATION
\mathbf{K}	$\mathbf{A}(\mathbf{w}^h, \dot{\mathbf{v}}^h)$
\mathbf{G}	$(\operatorname{div} \mathbf{w}^h, \dot{\varrho}^h)$
\mathbf{G}^T	$(q^h, \operatorname{div} \dot{\mathbf{v}}^h)$
\mathbf{M}	$-\bar{\mathbf{A}}(q^h, \varrho^h)$
$\dot{\mathbf{F}}$	$(\mathbf{w}^h, \dot{\mathbf{f}}) + (\partial \mathbf{w}^h, \dot{\sigma}^t) + (\mathbf{w}^h, \dot{\mathbf{h}})_\Gamma$ $- [\mathbf{A}(\mathbf{w}^h, \dot{\mathbf{g}}^h) + (\operatorname{div} \mathbf{w}^h, \dot{r}^h)]$
$\dot{\mathbf{H}}$	$(q^h, s)_\Gamma - [(q^h, \operatorname{div} \dot{\mathbf{g}}^h) - \bar{\mathbf{A}}(q^h, r^h)]$

pressure at b ; $(\eta - \eta_g)$ and $(\zeta - \zeta_r)$ are the node numbers at which the displacements and pressures, respectively, are unknown; $\bar{\mathbf{w}}_a$ and \bar{q}_b are any arbitrary non-zero counterparts of \mathbf{d}_a and p_b .

The arbitrariness of $\bar{\mathbf{w}}_a$ and \bar{q}_b leads to the matrix form (M) of the Galerkin equation, written in segregated d-p form as follows:

$$\mathbf{K} \dot{\mathbf{d}} + \mathbf{G} \dot{\mathbf{p}} = \dot{\mathbf{F}} \quad (4.15a)$$

$$\mathbf{G}^T \dot{\mathbf{d}} + \mathbf{M} \mathbf{p} = \dot{\mathbf{H}}, \quad (4.15b)$$

where the global arrays \mathbf{K} , \mathbf{G} , \mathbf{G}^T , \mathbf{M} , $\dot{\mathbf{F}}$, and $\dot{\mathbf{H}}$ are given in Table 4.1.

To express these global arrays explicitly on the element level, consider the indicial contraction scheme of Sec. 3.2. In this scheme, the stress and strain rate tensors $\dot{\sigma}$ and $\dot{\epsilon}$, respectively, are vectorized while the rank-four stress-strain tensor c_{ijkl} is reduced to a two-dimensional matrix \mathbf{C} .

Using the element nodal values \mathbf{d}^e and \mathbf{p}^e ,

$$\dot{\epsilon} = - \sum_{a=1}^{n_{en}^4} \mathbf{B}_a^e \mathbf{d}_a^e \quad (4.16)$$

$$\epsilon_v = - \sum_{a=1}^{n_{en}^4} \mathbf{b}_a^T \mathbf{d}_a^e \quad (4.17)$$

$$\text{grad } \rho = \sum_{b=1}^{n_{en}^p} \mathbf{E}_b p_b^\epsilon, \quad (4.18)$$

where n_{en}^d and n_{en}^p are the number of element nodes interpolating \mathbf{u} and ρ in the element domain Ω^e , respectively; $\tilde{\epsilon} = \{\epsilon_{11}, \epsilon_{22}, \dots\}^T$ is the vector of strain components (consult Sec. 3.2 for the ordering of elements); ϵ_v is the volumetric strain, and $\text{grad } \rho$ is the n_{ed} -dimensional pressure gradient vector; matrix \mathbf{B}_a^ϵ is the strain-displacement matrix with superscript ϵ used to distinguish its *deformation part* from the *spin part* (see Sec. 4.4). The negative signs for $\tilde{\epsilon}$ and ϵ_v are consistent with the definition for compressive strains being positive.

In three-dimensional analysis,

$$\mathbf{B}_a^\epsilon = \begin{bmatrix} B_1 & 0 & 0 \\ 0 & B_2 & 0 \\ 0 & 0 & B_3 \\ B_2 & B_1 & 0 \\ 0 & B_3 & B_2 \\ B_3 & 0 & B_1 \end{bmatrix} \quad (4.19)$$

$$\mathbf{b}_a^T = (1, 1, 1, 0, 0, 0) \cdot \mathbf{B}_a^\epsilon, \quad (4.20)$$

in which $B_i = \partial N_a / \partial x_i$, where N_a is the displacement shape function associated with node a , while

$$\mathbf{E}_b = \left[\frac{\partial \hat{N}_b}{\partial x_1}, \frac{\partial \hat{N}_b}{\partial x_2}, \frac{\partial \hat{N}_b}{\partial x_3} \right]^T, \quad (4.21)$$

where \hat{N}_b is the pressure shape function associated with pressure node b .

In axisymmetric (torsionless) and plane strain analysis,

$$\mathbf{B}_a^\epsilon = \begin{bmatrix} B_1 & 0 \\ 0 & B_2 \\ B_0 & 0 \\ B_2 & B_1 \end{bmatrix}, \quad B_0 = \begin{cases} N_a/x, & \text{axisymmetric} \\ 0, & \text{plane strain} \end{cases} \quad (4.22)$$

$$\mathbf{b}_a^T = (1, 1, 1, 0) \mathbf{B}_a^\epsilon \quad (4.23)$$

$$\mathbf{E}_b = \left[\frac{\partial \hat{N}_b}{\partial x_1}, \frac{\partial \hat{N}_b}{\partial x_2} \right]^T. \quad (4.24)$$

The element arrays are then defined as follows (cf. Table 4.1) ⁽¹⁾:

⁽¹⁾ Note sign reversals in all terms containing (compressive) stresses σ^t and pressures ρ and r .

- The element tangent stiffness matrix is given by

$$\mathbf{K}_e^{(n_{ed} \times n_{ed})} = \int_{\Omega^e} (\mathbf{B}^e)^T \mathbf{C} \mathbf{B}^e d\Omega \quad (4.25)$$

where n_{ed} is the number of displacement components for element e (= number of displacement degrees of freedom per node \times number of displacement nodes), and \mathbf{C} is the rank-two stress-strain matrix obtained by contracting the indices of c_{ijkl} . The strain-displacement matrix \mathbf{B}^e consists of nodal submatrices $\mathbf{B} = [\mathbf{B}_1, \mathbf{B}_2, \dots, \mathbf{B}_{n_{en}}]$, where n_{en} is the number of element nodes.

- The element coupling matrices \mathbf{G}^e and $(\mathbf{G}^e)^T$ are as follows:

$$\mathbf{G}_e^{(n_{ed} \times n_p)} = - \int_{\Omega^e} \mathbf{b} \hat{\mathbf{N}}^T d\Omega \quad (4.26a)$$

$$(\mathbf{G}^e)^T_{(n_p \times n_{ed})} = - \int_{\Omega^e} \hat{\mathbf{N}} \mathbf{b}^T d\Omega, \quad (4.26b)$$

where n_p is the number of element pressure nodes and $\hat{\mathbf{N}} = \{\hat{N}_1, \hat{N}_2, \dots, \hat{N}_{n_p}\}^T$, see (4.14a, b).

- The element flux matrix \mathbf{M}^e is given by

$$\mathbf{M}_e^{(n_p \times n_p)} = - \frac{1}{\gamma_w} \int_{\Omega^e} \mathbf{E}^T \mathbf{k} \mathbf{E} d\Omega. \quad (4.27)$$

- The element force vectors $\dot{\mathbf{F}}^e$ and $\dot{\mathbf{H}}^e$ are as follows:

$$\begin{aligned} \dot{\mathbf{F}}_e^{(n_{ed} \times 1)} &= \int_{\Omega^e} \mathbf{N}^T \dot{\mathbf{f}} d\Omega - \int_{\Omega^e} (\mathbf{B}^e)^T \dot{\sigma}^e d\Omega \\ &\quad + \int_{\Gamma_h^e} \mathbf{N}^T \dot{\mathbf{h}} d\Gamma - [\mathbf{K}^e \cdot \dot{\mathbf{d}}_g - \mathbf{G}^e \cdot \dot{\mathbf{p}}_r] \end{aligned} \quad (4.28)$$

$$\dot{\mathbf{H}}_e^{(n_p \times 1)} = \int_{\Gamma_h^e} \hat{\mathbf{N}}^T \dot{s} d\Gamma - [-(\mathbf{G}^e)^T \cdot \dot{\mathbf{d}}_g - \mathbf{M} \dot{\mathbf{p}}_r], \quad (4.29)$$

where \mathbf{N} is an array consisting of element shape functions N_a such that $\mathbf{u} = \mathbf{N}\mathbf{d}$ (cf. (4.13a, b)); $\dot{\mathbf{d}}_g$ is an $(n_{ed} \times 1)$ vector containing prescribed g -displacements, i.e., $d_{g_i} = g_i$ if g_i is prescribed and $d_{g_i} = 0$, otherwise; \mathbf{p}_r and $\dot{\mathbf{p}}_r$ are $(n_p \times 1)$ vectors containing prescribed r -pressures and pressure rates, respectively (similar definitions as for $\dot{\mathbf{d}}_g$).

4.3 TIME INTEGRATION

Suppose that the solution $(\mathbf{d}_n, \mathbf{p}_n)$ is known at time t_n , and that (4.15a, b) can be transformed into an incremental form in $(\Delta\mathbf{d}, \Delta\mathbf{p})$. A marching algorithm can then be employed to obtain the solution at time t_{n+1} .

Integrating (4.15a, b),

$$\int_{t_n}^{t_{n+1}} \mathbf{K} \dot{\mathbf{d}} dt + \int_{t_n}^{t_{n+1}} \mathbf{G} \dot{\mathbf{p}} dt = \int_{t_n}^{t_{n+1}} \dot{\mathbf{F}} dt \quad (4.30a)$$

$$\int_{t_n}^{t_{n+1}} \mathbf{G}^T \dot{\mathbf{d}} dt + \int_{t_n}^{t_{n+1}} \mathbf{M} \mathbf{p} dt = \int_{t_n}^{t_{n+1}} \dot{\mathbf{H}} dt \quad (4.30b)$$

or

$$\bar{\mathbf{K}} \cdot \Delta\mathbf{d} + \mathbf{G} \cdot \Delta\mathbf{p} = \Delta\mathbf{F} \quad (4.31a)$$

$$\mathbf{G}^T \cdot \Delta\mathbf{d} + \mathbf{M} \cdot \int_{t_n}^{t_{n+1}} \mathbf{p} dt = \Delta\mathbf{H}, \quad (4.31b)$$

where $\bar{\mathbf{K}}$ represents an average value of the tangent stiffness \mathbf{K} over the time interval (t_n, t_{n+1}) . The global matrices \mathbf{G} and \mathbf{G}^T depend on the shape functions only, while \mathbf{M} is also a function of the (assumed) time-independent components of the permeability \mathbf{k} .

The parameter β

Equation (4.31b) may be transformed into a similar incremental form as (4.31a) using a discrete approximation to the remaining integral as follows:

$$\int_{t_n}^{t_{n+1}} \mathbf{p} dt \approx \Delta t [\beta \mathbf{p}_{n+1} + (1 - \beta) \mathbf{p}_n] = \Delta t (\mathbf{p}_n + \beta \Delta\mathbf{p}). \quad (4.32)$$

An algorithm that uses $\beta = 0$ for the above approximation is called an *explicit Euler algorithm*. If $\beta = 1$, the algorithm is *purely implicit*. Booker and Small [12] have shown that for $\Delta t > 0$, this solution is *unconditionally stable* if $\beta \geq 1/2$.

To illustrate the validity of the above approximation, consider the following cases:

■ **Case 1.** If \mathbf{p} is linear in (t_n, t_{n+1}) , then

$$\int_{t_n}^{t_{n+1}} \mathbf{p} dt = \frac{1}{2} \Delta t (\mathbf{p}_n + \mathbf{p}_{n+1}), \quad (4.33)$$

i.e., $\beta = 1/2$.

■ **Case 2.** If \mathbf{p} is logarithmic in (t_n, t_{n+1}) , then [53]

$$\int_{t_n}^{t_{n+1}} \mathbf{p} dt = \Delta t \left[\mathbf{p}_n + \left(1 + \frac{1}{\Delta t} - \frac{1}{\ln(1 + \Delta t)} \right) \cdot \Delta \mathbf{p} \right], \quad (4.34)$$

i.e., $\beta = (1 + \frac{1}{\Delta t} - \frac{1}{\ln(1 + \Delta t)})$. For any positive Δt , $\beta > 1/2$ and approaches $1/2$ as $\Delta t \rightarrow 0$.

■ **Case 3.** If \mathbf{p} is any general vector function in (t_n, t_{n+1}) whose Taylor's series expansion is

$$\mathbf{p}(t) = \sum_{m=0}^{\infty} \frac{\mathbf{p}^{(m)}(t_\xi)}{m!} (t - t_\xi)^m \quad (4.35)$$

for $t_n \leq t_\xi \leq t_{n+1}$, and where $\mathbf{p}^{(m)}$ denotes the m th- time derivative of \mathbf{p} , then

$$\begin{aligned} \int_{t_n}^{t_{n+1}} \mathbf{p} dt &= \Delta t \left[\frac{1}{2} (\mathbf{p}_n + \mathbf{p}_{n+1}) + \frac{1}{2!} \left(\frac{\dot{\mathbf{p}}_n - \dot{\mathbf{p}}_{n+1}}{2} \right) \Delta t \right. \\ &\quad \left. + \frac{1}{3!} \left(\frac{\ddot{\mathbf{p}}_n - \ddot{\mathbf{p}}_{n+1}}{2} \right) \Delta t^2 + \dots \right], \end{aligned} \quad (4.36)$$

where $\dot{\mathbf{p}} = \partial \mathbf{p} / \partial t$, $\ddot{\mathbf{p}} = \partial^2 \mathbf{p} / \partial t^2$, etc. These time derivatives will vanish if \mathbf{p} is linear in t in which case, $\beta = 1/2$ (a restatement of Case 1). If the discrete approximation given by (4.32) is to be used, the value $\beta = 1/2$ yields optimum accuracy as well as unconditional stability. If \mathbf{p} is an unknown vector function, it is generally recommended that β be set equal to $1/2$.

Using β as the integration parameter, a general incremental matrix equation is obtained, viz.:

$$\begin{bmatrix} \bar{\mathbf{K}} & \mathbf{G} \\ \mathbf{G}^T & \beta \Delta t \mathbf{M} \end{bmatrix} \begin{Bmatrix} \Delta \mathbf{d} \\ \Delta \mathbf{p} \end{Bmatrix} = \begin{Bmatrix} \Delta \mathbf{F} \\ \Delta \mathbf{H} - \Delta t \mathbf{M} \mathbf{p}_n \end{Bmatrix}, \quad (4.37)$$

where \mathbf{p}_n is the nodal pressure vector at the start of the increment.

The parameter α

The tangent stiffness $\bar{\mathbf{K}}$ in (4.37) may be taken as the stiffness \mathbf{K}_n at the start of the increment. However, an 'improved' estimate can be obtained by predicting, with \mathbf{K}_n , the stress state at some intermediate time

$$t_{n+\alpha} = t_n + \alpha \Delta t, \quad 0 \leq \alpha \leq 1 \quad (4.38)$$

where $t_n \leq t_{n+\alpha} \leq t_{n+1}$, and using the stresses at $t_{n+\alpha}$ to construct an improved $\bar{\mathbf{K}} = \mathbf{K}_{n+\alpha}$. For example, if $\alpha = 0$, the corrector phase is omitted. If $\alpha = 1/2$, the corrector phase uses the stiffness $\mathbf{K}_{n+1/2}$ in the middle of the time interval.

Hughes and Prévost [24] employed this predictor-corrector scheme and recommended that α be set equal to 1/2.

4.4 LARGE DEFORMATION PROBLEMS

This section is concerned with finite element formulation for problems in which large deformations and rotations are involved. This type of formulation also applies to small strain problems when the stress levels attain a magnitude comparable to the plastic-hardening moduli (as in lightly hardening clays with large virgin compression index λ).

Large movements which may change the overall geometry can be accounted for by updating the material coordinates. In addition, a more meaningful measure of strains and a constitutive equation satisfying objectivity requirements must be considered. These topics in continuum mechanics of large strains and objectivity will be dealt with in this section.

Kinematics

The two most common types of description of the motion of a continuum are the: (1) material or Lagrangian description, whose independent variables are the material coordinates \mathbf{X} in the *initial* (usually undeformed) configuration, and the

(2) *spatial* or *Eulerian* description, whose independent variables, at any time t , are the coordinates \mathbf{x} in the current configuration of a particle that is initially at \mathbf{X} . Symbolically,

$$\mathbf{x} = \mathbf{x}(\mathbf{X}, t) = \mathbf{X} + \mathbf{u}(\mathbf{x}, t), \quad (4.39)$$

where \mathbf{u} is the displacement vector with (Cartesian) component u_i .

The *deformation gradient* \mathbf{F} with components F_{iJ} ⁽¹⁾ is a tensor of partial derivatives

$$F_{iJ} = \frac{\partial x_i}{\partial X_J} \quad (3.40a)$$

with inverse

$$F_{Ji}^{-1} = \frac{\partial X_J}{\partial x_i}. \quad (4.40b)$$

Lagrangian strains are given by the tensor \mathbf{E} with Cartesian components⁽²⁾

$$E_{IJ} = \frac{1}{2}(F_{Ik}F_{kJ} - \delta_{IJ}) \quad (4.41a)$$

$$= \frac{1}{2} \left[\frac{\partial u_I}{\partial X_J} + \frac{\partial u_J}{\partial X_I} + \frac{\partial u_K}{\partial X_I} \frac{\partial u_K}{\partial X_J} \right]. \quad (4.41b)$$

Eulerian strains are given by the tensor \mathbf{E}^* with Cartesian components

$$E_{ij}^* = \frac{1}{2}(\delta_{ij} - F_{iK}^{-1}F_{Kj}^{-1}) \quad (4.42a)$$

$$= \frac{1}{2} \left[\frac{\partial u_i}{\partial x_j} + \frac{\partial u_j}{\partial x_i} - \frac{\partial u_k}{\partial x_i} \frac{\partial u_k}{\partial x_j} \right]. \quad (4.42b)$$

In a Lagrangian formulation, the mesh of finite elements represents some fixed reference state for strain. Hibbit, Marcal, and Rice [21] employed this scheme and obtained four types of stiffness terms in addition to the material stiffness \mathbf{C} , namely, the small strain stiffness, initial load stiffness, initial strain stiffness, and the initial stress stiffness.

In an Eulerian formulation, the finite element mesh represents the current state of deformation. This formulation, also called an *updated Lagrangian* because

⁽¹⁾ Upper-case and lower-case subscripts pertain to material and spatial coordinates, respectively.

⁽²⁾ Strains are actually coded with $-u_{ij}$ in place of u_{ij} to conform with the convention that compressive strains are positive.

the mesh moves with the material [43], will be adopted in obtaining a modified constitutive equation incorporating large deformation effects.

Rate of deformation, spin, and natural strain increments

The process of *plastic deformation* is irreversible and the final stress states are generally path-dependent. Thus, any equation describing plastic deformation must be in *differential* or *rate* form. Choosing the latter, the following definitions are adopted:

- The tangent motion is given by the *velocity vector* \mathbf{v} with component

$$v_i = \frac{d(u_i)}{dt} \Big|_{\mathbf{x}} \quad (4.43)$$

in which the symbol “ $|_{\mathbf{x}}$ ” implies that the time-derivative is taken with \mathbf{X} held fixed.

- The *velocity gradient tensor* \mathbf{L} with components L_{ij} is defined viz.:

$$L_{ij} = v_{i,j} . \quad (4.44)$$

- The *rate of deformation tensor* $v_{(i,j)}$ is the symmetric part of \mathbf{L} and is given by

$$v_{(i,j)} = \frac{1}{2}(L_{ij} + L_{ji}) = \frac{1}{2}(v_{i,j} + v_{j,i}) . \quad (4.45)$$

- The skew-symmetric part $v_{[i,j]}$ is the *spin tensor*

$$v_{[i,j]} = \frac{1}{2}(L_{ij} - L_{ji}) = \frac{1}{2}(v_{i,j} - v_{j,i}) , \quad (4.46)$$

which represents the rigid-body rotational component of \mathbf{L} .

- The rate of deformation $v_{(i,j)}$ differs from the *strain rate*

$$-\dot{\epsilon}_{ij} = \frac{1}{2} \left[\frac{\partial v_i}{\partial X_j} + \frac{\partial v_j}{\partial X_i} \right] , \quad (4.47)$$

whose derivatives are taken with respect to the material coordinates \mathbf{X} . In small strain theory, $\mathbf{X} = \mathbf{x}$ and this difference disappears.

- The natural or true strain increment in time Δt is

$$-\Delta\epsilon_{ij}^* = \int_{t_0}^{t_0 + \Delta t} v_{(i,j)} dt . \quad (4.48)$$

This three-dimensional definition reduces to a logarithmic-strain form for the uniaxial compression case.

Objectivity

The term *objectivity* is used to mean invariance of a quantity or a function under changes of reference frames. Such objective quantities or functions satisfy requisite transformation laws such that any two observers at different reference frames observe the same quantity or function. For example, it can be shown [39] that the Cauchy stress tensor σ_{ij} and the rate of deformation tensor $v_{(i,j)}$ are objective; however, the Cauchy stress rate tensor $\dot{\sigma}_{ij}$ and the strain rate tensor $\dot{\epsilon}_{ij}$ that appear in the (infinitesimal) constitutive equation (3.30) are *not* objective.

Modified constitutive equation

To satisfy the objectivity requirement, consider a class of rate constitutive equations of the form [26].

$$-(\dot{\sigma}_{ij} + \dot{\sigma}_{ij}^t) = \bar{c}_{ijkl}v_{(k,l)} + s_{ijkl}v_{[k,l]} \quad (4.49)$$

in which

$$\bar{c}_{ijkl} = c_{ijkl} + c_{ijkl}^* \quad (4.50)$$

is a material response tensor which typically depends upon the stresses, deformation gradient, and material parameters, and

$$s_{ijkl} = \frac{1}{2}(\sigma_{ik}\delta_{jl} + \sigma_{jk}\delta_{il} - \sigma_{il}\delta_{jk} - \sigma_{jl}\delta_{ik}) \quad (4.51)$$

is the tensor uniquely specified by objectivity requiring that $(\dot{\sigma}_{ij} + \dot{\sigma}_{ij}^t)$ transform properly under rigid-rotations.

Using the Jaumann rate of the Kirchhoff stress tensor, define

$$c_{ijkl}^* = \sigma_{ij}\delta_{kl}, \quad (4.52)$$

and use the same c_{ijkl} developed in Sec. 3.2.

The modified constitutive equations, accounting for finite deformations, are then written in the following forms (see development in Appendix 1.2) [24]

$$-c_{ijkl}v_{(k,l)} = \begin{cases} \dot{\sigma}_{ij} + \dot{\sigma}_{ij}^t, & \text{small deformations;} \\ \sigma_{ij}^* + \sigma_{ij}v_{k,k}, & \text{finite deformations,} \end{cases} \quad (4.53)$$

where

$$\sigma_{ij}^* = (\dot{\sigma}_{ij} + \dot{\sigma}_{ij}^t) + \sigma_{ik}v_{[k,j]} + \sigma_{jk}v_{[k,i]} \quad (4.54)$$

is the Jaumann derivative.

The stress-strain tensor which appears in the linearized variational equations is as follows:

$$d_{ijkl} = \begin{cases} c_{ijkl}, & \text{small deformations;} \\ c_{ijkl} + \frac{1}{2}(\sigma_{il}\delta_{jk} + \sigma_{ik}\delta_{jl} + \sigma_{jk}\delta_{il} - \sigma_{jl}\delta_{ik}), & \text{finite deformations.} \end{cases} \quad (4.55)$$

The tensor d_{ijkl} possesses the major symmetry (i.e., $d_{ijkl} = d_{klji}$) if and only if c_{ijkl} possesses the major symmetry, which would lead to a symmetric tangent stiffness.

Initial stress stiffness

Equation (4.55) shows that the tensor of moduli d_{ijkl} contains initial stress components in addition to the c_{ijkl} -terms when finite deformations are included. One way of treating these extra terms is to form an *initial stress stiffness matrix*, in addition to the *material tangent stiffness matrix*, that is consistent with the linearized variational equation [43]. Another way is to lump the initial stress terms and the c_{ijkl} 's together and re-define the matrix \mathbf{B}^e to include the spin component. Choosing the latter approach, the contribution of the e th-element to the global tangent stiffness matrix is written thus:

$$\mathbf{K}_{ab}^e = \int_{\Omega^e} \mathbf{B}_a^T \mathbf{D} \mathbf{B}_b d\Omega, \quad (4.56)$$

in which

$$\mathbf{D} = \begin{bmatrix} \mathbf{C}_{(k \times k)} & \mathbf{0}_{(k \times l)} \\ \mathbf{0}_{(l \times k)} & \mathbf{0}_{(l \times l)} \end{bmatrix} + \mathbf{T}_{(k+l) \times (k+l)} \quad (4.57)$$

and

$$\mathbf{B}_a = \begin{bmatrix} (\mathbf{B}_a^\epsilon)_{(k \times n_{dof})} \\ (\mathbf{B}_a^\theta)_{(l \times n_{dof})} \end{bmatrix}, \quad (4.58)$$

where the dimensions (n_{dof}, k, l) are $(3, 6, 3)$ in three-dimensional analyses and $(2, 4, 1)$ in axisymmetric and plane strain analyses; \mathbf{T} , \mathbf{B}_a^ϵ , and \mathbf{B}_a^θ are as defined in Fig. 4.2, and \mathbf{C} is the material stress-strain matrix of Sec. 4.2.

The component \mathbf{B}_a^ϵ of the B-matrix is due to deformation (refer to Sec. 4.2), while the component \mathbf{B}_a^θ is due to spin, whose contributions vanish when $\mathbf{T} = \mathbf{0}$ as in small strain formulation.

The above definitions lead to a modified constitutive equation in matrix form given by

$$-(\Delta\tilde{\sigma} + \Delta\tilde{\sigma}^t) = (\mathbf{C} + \mathbf{C}^*)\Delta\tilde{\epsilon} + \mathbf{S}\Delta\tilde{\theta}, \quad (4.59)$$

in which $\Delta\tilde{\theta}$ is the vector of spin components

$$\Delta\tilde{\theta} = \{v_{[1,2]}, v_{[2,3]}, v_{[1,3]}\}^T, \text{ three dimensional analysis,} \quad (4.60a)$$

$$= v_{[1,2]}, \quad \text{plane strain/axisymmetric analysis} \quad (4.60b)$$

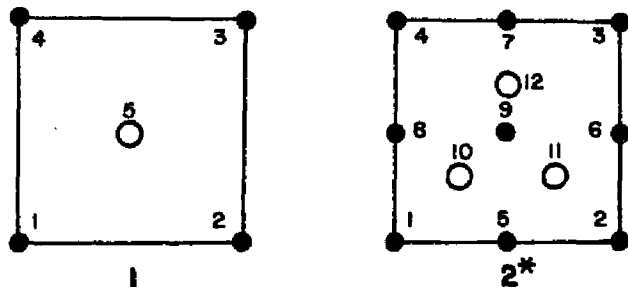
while the matrices \mathbf{C}^* and \mathbf{S} are as defined in Fig. 4.2. The negative sign in the stress terms is introduced to account for compressive stresses considered as positive.

4.5 ANALYSIS OPTIONS

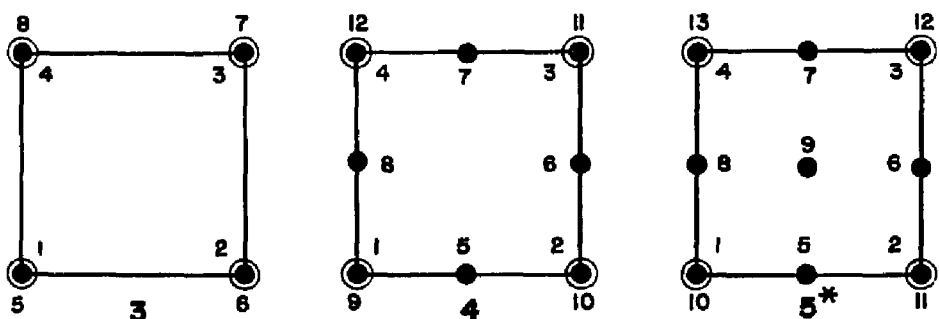
The incremental “mixed-form” solution (4.37) may be used in conjunction with an appropriate choice of finite elements in solving specific types of problem. Figure 4.3 shows an element library consisting of 8 quadrilateral elements that have been implemented in the finite element program **SPIN 2D** for plane-strain and axisymmetric (torsionless) cases.

THREE DIMENSIONS		AXISYMMETRIC & PLANE STRAIN
B_a^ϵ	$\begin{pmatrix} B_1 & \cdot & \cdot \\ \cdot & B_2 & \cdot \\ \cdot & \cdot & B_3 \\ B_2 & B_1 & \cdot \\ \cdot & B_3 & B_2 \\ B_3 & \cdot & B_1 \end{pmatrix}$ $B_1 = \frac{\partial N_a}{\partial x_1}$	$\begin{pmatrix} B_1 & \cdot & \cdot \\ \cdot & B_2 & \cdot \\ B_0 & \cdot & \cdot \\ B_2 & B_1 & \cdot \end{pmatrix}$ $B_0 = \frac{N_a}{x_1}, \text{ axisymmetric}$ $= 0, \text{ plane strain}$
B_a^θ	$\begin{pmatrix} B_2 & -B_1 & \cdot \\ \cdot & B_3 & -B_2 \\ B_3 & \cdot & -B_1 \end{pmatrix}$	$\begin{pmatrix} B_2 & -B_1 \end{pmatrix}$
C^*	$\begin{pmatrix} \sigma_{11} & \sigma_{11} & \sigma_{11} & \cdot & \cdot & \cdot \\ \sigma_{22} & \sigma_{22} & \sigma_{22} & \cdot & \cdot & \cdot \\ \sigma_{33} & \sigma_{33} & \sigma_{33} & \cdot & \cdot & \cdot \\ \sigma_{12} & \sigma_{12} & \sigma_{12} & \cdot & \cdot & \cdot \\ \sigma_{23} & \sigma_{23} & \sigma_{23} & \cdot & \cdot & \cdot \\ \sigma_{13} & \sigma_{13} & \sigma_{13} & \cdot & \cdot & \cdot \end{pmatrix}$	$\begin{pmatrix} \sigma_{11} & \sigma_{11} & \sigma_{11} & \cdot \\ \sigma_{22} & \sigma_{22} & \sigma_{22} & \cdot \\ \sigma_{33} & \sigma_{33} & \sigma_{33} & \cdot \\ \sigma_{12} & \sigma_{12} & \sigma_{12} & \cdot \\ \sigma_{13} & \sigma_{13} & \sigma_{13} & \cdot \end{pmatrix}$
S	$\begin{pmatrix} \sigma_{12} & \cdot & \sigma_{13} \\ -\sigma_{12} & \sigma_{23} & \cdot \\ \cdot & -\sigma_{23} & -\sigma_{13} \\ \frac{1}{4}(\sigma_{22}-\sigma_{11}) & \frac{1}{4}\sigma_{13} & \frac{1}{4}\sigma_{23} \\ -\frac{1}{4}\sigma_{13} & \frac{1}{4}(\sigma_{33}-\sigma_{22}) & -\frac{1}{4}\sigma_{12} \\ \frac{1}{4}\sigma_{23} & -\frac{1}{4}\sigma_{12} & \frac{1}{4}(\sigma_{33}-\sigma_{11}) \end{pmatrix}$	$\left\{ \begin{array}{l} \sigma_{12} \\ -\sigma_{12} \\ \cdot \\ \frac{1}{4}(\sigma_{22}-\sigma_{11}) \end{array} \right\}$
T	$\begin{pmatrix} \sigma_{11} & \cdot & \cdot & \frac{1}{4}\sigma_{12} & \cdot & \frac{1}{4}\sigma_{13} & -\frac{1}{4}\sigma_{12} & \cdot & -\frac{1}{4}\sigma_{13} \\ \sigma_{22} & \cdot & \cdot & \frac{1}{4}\sigma_{12} & \frac{1}{4}\sigma_{23} & \cdot & \frac{1}{4}\sigma_{12} & -\frac{1}{4}\sigma_{23} & \cdot \\ \sigma_{33} & \cdot & \cdot & \frac{1}{4}\sigma_{23} & \frac{1}{4}\sigma_{13} & \cdot & \frac{1}{4}\sigma_{23} & \frac{1}{4}\sigma_{13} & \cdot \\ \frac{1}{4}(\sigma_{11}+\sigma_{22}) & \frac{1}{4}\sigma_{13} & \frac{1}{4}\sigma_{23} & \frac{1}{4}(\sigma_{11}-\sigma_{22}) & -\frac{1}{4}\sigma_{13} & -\frac{1}{4}\sigma_{23} & \frac{1}{4}(\sigma_{11}-\sigma_{22}) & \frac{1}{4}(\sigma_{11}+\sigma_{22}) & -\frac{1}{4}(\sigma_{11}-\sigma_{22}) \\ \frac{1}{4}(\sigma_{22}+\sigma_{33}) & \frac{1}{4}\sigma_{12} & \frac{1}{4}\sigma_{13} & \frac{1}{4}(\sigma_{22}-\sigma_{33}) & \frac{1}{4}\sigma_{12} & \frac{1}{4}(\sigma_{22}+\sigma_{33}) & -\frac{1}{4}\sigma_{12} & -\frac{1}{4}(\sigma_{22}+\sigma_{33}) & \frac{1}{4}(\sigma_{22}-\sigma_{33}) \\ \frac{1}{4}(\sigma_{11}+\sigma_{33}) & -\frac{1}{4}\sigma_{23} & -\frac{1}{4}\sigma_{13} & \frac{1}{4}(\sigma_{11}-\sigma_{33}) & -\frac{1}{4}\sigma_{23} & -\frac{1}{4}(\sigma_{11}+\sigma_{33}) & \frac{1}{4}\sigma_{12} & -\frac{1}{4}(\sigma_{11}-\sigma_{33}) & -\frac{1}{4}(\sigma_{11}+\sigma_{33}) \\ \frac{1}{4}(\sigma_{11}+\sigma_{22}) & -\frac{1}{4}\sigma_{12} & -\frac{1}{4}\sigma_{13} & -\frac{1}{4}(\sigma_{11}-\sigma_{22}) & -\frac{1}{4}\sigma_{12} & -\frac{1}{4}(\sigma_{11}+\sigma_{22}) & -\frac{1}{4}\sigma_{13} & -\frac{1}{4}(\sigma_{11}-\sigma_{22}) & -\frac{1}{4}(\sigma_{11}+\sigma_{22}) \end{pmatrix}$ <p style="text-align: center;">SYMM.</p>	$\begin{pmatrix} \sigma_{11} & \cdot & \cdot & \frac{1}{4}\sigma_{12} & -\frac{1}{4}\sigma_{12} \\ \sigma_{22} & \cdot & \cdot & \frac{1}{4}\sigma_{12} & \frac{1}{4}\sigma_{12} \\ \sigma_{33} & \cdot & \cdot & \cdot & \cdot \\ \text{SYMM.} & & & \frac{1}{4}(\sigma_{11}+\sigma_{22}) & \frac{1}{4}(\sigma_{11}-\sigma_{22}) \\ & & & & -\frac{1}{4}(\sigma_{11}-\sigma_{22}) \end{pmatrix}$

FIG. 4.2. ELEMENTS OF MATRICES B , C^* , S , AND T .

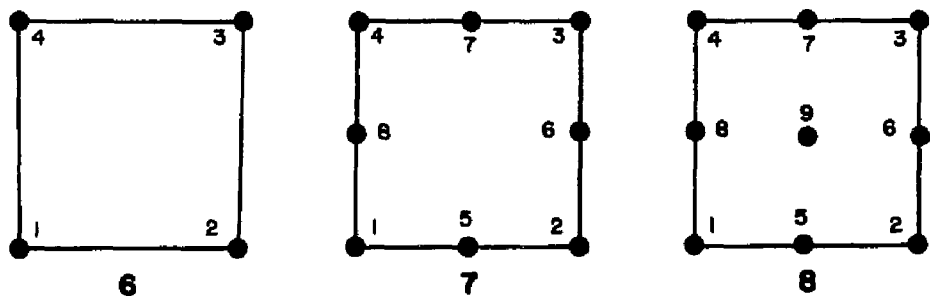


DISCONTINUOUS PRESSURE ELEMENTS



CONTINUOUS PRESSURE ELEMENTS

* CONVERGENCE PROOF ESTABLISHED



NO PRESSURE ELEMENTS

- PRESSURE
- DISPLACEMENT

FIG. 4.3. ELEMENT LIBRARY IN SPIN 2D.

Drained analysis

The word *drained* implies a condition in which pore water is allowed to flow freely into or out of a soil mass, resulting in *total dissipation of excess pore pressures*. This condition usually governs in cohesionless soils owing to their high permeability. A relatively impermeable clay may also exhibit this behavior when it is loaded at a very slow rate, allowing drainage to occur concurrently.

The *drained analysis option* provides the solution to the matrix problem

$$\bar{\mathbf{K}} \Delta \mathbf{d} = \Delta \mathbf{F}, \quad (4.61)$$

which is easily deduced from (4.37) by setting $\Delta p = 0$ throughout. Element numbers 6, 7, and 8 in Fig. 4.3 are applicable in this type of problem.

Undrained Analysis

The condition is ‘undrained’ when there is no flow of pore fluid involved. This condition makes the soil mass *incompressible* and causes it to deform at a constant water content (or void ratio).

Two methods of treating incompressibilities are discussed in this section, namely: (1) solution by *mixed formulation*, and (2) solution by *penalty formulation*.

- **Mixed formulation.** The undrained condition may be obtained by ‘instantaneously’ applying the load, i.e., applying the load quickly enough to prevent drainage. Thus, Δt in (4.37) may be set equal to zero to give

$$\begin{bmatrix} \mathbf{K} & \mathbf{G} \\ \mathbf{G}^T & 0 \end{bmatrix} \begin{Bmatrix} \Delta \mathbf{d} \\ \Delta p \end{Bmatrix} = \begin{Bmatrix} \Delta \mathbf{F} \\ \Delta \mathbf{H} \end{Bmatrix}. \quad (4.62)$$

Undrained problems do not require explicit boundary conditions on the pore pressures. Hence the set Φ (see Sec. 4.2) suffices as both a trial solution space as well as a weighting function space, i.e.,

$$\Psi \stackrel{\text{def}}{=} \Phi. \quad (4.63)$$

The exclusion of submatrix M in (4.62) also eliminates the requirement that the pore pressure functions possess first partial derivatives (i.e., pore pressure gradients). Thus ρ^h just needs to be square-integrable and may be discontinuous across element boundaries. This relaxation in continuity is computationally advantageous because the pore pressure degrees-of-freedom may be eliminated (and later recovered) on the element level, allowing the global equations to be structured without these unknown pressures. Element numbers 1 and 2 in Fig. 4.3 are typical discontinuous pore pressure elements that are included in the element library of SPIN 2D.

By relaxing the continuity of pore pressures, a wider range of permissible interpolations becomes available for pressures than for displacements (e.g., elements 1–5 in Fig. 4.3), providing more possible combinations of pore pressure and displacement interpolations to choose from. However, not all possible combinations of displacements and pressures work [27].

In general, the same interpolation for both displacement and pressure (e.g., element 3) should not be used in undrained cases, or if step loadings are to be used [16]. A dire consequence of such a combination is the so-called *mesh locking* [27], a numerical problem that arises when the incompressibility constraints are too many. An heuristic approach called *constraint counts* was proposed by Hughes [27] to establish the ability of an element to perform well in incompressible and nearly incompressible applications.

■ **Penalty formulation.** A matrix problem similar to (4.61) may be obtained by adding to the stiffness of the soil skeleton the *bulk stiffness* of water, i.e.,

$$\mathbf{C}_T = \mathbf{C} + \mathbf{C}_w , \quad (4.64)$$

in which \mathbf{C}_T is the resulting stress-strain matrix and

$$\mathbf{C}_w = \bar{\lambda}_w \cdot \begin{bmatrix} \mathbf{1}_{(3 \times 3)} & \mathbf{0}_{(3 \times m)} \\ \mathbf{0}_{(m \times 3)} & \mathbf{0}_{(m \times m)} \end{bmatrix} , \quad \mathbf{1} = \begin{bmatrix} 1 & 1 & 1 \\ 1 & 1 & 1 \\ 1 & 1 & 1 \end{bmatrix} \quad (4.65)$$

where the dimension $m = 3$ for three-dimensional analyses and $m = 1$ for axisymmetric and plane strain analyses; $\bar{\lambda}_w$ is the Lamé parameter for water (also equal to the bulk modulus K_w since the shear modulus $\bar{\mu}_w = 0$).

This approach is equivalent to introducing a volumetrically stiff elastic spring represented by a large but finite $\bar{\lambda}_w$, thus forcing the soil mass to become nearly incompressible.

The actual bulk stiffness $\bar{\lambda}_w$ is not relevant; this parameter is artificially selected to be large enough so that incompressibility errors are small, yet not too large to cause numerical problems. Hughes [27] suggested that, with computer floating-point words of length 60-64 bits, the ratio $\bar{\lambda}_w/\bar{\mu}_{soil}$ may be effectively taken in the range

$$10^7 \leq \bar{\lambda}_w/\bar{\mu}_{soil} \leq 10^9. \quad (4.66)$$

Slight compressibilities do not make the problem of mesh-locking go away. A numerical approach to this problem is by adopting a *reduced numerical integration rule*, a concept probably based on the presumption that errors in numerical integration compensate appropriately for the overestimation of structural stiffness due to finite element discretization [1].

A simple approach of *uniform reduced integration*, however, is a dangerous scheme which could reduce the rank of the stiffness matrix and cause it to become singular. An alternative approach is to use a *selective reduced integration* procedure, specifically the \bar{B} -method proposed by Hughes [25], which effectively sifts out the volumetrically stiff part of the stiffness matrix, and thus alleviates locking.

Figure 4.4 shows the *normal* and the *reduced* orders of Gauss numerical integration for the two-dimensional isoparametric elements of Fig. 4.3. A similar presentation may be made for isoparametric bricks in three-dimensions.

Employing the selective reduced integration technique, matrix B_a^e is decom-

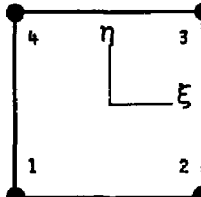
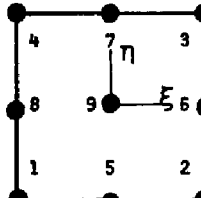
ELEMENT	NORMAL RULE	REDUCED RULE
	<p>2x2 QUADRATURE</p> <p>$n_{int} = 4$</p> $(\xi, \eta)_l = (+a, +a)_1, (+a, -a)_2$ $(-a, +a)_3, (-a, -a)_4$ $a = 1/\sqrt{3}$	<p>1-PT. QUADRATURE</p> <p>$\bar{n}_{int} = 1$</p> $(\bar{\xi}, \bar{\eta})_l = (0, 0)_1$ $\bar{N}_1 = 1$
 	<p>3x3 QUADRATURE</p> <p>$n_{int} = 9$</p> $(\xi, \eta)_l = (+b, +b)_1, (+b, 0)_2$ $(+b, -b)_3, (0, +b)_4$ $(0, 0)_5, (0, -b)_6$ $(-b, +b)_7, (-b, 0)_8$ $(-b, -b)_9, b = \sqrt{3}/5$	<p>2x2 QUADRATURE</p> <p>$\bar{n}_{int} = 4$</p> $(\bar{\xi}, \bar{\eta})_l = (+a, +a)_1, (+a, -a)_2$ $(-a, +a)_3, (-a, -a)_4$ <p>where $a = 1/\sqrt{3}$</p> $\bar{N}_1 = c(a+\xi)(a+\eta)$ $\bar{N}_2 = c(a+\xi)(a-\eta)$ $\bar{N}_3 = c(a-\xi)(a+\eta); c = \frac{3}{4}$ $\bar{N}_4 = c(a-\xi)(a-\eta)$

FIG. 4.4. COMPARISON BETWEEN NORMAL QUADRATURE RULE AND SELECTIVE REDUCED INTEGRATION RULE.

posed into a volumetric part $(\mathbf{B}_a^\epsilon)^{\text{vol}}$ and a deviatoric part $(\mathbf{B}_a^\epsilon)^{\text{dev}}$, i.e.,

$$(\mathbf{B}_a^\epsilon)^{\text{vol}} = \frac{1}{3} \begin{bmatrix} B_1 & B_2 & B_3 \\ B_1 & B_2 & B_3 \\ B_1 & B_2 & B_3 \\ 0 & 0 & 0 \\ 0 & 0 & 0 \\ 0 & 0 & 0 \end{bmatrix}, \quad (4.67a)$$

for three-dimensional analysis and

$$(\mathbf{B}_a^\epsilon)^{\text{vol}} = \frac{1}{3} \begin{bmatrix} (B_0 + B_1) & B_2 \\ (B_0 + B_1) & B_2 \\ (B_0 + B_1) & B_2 \\ 0 & 0 \end{bmatrix}, \quad (4.67b)$$

for axisymmetric and plane strain analysis;

$$(\mathbf{B}_a^\epsilon)^{\text{dev}} = \mathbf{B}_a^\epsilon - (\mathbf{B}_a^\epsilon)^{\text{vol}}, \quad (4.68)$$

where \mathbf{B}_a^ϵ is given by (4.19) or (4.22) and $B_i = \partial N_a / \partial x_i$, $1 \leq i \leq n_{ad}$.

The volumetric part $(\mathbf{B}_a^\epsilon)^{\text{vol}}$ is replaced by an 'improved' volumetric contribution $(\bar{\mathbf{B}}_a^\epsilon)^{\text{vol}}$, i.e.,

$$\bar{\mathbf{B}}_a^\epsilon = (\bar{\mathbf{B}}_a^\epsilon)^{\text{vol}} + (\mathbf{B}_a^\epsilon)^{\text{dev}}, \quad (4.69)$$

where

$$(\bar{\mathbf{B}}_a^\epsilon)^{\text{vol}} = \frac{1}{3} \begin{bmatrix} \bar{B}_1 & \bar{B}_2 & \bar{B}_3 \\ \bar{B}_1 & \bar{B}_2 & \bar{B}_3 \\ \bar{B}_1 & \bar{B}_2 & \bar{B}_3 \\ 0 & 0 & 0 \\ 0 & 0 & 0 \\ 0 & 0 & 0 \end{bmatrix} \quad (4.70a)$$

for three-dimensional analysis and

$$(\bar{\mathbf{B}}_a^\epsilon)^{\text{vol}} = \frac{1}{3} \begin{bmatrix} (\bar{B}_0 + \bar{B}_1) & \bar{B}_2 \\ (\bar{B}_0 + \bar{B}_1) & \bar{B}_2 \\ (\bar{B}_0 + \bar{B}_1) & \bar{B}_2 \\ 0 & 0 \end{bmatrix} \quad (4.70b)$$

for axisymmetric and plane strain analyses.

The \bar{B}_i 's are defined by the expression

$$\bar{B}_i(\xi_1, \dots, \xi_{n_{ad}}) = \sum_{l=1}^{n_{int}} \bar{N}_l(\xi_1, \dots, \xi_{n_{ad}}) B_{il}, \quad (4.71)$$

where ξ_j represents the j th component of the element natural coordinates⁽¹⁾, n_{int} is the number of integration points in the reduced rule, and the \bar{N}_l 's are special sets of shape functions associated with the locations $(\bar{\xi}_1, \dots, \bar{\xi}_{n_{sd}})_l$ of Gauss integration points in the reduced rule, i.e., $\bar{N}_k(\bar{\xi}_1, \dots, \bar{\xi}_{n_{sd}})_l = \delta_{kl}$ for $1 \leq k, l \leq n_{int}$ (Fig. 4.4).

Selective integration is obtained by taking

$$B_{il} = B_i(\bar{\xi}_1, \dots, \bar{\xi}_{n_{sd}})_l . \quad (4.72)$$

Figure 4.4 summarizes this scheme for various quadrilateral elements considered. The procedure may be applied to any arbitrary anisotropic and/or nonlinear situation, and to axisymmetric or rectilinear configurations.

Consolidation analysis

The transition from no flow to free flow is a transient pore pressure dissipation called *consolidation*.

A well-posed consolidation problem has all the needed boundary conditions on displacements and pore pressures, but not too many to make it ill-posed. The presence of pore-pressure boundary conditions makes it important to distinguish between the trial solution space Φ and the weighting function space Ψ .

Because pore pressure gradients appear in the variational equation, ρ^h needs to be of class H^1 , i.e., continuity of pore pressures must be preserved across element boundaries. If pressures are discontinuous across a boundary, pressure gradients would be meaningless for a *dirac*⁽²⁾ function on that boundary. Element numbers 3, 4, and 5 facilitate the solution to this problem.

An attempt to march out the consolidation solution from the undrained case may work provided that the boundary conditions in the consolidation phase match the pressures on that boundary at the end of the undrained phase. If a change in the pressure boundary condition occurs at a face containing pore pressure nodes, serious error is introduced for elements with pressure nodes on that face [16].

(1) Define $\xi_1 \equiv \xi$, $\xi_2 \equiv \eta$ for $n_{sd} = 2$.

(2) A dirac function is a discontinuous function.

It is also possible to march out the consolidation solution beyond the end of primary consolidation but a trivial solution $\Delta p = \mathbf{0}$ ⁽¹⁾ would make the approach numerically inefficient. If further deformation due to creep is to be investigated, it may be worthwhile to halt the program temporarily after all excess pore pressures have been dissipated, and then switch to the drained solution thereafter.

Creep options

Creep contributions are represented in the matrix equation by the pseudo-force term

$$\dot{\mathbf{F}}_{\text{creep}}^e = - \int_{\Omega^e} (\mathbf{B}^e)^T \dot{\sigma}^t d\Omega \quad (4.73)$$

which appears in the element force vector $\dot{\mathbf{F}}^e$ in (4.28). If a time-independent analysis (i.e., no creep) is to be performed, this pseudo-force term is not evaluated.

Creep contributions may also be numerically treated by "condensing" the pseudo-force term in the stiffness matrix by time-discretization and subsequent linearization. However, by allowing the creep effects to be expressed as artificial forces, stationary creep problems with no incremental applied loading (e.g., isotropic undrained stress relaxation experiment) may be numerically simulated as well.

To specify the approach for evaluating the creep strain rate tensor $\dot{\epsilon}_{kl}^t$, a flag "ICR" is provided which has the following meaning:

$$\left\{ \begin{array}{ll} \text{ICR} = 0, & \text{suppress creep contributions} \\ \text{= 1,} & \text{use nonassociative flow rule for } \dot{\epsilon}_{kl}^t \\ \text{= 2,} & \text{perform volumetric scaling on } \dot{\epsilon}_{kl}^t \\ \text{= 3,} & \text{perform deviatoric scaling on } \dot{\epsilon}_{kl}^t \end{array} \right\} \quad (4.74)$$

If the associative flow rule is used, a singularity may occur if the stress state is isotropic (or nearly isotropic) when performing deviatoric scaling (ICR=3), or if the stress point is on (or nearly on) the critical state line when performing volumetric scaling (ICR=2). In these cases, the program internally generates a numerical check and automatically reverses the scaling option to avoid numerical problems.

⁽¹⁾ Actually, pressure increments would oscillate around $\Delta p = \mathbf{0}$.

4.6 COMPUTER IMPLEMENTATION

A finite element computer program **SPIN 2D** was developed to verify the creep-inclusive constitutive equation of Chapter 3 for subsequent use in analyzing geotechnical structures of axisymmetric or plane strain configurations.

SPIN 2D is derived from "DIRT II", a program developed by Hughes and Prévost [24] for quasi-static nonlinear analysis, and contains additional features such as consolidation, time-dependency (creep), and selective reduced integration by \tilde{B} -method.

SPIN 2D has an expanded element library of 8 isoparametric quadrilateral elements and triangular elements to which some of these quadrilaterals may degenerate, for use in drained, consolidation, and undrained types of analysis. It also has an expanded material library (ELAS, SAND, CLAY) representing linear elastic, hyperbolic, and creep-inclusive elasto-plastic materials, respectively. These libraries are modularized and may be expanded easily with almost no alteration in the main code.

Finite deformation effects are incorporated using the Jaumann rate of the Kirchhoff stress, an Eulerian type of formulation, and a Lagrangian measure of finite strains.

The main algorithm is that of a predictor-corrector type of Sec. 4.3. An incremental numerical strategy is adopted using the β -parameter on pore pressures.

The data can be input using an isoparametric data generation scheme. External loadings and prescribed degrees of freedom can be described using different mode shapes.

The internal arrays are structured using dynamic allocation. This scheme makes the size of the internal memory grow with the size of the problem being analyzed. Thus no core storage is wasted.

SPIN 2D also has the capability to solve two-dimensional seepage problems containing prescribed pore pressure boundary conditions as well as prescribed velocities of hydraulic flow normal to the element faces.

Although the current version of the program applies only to problems in two dimensions, the internal arrays are so structured in a way that it would be easy to extend the program to three dimensions.

Input phase

Input data are read from data cards following the conventional FORTRAN format rules for column positioning and data-type description, e.g., integer, floating point, or literal. As these data are read, they are automatically processed and printed for inspection. A user's manual for inputting data is given in Appendix 3.1 for reference.

The input phase of the driving subroutine SPIN is an independent segment that allocates storage and determines the storage requirement. An execution mode parameter "MODE" enables a data-check-only routine, or an execution flag. The data-check-only option should be employed before making expensive executions.

A control parameter "NTSG" is available for analyses consisting of variable time steps. A typical consolidation/creep problem having a normal duration of several log-cycles of time can be run more efficiently using progressively increasing time steps.

■ **Floating point data generation.** An isoparametric data generation scheme is employed to internally generate floating point data that would otherwise require hundreds of data cards as input. Floating-point data such as nodal coordinates, prescribed displacements, and initial stresses can be generated along a line, over a surface, or over a volume ⁽¹⁾.

To generate data along a line, 2 or 3 generation points may be specified. The line may extend in two- or three-dimensional physical space.

A two-point generation scheme (NUMGP = 2) would result in linear interpolation between the two points. A three-point generation scheme (NUMGP = 3) would

⁽¹⁾ Should a three-dimensional version be developed.

result in a quadratic interpolation with spacing determined from the mapping

$$\tilde{x}_A = \tilde{x}(\xi_A) = \frac{1}{2}\xi_A(\xi_A - 1)\tilde{x}_1^g + \frac{1}{2}\xi_A(\xi_A + 1)\tilde{x}_2^g + (1 - \xi_A^2)\tilde{x}_3^g, \quad (4.75)$$

where \tilde{x}_A are the interpolated floating-point data for node A , \tilde{x}_i^g are the floating-point data for generation point i , and ξ_A is the location of node A in the ξ -space (nodes are spaced at equal intervals in the ξ -space), as shown in Fig. 4.5. The third generation point ($J=3$ in Fig. 4.5) does not generally coincide with any nodal point.

To generate floating-point data over a surface, 4 or 8 generation points may be specified. This surface may extend in two- or three-dimensional physical space.

A four-point generation scheme ($NUMGP = 4$) would result in *bilinear* interpolation with points interpolated linearly along the generating lines. An eight-point generation scheme ($NUMGP = 8$) would result in *biquadratic serendipity* interpolation. In the latter case, nodal generation points 5-8 may be placed off-center and do not generally coincide with any nodal point (Fig. 4.6).

■ **Integer data generation.** Integer data appear in *boundary condition codes* and *element nodal data specifications*.

Boundary condition data consists of codes "0" and "1" corresponding to "unspecified" and "specified" components, respectively. These data are generated in the array ID using a two-card sequence

$$\left\{ \begin{array}{l} \text{Card 1 : } L, LG, ID_{(1,L)}, \dots, ID_{(NDOF,L)} \\ \text{Card 2 : } N, NG, ID_{(1,N)}, \dots, ID_{(NDOF,L)} \end{array} \right\} \quad (4.76)$$

to set the boundary codes for nodes $L + LG, L + 2LG, \dots, L + kLG \leq N$ equal to those of node L (no generation if $LG = 0$). These data are subsequently processed to assign an *equation number* for each unknown component and to compute the *global number of equations* n_{eq} .

Element nodal data can be input individually, or generated as illustrated schematically in Fig. 4.7 (refer to cards 17.1-17.3 of Appendix 3.1 on element nodal data generation). The nodal data generation utilizes a grid pattern on node and element numbering. Consequently, the integer nodal data for a finite element mesh

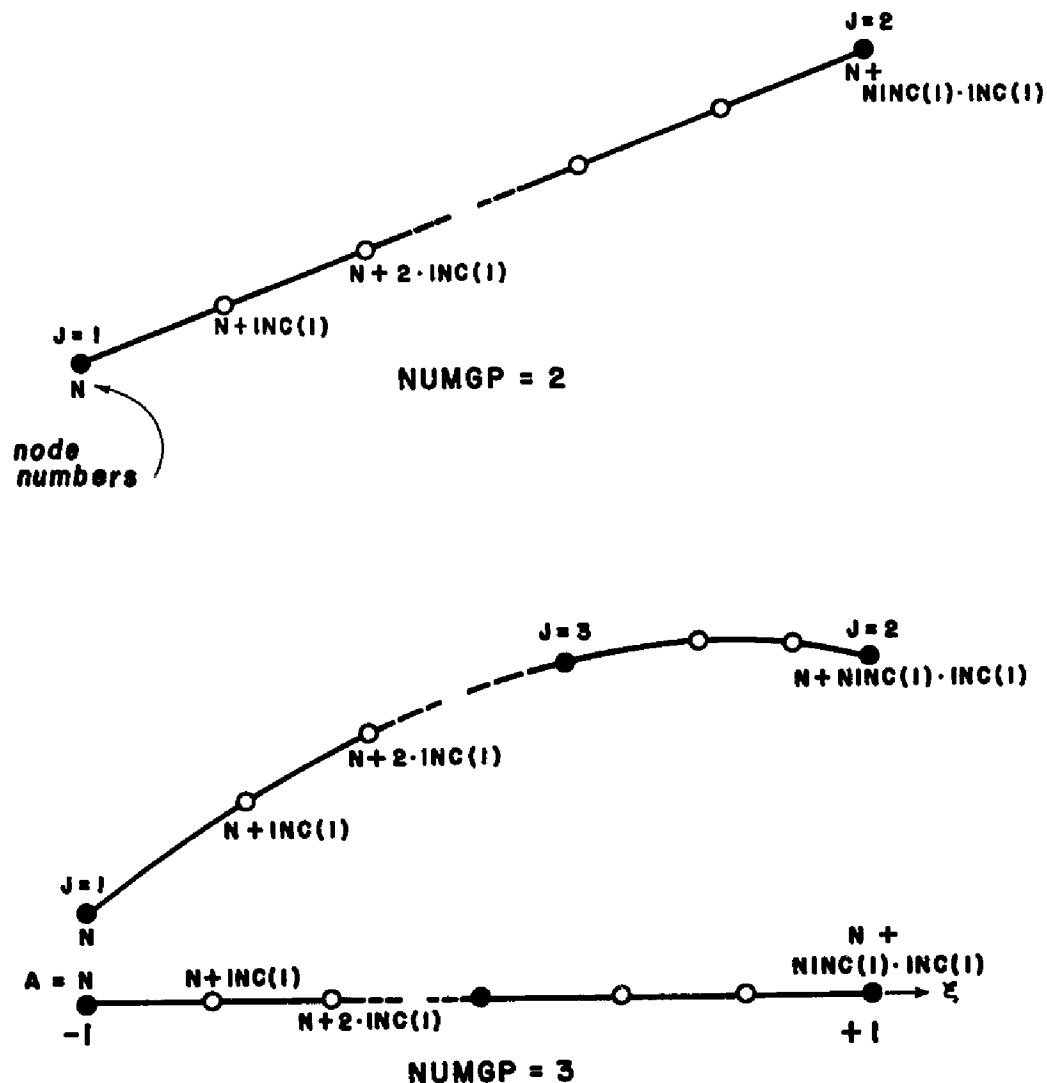
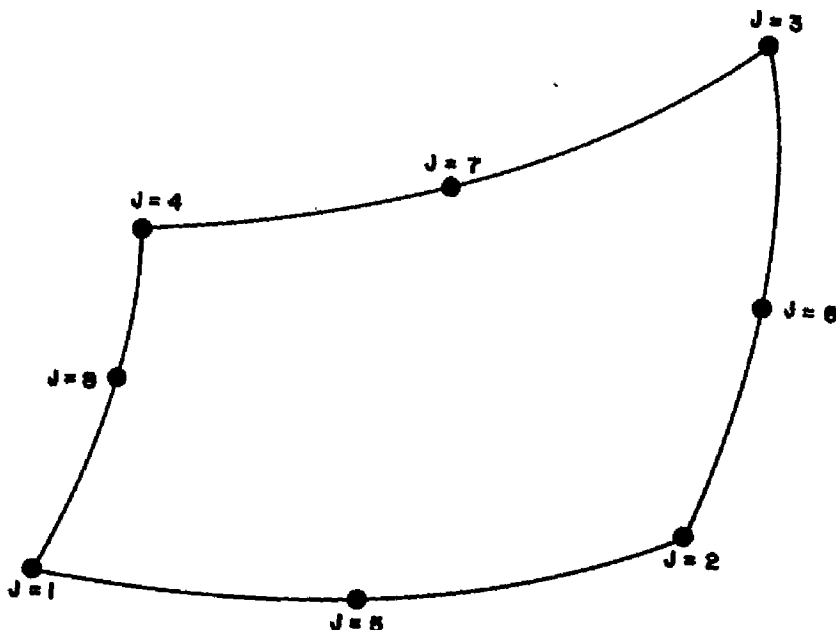
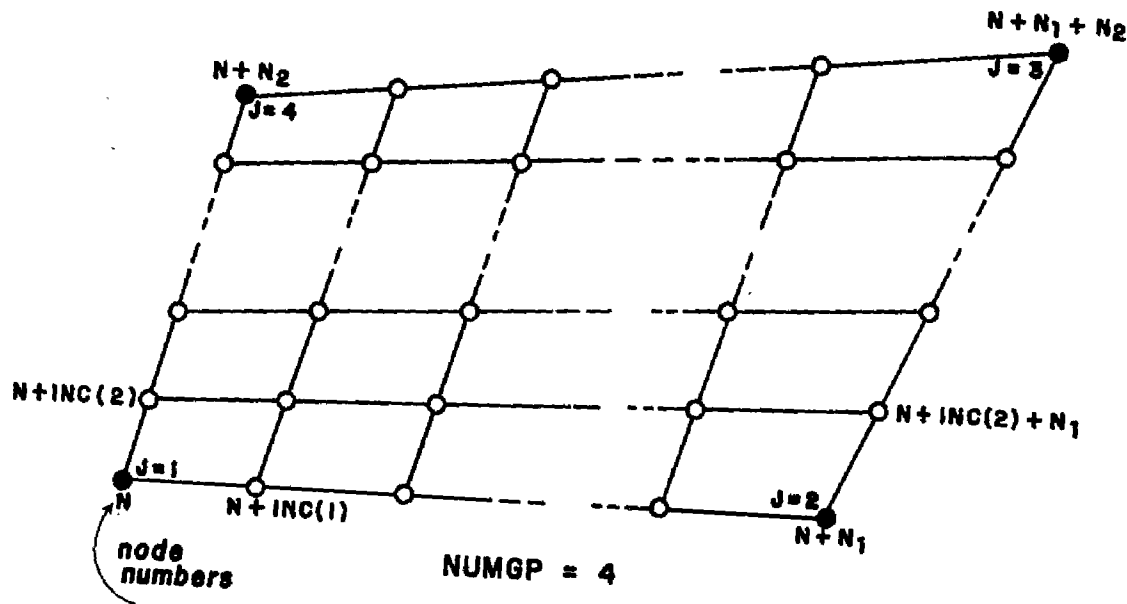


FIG. 4.5. ISOPARAMETRIC FLOATING POINT DATA GENERATION ALONG A LINE.

$$N_1 = NINC(1) \cdot INC(1)$$

$$N_2 = NINC(2) \cdot INC(2)$$



$NUMGP = 8$

FIG. 4.6. ISOPARAMETRIC FLOATING POINT DATA
GENERATION OVER A SURFACE.

consisting of 9-node Lagrangian elements can be generated more conveniently than the integer nodal data for a mesh consisting of 8-node serendipity elements⁽¹⁾ despite the former having more nodes.

■ **Load-time functions.** Load-time functions describe time-histories of applied nodal loads (or velocities) and prescribed displacements (or pressures). There must be at least one load-time function.

Each load-time function is defined by a set of ($NLS + 1$) pairs of time instant t_j and function value $G_i(t_j)$, where NLS is the number of piece-wise linear load steps (see Fig. 4.8).

Applied nodal forces \mathbf{F} , prescribed displacements \mathbf{d}_g , nodal velocities s , and prescribed pressures p_r at node A are defined by the expansion

$$\left\{ \begin{array}{l} \mathbf{F}(\mathbf{x}_A, t) = \sum_{i=1}^{NLC} G_i(t) \mathbf{F}_i(\mathbf{x}_A) \\ \mathbf{d}_g(\mathbf{x}_A, t) = \sum_{i=1}^{NLC} G_i(t) (\mathbf{d}_g)_i(\mathbf{x}_A) \\ s(\mathbf{x}_A, t) = \sum_{i=1}^{NLC} G_i(t) s_i(\mathbf{x}_A) \\ p_r(\mathbf{x}_A, t) = \sum_{i=1}^{NLC} G_i(t) (p_r)_i(\mathbf{x}_A) \end{array} \right\}, \quad (4.77)$$

where NLC is the number of load conditions (i.e., number of time-histories) and \mathbf{F}_i , $(\mathbf{d}_g)_i$, s_i and $(p_r)_i$ are the "mode shapes" for the i th load condition.

As an example, suppose a force $\mathbf{F}(\mathbf{x}_A) = \{ F_x, F_y \} = \{ 0, 10 \}$, initially applied at node A , rotates clockwise at a constant angular velocity ω until $t = \pi/2\omega$ at which time, $\mathbf{F}(\mathbf{x}_A) = \{ F_x, F_y \} = \{ 10, 0 \}$. An application of the above example is the "coriolis force" whose direction changes when the soil specimen is spun in a centrifuge [55].

⁽¹⁾ Serendipity elements are finite elements which contain nodes only on element edges.

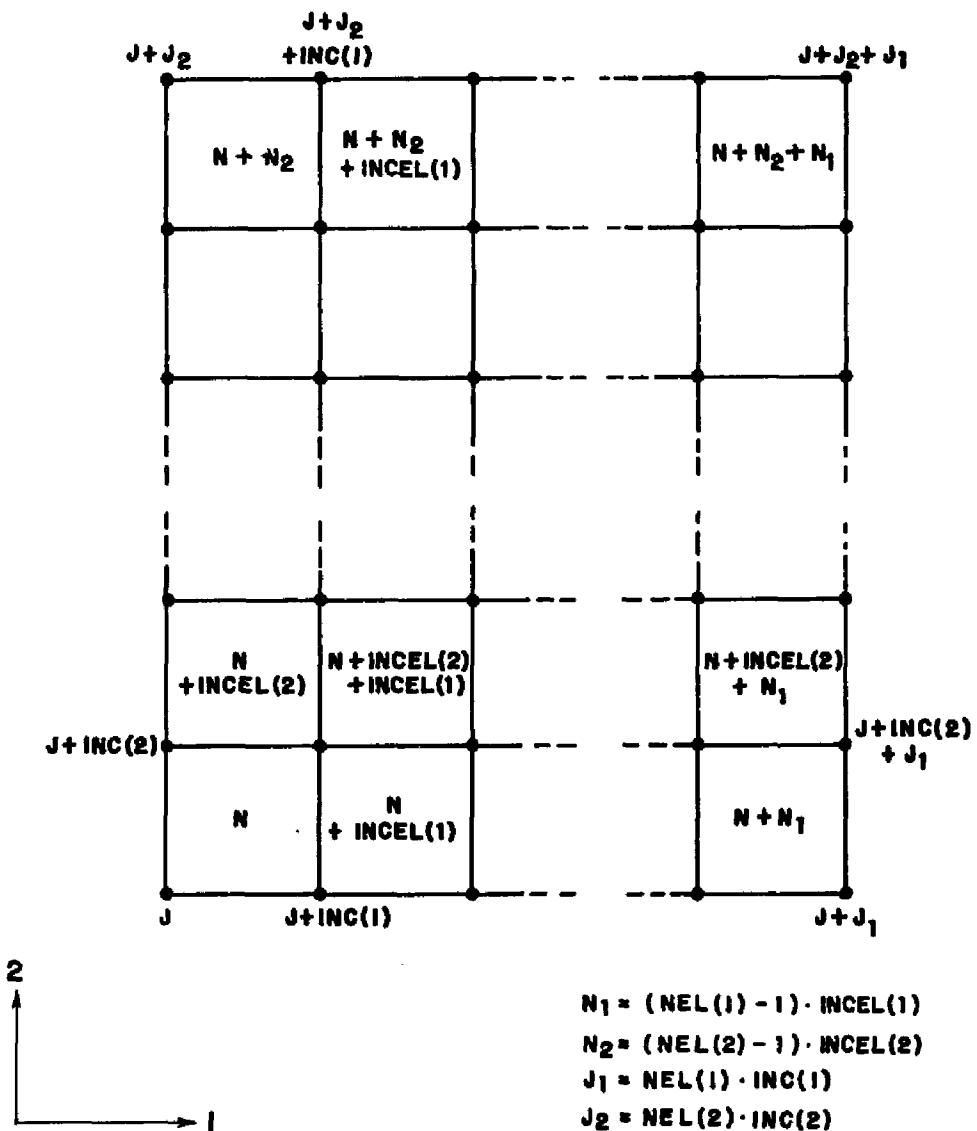


FIG. 4.7. ELEMENT NODAL DATA GENERATION.

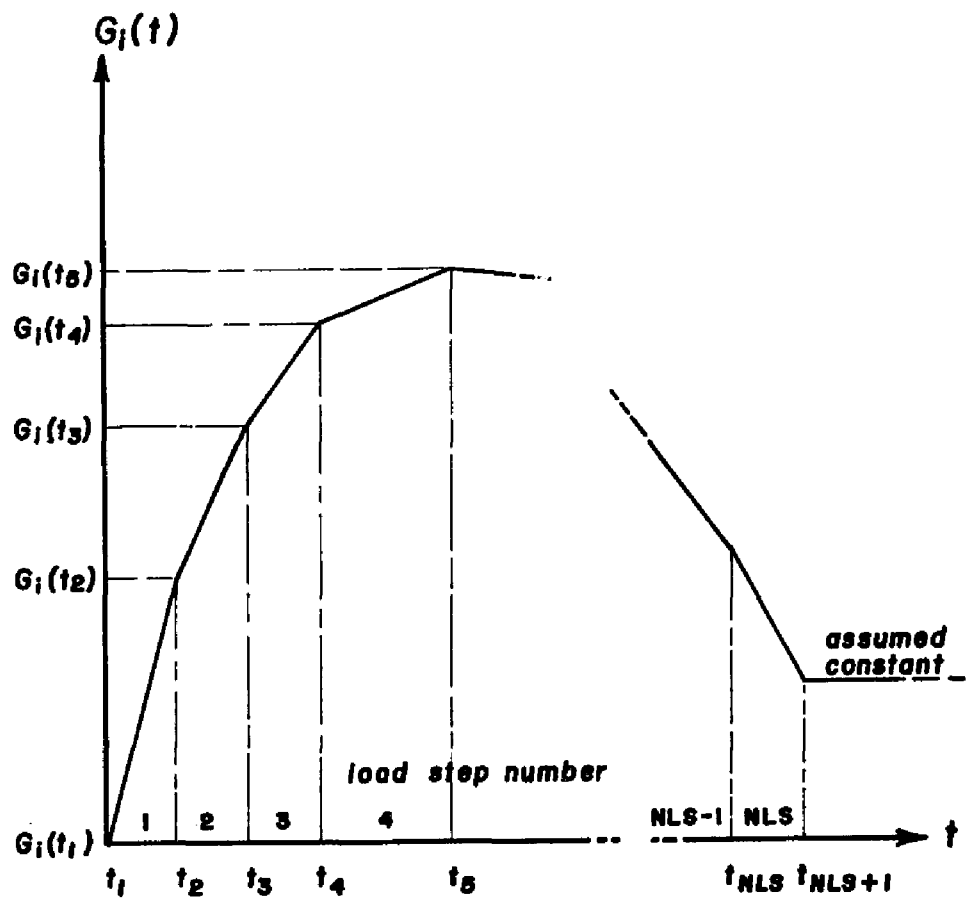


FIG. 4.8 . LOAD-TIME FUNCTION FOR LOAD CASE i.

The above situation can be defined by two load conditions (i.e., $NLC = 2$) as follows:

Load condition 1:

$$G_1 = \cos \omega t, \quad \mathbf{F}_1(\mathbf{x}_A) = \{ 0, 10 \}, \quad 0 \leq t \leq \pi/2\omega. \quad (a)$$

Load condition 2:

$$G_2 = \sin \omega t, \quad \mathbf{F}_2(\mathbf{x}_A) = \{ 10, 0 \}, \quad 0 \leq t \leq \pi/2\omega, \quad (b)$$

and the resultant force becomes

$$\mathbf{F}(\mathbf{x}_A, t) = \sum_{i=1}^{NLC=2} G_i(t) \mathbf{F}_i(\mathbf{x}_A). \quad (c)$$

The G_i 's are input as piecewise linear functions over $t = (0, \pi/2\omega)$ (see also Example 6, Sec. 4.7).

Solution phase

A simplified flow chart of the main algorithm employed in SPIN 2D is shown in Fig. 4.9. It consists of a main time-step loop within which the “ Δd ” for each time increment is evaluated using the predictor/corrector scheme of Sec. 4.3. If $\alpha = 0$, the corrector phase is omitted. This reduces computational cost but accuracy is jeopardized.

An iteration counter i controls accuracy based on an internally pre-set tolerance CONV. This iteration is used since the trial strain $\Delta\hat{\epsilon}^{\text{tr}}$ during the first pass is computed from the “ Δd ” of the previous time step, a procedure which will not work for problems with different time steps. If the time step Δt is constant and reasonably small, a single pass on this iteration loop is usually adequate.

The arrays \mathbf{K} and $\Delta\mathbf{F}$ in Fig. 4.9 are “generic” stiffness and incremental force arrays, respectively, and may contain pressure contributions such as \mathbf{G} , \mathbf{G}^T , and $\beta\Delta t\mathbf{M}$. A flow chart describing the algorithm for constructing \mathbf{K} is shown in Fig. 4.10.

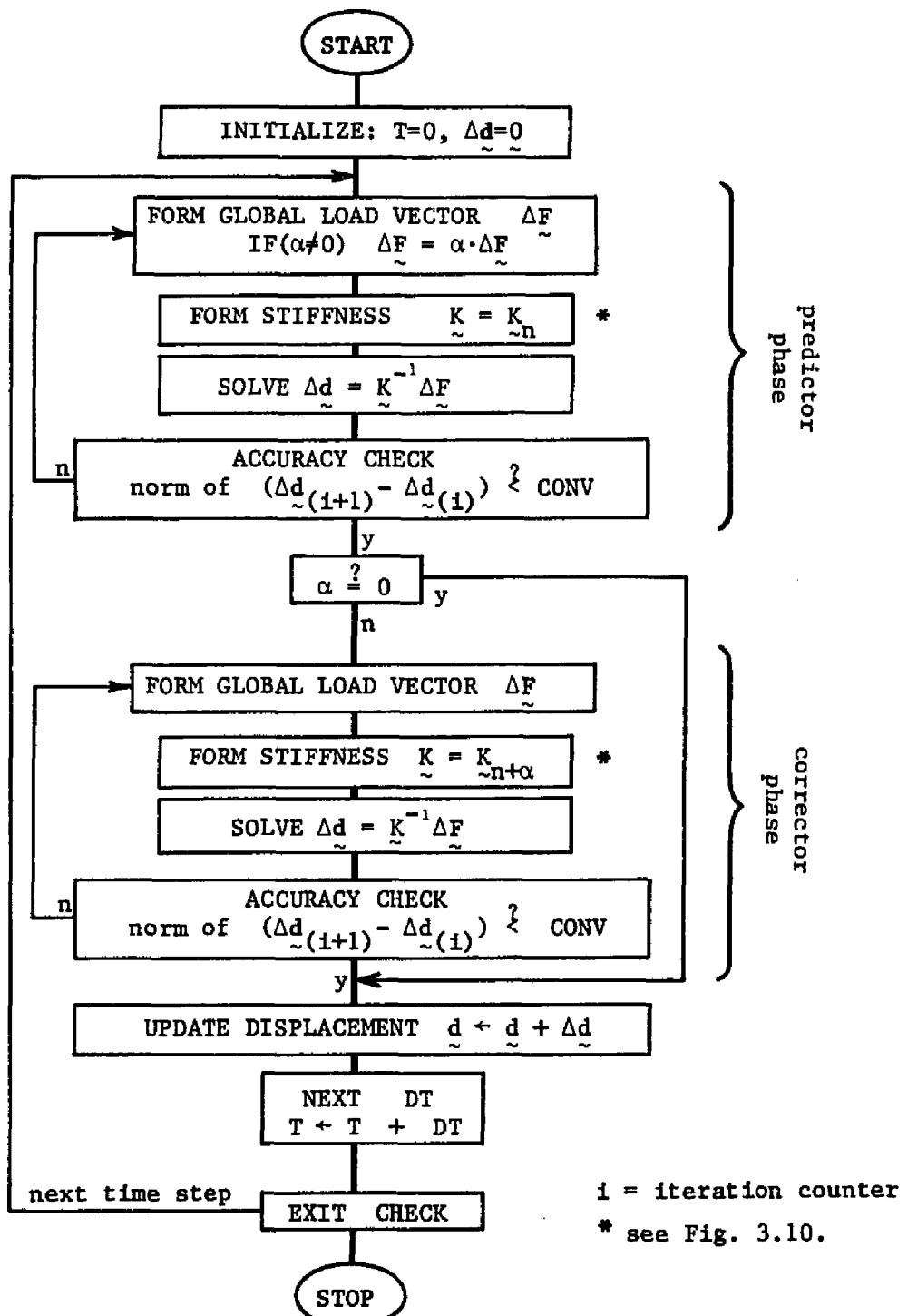


FIG. 4.9. FLOW CHART OF A TYPICAL QUASI-STATIC FINITE ELEMENT PROGRAM.

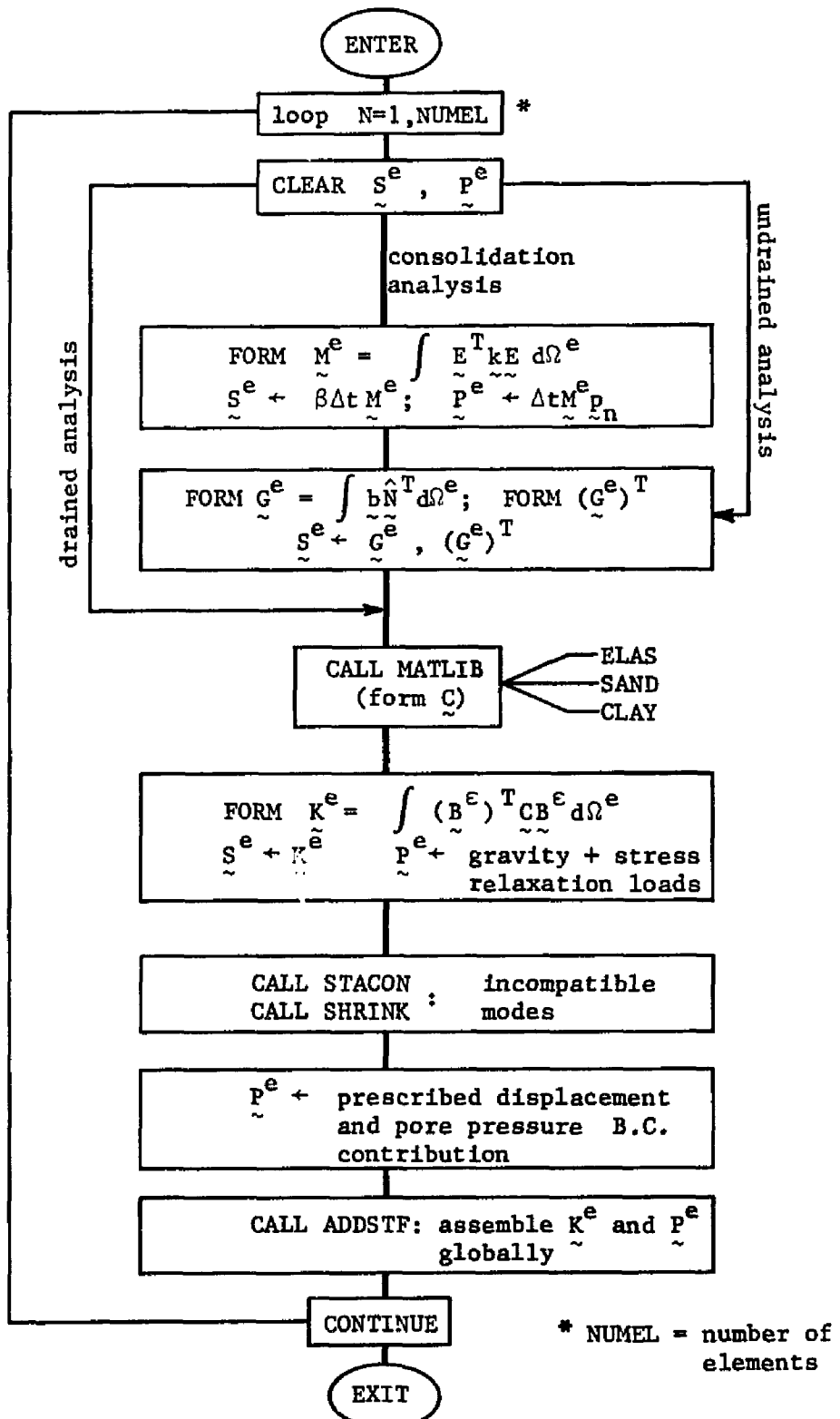


FIG. 4.10. FLOW CHART OF STIFFNESS ASSEMBLY ROUTINE.

■ **Element calculations.** Figure 4.10 shows how the global stiffness matrix \mathbf{K} is assembled from a collection of element contributions. An option flag "IDR" determines whether the analysis is drained, undrained, or if it involves consolidation.

Integration of element matrices may be performed either by the normal Gaussian quadrature rule, by the uniform reduced rule, or by selective reduced integration (see Fig. 4.4). Numerical integration codes are input as element control information.

The elements of the stress-strain matrix \mathbf{B}^e (or \mathbf{B} , if finite deformations are included) are generated by a shape function routine that utilizes the algorithm shown in Fig. 4.11. This routine generates shape function data for isoparametric quadrilateral elements consisting of at most nine nodes.

An incompatible mode or "bending mode" feature is available for four-node quadrilateral elements. The element stiffness and incremental force arrays are initially constructed with extra "bending nodes", which are subsequently condensed by Gaussian elimination on the element level prior to global assembly. This task of static condensation is performed by subroutine STACON. If the mixed formulation is employed, the static condensation procedure creates "voids" in the element stiffness and force arrays. Subroutine SHRINK removes these extra spaces by moving the elements of these arrays appropriately.

■ **Constitutive routines.** The elasto-plastic constitutive routine CLAY and its subroutines compute the stress-strain matrix \mathbf{C} based on the following procedure:

First, the behavior is assumed to be perfectly elastic. A trial strain $\Delta\tilde{\epsilon}^{tr}$ is computed from the current $\Delta\mathbf{d}$ (localized on the element level), and the elastic stress-strain matrix \mathbf{C}^e is constructed.

A trial stress $\tilde{\sigma}_{n+1}^{tr}$ (or $\tilde{\sigma}_{n+\alpha}^{tr}$) is computed. If $\tilde{\sigma}_{n+1}^{tr}$ (or $\tilde{\sigma}_{n+\alpha}^{tr}$) goes beyond the current yield surface of size p_e , an elasto-plastic \mathbf{C}^{ep} is formed. Otherwise, the constitutive routine returns \mathbf{C}^e . A summary of this algorithm is shown in Fig. 4.12.

Because the matrix \mathbf{C} depends on element stresses at the beginning of the increment, it is necessary to store the stresses $\tilde{\sigma}_n$ (and $\tilde{\sigma}_{n+\alpha}$ if $\alpha \neq 0$) during the evolution

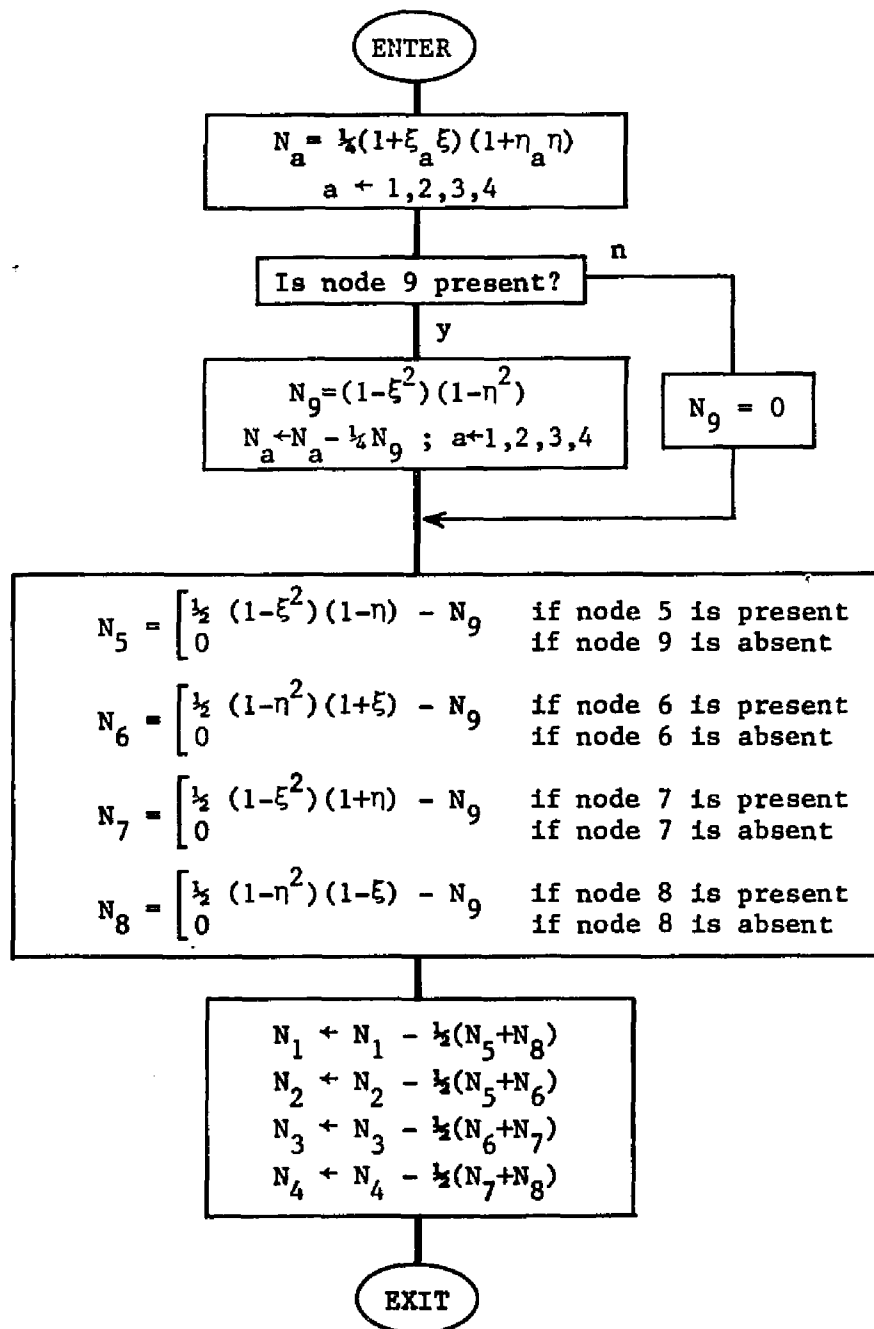


FIG. 4.11. SKETCH OF THE SHAPE FUNCTION ROUTINE [after Hughes, 1982].

GIVEN σ_n , Δd

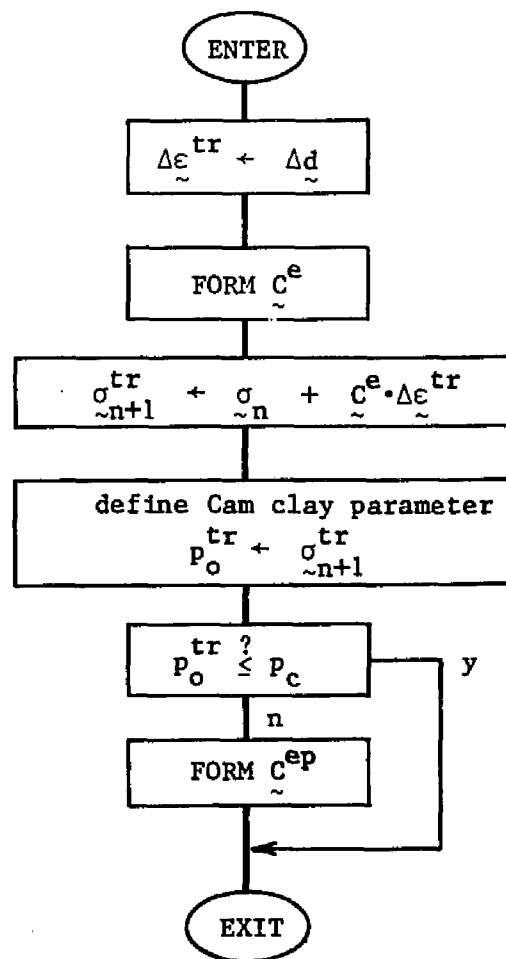


FIG. 4.12 . FLOW CHART OF STRESS-STRAIN MATRIX ASSEMBLY ROUTINE.

of the solution. These stresses are updated every time step due to incremental deformation, stress relaxation, and rigid-body motion (if the finite deformation option is on). A sketch of subroutine UPDATE (and the CLAY-constitutive routines) is given in Appendix 2.1.

■ **Equation solving routine.** The element arrays in their compacted form (i.e., with dimensions equal to the number of element degrees of freedom) are assembled in the global arrays using a connectivity matrix LM. The global stiffness matrix contains only the upper triangular elements, on account of symmetry, that are enveloped by the “profile” or “skyline”.

Internally, all global arrays are stored in a blank common that resides in the central memory. The global incremental force vector $\Delta\mathbf{F}$ is stored in array B, while \mathbf{K} is stored in a one-dimensional array AUPPER in the order shown in Fig. 4.13. The zero elements of the global stiffness matrix below the skyline are also stored because they become nonzero during the solution process. The addresses of the diagonal elements are stored in the vector IDIAG of length equal to the number of equations, n_{eq} .

The solution of the matrix equations, provided by subroutine SOLVE, involves factorization of the symmetric \mathbf{K} by Crout elimination [65] as follows:

$$\mathbf{K} = \mathbf{U}^T \mathbf{D} \mathbf{U}, \quad (4.78)$$

where \mathbf{U} contains unit diagonal elements and has the same profile as \mathbf{K} , and \mathbf{D} is a diagonal array. The elements of \mathbf{U} and \mathbf{D} overwrite the elements of AUPPER so that no auxiliary storage is required.

A three-step solution involving *forward reduction* and *back substitution* is performed after factorization as follows:

$$\mathbf{U}^T \mathbf{x}_1 = \Delta\mathbf{F} \quad (\text{forward reduction}) \quad (4.79a)$$

$$\mathbf{D} \mathbf{x}_2 = \mathbf{x}_1 \quad (4.79b)$$

$$\mathbf{U} \Delta \mathbf{d} = \mathbf{x}_2 \quad (\text{back substitution}), \quad (4.79c)$$

K							
K_{11}	K_{12}	K_{13}	0	K_{15}	0	0	0
K_{22}	K_{23}	K_{24}	0	0	0	0	0
K_{33}	0	K_{35}	0	0	K_{37}	0	0
K_{44}	K_{45}	K_{46}	K_{47}	K_{48}			
	K_{55}	K_{56}	K_{57}	K_{58}			
SYMMETRIC							
	K_{66}	K_{67}	K_{68}				
	K_{77}	K_{78}					
	K_{88}						

AUPPER							
A_1	A_2	A_4	0	A_{10}	0	0	0
A_3	A_5	A_7	A_{11}	0	0	0	0
A_6	A_8	A_{12}	0	0	A_{18}	0	0
A_9	A_{13}	A_{15}	A_{19}	A_{23}			
	A_{14}	A_{16}	A_{20}	A_{24}			
	A_{17}	A_{21}	A_{25}				
	A_{22}	A_{26}					
	A_{27}						

IDIAG							
1	3	6	9	14	17	22	27

FIG. 4.13 . STORAGE SCHEME FOR A TYPICAL STIFFNESS MATRIX.

with intermediate vectors \mathbf{x}_1 and \mathbf{x}_2 overwriting array B in turn. Thus only the arrays AUPPER, B, and IDIAG are necessary to carry out the factorization and solution process.

4.7 ILLUSTRATIONS

The objective of this section is to establish the validity of the program SPIN 2D using several basic example problems.⁽¹⁾ The numerical results are compared with available explicit solutions or experimental data. These examples are a prelude to more detailed parametric studies presented in Chapter 5.

Example 1. Drained test on Weald clay.

Bishop and Henkel [5] investigated the stress-strain behavior of Weald clay in drained 'triaxial' compression. The test consisted of consolidating a cylindrical soil sample to an isotropic stress of $p_c = 207 \text{ KN/m}^2$, and then shearing the sample very slowly at an axial strain rate of $\dot{\epsilon}_{22}$ while holding the radial stress $\sigma_{11} = \sigma_{33}$ constant. The test result is shown in Fig. 4.14.

Johnston [28] numerically duplicated this test, without accounting for creep, using a Cam clay-based finite element program "PEPCO". The material properties he used are as follows: $\kappa = 0.031$, $\lambda = 0.088$, $M = 0.882$, $G = 3,000 \text{ KN/m}^2$, and $e_c = 1.0575$ = void ratio at $p = 1 \text{ psi}$ on the critical state line.

Assuming $R_f = 1.00$, the hyperbolic parameter $a = p_c R_f / 3G = 0.023$, and e_a is backfigured as $e_a = e_c - \kappa \ln 2 + \lambda \ln(2 \cdot 6.89) = 1.31$ = void ratio at $p_c = 1 \text{ KN/m}^2$. Using a four-node quadrilateral element⁽²⁾ representing the upper quadrant of a circular cylindrical 'triaxial' specimen, SPIN 2D yields the same stress-strain curve obtained by the program PEPCO for the case when creep is ignored.

The influence of creep was then investigated. To illustrate the development of a

⁽¹⁾ For instructions on how to prepare the input deck, consult Appendix 3.

⁽²⁾ An inset is drawn in each subsequent figure to show which element is used.

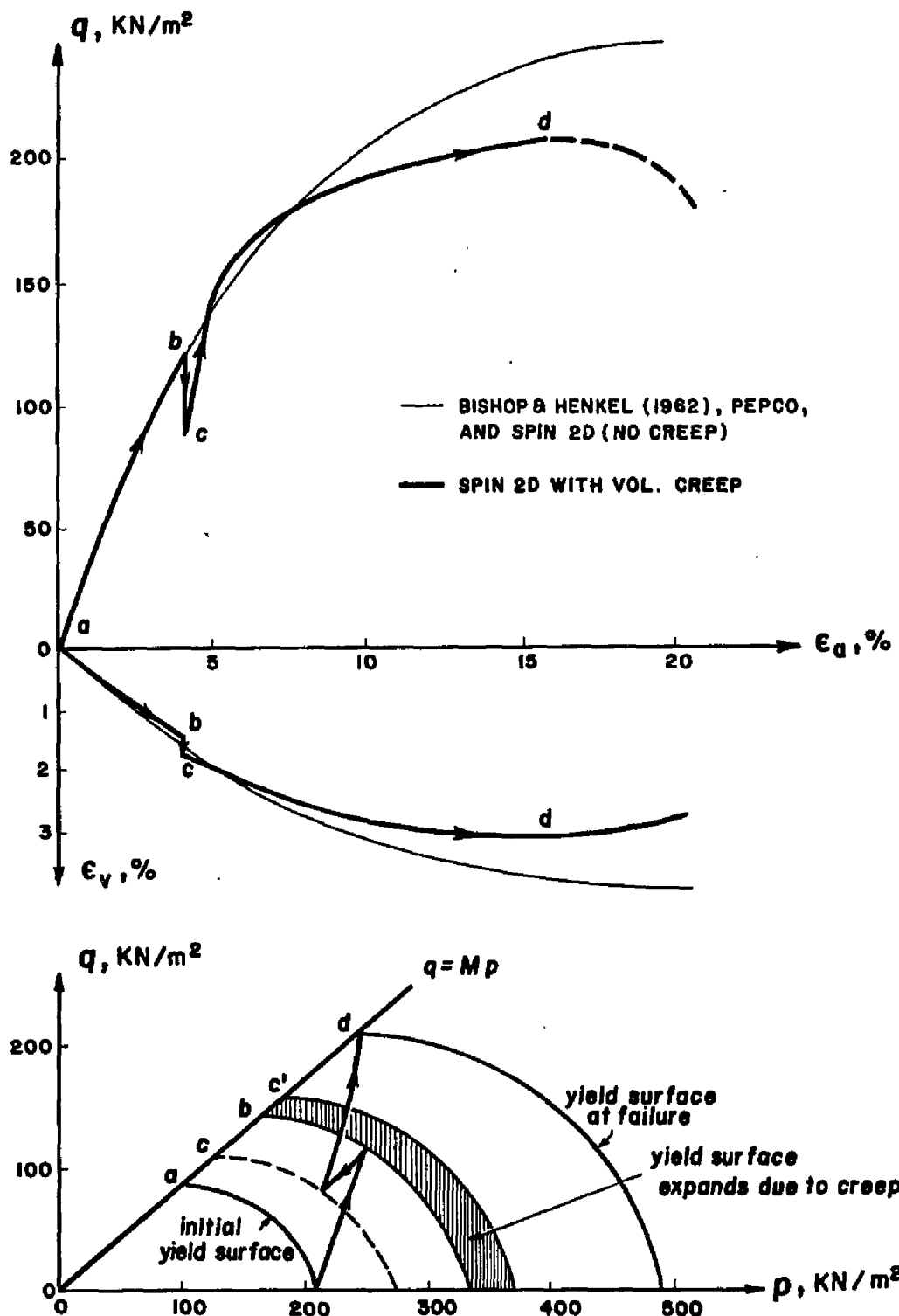


FIG. 4.14. DRAINED TEST ON WEALD CLAY.

quasi-preconsolidation pressure due to volumetric creep, a stress relaxation numerical test was performed, with secondary compression coefficient $\psi = 0.22$ and load-time history $G(t)$ artificially selected. The results superimposed in Fig. 4.14 show the stiffening of the stress-strain response expected due to quasi-preconsolidation during the relaxation increment.

The results shown in Fig. 4.14 also demonstrate how the yield surface expands with time during the stress relaxation stage due to creep. When further straining is imposed, this expanded yield surface is again engaged until the stress state reaches the critical state line. At this point the numerical solution became unstable, giving unusually large strain. Further computations were then terminated. ■

Example 2. Undrained test on undisturbed Bay Mud, no creep.

Undrained ‘triaxial’ compression test results on undisturbed Bay Mud were reported by Bonaparte [11] along with the following material properties: $\lambda = 0.37$, $\kappa = 0.054$, $a = 0.0062$, and $e_a = 2.52$. The normalized hyperbolic curves for the “immediate response” shown in Figs. 4.15 and 4.16 represent the deviator stress vs. axial strain and pore pressure vs. axial strain curves, respectively.

Undrained numerical analyses were performed, without accounting for creep, using a nine-node displacement/three-node pore pressure ⁽¹⁾ finite element (element 2) along with the above properties of the Bay Mud. A value of $M = 1.20$ was chosen, which is smaller than the reported value of $M = 1.40$ for the Bay Mud. This reduction in M made the ellipsoidal yield surface “more flat” to compensate for “lack of creep”, the absence of which makes the stress-strain curve steeper (soil stiffer) than it really is. In Sec. 5.4, the same example problem will be performed using the true $M (=1.40)$ while incorporating for the influence of creep.

At initial confining stresses of 98 KN/m² and 392 KN/m², Figs. 4.15 and 4.16 demonstrate that not only do the hyperbolas normalize experimentally, but they

⁽¹⁾ A more concise description “Q9P3”, i.e., Quadrilateral with 9 displacement/ 3 Pressure nodes is also adopted.

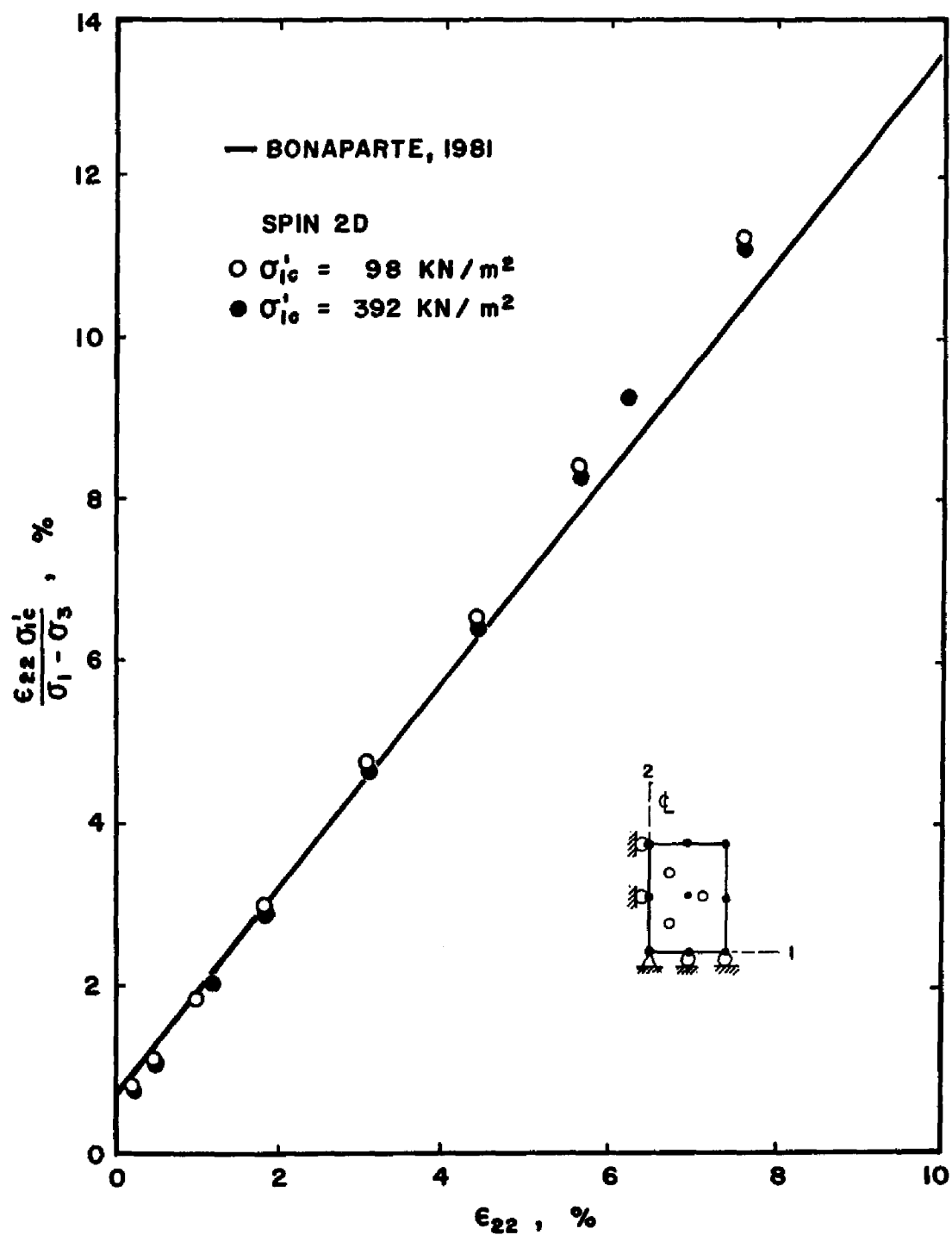


FIG. 4.15. HYPERBOLIC STRESS-STRAIN DIAGRAM,
UNDISTURBED BAY MUD.

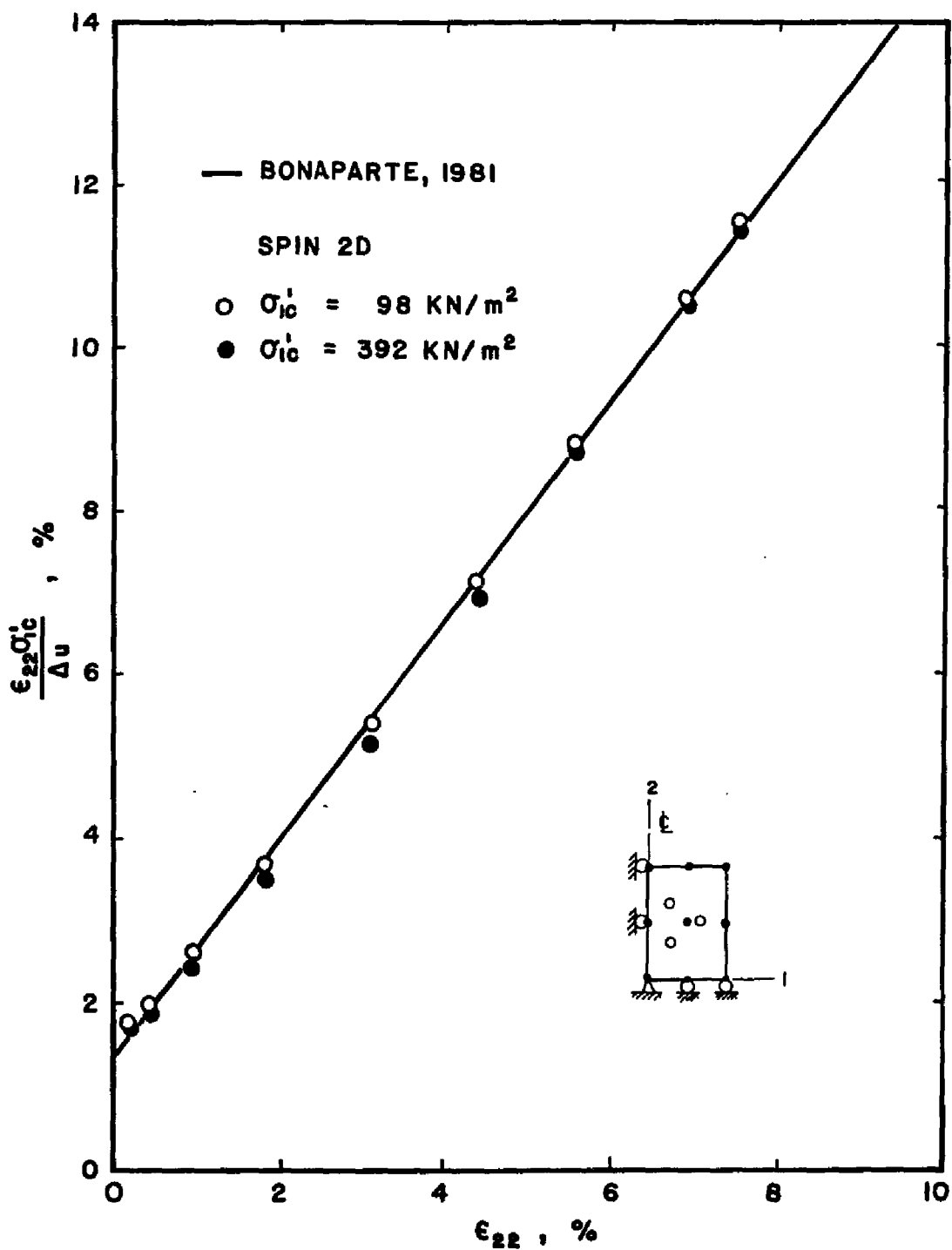


FIG. 4.16. HYPERBOLIC PORE PRESSURE-STRAIN DIAGRAM, UNDISTURBED BAY MUD.

also normalize numerically, with open and closed dots lining up together. ⁽¹⁾

This example likewise shows that the immediate hyperbolic deviator stress-strain and pore pressure-strain curves can be deduced from the volumetric Cam clay model and that a good fit on the stress-strain curve is accompanied by an equally good fit on the pressure-strain curve. This observation has its significance when running creep-inclusive numerical tests since deviatoric ages are computed on the basis of how far the current stress point is from the immediate curve. Substitution of the stress-strain hyperbola in place of the trace of the Cam clay yield surface on the deviator stress-strain plane (which does not have its own explicit form) is an important numerical simplification. ■

Example 3. Isotropic undrained test with volumetric creep.

A sample initially consolidated to an isotropic confining pressure p_o is left undrained and allowed to undergo volumetric creep. Consequently, excess pore pressure develops with time.

The change in void ratio due to creep is given by

$$\Delta e_1 = -\psi \ln \left(\frac{t}{t_o} \right), \quad (4.80)$$

where t_o is the (initial) time at which $p = p_o$. As a result, the soil skeleton swells by an amount

$$\Delta e_2 = \kappa \ln \left(\frac{p_o}{p} \right). \quad (4.81)$$

Imposing the incompressibility constraint,

$$\Delta e_1 + \Delta e_2 = 0. \quad (4.82)$$

The isotropic stress p at any time t is, therefore,

$$p = p_o \left(\frac{t_o}{t} \right)^{\psi/\kappa}, \quad (4.83)$$

⁽¹⁾ The input and output data for this problem are presented in Appendix 3.2 for the case $\sigma_e = 392 \text{ KN/m}^2$.

and the excess pore pressure that develops with time is

$$\rho = p_o - p = p_o \left[1 - \left(\frac{t_o}{t} \right)^{\psi/\kappa} \right]. \quad (4.84)$$

The validity of equation (4.84) has been demonstrated by Bonaparte [11].

Equation (4.83) is plotted in Fig. 4.17 for the case $\psi/\kappa = 0.145$. A constrained 9-node displacement/3-node pressure element (element 2) was used, with material parameters $\psi = 0.0065$ and $\kappa = 0.045$. The results, also plotted in Fig. 4.17, show excellent agreement. ■

Example 4. Terzaghi's one-dimensional consolidation theory.

Explicit solutions are available for problems involving consolidation in one dimension. The pore pressure distribution along the normalized depth $Z = z/H$ at any time factor $T_v = c_v t/H^2$, where H is half the distance between opposite drainage boundaries and c_v is the coefficient of consolidation, is given by [56]

$$\rho(Z, T_v) = \frac{4}{\pi} \rho_o \sum_{m=0}^{\infty} \frac{1}{(2m+1)} e^{-[\pi^2(2m+1)^2/4]T_v} \sin \frac{\pi}{2}(2m+1)Z, \quad (4.85)$$

where ρ_o is the initial pore pressure and m is an integer. For any time factor T_v , (4.85) defines an isochrone. Three isochrones are plotted in Fig. 4.18 for $T_v = 0.1$, 0.3, and 0.7.

The average value of ρ over the depth H is

$$\bar{\rho}(T_v) = \frac{8}{\pi^2} \rho_o \sum_{m=0}^{\infty} \frac{1}{(2m+1)^2} e^{-[\pi^2(2m+1)^2/4]T_v}, \quad (4.86)$$

while the average degree of consolidation is given by

$$\bar{U} = 1 - \bar{\rho}(T_v)/\rho_o. \quad (4.87)$$

The average degree of consolidation also gives the ratio between the current vertical settlement and the ultimate settlement at 100 percent pore pressure dissipation. A plot of U versus $\log T_v$ is shown in Fig. 4.19.

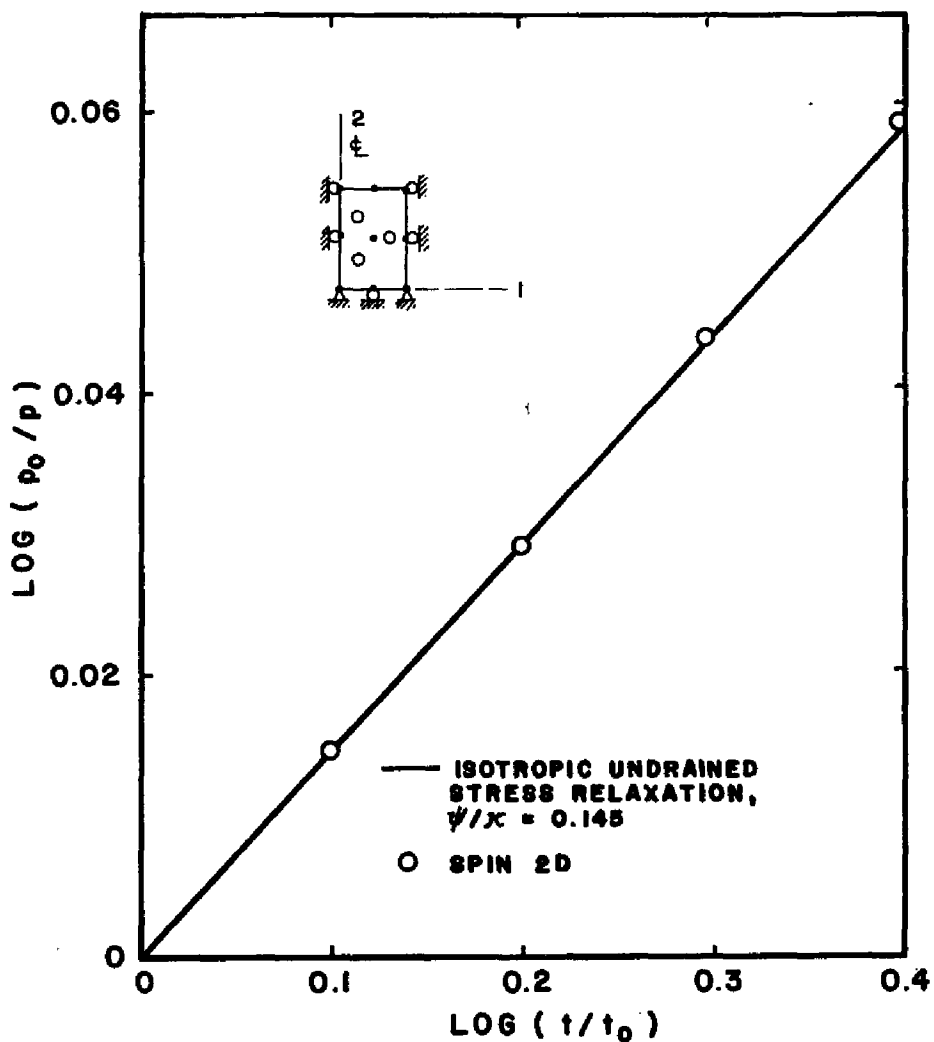


FIG. 4.17. ISOTROPIC UNDRAINED STRESS RELAXATION,
 $\psi = 0.0065$, $\kappa = 0.045$.

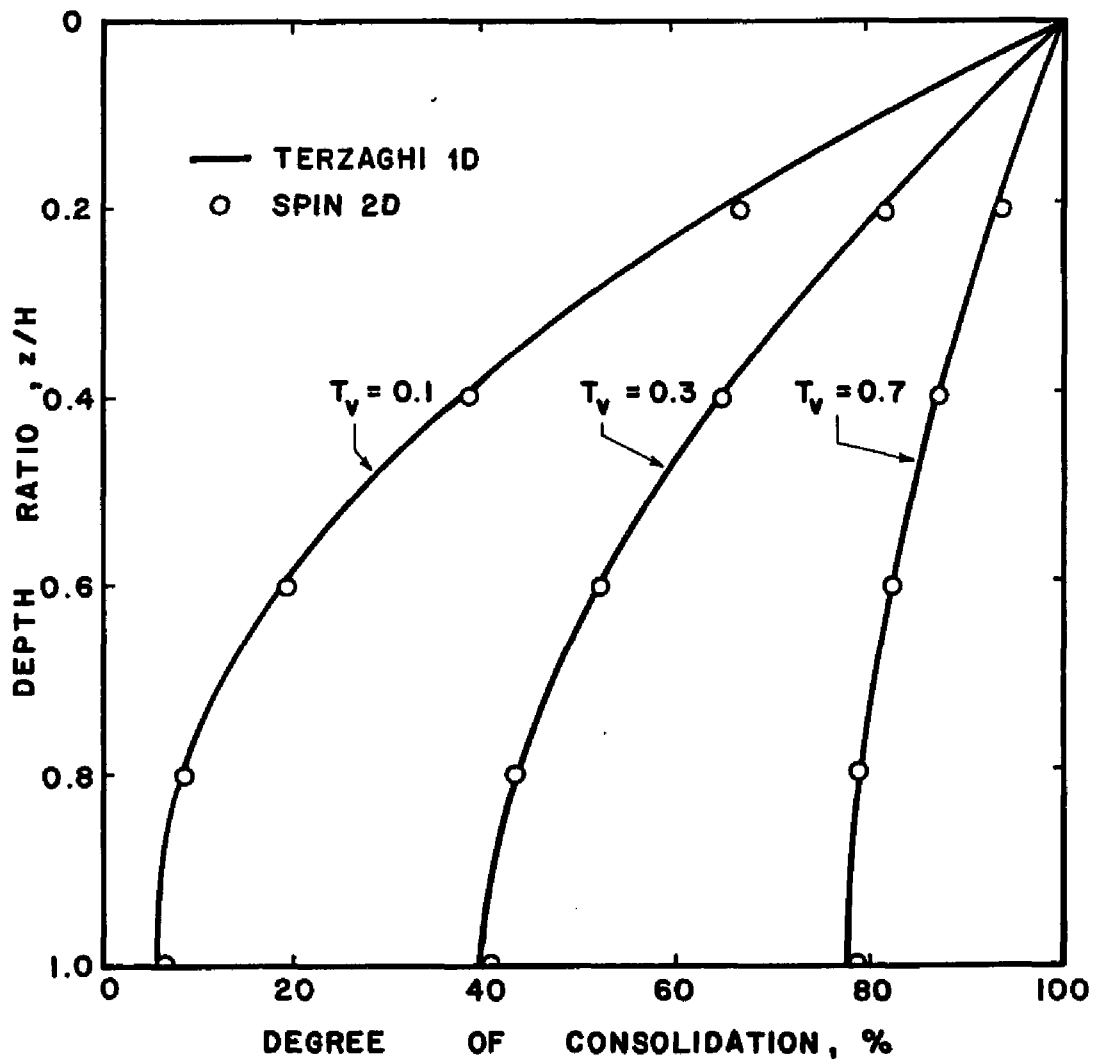


FIG. 4.18. ISOCHRONES FOR ONE-DIMENSIONAL CONSOLIDATION.

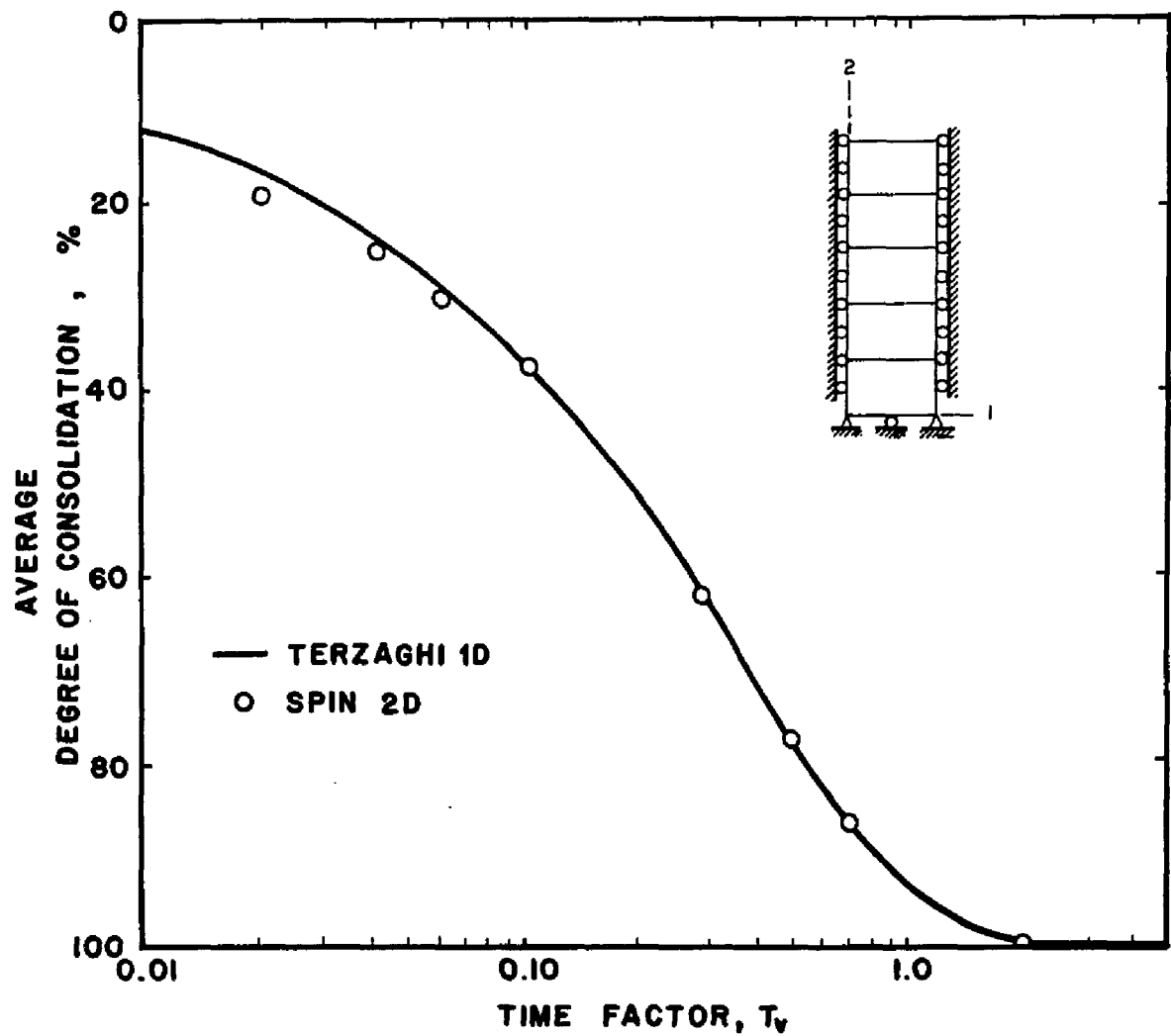


FIG. 4.19. ONE-DIMENSIONAL CONSOLIDATION.

Five Q8P4 finite elements (element 4) of linearly elastic material were constrained laterally to simulate one-dimensional behavior. Letting $z = Z$ and $H = 1.0$, $c_v = 1.0$, and hence $T_v = t$, the elements were allowed to "consolidate". A combination of Poisson's ratio $\nu = 0.3$ and Young's modulus $E = 7,280$ were assigned to the soil skeleton, giving a constrained modulus $E_c = 9,800$ and a permeability of $k = c_v \gamma_w / E_c = 0.001$ (consistent units are implied).

The numerical results are plotted in Figs. 4.18 and 4.19. Very good fit can be observed specially at large values of T_v . The results for small T_v can be improved by subdividing Δt further into smaller increments. ■

Example 5. Radial consolidation, free strain.

Explicit solutions are also available for the condition in which drainage goes radially, while allowing the loading surface to deform so that the stress distribution on the soil remains constant. This condition of radial flow and vertical compression governs the behavior of triaxial test samples consolidated radially, although free radial strain at the top cap is generally not realized.

The average degree of consolidation for free-strain, radial drainage is given by [56]

$$U = 1 - 4 \sum_{n=1}^{\infty} \frac{1}{\beta_n^2} e^{-\beta_n^2 T_v}, \quad (4.88)$$

where $\pm\beta$ are the roots of the equation $J_0(\beta) = 0$, in which J_0 is a Bessel function of the first kind and order zero. A plot of U versus T_v is shown in Fig. 4.20.

Five Q8P4 finite elements were assembled radially and allowed to consolidate using the data of Example 4, with coefficient of radial consolidation c_r and radius R taking the places of c_v and H , respectively. The average value of ρ was evaluated on a volume basis, e.g., volume of the pressure diagram about the axis of revolution.

The numerical results are also plotted in Fig. 4.20. The same conclusion can be drawn as in Example 4. ■

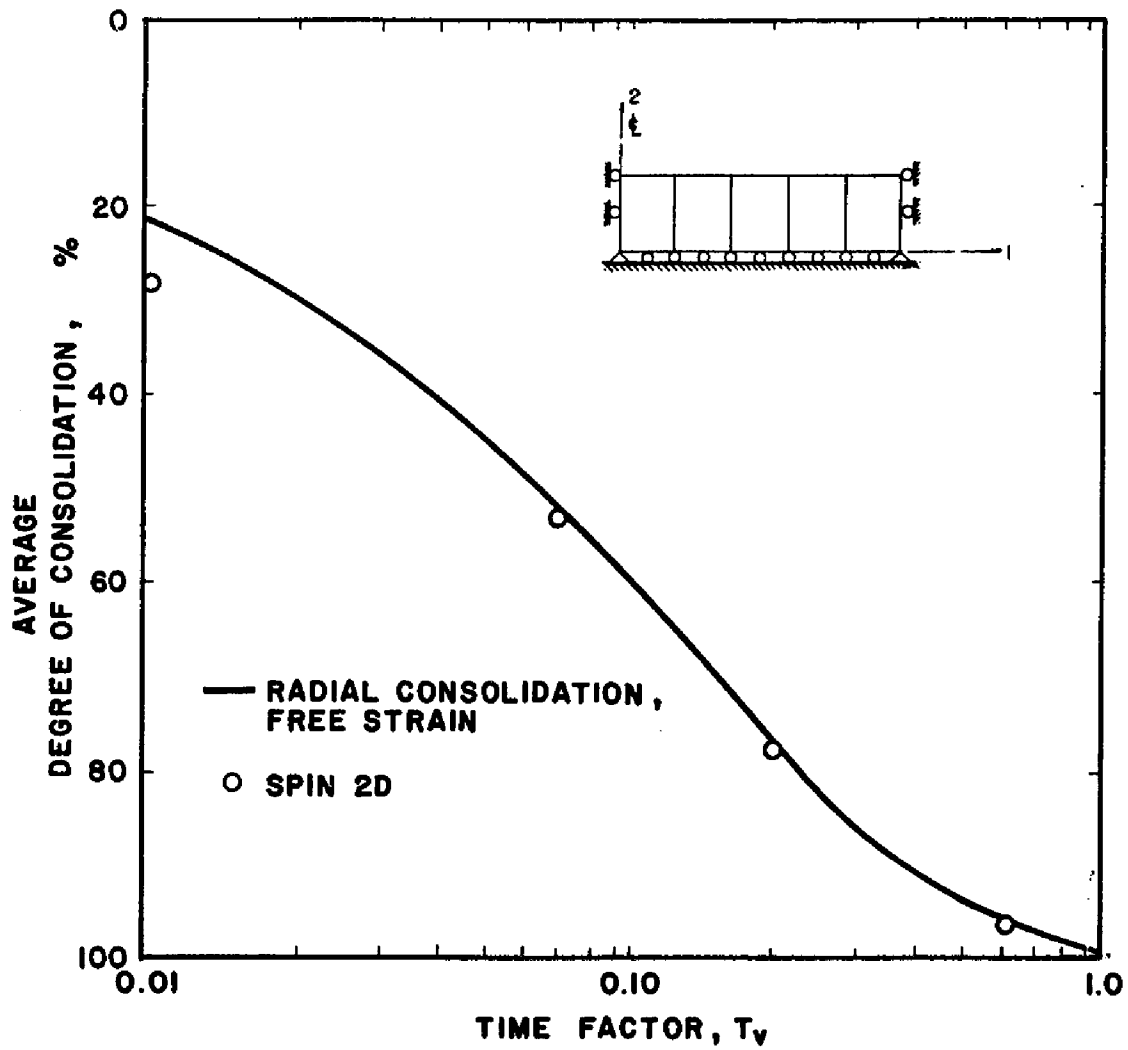


FIG. 4.20. RADIAL CONSOLIDATION,
FREE STRAIN.

Example 6. Rigid body rotation using finite deformation.

A 1×1 square element was initially prestressed to $\sigma_o = \{\sigma_{11}, \sigma_{22}, \sigma_{12}\} = \{0, 1, 0\}$. At an angular velocity ω about its center, the element rotated as a rigid body in the counterclockwise direction until $t_f = \pi/2\omega$. To analyze the problem, the finite deformation option was used and stresses were updated to account for rigid body motion.

The above condition can be defined by two time-history functions (i.e., NLC = 2) of prescribed displacements $\mathbf{d}_g = \{d_{1x}, d_{1y}, d_{2x}, d_{2y}, d_{3x}, d_{3y}, d_{4x}, d_{4y}\}$ as follows:

Load condition 1:

$$G_1 = \frac{1}{2} - \frac{1}{\sqrt{2}} \cos\left(\frac{\pi}{4} + \omega t\right), \quad 0 \leq t \leq \pi/2\omega \quad (a)$$

$$(\mathbf{d}_g)_1 = \{1, 0, 0, 1, -1, 0, 0, 1\}. \quad (b)$$

Load condition 2:

$$G_2 = \sin\left(\frac{\pi}{4} + \omega t\right), \quad 0 \leq t \leq \pi/2\omega \quad (c)$$

$$(\mathbf{d}_g)_2 = \frac{\sqrt{2}-1}{2} \{0, -1, 1, 0, 0, 1, -1, 0\}. \quad (d)$$

Two computer runs were made, the first with 18 time increments, and the second with 36 time increments. Figure 4.21 shows that the computed stresses compare well with the exact solution using Mohr's circle for stress transformation, with results getting better as more time increments are used. ■

Example 7. Uniaxial compression, Lagrangian measure of strains.

The one-dimensional motion along axis 1 of a continuum is given by

$$x = \Lambda(t)X, \quad (4.89)$$

where $-\Lambda$ is the stretch, such that $\Lambda(t=0) = \Lambda_o = 1$.

From (4.48), the natural or true strain increment in time Δt for a one-dimensional motion is

$$-\Delta\epsilon^* = \int_0^{\Delta t} v_{,x} dt = \int_0^{\Delta t} v_{,X} X_{,x} dt, \quad (4.90)$$

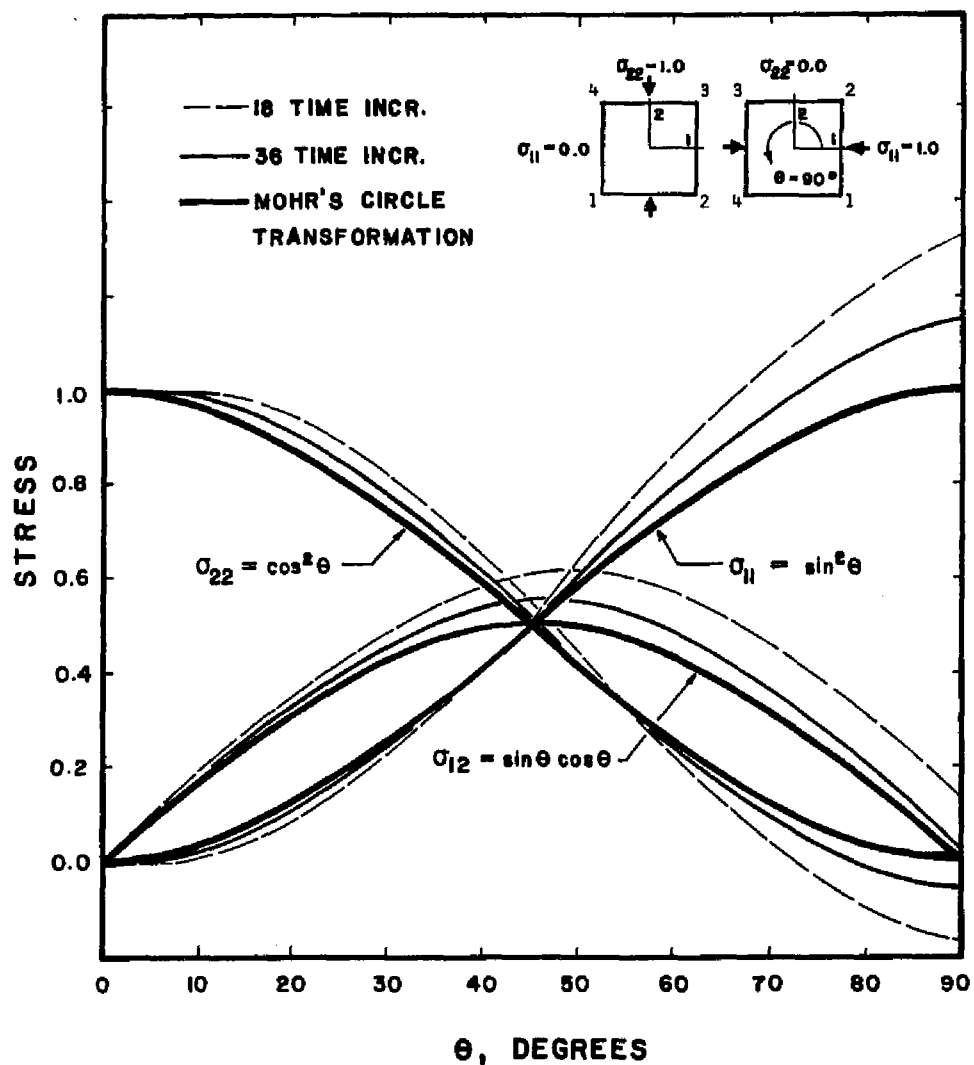


FIG. 4.21. STRESSES DURING RIGID BODY ROTATION.

where the latter is obtained upon application of chain rule.

By definition (4.43), $v = \dot{x} = \frac{\partial \mathbf{x}}{\partial t} |_{\mathbf{x}}$. Differentiating v with respect to X ,

$$v_{,X} = \dot{x}_{,X} = (\dot{\mathbf{x}}_{,X}) = \dot{F}, \quad (4.91)$$

where $F = \mathbf{x}_{,X}$ is the deformation gradient defined by (4.40a).

Hence,

$$-\Delta\epsilon^* = \int_0^{\Delta t} \dot{F} F^{-1} dt = \ln F |_0^{\Delta t} = \ln(\Delta\Lambda). \quad (4.92)$$

Assuming that $\Lambda(t) = 1 - t/2$ for $0 \leq t \leq 1$, the true strain increment is obtained as $\Delta\epsilon^* = -\ln(1 - \Delta t/2) = \ln(1 - \Delta t/2)^{-1}$, while the nominal strain increment $\Delta\epsilon = \Delta t/2$; the latter would have also been predicted by the small strain assumption.

The strain measures $\Delta\epsilon^*$, $\Delta\epsilon$, and the Lagrangian strain, (4.41a, b) adopted in SPIN 2D are all plotted in Fig. 4.22. It can be seen that the Lagrangian strain is a better measure of true strain than of nominal strain. ■

Example 8. Combined compression and simple shear.

Consider the following motion of a 1×1 square continuum on the 1-2 plane:

$$\mathbf{x} = \Lambda(t)\mathbf{X}, \quad (4.93)$$

in which

$$\Lambda(t) = \begin{bmatrix} \Lambda_{11} & \Lambda_{12} \\ 0 & 1 \end{bmatrix}. \quad (4.94)$$

This motion describes a combined compression and simple shear on the 1-2 plane.

As an illustration, suppose that $\Lambda_{11} = 1 - t/2$ and $\Lambda_{12} = -t/2$. In this case, Λ is a homogeneous function of t alone, and not of \mathbf{X} ; hence, $\mathbf{F} = \Lambda$.

Following the procedure of Example 7,

$$\begin{aligned} \Delta\mathbf{u}_{,X} &= \int_0^{\Delta t} \mathbf{v}_{,X} dt = \int_0^{\Delta t} \dot{\Lambda} \Lambda^{-1} dt \\ &= \ln(1 - \Delta t/2) \begin{bmatrix} 1 & 1 \\ 0 & 0 \end{bmatrix}. \end{aligned}$$

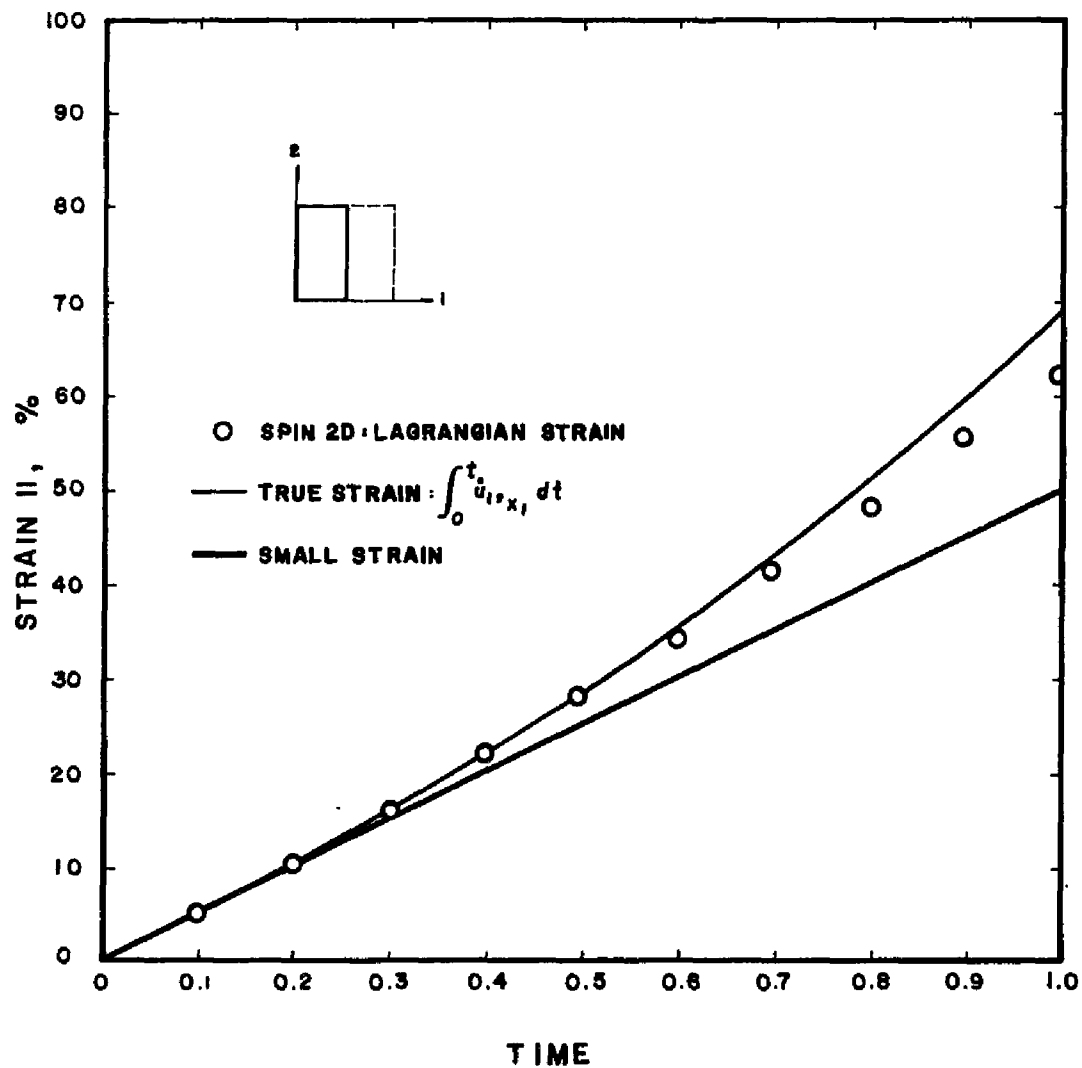


FIG. 4.22. NORMAL STRAIN IN UNIAXIAL COMPRESSION;
STRAIN II IN COMBINED COMPRESSION
AND SIMPLE SHEAR (see also Fig. 3.23).

The natural strain increment is obtained by extracting the symmetric part of $-\Delta u_{,x}$ ⁽¹⁾, i.e.,

$$\Delta \tilde{\epsilon}^* = \begin{bmatrix} \Delta \epsilon_{11}^* & \Delta \epsilon_{12}^* \\ \Delta \epsilon_{21}^* & \Delta \epsilon_{22}^* \end{bmatrix} = \ln(1 - \Delta t/2)^{-1} \begin{bmatrix} 1 & 0.5 \\ 0.5 & 0 \end{bmatrix}.$$

The engineering strains $\Delta \epsilon_{11}^*$ and $2\Delta \epsilon_{12}^*$ are plotted in Figs. 4.22 and 4.23. The Lagrangian strains from SPIN 2D are also plotted along with the nominal strains which can easily be deduced from geometry. The same conclusion as in Example 7 can be drawn. Moreover, the Lagrangian strain also predicts a second order normal strain E_{22} arising from the product terms of (4.41a, b). ■

4.8 SUMMARY

A finite element program was developed to solve creep/consolidation types of boundary value problems using the variational principle. The program, called **SPIN 2D**, is a quasi-static finite element program that can solve two-dimensional axisymmetric (torsionless) and plane strain problems. It uses the Jaumann rate of the Kirchhoff stress, an Eulerian type of formulation, and a Lagrangian measure of finite strains to account for finite deformations. It has the capability to solve consolidation and creep problems, and to treat incompressibility problems by selective integration.

SPIN 2D has eight isoparametric quadrilateral elements in its library, each element having the capability to perform well in specific cases. This library can be easily expanded to include higher order triangular elements as well.

SPIN 2D uses an incremental numerical strategy to march out the solution following a given load history. No specific rule is mentioned as to the magnitude of time step Δt except that it be "small enough". In practice, the sufficiency in the choice of Δt is verified by continually halving the time step until the solution converges to its final value.

⁽¹⁾ Recall that compressive strains are positive.

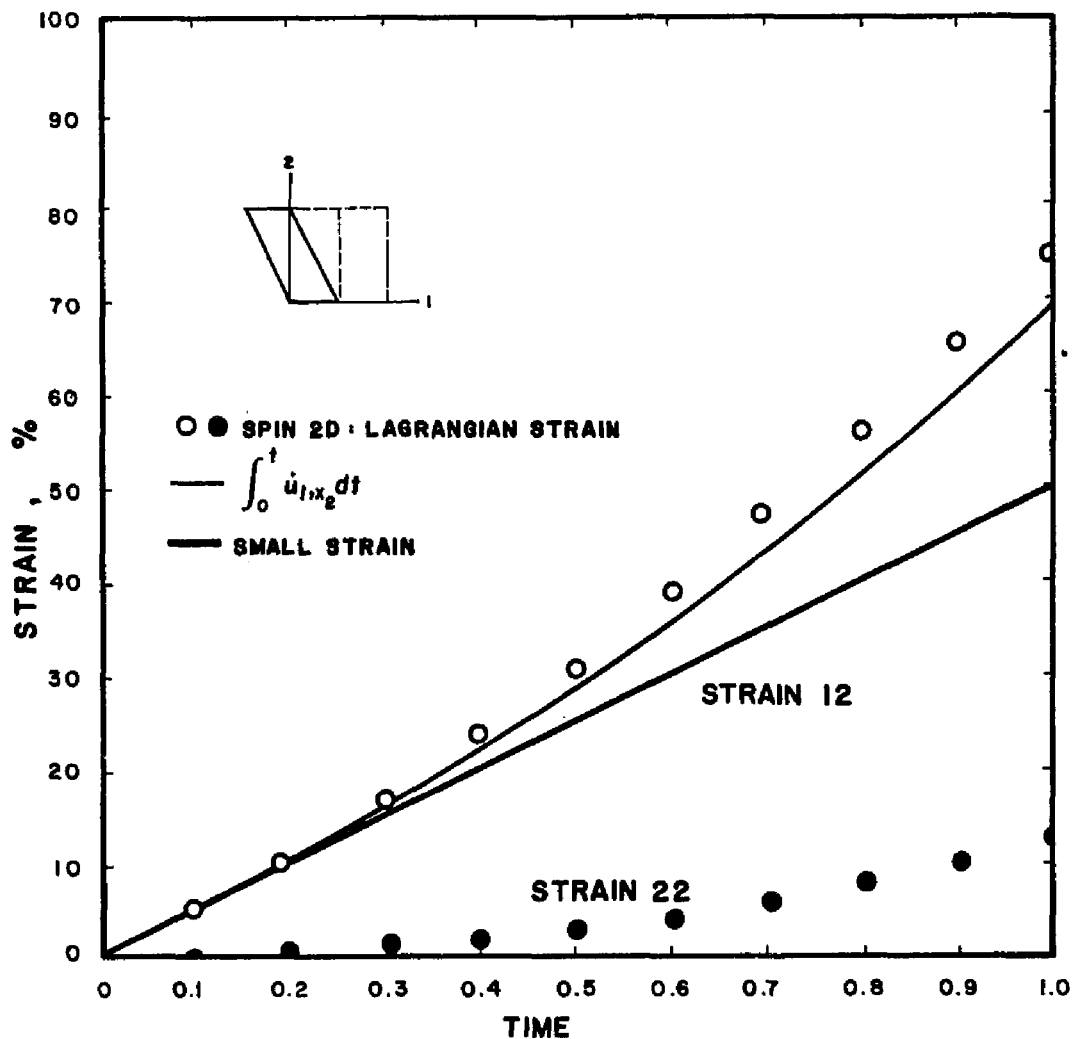


FIG. 4.23. STRAINS IN COMBINED COMPRESSION AND SIMPLE SHEAR.

Finally, the primary/secondary consolidation concept presented in Chapter 2 may likewise be implemented in the program, rather than the immediate/delayed concept used herein. In such a case, a few lines may be added in the code to do a *time-independent analysis* on the element still undergoing consolidation, and incorporate creep effects when excess pore pressures have been completely dissipated, or reach some arbitrarily small value. The extra lines necessary to implement this concept may be offset by the savings realized due to the absence of creep effect computations during the initial consolidation stage, but this concept is not really consistent with the assumption of strain rate tensor decomposition into time-independent and time-dependent parts. It will be shown in Chapter 5, however, that the consistency of the concept of immediate/delayed compression in the context of strain tensor decomposition has additional merits in accurately predicting experimental results as well.

Chapter 5

EVALUATION OF THE CONSTITUTIVE MODEL

5.1 INTRODUCTION

This chapter investigates the validity of the constitutive model using the finite element program SPIN 2D. The constitutive model is evaluated on the basis of its ability to predict accurately the results of simple 'triaxial' and plane strain laboratory tests on San Francisco Bay Mud specimens subjected to different stress and strain paths, and its ability to predict the long-term field behavior of a test embankment founded on a compressible Boston Blue Clay deposit.

In *Part A* of this chapter, parametric studies of the behavior of undisturbed and remolded San Francisco Bay Mud are performed. The numerical experiments include drained, undrained, and consolidation tests, creep and stress relaxation tests, and combined stress relaxation and creep tests in 'triaxial' and plane strain stress conditions.

Comparisons are made between numerical test results, with and without creep effects, and the results of actual laboratory tests. A consistent set of soil parameters taken from published information on Bay Mud is used in the numerical prediction.

In *Part B* of this chapter, SPIN 2D is used to analyze the long-term field behavior of the I-95 test embankment, outside of Boston, Massachusetts. Predictions are made of centerline settlement at the ground surface and of centerline pore pressures within the clay layer, where data obtained from field instrumentation are available. Analyses are made using soil parameters taken from published information on Boston Blue Clay.

Table 5.1

MODEL PARAMETERS FOR UNDISTURBED BAY MUD		
Parameter	Symbol	Value
Virgin compression index ¹	λ C_c	0.37 0.85
Recompression index ¹	κ C_r	0.054 0.124
Secondary compression coefficient ¹	ψ C_a	0.0065 0.0150
Hyperbolic stress-strain parameters ²	a b R_f	0.0062 1.36 (=1.23 from (3.63)) 0.95
Singh-Mitchell creep parameters ³	A \bar{a} m	$3.5 \times 10^{-5}/\text{min}$ 4.45 0.75
Permeability ¹	k_h, k_v	variable
Angle of internal friction ²	ϕ'	34.5°
M from equation (2.30)	M	1.40
Void ratio at $p_c = 1 \text{ KPa}$	e_a	2.52
Instant volumetric time	$(t_v)_i$	1.00 min
Instant deviatoric time	$(t_d)_i$	1.00 min

¹ From 'triaxial' IC or conventional consolidation test² From ICU test with pore pressure measurement³ From ICU-creep test

PART A.
PARAMETRIC STUDIES
ON SAN FRANCISCO BAY MUD

5.2 SOIL PARAMETERS FOR BAY MUD

The soil parameters used to model undisturbed Bay Mud (UBM) and remolded Bay Mud (RBM) are shown in Tables 5.1 and 5.2, respectively. These soil properties are taken from a comprehensive summary of Bay Mud properties presented by Bonaparte and Mitchell [10].

The Bay Mud was obtained from Hamilton Air Force Base in Novato, California

Table 5.2

MODEL PARAMETERS FOR REMOLDED BAY MUD		
Parameter	Symbol	Value
Virgin compression index ¹	λ C_c	0.33 0.75
Recompression index ¹	κ C_r	0.043 0.100
Secondary compression coefficient ¹	ψ C_α	0.022 0.050
Hyperbolic stress-strain parameters ²	a b R_f	0.0089 1.17 (=1.24 from (3.63)) 0.95
Singh-Mitchell creep parameters ³	A $\bar{\alpha}$ m	$0.88 \times 10^{-5}/\text{min}$ 5.40 0.73
Permeability ¹	k_h, k_v	variable
Angle of internal friction ²	ϕ'	34.5°
M from equation (2.30)	M	1.40
Void ratio ¹ at $p_c = 1 \text{ KPa}$	e_a	3.07
Instant volumetric time	$(t_v)_i$	1.00 min
Instant deviatoric time	$(t_d)_i$	1.00 min

¹ From 'triaxial' IC or conventional consolidation test

² From ICU test with pore pressure measurement

³ From ICU-creep test

and generally has a moderate sensitivity to remolding, a low undisturbed strength, is very compressible, and possesses a medium to high plasticity. It has a saturated unit weight of 14.8 KN/m³ (94 pcf), a natural water content of about 90%, a liquid limit of 88%, and a plasticity index of 40%.

For both UBM and RBM, the index parameters C_c , C_r , and C_α were determined from isotropically consolidated 'triaxial' consolidation or conventional one-dimensional consolidation tests. The hyperbolic parameters a , b , and R_f were determined from isotropically consolidated undrained 'triaxial' compression tests. Comparison of the experimental values of b and the values predicted by (3.63) shows that the Cam clay predictions for b are off by about 6 and 9 percent for RBM and UBM, respectively. The experimental values were used in the numerical tests.

The Singh-Mitchell parameters A , $\bar{\alpha}$, and m were determined from the results of isotropically consolidated undrained 'triaxial' creep tests. The parameter e_a which defines the location of the immediate compression curve has been determined by Kavazanjian for RBM using a trial and error procedure [30].

There is no direct way of determining e_a . However, the sensitivity analysis shown in Fig. 5.1 indicates that the stress-strain and the pore pressure-strain diagrams are not seriously affected by the uncertainty in the values of e_a . Thus, e_a for UBM was extrapolated from the primary consolidation plot, under the assumption that this would not introduce significant numerical inaccuracies.

5.3 DRAINED 'TRIAXIAL' TESTS ON UNDISTURBED BAY MUD

Results of four drained 'triaxial' compression tests on undisturbed San Francisco Bay Mud were reported by Lacerda [34]. The specimens were initially isotropically consolidated to confining pressures $\sigma_c = 53.9, 102.9, 156.8$, and 313.6 KN/m^2 and sheared at a strain rate of $\dot{\epsilon}_a = 3.2 \times 10^{-3} \text{ \% per minute}$.

Lacerda showed that the deviator stress versus axial strain diagram can be normalized by dividing the deviator stress by the initial consolidation pressure. A plot of this normalized curve is shown in Fig. 5.2.

Numerical tests were run with and without creep effects. Using the data of Table 5.1, the initial consolidation pressure was set at $\sigma_{11} = \sigma_{22} = \sigma_{33} = 100 \text{ KN/m}^2$ and normal displacements were prescribed in the 2-direction.

When creep is ignored, the load-time function $G_i(t_j)$ becomes arbitrary since the time-independent stress-strain behavior of the soil does not depend on the imposed strain rate. The results of the numerical analysis using one Q4P0 element representing the upper quadrant of the 'triaxial' specimen are shown by the open dots in Fig. 5.2.

For the creep-inclusive predictions, the deviatoric scaling option was employed. It was observed from the preliminary results, however, that the deviatoric age $t_d =$

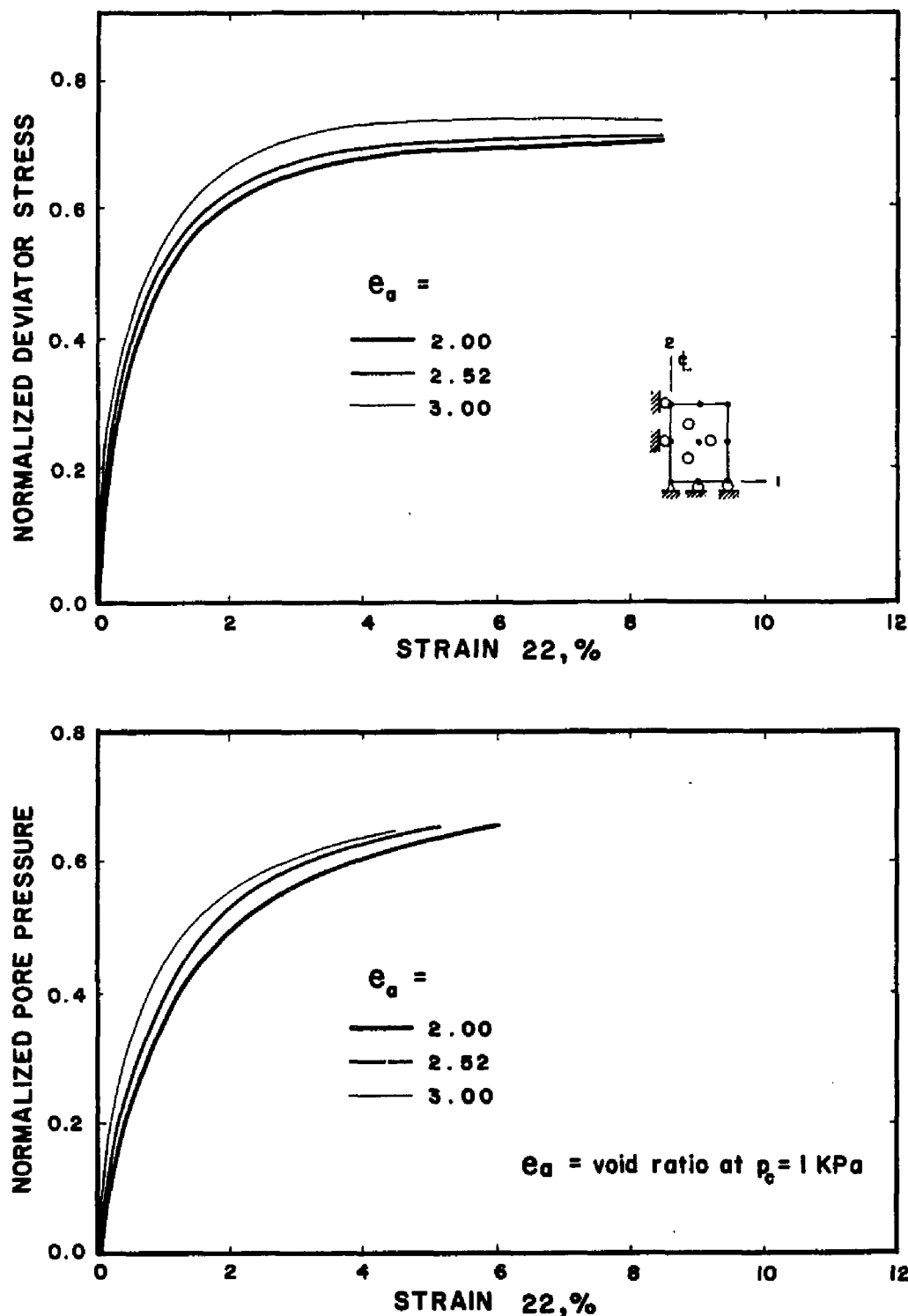


FIG. 5.1. SENSITIVITY OF THE STRESS-STRAIN AND PORE PRESSURE-STRAIN DIAGRAMS TO VALUES OF e_a .

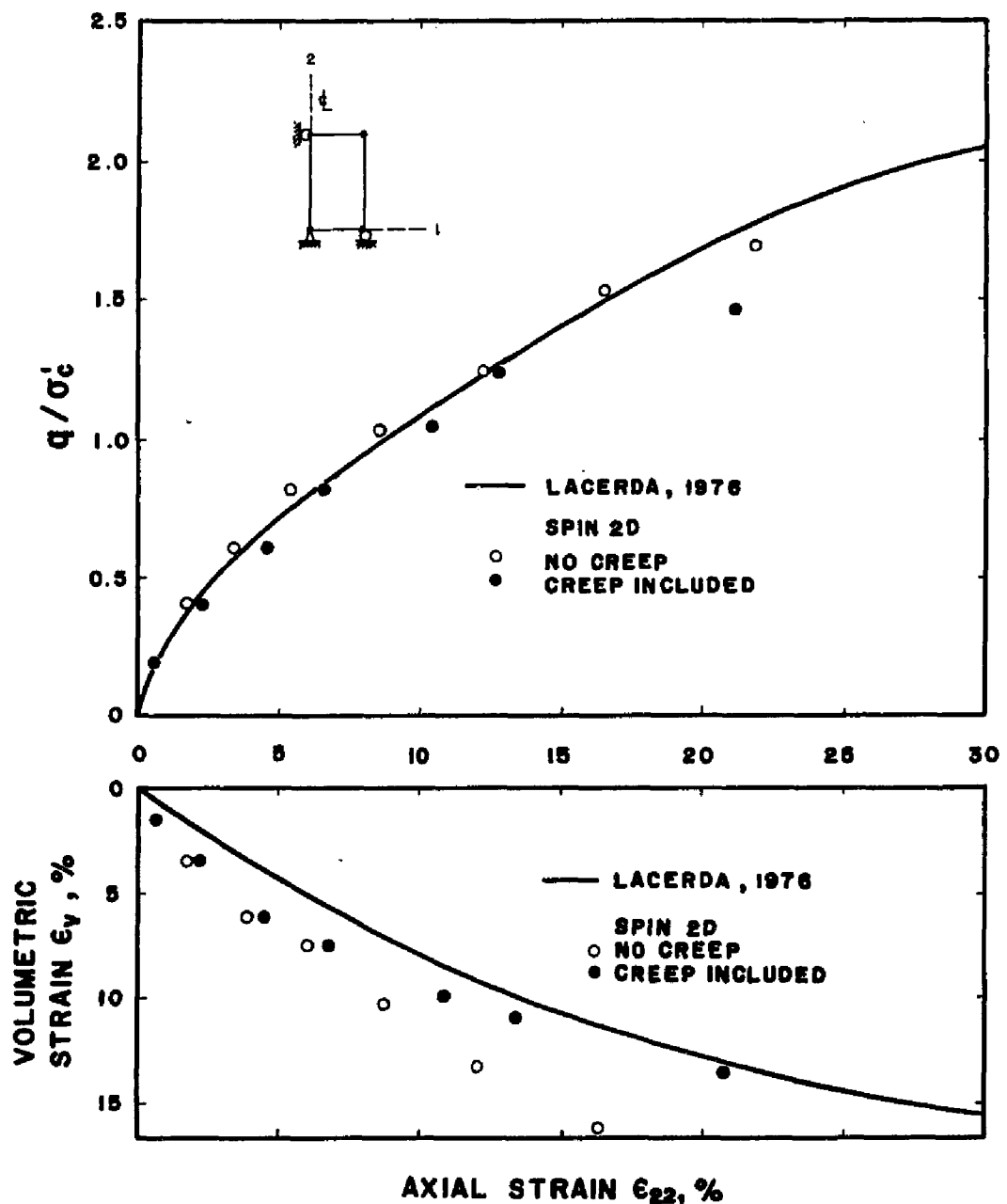


FIG. 5.2. DRAINED TEST ON UNDISTURBED SAN FRANCISCO BAY MUD.

$(t_d)_i$, i.e., the state point always remains on the immediate hyperbola. For this to occur, the Singh-Mitchell creep equation (2.41) should predict a minimum strain rate of

$$\dot{\epsilon}_a^t = A e^{aD} = 0.0035 e^{4.45D} \text{ % per min.} \quad (5.1)$$

This strain rate exceeds the strain rate at which the test was performed ($\dot{\epsilon}_{22} = 3.2 \times 10^{-3}$ % per minute). At this strain rate, therefore, a strain-controlled numerical test with the deviatoric scaling creep option cannot be carried out.

To remedy this problem, an equivalent stress-controlled numerical test was performed in which the stress-time history was determined directly from the normalized plot of Lacerda. The stress-time history was used to construct an equivalent load-time function $G_i(t_j)$ for deviator stresses consisting of two piece-wise linear load steps (NLS = 2, refer to Sec. 4.6) divided into seven equal load increments (NTS = 7). The axial strains $\epsilon_a = \epsilon_{22}$ were then calculated numerically and the results plotted in Fig. 5.2.

The predictions for both the deviator stress below failure and the volumetric strain are improved by the inclusion of creep effects. As should be expected, the inclusion of creep reduces the deviator strength.

5.4 UNDRAINED TESTS ON UNDISTURBED BAY MUD

The objective of this section is to verify the validity of the constitutive model in undrained problems. The "mixed" formulation is generally employed to treat incompressibility although the penalty formulation should give nearly identical results as long as the incompressibility errors are "sufficiently small". The numerical experiments cover undrained creep and stress relaxation tests under plane strain and 'triaxial' stress conditions.

Choice of finite element

Figure 5.3a shows a mesh consisting of twenty five Q4P1 finite elements representing the upper quadrant of a circular cylindrical specimen in a 'triaxial' stress condition. To represent the influence of the top cap, a horizontal constraint was introduced at the upper right-hand corner of the mesh. The specimen was then sheared by prescribing uniform vertical displacements over the top nodes.

In the evolution of the solution, a typical deformed mesh is plotted in Fig. 5.3b. The rotations of the principal stress axes for the individual elements are also shown in Fig. 5.3c, while the element pore pressures are tabulated in Fig. 5.3d.

It can be seen from Fig. 5.3c that the horizontal restraint at the top cap causes the principal stress axes to rotate by about 15 degrees in the element directly in contact with the lateral constraint. Within the same element, the pore pressure is 37 percent higher than average. Below the elements directly in contact with the top cap, however, the principal stress directions are virtually unrotated and the pore pressures are generally uniform. The influence of the top cap, therefore, is rather localized in one particular row of elements.

Figure 5.4 shows the total axial load plotted against the total axial compression for the 89-mm high 'triaxial' specimen. This axial load was evaluated by individually summing the products of vertical stresses σ_{22} and the corresponding areas of influence for the uppermost five elements.

Also plotted in Fig. 5.4 is the average pore pressure, with and without lateral restraint at the top cap, against the total axial compression. As should be expected, the lateral constraint "stiffens" the test specimen overall. However, the difference is generally insignificant and highly localized in one particular row of elements. Therefore, the influence of the top cap will be ignored henceforth.

The behavior of the test specimen in the finite element simulation without top cap restraint under 'triaxial' shearing is characterized by a uniform axial compression and a uniform radial expansion. A single quadrilateral element has the capability to represent this mode of deformation; one Q9P3 element is as good as the twenty five elements previously considered. In fact, a single Q4P1 element is

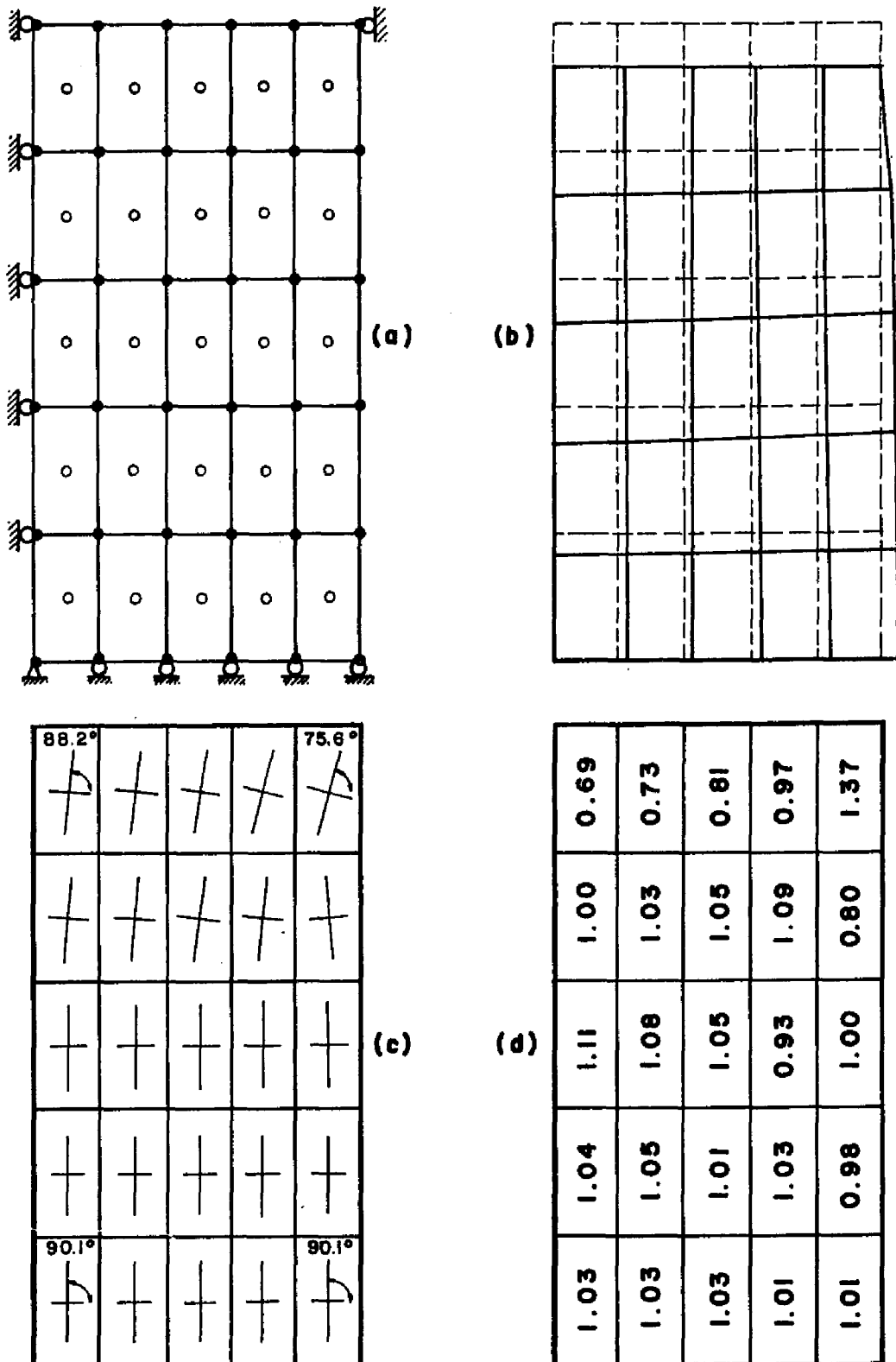


FIG. 5.3. UNDRAINED TEST ON SAN FRANCISCO BAY MUD:
 (a) UNDEFORMED MESH, (b) DEFORMED MESH, (c) ROTATION
 OF PRINCIPAL STRESS AXES, (d) PORE PRESSURE DISTRI-
 BUTION ($= u/u_{ave}$).

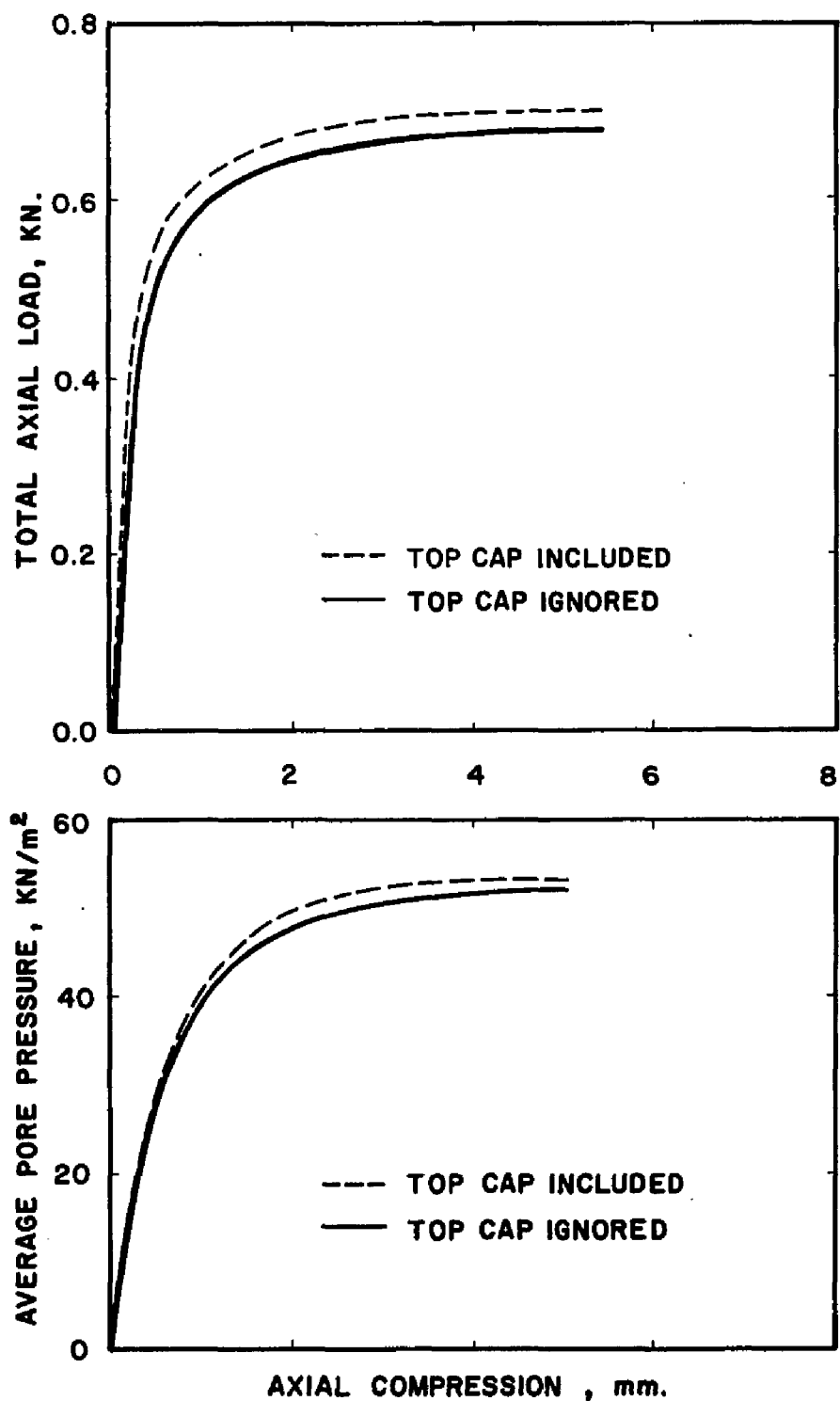


FIG. 5.4. INFLUENCE OF TOP CAP ON THE BEHAVIOR OF SOIL IN A 'TRIAXIAL' TEST.

equally acceptable because no "bending mode" need be represented. Thus, a single quadrilateral element will be employed throughout this section to model 'triaxial' test results.

Undrained creep tests

Undrained creep tests were performed by Lacerda [34] using cylindrical specimens in a standard 'triaxial' cell. The results of three of these tests are shown in Fig. 5.5.

The undisturbed Bay Mud samples for these tests were initially consolidated to an isotropic stress of $\sigma_c = 78.40 \text{ KN/m}^2$ and sheared to different deviatoric stress levels, either by increasing the axial stress (CR-1-2) or by decreasing the lateral stress (SR-1-2 and SR-1-3). The preliminary calculations in Table 5.3 were made to obtain an accurate representation of the events that occurred before the samples were allowed to creep.

Given p_c (the initial isotropic consolidation stress) and q (the applied deviator stress), the volumetric effective stress p at the end of the immediate phase of the undrained deformation was computed from the yield surface (3.5). ⁽¹⁾ The ultimate strength was predicted accurately from (3.62), which gave a value of q_{ult} less than 1.0 percent smaller than that determined from the tests.

Input initial stresses were computed from the values of p and q (see definitions (3.1) and (3.2)), while the immediate strain γ was calculated from the hyperbola (3.64).

One Q9P3 'triaxial' finite element was employed to duplicate the results of the above creep tests. The deviatoric scaling option was used. Excellent agreement between the numerical and the actual results can be observed in Fig. 5.5, but only in so far as the actual behavior of the soils follows the phenomenological Singh-Mitchell creep relationship. Test sample CR-1-2, for example, shows significant deviation from this relationship beyond $t = 1,000$ minutes. For conditions near

⁽¹⁾ More appropriately, the undrained stress path (2.22) through p_c should be used. For small κ/λ ratio (as in this example), however, the difference is small.

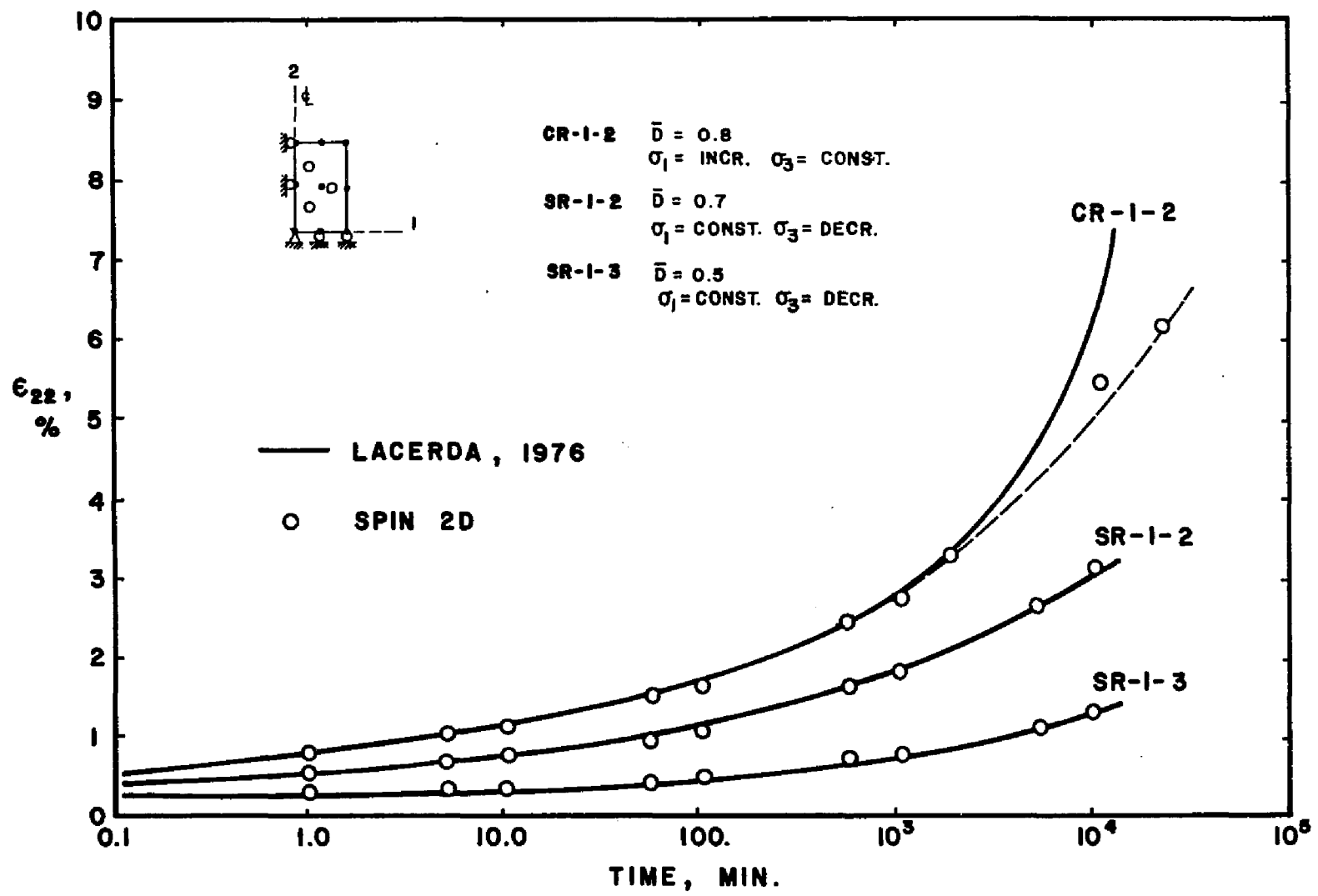


FIG. 5.5. UNDRAINED CREEP TESTS ON UNDISTURBED BAY MUD.

Table 5.3

CREEP TESTS ON UNDISTURBED BAY MUD			
Test Number*	SR-1-3	SR-1-2	CR-1-2
Volumetric stress p	71.74	63.74	56.85
Deviatoric stress q	30.60	42.80	49.00
Preconsolidation pressure p_c	78.40	78.40	78.40
Ultimate strength q_{ult} from (3.62)	60.70	60.70	60.70
Strength q_{ult} from test	61.25	61.25	61.25
Deviatoric stress level D	0.5	0.7	0.8
Initial axial stress σ_{22}	92.14	92.27	89.52
Initial radial stress $\sigma_{11} = \sigma_{33}$	61.54	49.47	40.52
Immediate strain γ from (3.64)	0.58	1.63	3.88
Accumulated creep γ in $(t_d)_i = 1$ min	0.20	0.50	0.80
Initial total strain γ	0.78	2.13	4.68

* Stresses are in KN/m², strains are in percent.

failure, the actual behavior is not characterized by the Singh-Mitchell relationship at all.

It should be noted that this numerical experiment does not involve time-independent plasticity effects. As the soil creeps, excess pore pressures develop due to the arresting of secondary compression, resulting in the reduction of p at a constant q . Whereas such a stress increment always points inwards relative to the yield surface, the yield surface continually expands due to quasi-preconsolidation that occurs concurrently. Thus no time-independent plastic yielding is involved.

Creep tests at different strain rates

It was pointed out in Sec. 2.5 that the hyperbolic curves given by (2.37) and obtained from conventional undrained 'triaxial' tests do not exactly represent the time-independent behavior because they also contain creep components. Kondner [33] suggested that the initial tangent modulus E_i of the hyperbolic stress-strain curve varies with the logarithm of strain rate $\dot{\epsilon}_a$. The degradation of the initial tangent modulus due to strain-rate effects is accompanied by a reduction in failure strength.

Lacerda [34] performed a series of undrained 'triaxial' compression tests at different strain rates, ranging from 1.1 % per minute to 7.3×10^{-4} % per minute, and observed that both E_i and q_{ult} tend to vary linearly with the logarithm of $\dot{\epsilon}_a$. Interpolating E_i and q_{ult} from his plots for $\dot{\epsilon}_a = 1.0, 0.1, 0.01$, and 0.001 % per minute, the corresponding transformed hyperbolic curves are plotted in Fig. 5.6.

Also plotted in Fig. 5.6 is the hyperbolic curve obtained by Bonaparte [11] from conventional undrained 'triaxial' compression tests (see also Example 2, Sec. 4.7). These stress-controlled tests were completed in about 250 to 300 minutes to allow pore pressure equalization, compressing the samples to about 10 percent axial strain during this period. This is roughly equivalent to compressing the samples at a strain rate of about 0.01 % per minute. This is confirmed by the observation that Bonaparte's results plot very close to the hyperbola corresponding to this strain rate.

Numerical analyses were run using one Q9P3 element. The deviatoric scaling option was used, and the load-time function $G_i(t_j)$ was made to vary linearly with natural time. The slopes of these lines represent the rates at which axial displacements are prescribed.

For the case when creep is ignored, the data points define a unique hyperbola regardless of whether the numerical tests are stress-controlled or strain-controlled. For the case when $\dot{\epsilon}_a = 1.0$ % per minute, the transformed hyperbola plots very slightly above the points where creep effects are suppressed, showing virtually no influence of creep at all. The influence of creep becomes more evident for the case when $\dot{\epsilon}_a = 0.1$ % per minute.

The agreement of the numerical analyses with Bonaparte's stress-controlled tests is noteworthy. Recall that the same test was mimicked in Example 2, Sec. 4.7, by reducing the slope M of the critical state line while not accounting for creep to obtain a best fit on the hyperbola. This time, the same curve is duplicated using the true M while accounting for creep effects.

Like the drained test problem of Sec. 5.3, the hyperbolic curve corresponding to a strain rate of $\dot{\epsilon}_a = 0.001$ % per minute can not be numerically duplicated since

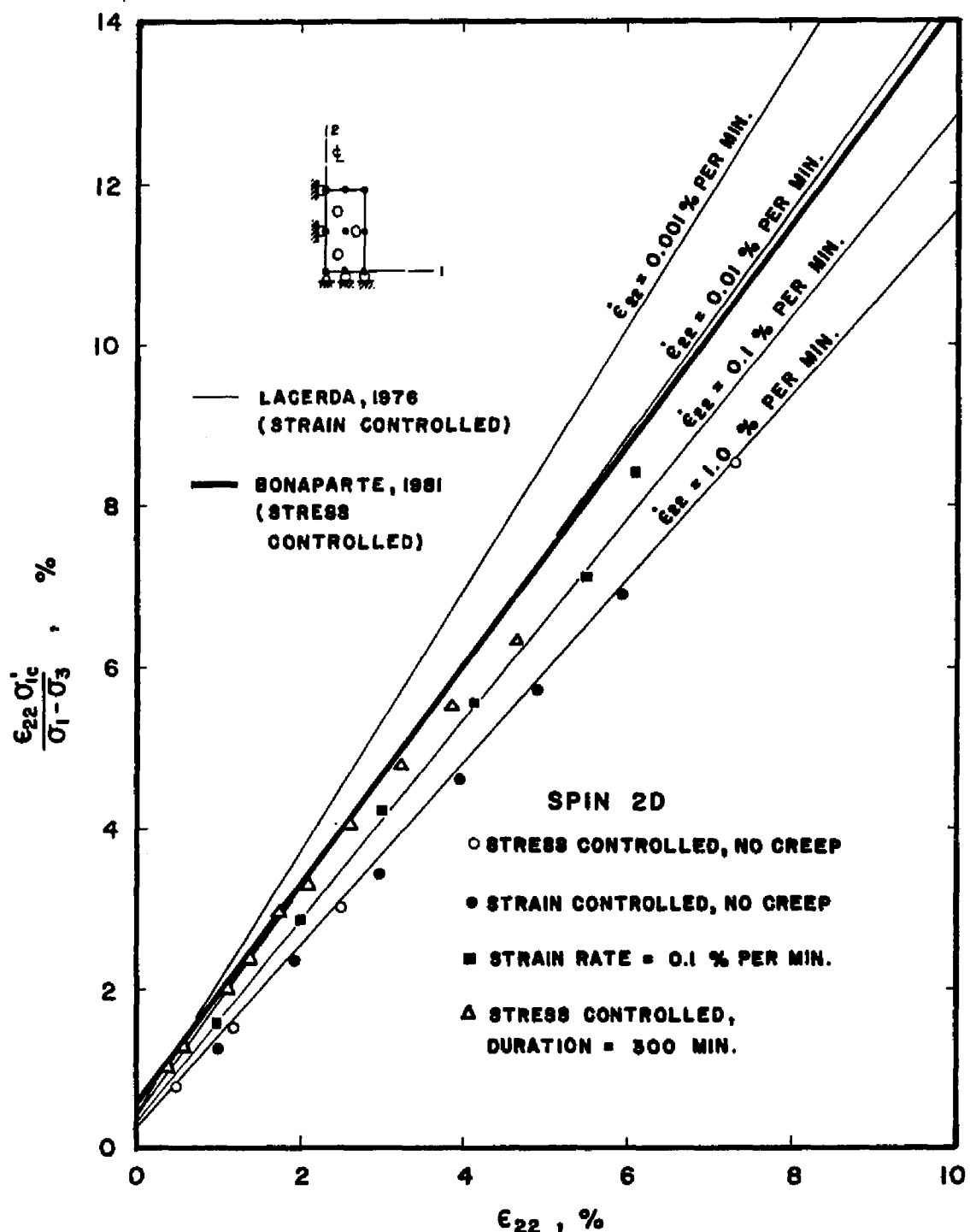


FIG. 5.6. UNDRAINED 'TRIAXIAL' TESTS ON UNDISTURBED BAY MUD
PERFORMED AT DIFFERENT STRAIN RATES.

the creep strain rate evaluated from equation (5.1) exceeds the actual strain rate at any value of $\bar{D} \geq 0$.

Combined creep and stress-relaxation test

Undrained creep and stress-relaxation tests on undisturbed Bay Mud were performed by Lacerda [34]. Results for test number SR-1-5 are shown dashed in Fig. 5.7.

The specimen was initially consolidated to an isotropic effective stress of 78.4 KN/m², and then sheared undrained at a constant axial strain rate of $\dot{\epsilon}_a = 1.52\%$ per minute up to a strain of $\epsilon_a = 0.38$ percent. At this point, the deviator stress $q = 42.6$ KN/m² (point A in Fig. 5.7).

After about 3,000 minutes of stress relaxation (AB) during which the axial strain is maintained constant, shearing was resumed at the same strain rate until the stress level was close to failure (C). The strain was then held at about 2.3 percent for 1,320 minutes after which the specimen was sheared again at a reduced rate of $\dot{\epsilon}_a = 1.6 \times 10^{-2}\%$ per minute.

A numerical test was performed to simulate the above loading. One Q9P3 finite element was used and the deviatoric scaling option was employed. The results of this numerical test are also plotted in Fig. 5.7.

Very good agreement can be observed during stages OA, AB, BC, and CD. However, great care was required to safeguard against numerical instability when the stress level was close to failure (C). At this point, the solution becomes very sensitive to the time step Δt , necessitating the use of the predictor-corrector algorithm to prevent the numerical solution from becoming unstable.

During reloading at a reduced strain rate (DE), the state point returned back to the immediate curve. The creep strain rate obtained from (5.1) exceeded the actual strain rate for $\bar{D} \geq 0.342$. Thus the numerical solution had to be terminated.

Pore pressures are reasonably well predicted except that the predicted curve beyond A overestimated the experimental curve by the amount \overline{AB} . The overestimation of excess pore pressures during this stress-relaxation stage is due to the

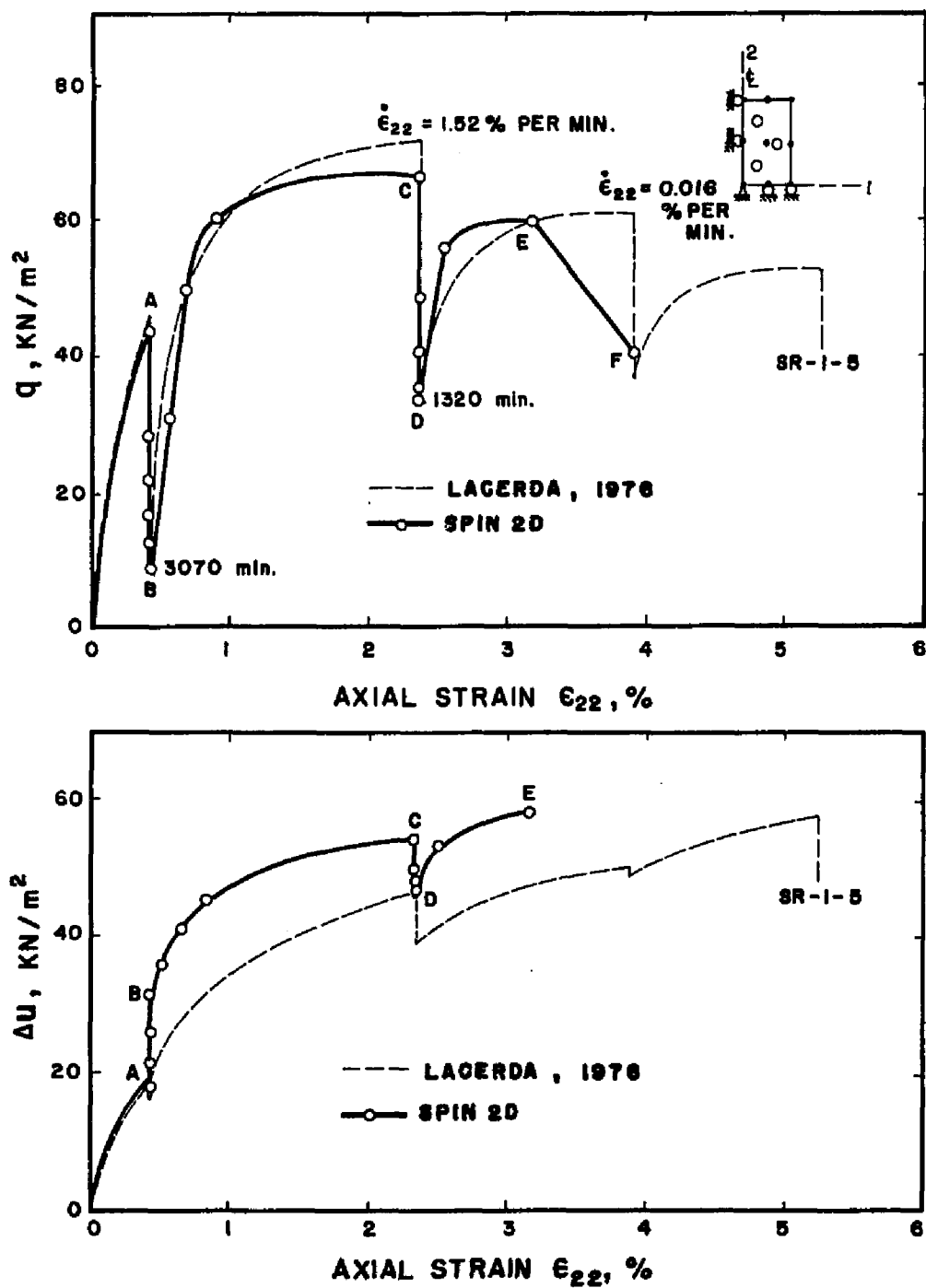


FIG. 5.7. COMBINED CREEP AND STRESS RELAXATION TEST ON UNDISTURBED BAY MUD.

arresting of secondary consolidation occurring in a near-isotropic condition (*B*). As pointed out in Sec. 3.3, Singh-Mitchell scaling tends to overpredict the creep strain rate for values of \bar{D} close to zero, resulting in overprediction of excess pore pressures as well. On the other hand, the reduction in excess pore pressure during stress relaxation stage *CD* does not show the same influence of secondary consolidation because the stress state at this point is close to failure, the normal to the yield surface is almost vertical, and thus the volumetric component of the plastic strain is very small.

Undrained plane strain test

Undrained plane strain tests on undisturbed Bay Mud were performed by Sinram [60] to simulate a deep pressuremeter test stress condition. In this condition, the normal off-plane stress changes as a result of Poisson effects. Sinram measured these stress changes as well as the in-plane strains and pore pressures in his tests.

The loading history is shown by the points on the total stress path in Figs. 5.8 and 5.9. The major and minor principal stresses lie on the plane, while the off-plane intermediate principal stress is equal to:

$$\sigma_2 = \frac{1}{2}(\sigma_1 + \sigma_3) \quad (5.2)$$

since Poisson's ratio $\nu = 0.5$ for the undrained (incompressible) case.

One Q4P1 element was employed to investigate the validity of the constitutive model in this plane strain situation. The deviatoric scaling option was used for creep strains. The unloading-reloading part *OA* was omitted due to the similar unloading stage *CD*.

Generally good agreement can be observed. In the initial (loading) stage *OA*, however, excess pore pressures were overpredicted, resulting in a reduction of volumetric stress p . The stress-strain curve in the loading stage *OA*, therefore, did not contain any time-independent plastic contributions because the stress point never touched the yield surface until the near-rupture condition. Still, the constitutive model predicted very well the rupture strength $(\sigma_1 - \sigma_3)_{\max}$, the pore pressure at

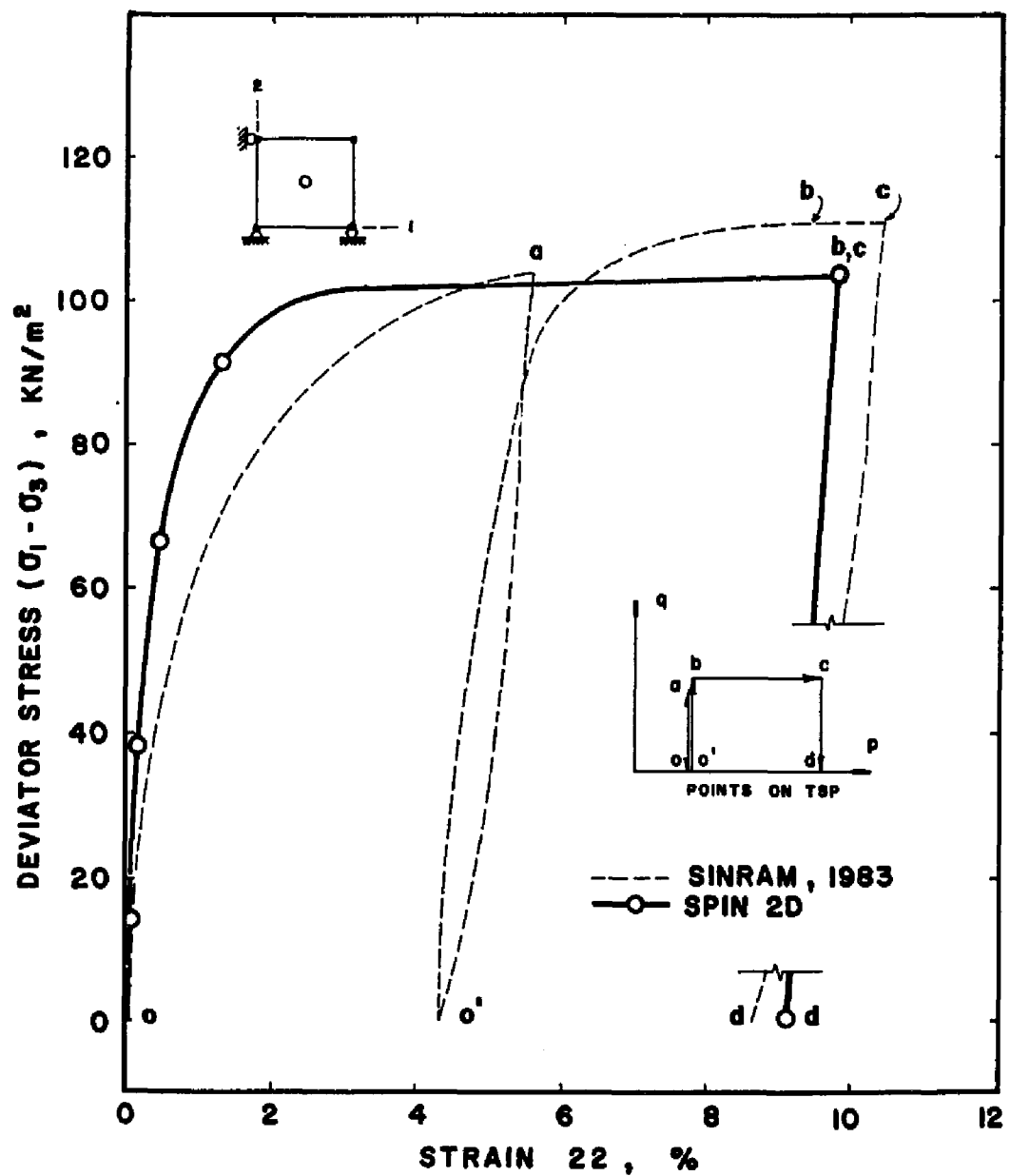


FIG. 5.8. STRESS-STRAIN DIAGRAM FOR A PLANE STRAIN TEST ON UNDISTURBED BAY MUD.

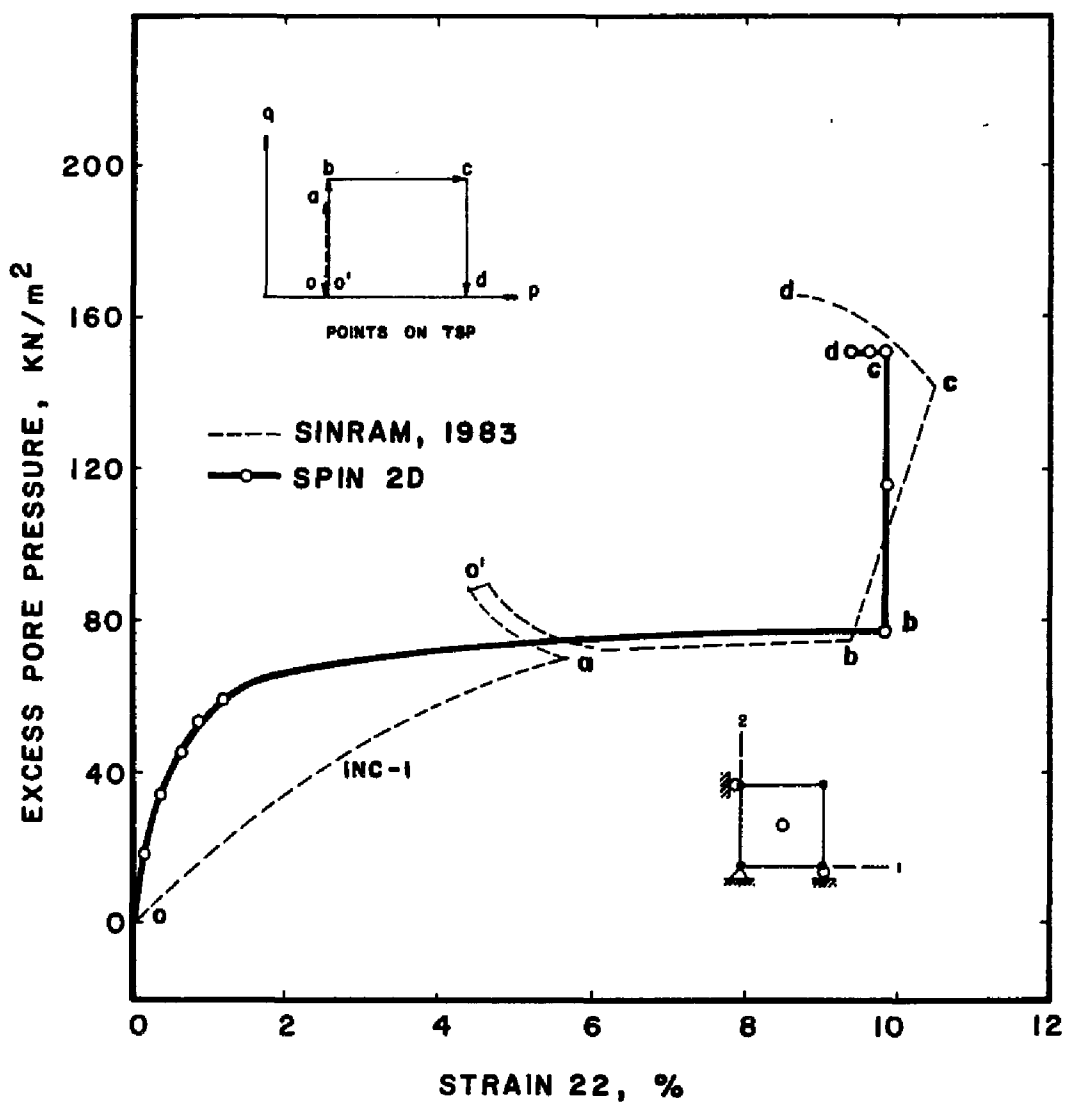


FIG. 5.9. PORE PRESSURE-STRAIN DIAGRAM FOR A PLANE STRAIN UNDRAINED TEST ON UNDISTURBED BAY MUD.

failure (asymptotic part *AB* in Fig. 5.9), and the additional excess pore pressures that developed during isotropic loading *BC*.

Inclusion of plastic shear distortion beneath the state boundary surface would allow time-independent plastic yielding to take place even at stress states below the volumetric yield surface. This feature can be utilized to improve predictions not only of stress-strain behavior but of pore pressure-strain behavior as well.

5.5 CONSOLIDATION TESTS ON REMOLDED BAY MUD

Isotropic consolidation tests

Three isotropic consolidation tests were performed by Kavazanjian [30] on samples of remolded Bay Mud having the same stress history. The samples were individually consolidated in a 'triaxial' cell by allowing vertical drainage through the top and bottom porous stones, and radial drainage through the filter paper strips aligned symmetrically within the mold.

The consolidation curve is shown dashed in Fig. 5.10, with results for the three samples exhibiting good reproducibility. By Casagrande construction, the time t_{100} required for 100 percent pore pressure dissipation was found to be about 1,000 minutes. Kavazanjian also estimated the permeability k using the Terzaghi theory to be about 3.2×10^{-9} meter/min. It can be seen from both figures that the samples continue to creep beyond t_{100} as a result of secondary compression.

Numerical tests were run using a mesh of twenty five Q8P4 finite elements. The volumetric scaling option was employed. Figure 5.10 compares the numerical results for the cases with and without the effects of creep.

The numerical result for the case when creep is suppressed shows compression ceasing after about $t_{100} = 1,000$ minutes, which is very close to the estimate made for t_{100} using the Casagrande construction. By including secondary compression effects ($\psi = 0.022$), the prediction is improved. It can be observed from Fig. 5.10 that creep constitutes a major fraction of the overall compression for this soil.

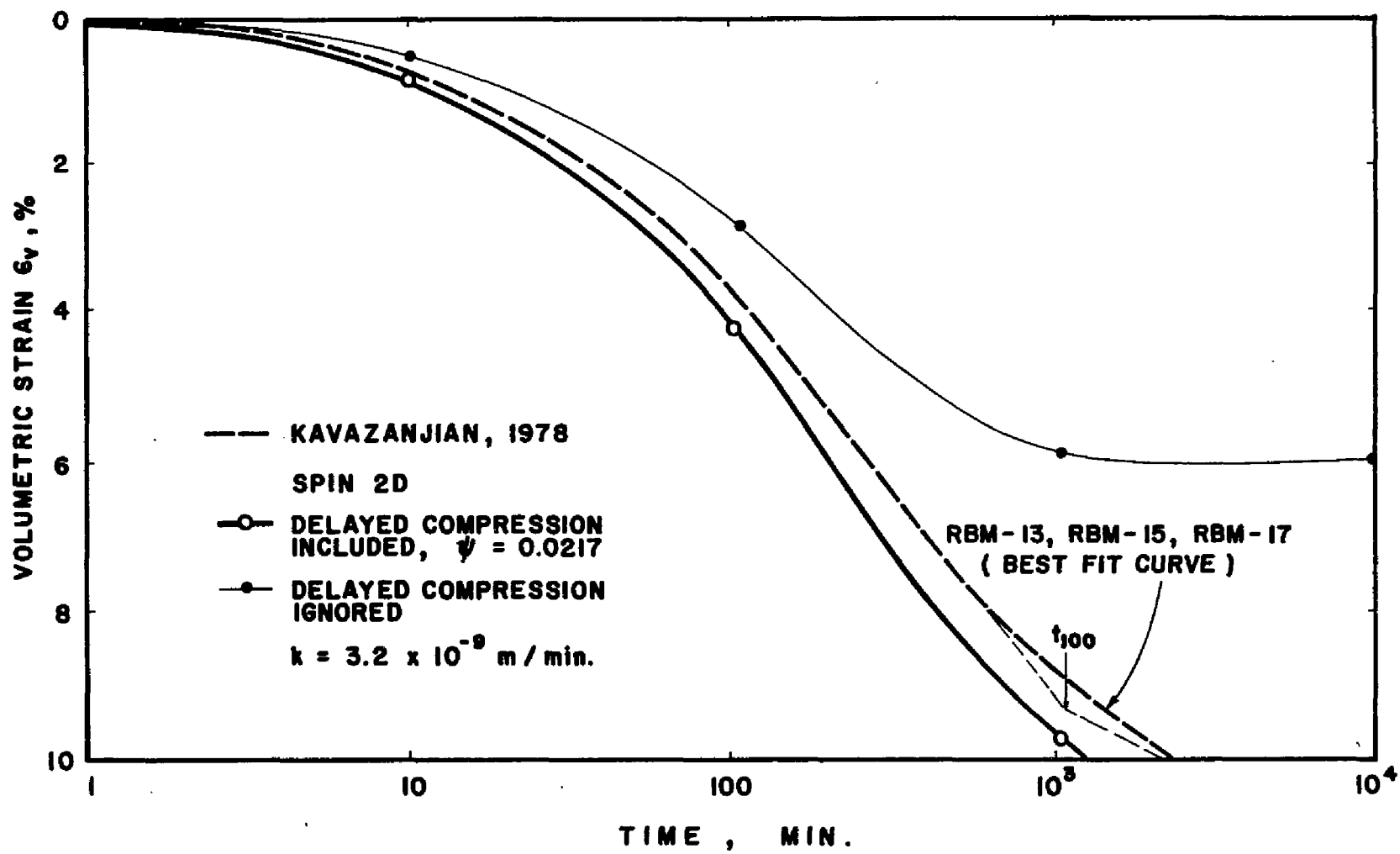


FIG. 5.10. CONSOLIDATION TEST ON REMOLDED BAY MUD SHOWING THE INFLUENCE OF SECONDARY COMPRESSION.

Figure 5.11 illustrates how pore pressures develop and dissipate in a typical 'triaxial' isotropic consolidation test on remolded Bay Mud. As pore pressures initially dissipate in the outer elements located nearest the drainage zones, they also build up in the inner elements as a result of arrested secondary compression. Between times $t = 11$ minutes and $t = 100$ minutes, the inner elements start to "feel" the consolidation process going on as pore pressures in these elements begin to dissipate.

Figure 5.12 shows the volumetric age profile computed from (3.53a, b) at various stages of consolidation. At $t = 0$, the normally consolidated clay elements have volumetric ages all equal to $(t_v)_i = 1.0$ min. During the initial stage of consolidation, the outermost elements experience primary loading as they age in the same order of magnitude as the natural time. During the same initial stage of consolidation, the inner elements experience unloading as pore pressures build up due to undrained secondary compression. Hence, they age faster than do outermost elements during this period.

It should be noted that the volumetric ages in this example were computed from (3.53a, b) in each time step, with no reference made to natural time. Hence, occasional numerical inaccuracies (such as $t_v = 239$ min. at natural $t = 100$ min. for the lower outer element) are not uncommon and do not adversely influence computations during subsequent time steps.

One-dimensional consolidation tests

Experimental curves from one-dimensional consolidation tests do not usually agree with Terzaghi's one-dimensional consolidation equation (4.85) due to the following major reasons: (a) the Terzaghi equation does not account for secondary compression which can be a major fraction of the overall compression particularly when C_a is large, (b) the Terzaghi equation does not consider the elasto-plastic stress-strain behavior of soils under compression, and (c) the Terzaghi theory assumes that all the clay elements follow the same linear-elastic effective stress-strain curve regardless of their distances from the drainage boundary [3].

Sec. 5.5 Consolidation tests on RBM

1.00	1.00	1.00	1.00	1.00
1.00	1.00	1.00	1.00	1.00
1.00	1.00	1.00	1.00	1.00
1.00	1.00	1.00	1.00	1.00
1.00	1.00	1.00	1.00	1.00

TIME = 0 MIN.

0.64	0.64	0.65	0.64	0.31
1.23	1.23	1.24	1.20	0.57
1.20	1.20	1.21	1.15	0.54
1.21	1.21	1.21	1.16	0.55
1.20	1.20	1.21	1.16	0.55

TIME = 1 MIN.

0.66	0.66	0.67	0.56	0.24
1.47	1.45	1.39	1.12	0.46
1.64	1.61	1.42	1.11	0.44
1.62	1.49	1.39	1.09	0.43
1.62	1.49	1.39	1.09	0.43

TIME = 11 MIN.

0.48	0.46	0.42	0.35	0.15
1.15	1.09	0.98	0.75	0.30
1.37	1.30	1.14	0.83	0.32
1.42	1.35	1.16	0.86	0.34
1.43	1.35	1.19	0.89	0.36

TIME = 100 MIN.

FIG. 5.11. PORE PRESSURE DISTRIBUTION DURING ISOTROPIC CONSOLIDATION; NUMBERS REPRESENT THE RATIO u/u_0 .

Sec. 5.5 Consolidation tests on RBM

1	1	1	1	1
1	1	1	1	1
1	1	1	1	1
1	1	1	1	1
1	1	1	1	1

TIME = 0 MIN.

7	7	7	6	3
14	14	16	12	5
12	12	12	8	4
12	12	13	9	4
12	12	13	9	4

TIME = 1 MIN.

34	30	21	13	7
58	45	24	9	9
113	87	42	12	11
78	63	35	11	11
77	64	36	11	11

TIME = 11 MIN.

111	95	107	170	38
160	67	66	73	85
132	101	61	46	68
166	91	52	49	184
218	100	57	58	239

TIME = 100 MIN.

FIG. 5.12. VOLUMETRIC AGE PROFILE DURING ISOTROPIC CONSOLIDATION.

To illustrate the effect of secondary compression in a one-dimensional situation, three numerical one-dimensional consolidation experiments were performed using the material parameters for RBM, with specimen heights (i.e., distance between drainage ends) of $2H_1 = 0.089$ meter, $2H_2 = 0.890$ meter, and $2H_3 = 8.900$ meters. The mesh consists of six Q9P4 finite elements and the volumetric scaling option was employed. Assuming a permeability $k_2 = 1.0 \times 10^{-8}$ meter/min., the average consolidation curves are plotted in Fig. 5.13.

Like the isotropic consolidation tests on RBM, the higher specimens exhibit negative initial average consolidation values due to undrained secondary compression in the innermost elements in the early phase of consolidation. This is further illustrated by the isochrones for the specimen with height $2H_2 = 0.890$ meter in Fig. 5.14 (compare the isochrones of Fig. 4.18 obtained from Terzaghi's equation), which shows that excess pore pressures build up faster in the inner elements than they dissipate in the outermost elements in the initial phase of consolidation. Except for the undrained secondary compression in the inner elements, however, the overall features of the consolidation curves of Fig. 5.13 do not deviate significantly from the Terzaghi equation corresponding to the respective specimen heights despite the inclusion of secondary compression. This can be verified by observing in Fig. 5.13 that pore pressure dissipation is about one hundred times slower for specimens ten times thicker. This observation is consistent with the theory of Terzaghi which predicts that the degree of consolidation is proportional to the square of the specimen height.

Figure 5.15 shows the volumetric strain versus log time consolidation plots. These plots are similar to the pore pressure-based consolidation curves of Fig. 5.13 except that further compression persists due to C_a -effects beyond the primary compression region. The time t_{100} for complete pore pressure dissipation is denoted by the downward arrow for each case. For comparison, the empirical value of t_{100} obtained from the Casagrande construction is denoted by the upward arrow for the case $2H_1 = 0.089$ meter in Fig. 5.15.

The compression curves in Fig. 5.15 show little influence of the specimen height,

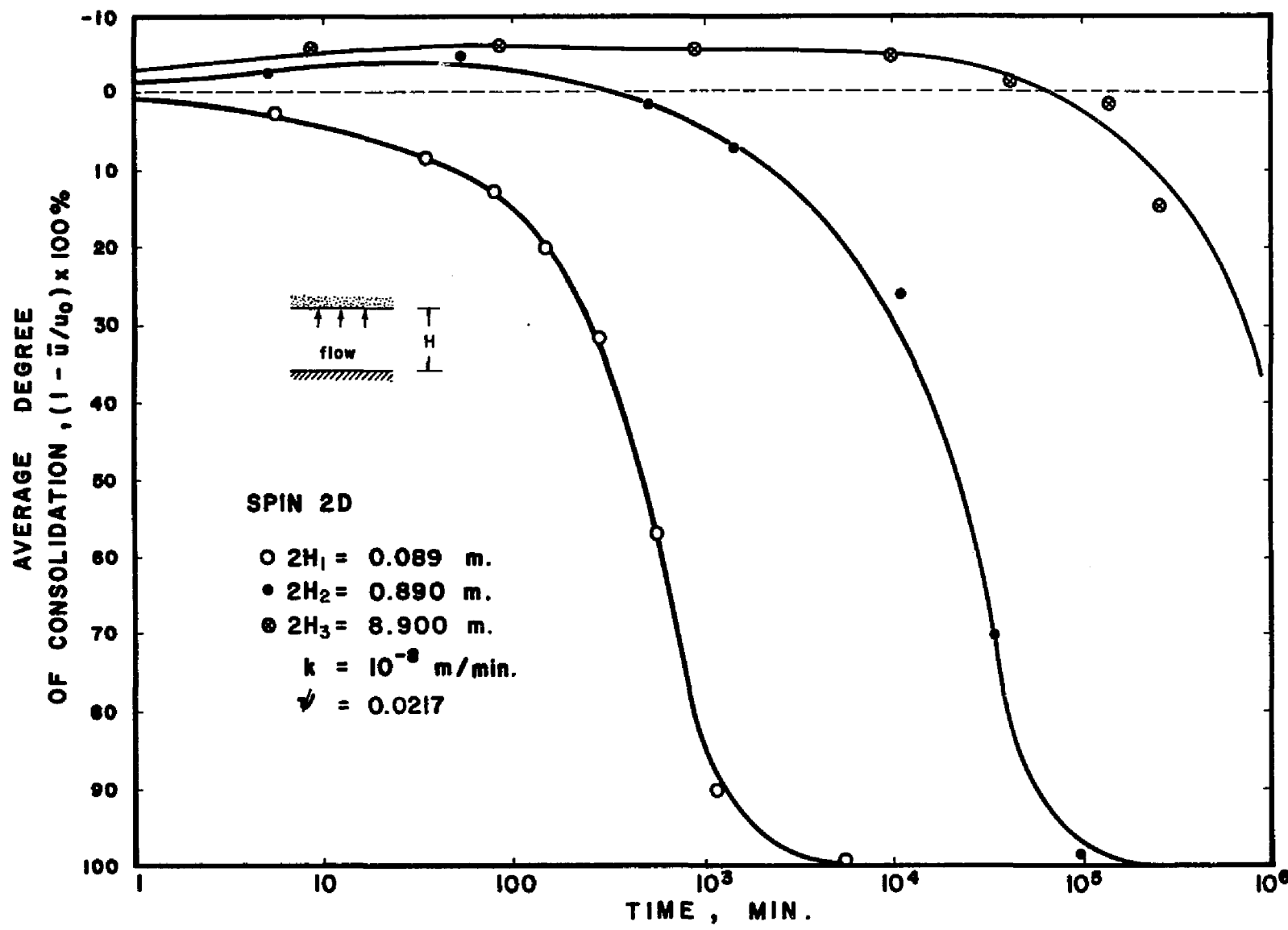


FIG. 5.13. ONE-DIMENSIONAL CONSOLIDATION CURVES WITH CREEP.

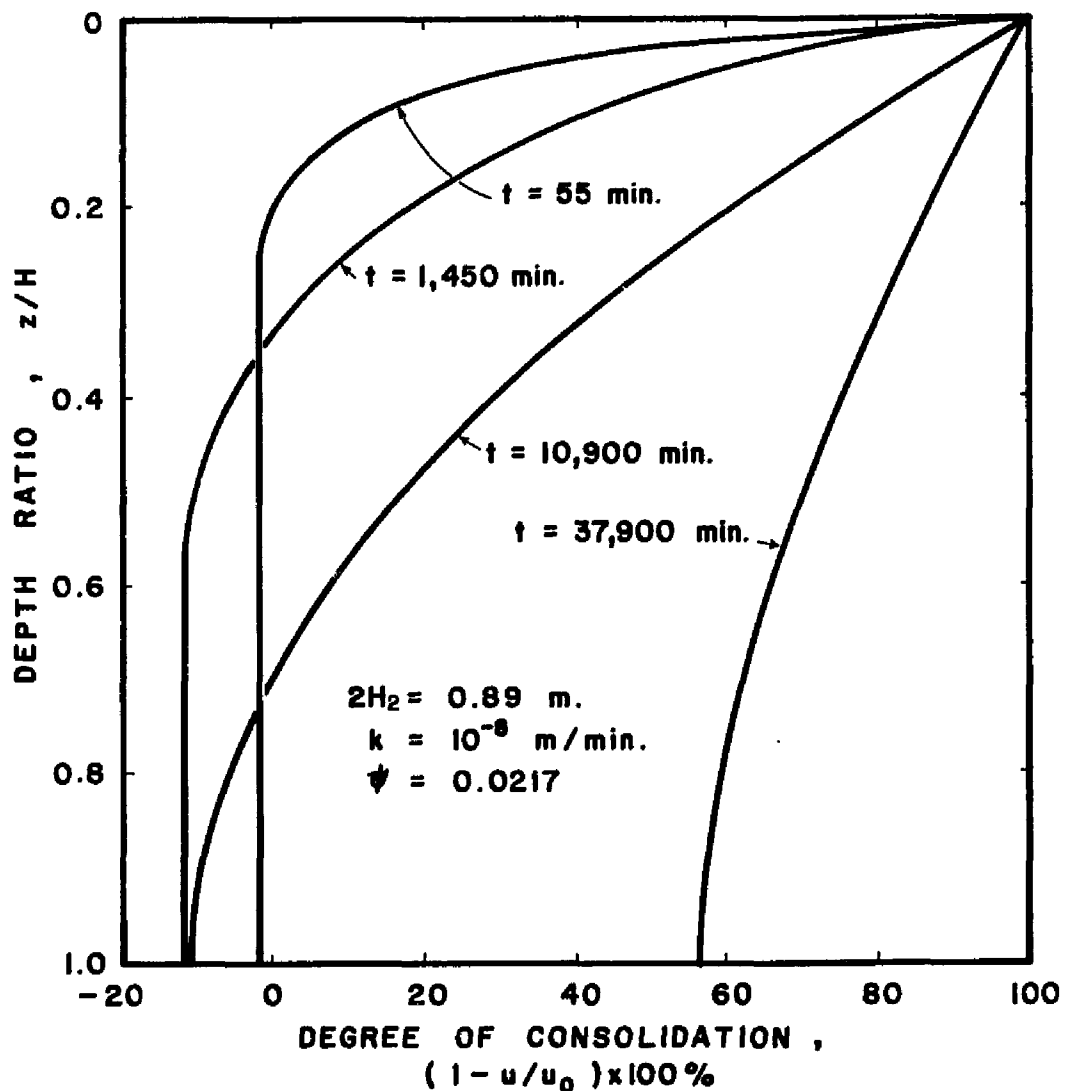


FIG. 5.14. ISOCHRONES FOR ONE-DIMENSIONAL CONSOLIDATION WITH CREEP.

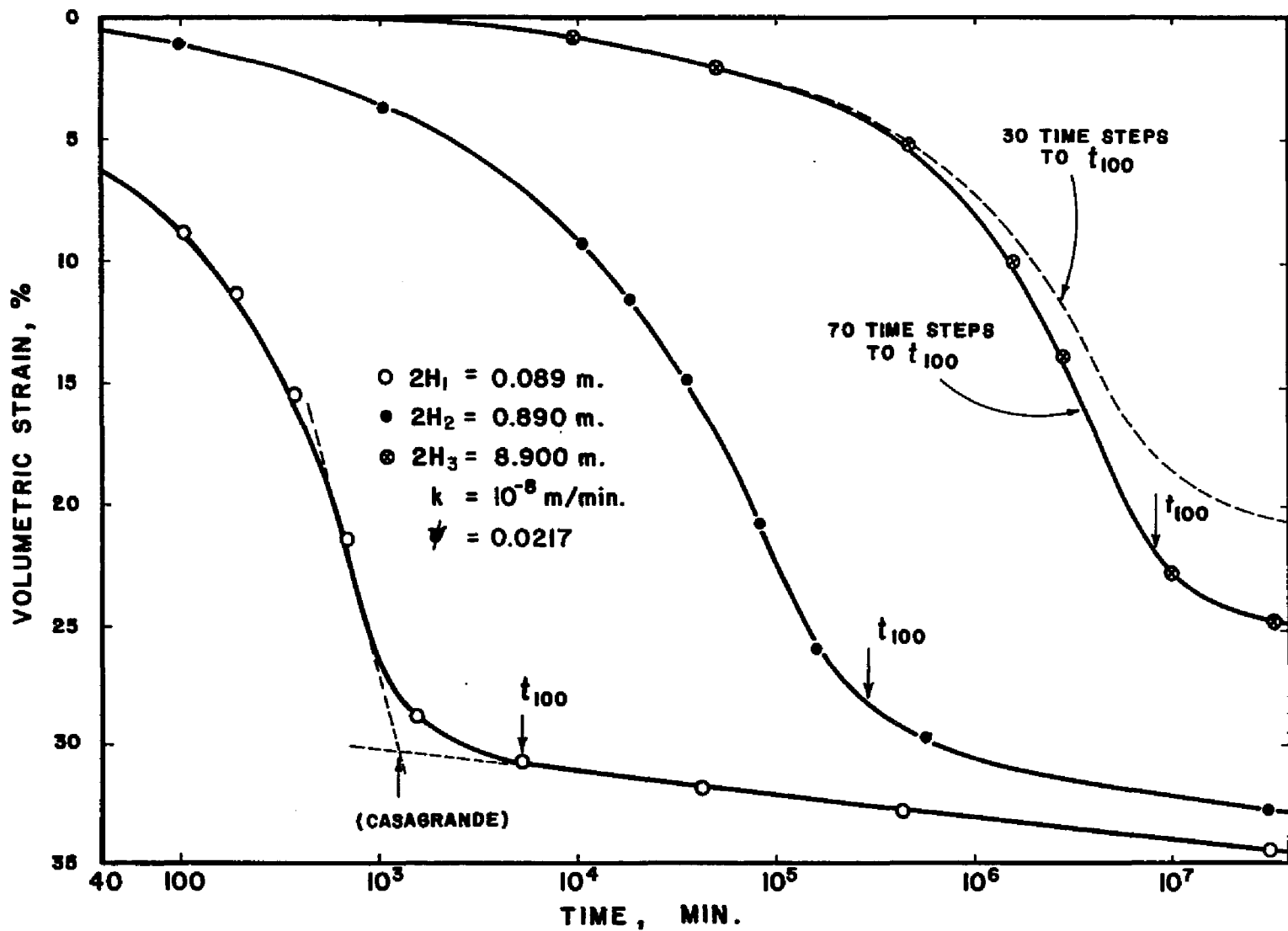


FIG. 5.15. COMPRESSION VERSUS LOG-TIME FOR SPECIMENS OF DIFFERENT HEIGHTS.

the volumetric strains after primary consolidation being virtually unaffected at values of about 25 to 30 percent. The apparent "stiffening" of the specimen noted for the case $2H_3 = 8.900$ meters is attributed to the accumulated numerical errors. The solution can be improved by using more time increments particularly in the time interval { 10^{-5} min. < t < 10^{-7} min.} where pore pressure dissipation (or primary loading) is large.

5.6 DEPENDENCE OF C_α ON \bar{D}

It was pointed out in Sec. 3.3 that the volumetric and the deviatoric scaling procedures which are used to define the creep strain tensor $\dot{\epsilon}_{kl}^t$ would not give identical results unless the secondary compression index ψ varies with \bar{D} in some specific way.

Suppose ψ is allowed to vary with \bar{D} . Uniqueness in $\dot{\epsilon}_{kl}^t$ is obtained by equating (3.49) with (3.58) as follows:

$$\frac{\psi}{(1 + e_{vr}) t_v} \left(\frac{\partial F}{\partial \sigma_{ii}} \right)^{-1} = \sqrt{\frac{3}{2}} A e^{\alpha \bar{D}} \left[\frac{(t_d)_i}{t_d} \right]^m \left[\frac{\partial F}{\partial \sigma_{kl}} \frac{\partial F}{\partial \sigma_{kl}} - \frac{1}{3} \left(\frac{\partial F}{\partial p} \right)^2 \right]^{-1/2}, \quad (5.3)$$

with appropriate distinction made between void ratio e_{vr} and the natural number e .

Assuming that the soil is normally consolidated, then $t_v = (t_v)_i$ and $t_d = (t_d)_i$. Noting that $\partial F / \partial \sigma_{ii} = \partial F / \partial p$ and solving for ψ ,

$$\psi = \sqrt{\frac{3}{2}} (1 + e_{vr}) A t_v e^{\alpha \bar{D}} \left(\frac{\partial F}{\partial p} \right) \left[\frac{\partial F}{\partial \sigma_{kl}} \frac{\partial F}{\partial \sigma_{kl}} - \frac{1}{3} \left(\frac{\partial F}{\partial p} \right)^2 \right]^{-1/2}. \quad (5.4)$$

Using chain rule on $\partial F / \partial \sigma_{kl}$ (consult (3.36)),

$$\frac{\partial F}{\partial \sigma_{kl}} \frac{\partial F}{\partial \sigma_{kl}} = \frac{\partial q}{\partial \sigma_{kl}} \frac{\partial q}{\partial \sigma_{kl}} \left(\frac{\partial F}{\partial q} \right)^2 + \frac{1}{3} \left(\frac{\partial F}{\partial p} \right)^2 \quad (5.5a)$$

$$= \frac{3}{2} \left(\frac{\partial F}{\partial q} \right)^2 + \frac{1}{3} \left(\frac{\partial F}{\partial p} \right)^2, \quad (5.5b)$$

where (5.5b) is obtained by expanding $\partial q/\partial\sigma_{kl}$ about the principal stress axes.

Substituting (5.5b) in (5.4) and using the derivatives (3.31) and (3.32),

$$\psi = A t_v M e^{\alpha \bar{D}} (1 + e_{vr}) \frac{\sqrt{1 - \bar{D}^2}}{\bar{D}}, \quad \bar{D} \neq 0. \quad (5.6)$$

Equation (5.6) is plotted in Fig. 5.16 assuming $t_v = 1$ minute and using the soil properties for undisturbed Bay Mud. Singularity considerations suggest that this relationship does not hold when $\bar{D} \rightarrow 0$ because the Singh-Mitchell creep equation overpredicts $\dot{\epsilon}_{kl}^t$ in near isotropic conditions. Furthermore, (5.6) does not hold when $\bar{D} = 1$ because the Singh-Mitchell equation seriously underpredicts $\dot{\epsilon}_{kl}^t$ in near-failure conditions (consult Fig. 2.10).

Equation (5.6) yields ψ as an almost linearly increasing function of \bar{D} for $0.24 \leq \bar{D} \leq 0.83$, which is a typical range of the validity of the Singh-Mitchell equation. Comparison of the values of ψ obtained from (5.6) with the measured value of 6.5×10^{-3} for UBM shows that the latter is larger. The difference could be due to volumetric aging which drives t_v exponentially with void ratio change due to creep, i.e., the measured value of ψ corresponds to a condition where $t_v > 1$ min. It could also be that the associative flow rule assumption for plastic creep strain rates does not hold for this material and thus the model underpredicts the parameter ψ .

Figure 5.17 shows the plot of the Singh-Mitchell equation on the $\log \dot{\epsilon}_a$ - \bar{D} plane. Superimposed on the same figure is a contour of constant ψ obtained from (3.50) for the case $t_v = 1.0$ minute. It can be concluded from the figure that: (1) if the contour lines representing constant secondary compression index ψ are parallel to the Singh-Mitchell line, no explicit relationship such as (5.6) need be established between ψ and \bar{D} to insure uniqueness of $\dot{\epsilon}_{kl}^t$; i.e., the volumetric and the deviatoric scaling procedures would yield the same result, (2) the value ψ on the contour line collinear with the Singh-Mitchell line in Fig. 5.17 is the secondary compression index necessary to establish uniqueness in $\dot{\epsilon}_{kl}^t$.

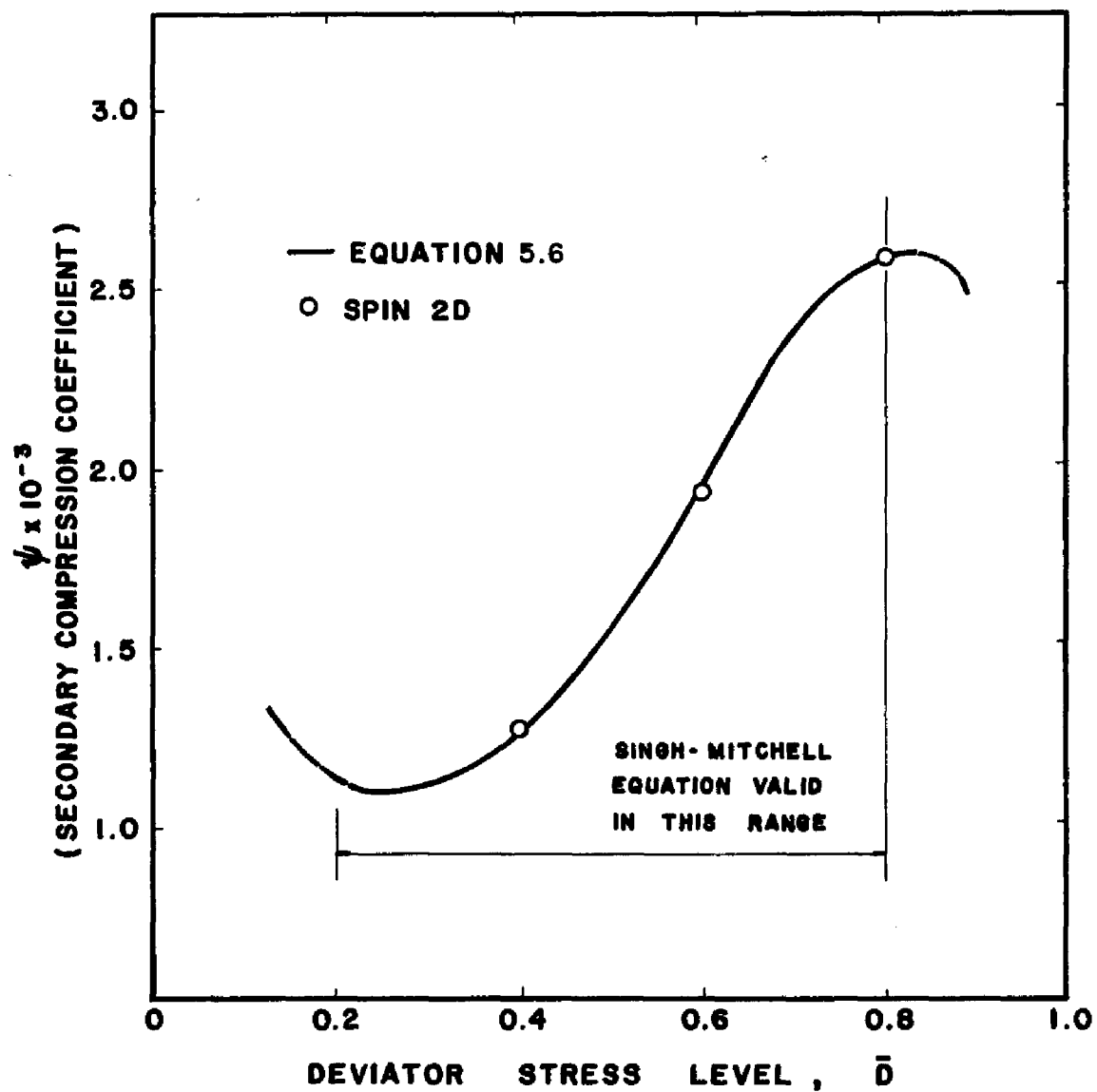


FIG. 5.16. RELATIONSHIP BETWEEN SECONDARY COMPRESSION COEFFICIENT AND DEVIATOR STRESS LEVEL.

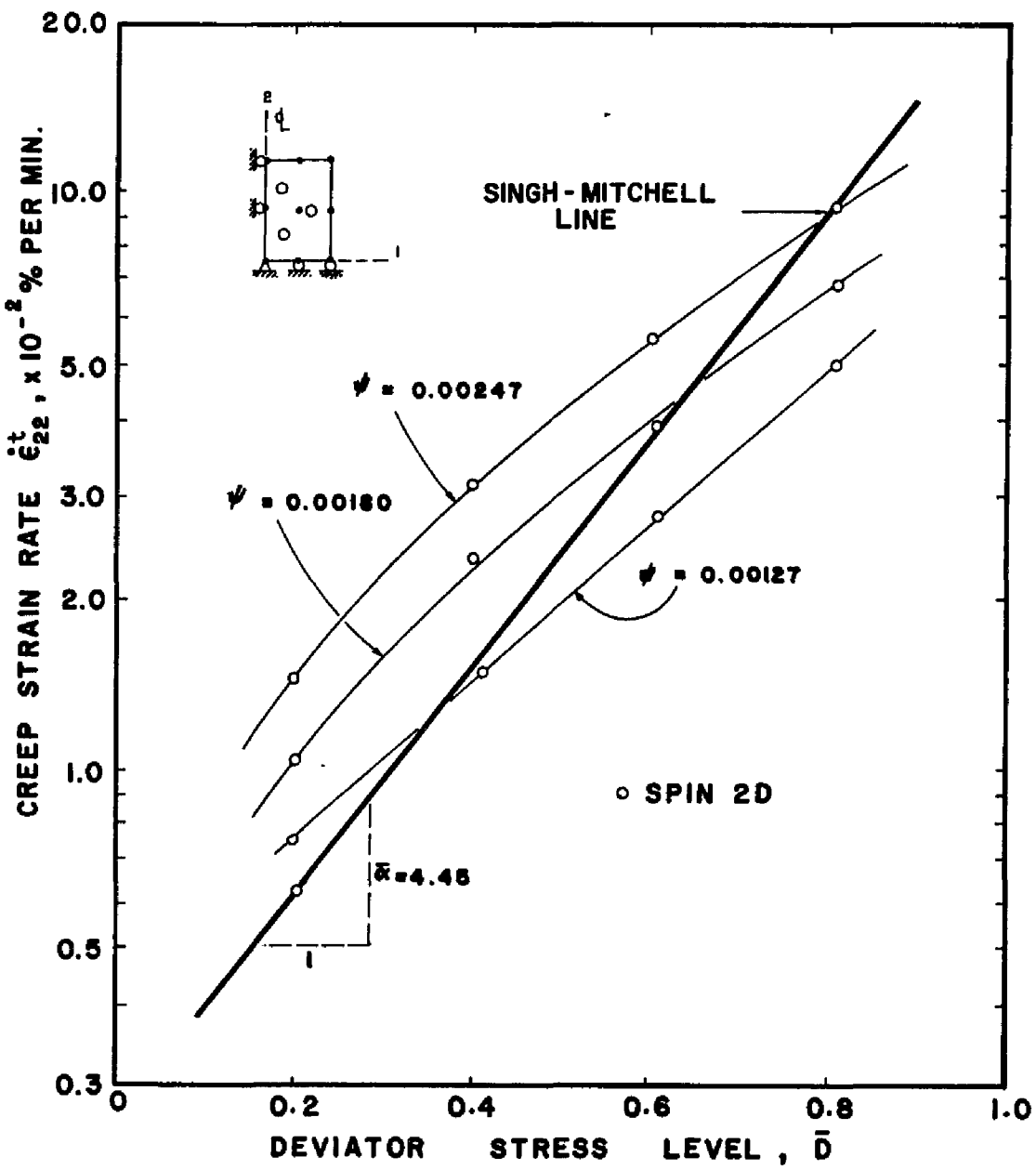


FIG. 5.17. CONTOUR OF CONSTANT ψ ON LOG $\dot{\epsilon}_{22}^t - \bar{D}$ PLANE.

5.7 ON THE LATERAL PRESSURE COEFFICIENT K_o

Determination of the geostatic lateral earth pressure coefficient K_o is important in the design and analysis of earth structures. Although this quantity is usually assumed to be a soil constant, test data are available to show that K_o tends to increase with time.

The major problem that prohibits intensive investigation on the variation of K_o with time is the long duration of testing which requires a period comparable to the geological age of the soil deposit. Consequently, test data for this type of test are scarce and are usually obtained at strain rates that are several orders of magnitude higher than field strain rates [34].

Values of K_o obtained from time-independent analyses

A K_o drained test on UBM was performed by Hsieh [23] in a standard 'triaxial' cell by axially compressing an isotropically consolidated cylindrical soil sample at a strain rate of $\dot{\epsilon}_a = 0.2\%$ per minute while monitoring the volume change. The zero-lateral strain condition is achieved by adjusting the cell pressure during axial compression while maintaining the condition

$$\Delta\epsilon_v = \Delta\epsilon_a \quad (5.7)$$

or,

$$\epsilon_v - \epsilon_a = \text{constant} \quad (5.8)$$

at any time during the test. The test result shown in Fig. 5.18 shows that K_o , evaluated as the ratio between the radial pressure and the axial load, converges to a value of about 0.54.

A numerical test was performed using one Q9P0 laterally constrained element. The above laboratory test was simulated by prescribing axial displacement and computing K_o as

$$K_o = \frac{\sigma_h}{\sigma_v}, \quad (5.9)$$

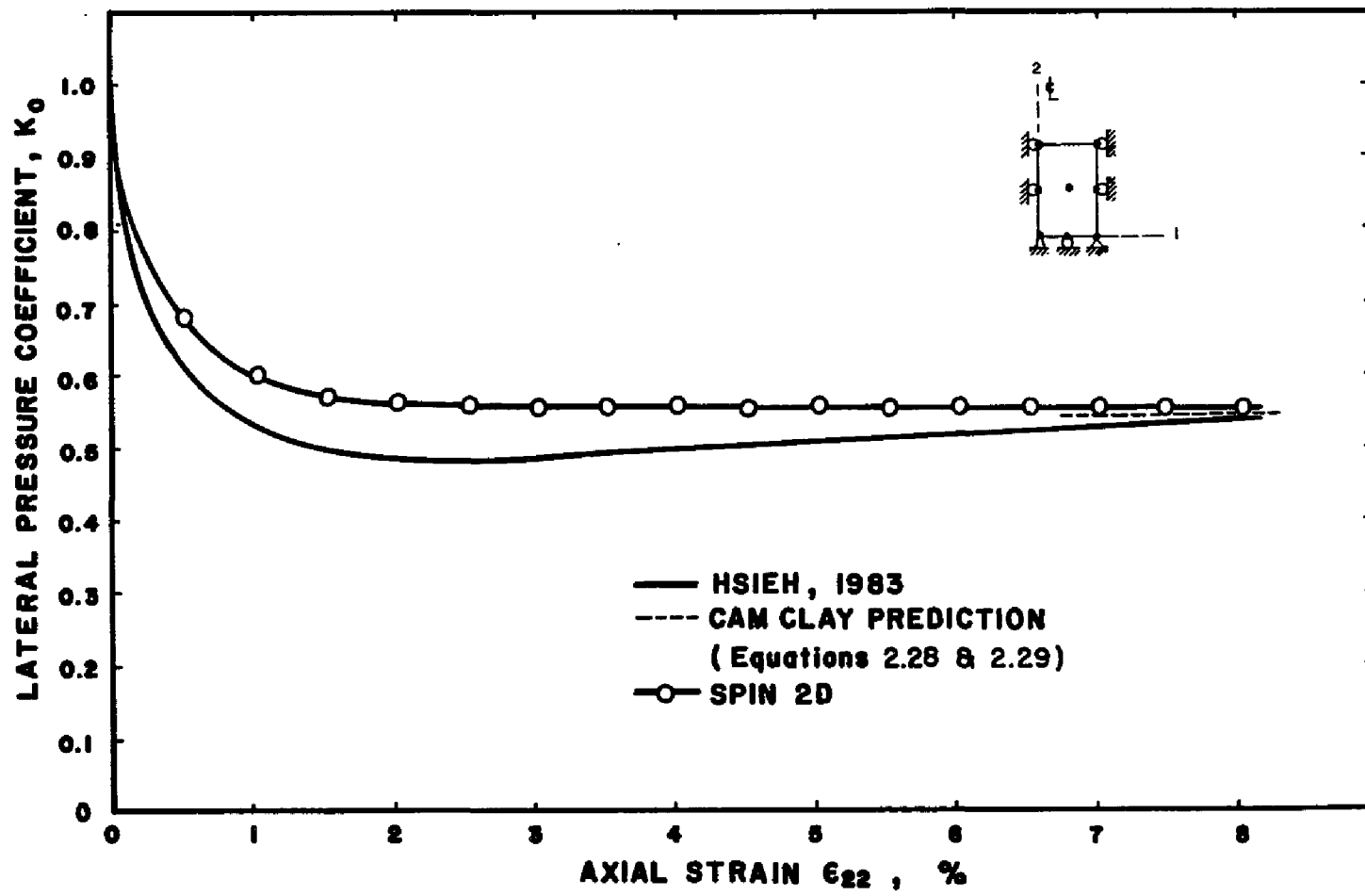


FIG. 5.18. DRAINED K_0 -TEST ON UNDISTURBED BAY MUD.

where σ_h and σ_v are the horizontal and vertical effective stresses, respectively, evaluated at the centroid of the quadrilateral element. The result of this numerical test without creep is also plotted in Fig. 5.18 and shows that K_o converges to a value of about 0.56. The inclusion of creep does not significantly affect the value of K_o during this relatively short period of time.

Using soil properties for UBM ($\kappa/\lambda = 0.146$), the Cam clay equations (2.28) and (2.29) yield $\eta_o = 0.62$ and $K_o = 0.56$. From Pender's equation (2.32), which was derived using a yield locus for a K_o -consolidated sample, $K_o = 0.56$.

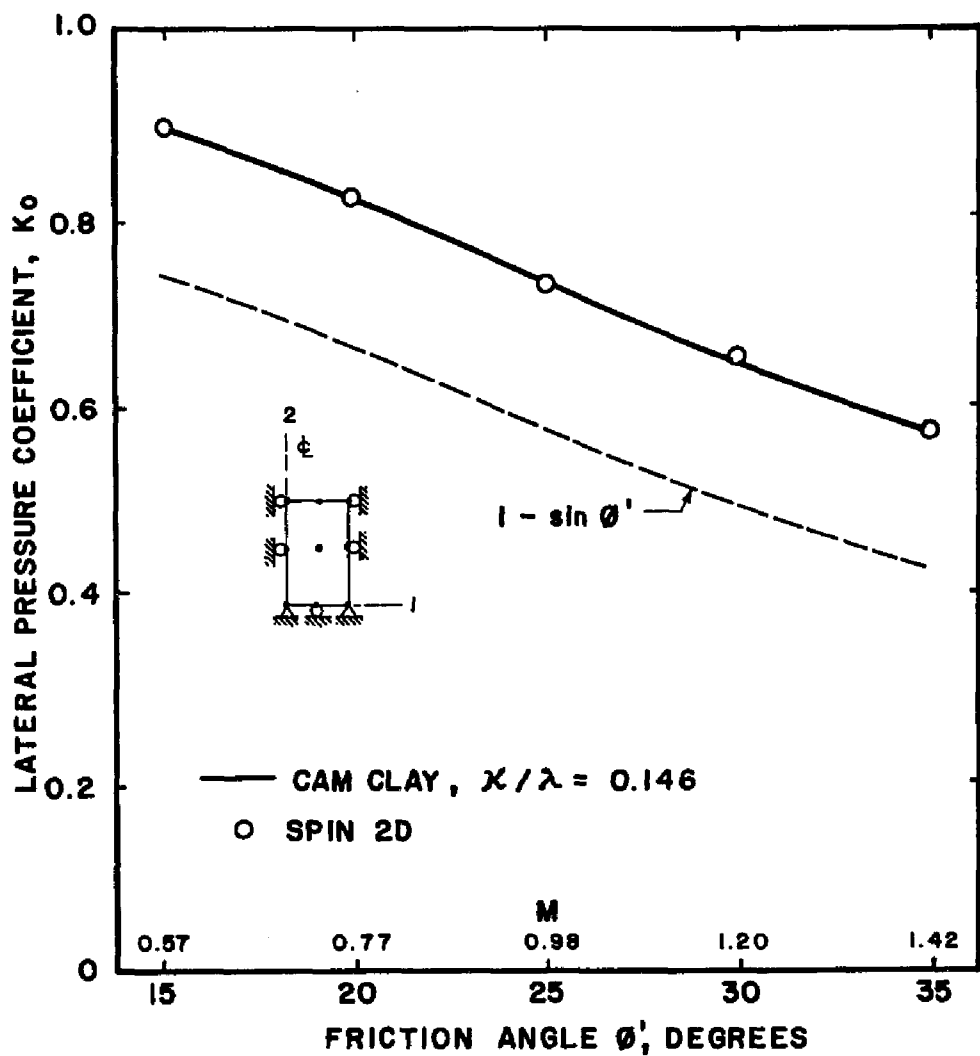
The ability of the above numerical schemes to accurately predict K_o is further verified in Fig. 5.19 which shows the variation of K_o with effective friction angle ϕ' (or M). Again, using (2.28) and (2.29) from the Cam clay theory, a contour on the K_o - ϕ' plane can be drawn for different values of κ/λ . One such plot is shown in Fig. 5.19 for UBM, and confirmed by results obtained from the finite element program. By comparison, the plot of the familiar formula $K_o = 1 - \sin \phi'$ lies significantly below the line previously obtained.

Values of K_o obtained from creep-inclusive analyses

Creep-inclusive numerical analyses were performed using a mesh of six laterally constrained Q8P4 finite elements to investigate the behavior of K_o during an extended period of seven log cycles of time. The deviatoric scaling option for creep strain rate was employed.

The elements were preconsolidated to an isotropic stress of 10 KN/m^2 and allowed to consolidate under an initial excess pore pressure of 100 KN/m^2 . To show the influence of permeability k , three permeability values were considered: $k_1 = 3.2 \times 10^{-9} \text{ meter/minute}$, $k_2 = 1.0 \times 10^{-8} \text{ meter/minute}$, and $k_3 \rightarrow \infty$ for the totally drained case. Beyond the primary consolidation region, the finite elements continue to creep under the resulting sustained load. The numerical results are plotted in Figs. 5.20 and 5.21.

Figure 5.20 shows the behavior of K_o with time for the upper, middle, and lower finite elements as they consolidate and creep for the case where $k = 3.2 \times 10^{-9}$

FIG. 5.19. DEPENDENCE OF K_o ON EFFECTIVE FRICTION ANGLE.

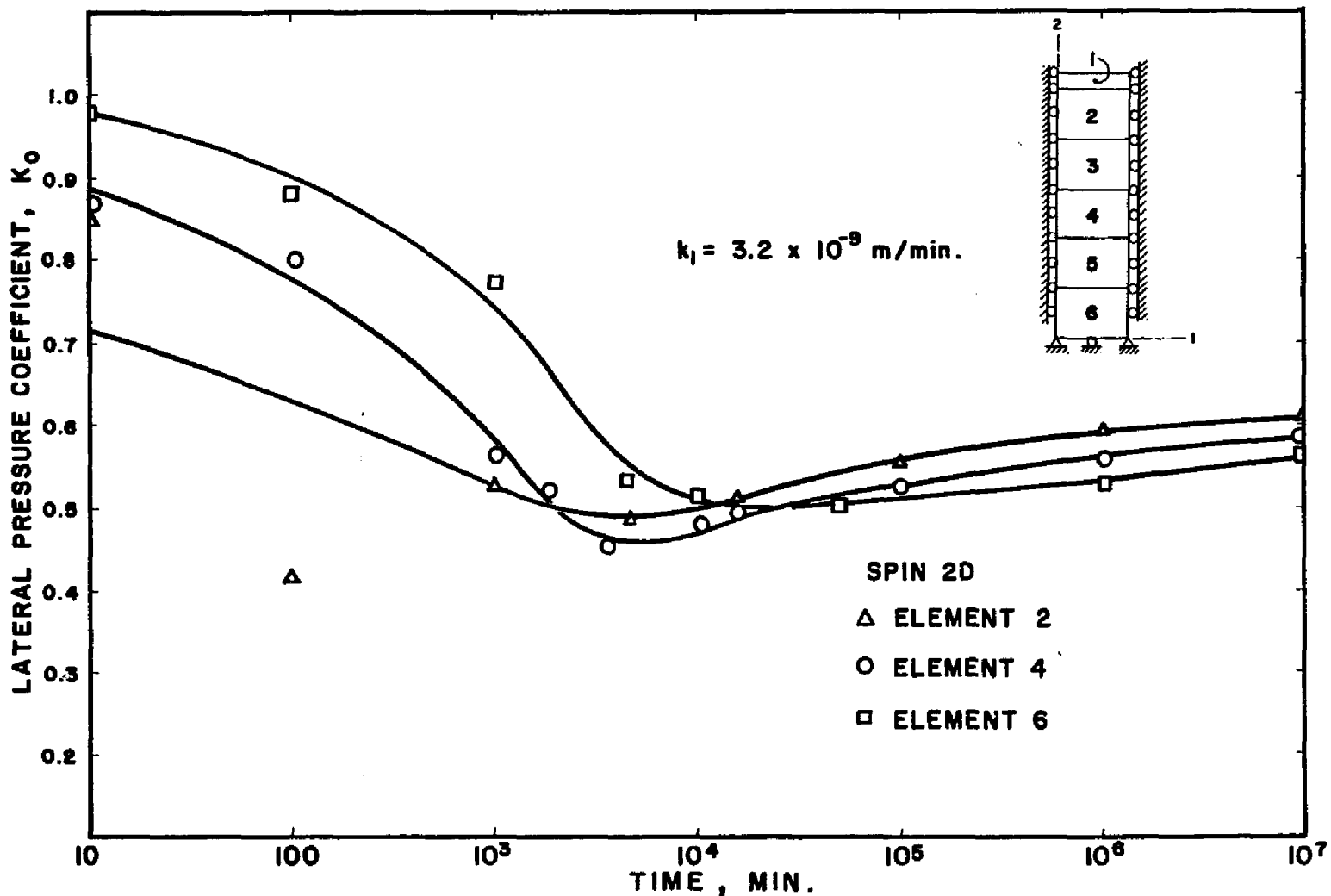


FIG. 5.20. VARIATION OF K_0 WITH TIME; FINITE ELEMENTS INITIALLY PRECONSOLIDATED TO AN ISOTROPIC STRESS.

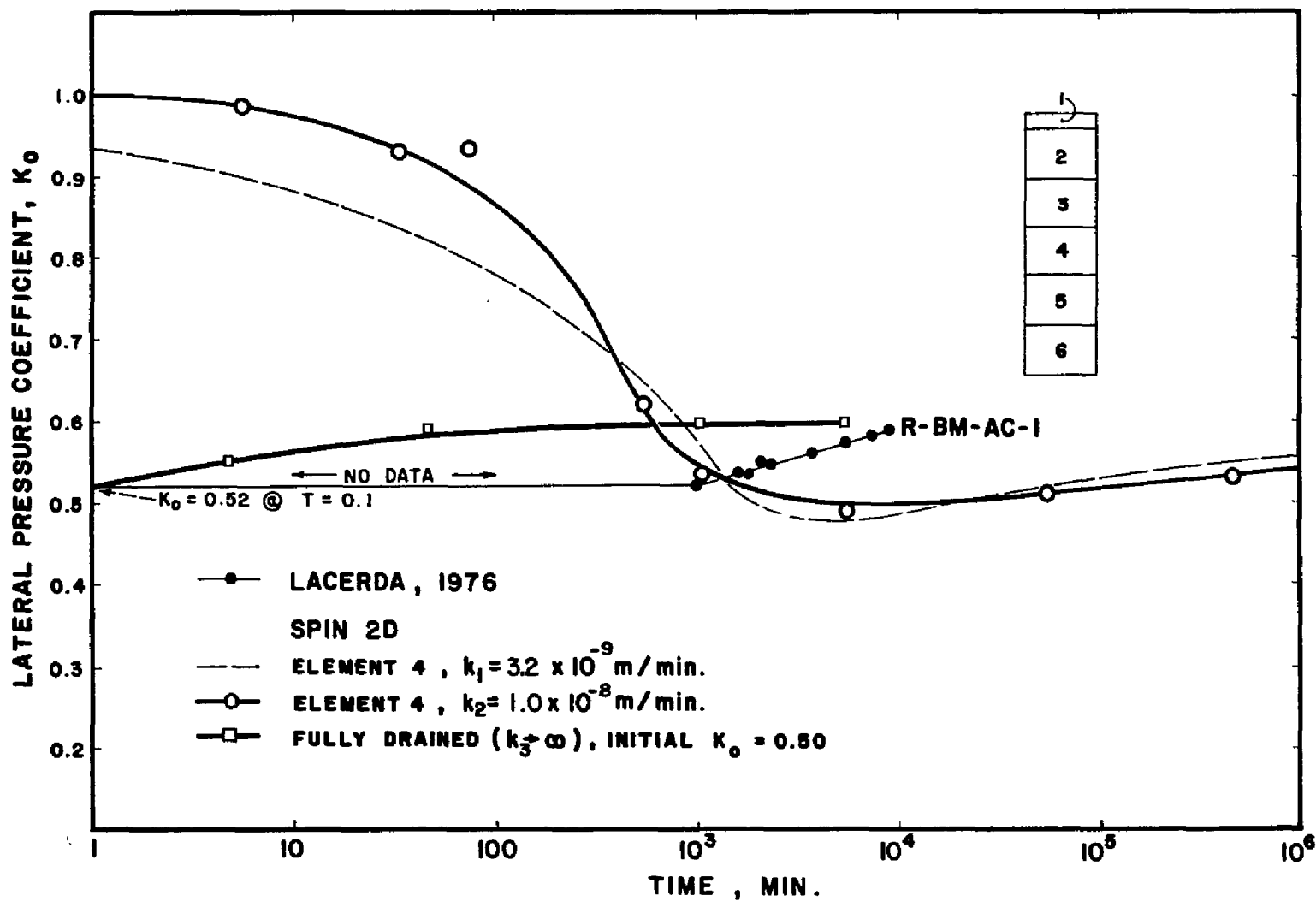


FIG. 5.21. PLOT OF K_o VERSUS TIME SHOWING INFLUENCE OF PERMEABILITY.

meter/minute. The uppermost element 1 is a thin layer of soil used to provide continuity in excess pore pressure from the uniform initial value (at the pressure nodes just below the uppermost nodes) to zero on the drainage boundary. It can be seen that after the elements consolidate, K_o monotonically increases with time.

Figure 5.21 shows that the influence of increased permeability is to hasten consolidation and achieve a higher value of K_o at an earlier time. This can be observed by comparing the K_o -log t curves for the extreme cases where $k = k_1$ and $k = k_3$.

Lacerda [34] performed two K_o 'triaxial' tests on UBM to determine the time-dependent behavior of K_o . Specimen R-BM-AC-1 was tested for 10,000 minutes, with results plotted in Fig. 5.21.

Lacerda observed that K_o tends to vary linearly with the logarithm of time between $t = 1,000$ minutes to $t = 10,000$ minutes beyond the primary compression period. However, the data during the early period of consolidation are unavailable except at $t = 0.1$ minute where $K_o = 0.52$. This point, however, does not lie along the previous line. The time period during which K_o was measured is too short to justify generalization of a linear relationship of K_o with the logarithm of time; however, it can be stated based on these results that K_o cannot be considered as an absolute constant.

Remark

The validity of the constitutive model was investigated through numerical experiments on San Francisco Bay Mud which include drained, undrained, and consolidation tests, creep and stress relaxation tests, and combined stress relaxation and creep tests in 'triaxial' and plane strain conditions.

It was shown that the usefulness of the numerical method goes even beyond performing the above tests; it also provides numerical solutions to problems like dependence of secondary compression coefficient ψ on deviator stress level \bar{D} , evaluation of lateral pressure coefficient K_o from time-independent analyses, and variation of K_o with time.

PART B.**LONG-TERM FIELD BEHAVIOR
OF THE I-95 TEST EMBANKMENT****5.8 BACKGROUND**

In 1967, construction of a highway embankment for a proposed extension of the I-95 interstate highway began across a marsh underlain by a deep deposit of soft clay north of the city of Boston. As part of the construction process, a test section was instrumented by the geotechnical group at M.I.T. and centerline settlements and pore pressures within the clay beneath the embankment were monitored.

In 1973, after plans for the highway were abandoned, ten different groups of geotechnical engineers made predictions of the deformation and pore pressure response of the foundation soil due to an additional six feet of fill placed on top of the embankment at a symposium sponsored by M.I.T. [40]. Most of these predictions were made using undrained analyses, with parameters derived from laboratory test data and adjusted to account for the consolidation deformations that occurred between the initial embankment construction in 1967 and the second phase of construction, for the M.I.T. symposium, in 1973.

Using the program SPIN 2D, the I-95 embankment problem was analyzed by considering the combined effects of hydrodynamic lag and creep on the deformation behavior of the clay foundation. Predictions were made of centerline settlements at the ground surface and of centerline pore pressures within the clay layer, where data obtained from field instrumentation are available.

5.9 SOIL PARAMETERS FOR BOSTON BLUE CLAY

The soil parameters used to model Boston Blue Clay (BBC) are shown in Table 5.4. The values of Cam clay parameters λ , κ , and M , as well as the ratio of the initial tangent modulus to undrained shear strength are those used by Wroth to

Table 5.4

MODEL PARAMETERS FOR BOSTON BLUE CLAY		
Parameter	Symbol	Value
Virgin compression index ¹	λ C_e	0.147 0.338
Recompression index ¹	κ C_r	0.060 0.138
Secondary compression coefficient ²	ψ C_α	0.00119 0.00274
Hyperbolic stress-strain parameters	a b R_f	0.0062 2.728 from (3.63) 0.90
Singh-Mitchell creep parameters ³	A $\bar{\alpha}$ m	1.44×10^{-4} /day 2.475 0.642
Permeability components	k_h k_v	0.00113 m/day 0.00054 m/day
Slope of critical state line ¹	M	1.05
Void ratio at $p_c = 1$ KPa	e_a	3.56
Instant volumetric time	$(t_v)_i$	1.00 day
Instant deviatoric time	$(t_d)_i$	1.00 day

¹ From Wroth's predictions [68].

² From Ladd and Preston [35].

³ From creep tests performed by Duncan [18].

make his symposium prediction [68]. The hyperbolic stress-strain parameters a , b , and R_f were backfigured from the available data for the initial tangent modulus to undrained strength ratio for BBC [40], in conjunction with equation (3.63).

The value of the secondary compression coefficient ψ was taken as the average of the six values reported by Ladd and Preston [35] obtained from isotropic consolidation and one-dimensional consolidation tests on BBC. The Singh-Mitchell creep parameters were evaluated from the results of two creep tests performed by Duncan for the symposium [18].

The vertical permeability k_v was backfigured from the coefficient of consolidation from standard one-dimensional compression tests. The horizontal permeability k_h was determined by Poepsel [50] on the basis of the value which gave the best

fit with measured behavior during embankment construction, as determined by a modified Cam clay finite element consolidation program.

5.10 PROBLEM GEOMETRY

The soil profile at the I-95 test site is shown in Fig. 5.22. The values of the initial overconsolidation ratio within the Boston Blue Clay layer was taken from the data package provided the symposium predictors.

The finite element mesh used to model the embankment problem consists of 126 isoparametric 9-node Lagrangian elements and 553 nodes of which 117 nodes contain both displacement and pore pressure degrees of freedom. A sketch of the finite element mesh is shown in Fig. 5.23.

The clay soil undergoing consolidation was modeled as a Cam clay material represented in the mesh by Q9P4 finite elements; the peat at the ground surface beyond the toe of the embankment was modeled as a drained Cam clay material represented by Q9P0 Lagrangian elements. The silty sand and embankment fill beneath the ground surface were modeled as linear elastic fully drained materials whose bulk and shear moduli are the average values used by Duncan in his symposium predictions. They are represented in the mesh by Q9P0 quadrilateral elements.

Embankment construction was simulated by applying vertical loads to the nodes at the ground surface Γ_h obtained from the traction contribution

$$\mathbf{F}_{\text{traction}} = \int_{\Gamma_h} \mathbf{N}^T \mathbf{h} d\Gamma \quad (5.10)$$

which appears in the matrix equation (4.28). The traction load vector \mathbf{h} follows a time-history of loading based upon the information derived from the symposium data package [40].

Centerline settlement at the ground surface and centerline pore pressures at points *B* and *C* within the BBC layer (refer to Fig. 5.22 for the approximate locations of these points) were predicted and compared with the field behavior. Three

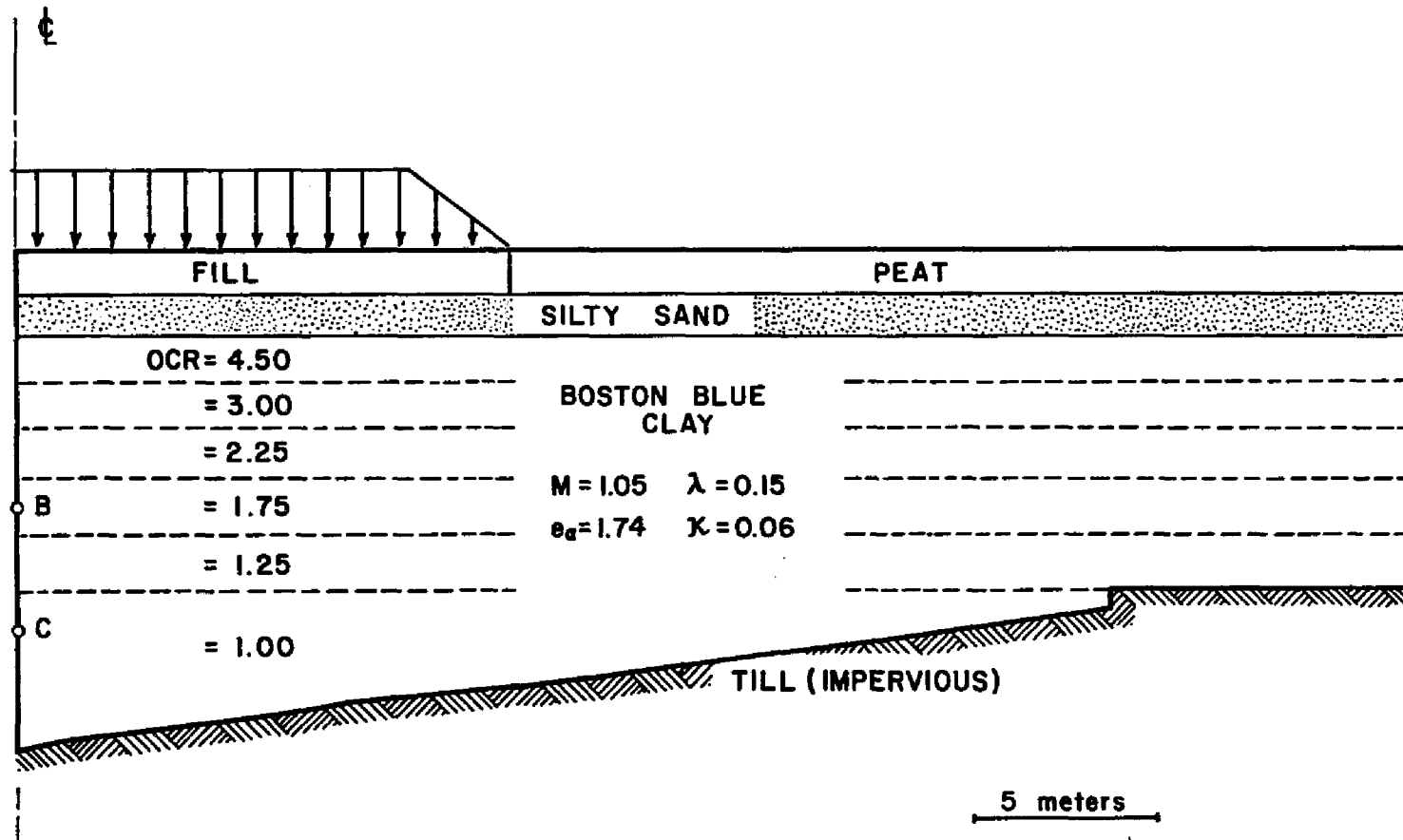


FIG. 5.22. SOIL PROFILE AT THE I-95 EMBANKMENT TEST SITE.

DISPLACEMENT VECTORS:

Deviatoric Scaling

No Creep

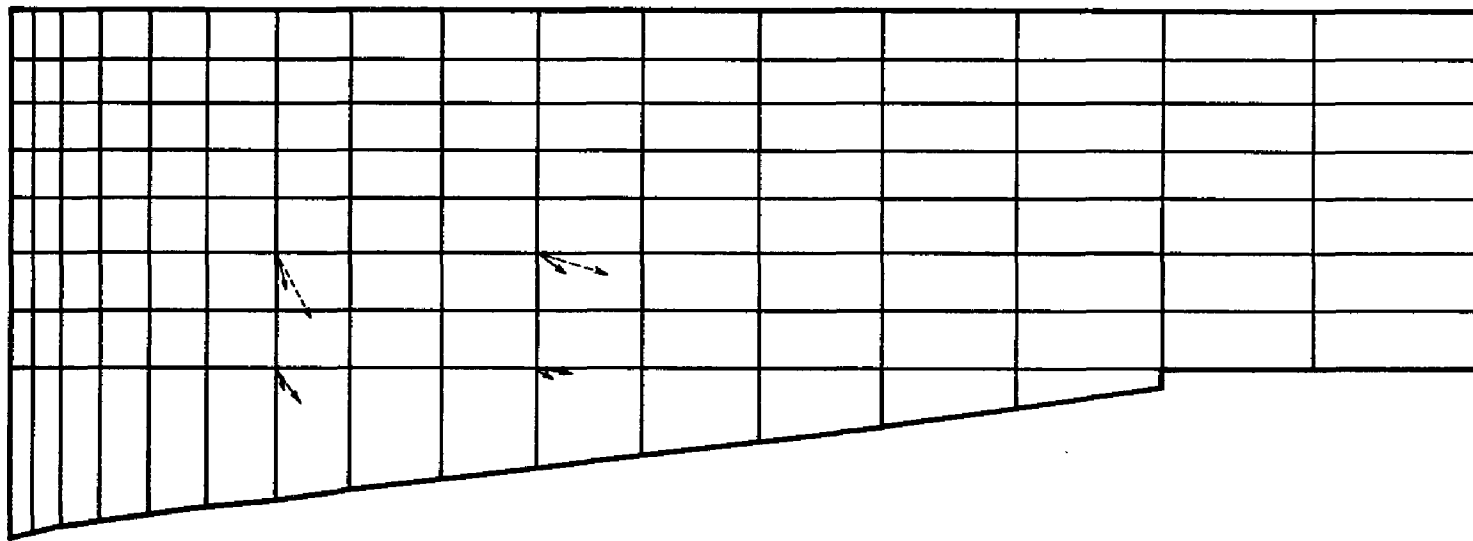


FIG. 5.23. FINITE ELEMENT MESH FOR THE I-95 EMBANKMENT PROBLEM.

sets of predictions were made: one each for volumetric and deviatoric scaling, and one suppressing all creep deformations. Figures 5.24 and 5.25 compare the results of these predictions to the field behavior.

5.11 DISCUSSION OF RESULTS

Figure 5.24 shows that creep constitutes a major fraction of the total centerline settlement for this embankment problem. Without creep effects, the centerline settlement due to pure hydrodynamic lag underpredicted the measured settlements by a steadily increasing margin, resulting in an error of more than 40 percent in a period of six years.

It can also be observed from Fig. 5.24 that the inclusion of creep effects using volumetric scaling does not significantly improve the prediction for centerline settlement. In contrast, the inclusion of creep effects using deviatoric scaling overestimated both the centerline settlement and the pore pressure response within the clay layer. Thus, the increased centerline settlement due to creep can be attributed to the increased lateral spreading induced by the deviatoric component rather than by time-dependent volumetric strains. This observation is further confirmed in Fig. 5.23 which compares the displacement vectors at the end of the consolidation period from the no-creep and the deviatoric-scaling analyses.

The overestimation of centerline settlement at longer times using the deviatoric scaling option could be due to an overestimate of the creep-induced lateral deformation, or it could be due to the overestimation of excess pore pressure development during the initial period of loading. The overprediction of the initial pore pressure response using the deviatoric scaling option may be due to the overestimation of the immediate deviatoric stiffness, inherent to the modified Cam clay model (refer to Sec. 2.3). The overprediction of initial excess pore pressures magnifies the pore pressure gradient and hastens the rate of pore pressure dissipation. An accelerated consolidation rate not only increases the rate of volume change, but also increases the rate at which the overconsolidated foundation soils become normally

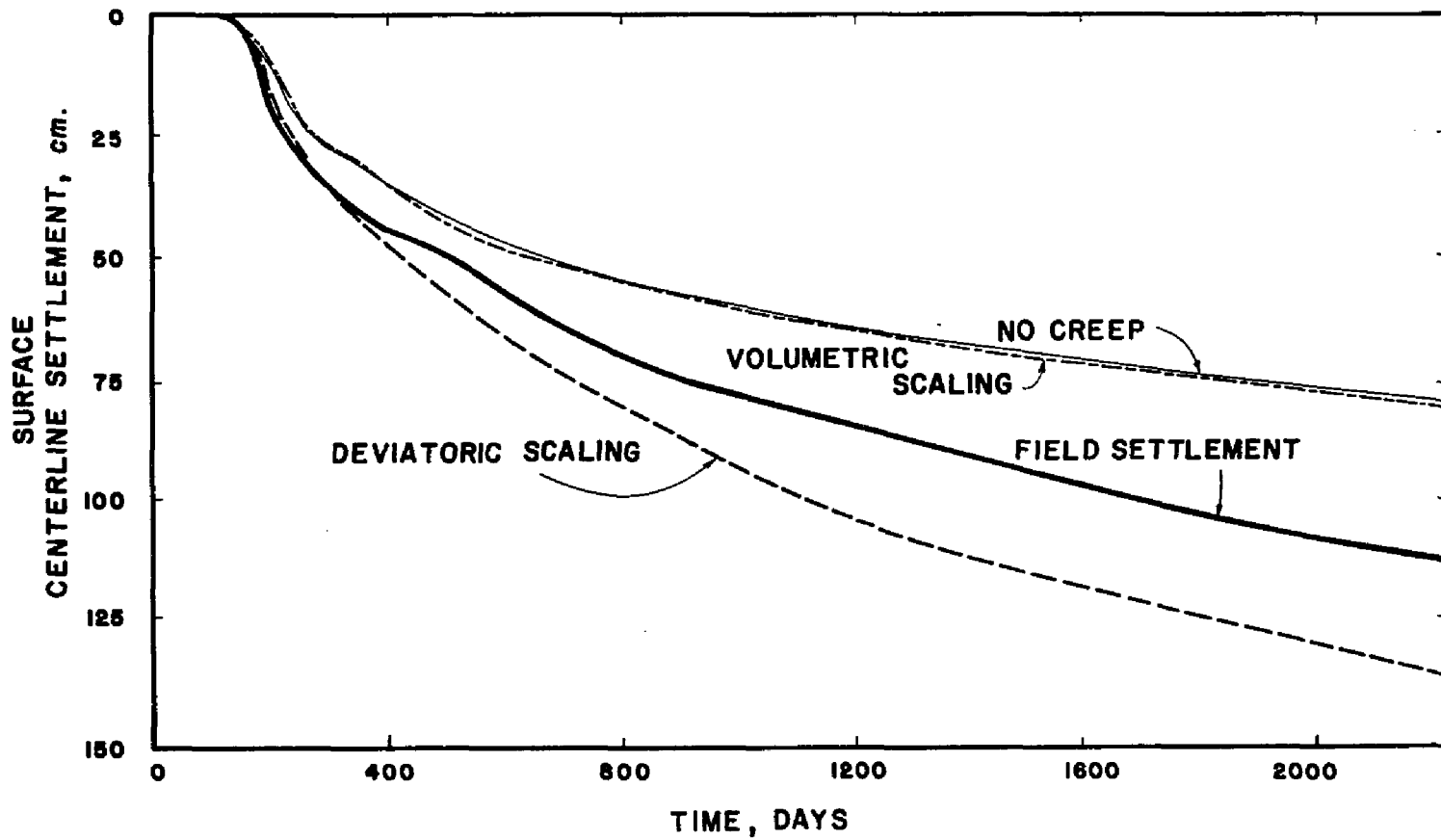


FIG. 5.24. SURFACE CENTERLINE SETTLEMENT VERSUS TIME
FOR THE I-95 EMBANKMENT PROBLEM.

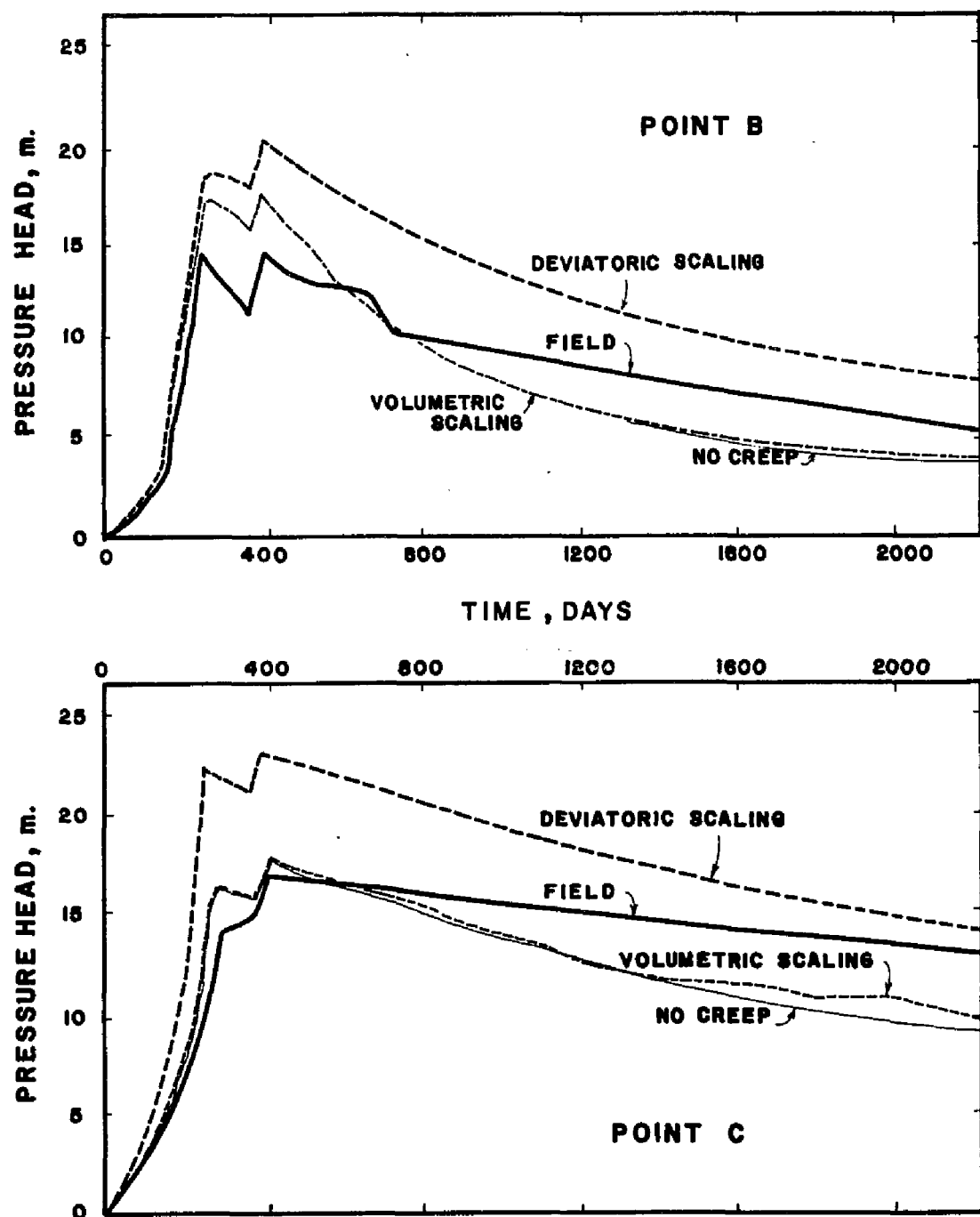


FIG. 5.25. PORE PRESSURE HEAD VERSUS TIME AT POINTS B AND C WITHIN THE BOSTON BLUE CLAY LAYER.

consolidated, accelerating lateral creep displacements.

The inclusion of volumetric creep in the numerical analysis does not significantly influence the result obtained from the no-creep analysis in this problem. Consulting equation (3.50), the creep strain rate tensor can be underpredicted if (1) the secondary compression coefficient ψ is underpredicted, or (2) the volumetric age is overpredicted (it was shown in Sec. 5.2 that the numerical solution is rather insensitive to the uncertainty in the value of void ratio). From equation (3.53a), the overprediction of the volumetric age t_v is also a consequence of the underprediction of ψ . If ψ is small compared to the virgin compression index λ , the rate of volumetric creep should be small compared to the immediate strain rate due to pore pressure dissipation. Hence, unless the ratio ψ/λ is large or the rate of pore pressure dissipation very small, an immediate/delayed compression model (used herein) will give the same result as a primary/secondary model.

It should be noted that the above statements were made under the assumption that the numerical algorithm in the program is reasonably accurate and that whatever behavior is observed is attributable to the feature of the constitutive model. It is worth mentioning, however, that numerical inaccuracies could also *creep* in, e.g., if the time steps used are not "sufficiently small" (see Sec. 4.8).

5.12 SUMMARY OF MAIN POINTS

The constitutive model has been used to analyze a documented case history of the deformation of a compressible embankment foundation. It was observed from the results of the numerical analyses that

- Creep-induced deformations constitute a large fraction of the overall deformation.
- Lateral spreading due to deviatoric creep deformations is the major contributor to the component of centerline settlement.
- Additional creep due to volumetric compression is not significant in this particular problem.

Chapter 6

CONCLUSIONS AND RECOMMENDATIONS

Conclusions

A constitutive model capable of accounting for time-dependent (creep) effects in a general three-dimensional stress condition has been developed. It was shown that the constitutive equation can always be written in the rate form

$$\dot{\sigma}_{ij} = c_{ijkl}\dot{\epsilon}_{kl} - \dot{\sigma}_{ij}^t$$

by defining the tensor of moduli c_{ijkl} and the stress relaxation rate $\dot{\sigma}_{ij}^t$, appropriately, before and during yielding. This constitutive model is an elasto-plastic strain-hardening model which uses the modified Cam clay yield surface [54] to model time-independent plasticity. Time-dependent (creep) effects are included based upon the phenomenological model for the stress-strain-time behavior of soft clays presented by Kavazanjian, Bonaparte, and Mitchell [32].

A finite element program called SPIN 2D was developed to (a) account for the effect of hydrodynamic lag which is not reflected in the above constitutive equation, (b) account for general displacement, traction, fluid velocity, and pore pressure boundary conditions, and (c) demonstrate, numerically, the predictive capability of the constitutive model in plane strain and axisymmetric (torsionless) stress conditions.

Results of numerical experiments on San Francisco Bay Mud and on Boston Blue Clay affirmed the validity of the constitutive model and demonstrated its capability to account for the following factors and conditions:

1. 'triaxial' and plane strain stress conditions
2. drained conditions
3. undrained conditions
4. isotropic, one-dimensional, radial, and two-dimensional consolidation

5. isotropic undrained stress relaxation
6. strain-rate effects
7. creep effects
8. combined creep and stress relaxation effects
9. rigid body rotation
10. large deformation

It was shown that creep deformations can become a major contributor to the total deformation for 'young' clays.

The above developments and results are significant because for the first time, to the knowledge of the author, a definitive numerical approach has been established to account for the combined effects of hydrodynamic lag and creep. The choice of the modified Cam clay model to characterize yielding does not impose a specific restriction on the general formulation because any other realistic and consistent plasticity model may be employed to obtain 'improved' results. To this end, the following recommendations are made for improvement of both the constitutive model and the finite element program:

Recommendations

■ On the constitutive model

1. Although the modified Cam clay model is in better agreement with 'triaxial' test results than the original Cam clay model, the underprediction of deviatoric strains (particularly in the undrained situation) is still a problem. This problem can be treated by incorporating the plastic shear distortion beneath the state boundary surface, as proposed by Roscoe and Burland [52]. To implement this concept numerically, two yield loci

$$F = F(\sigma_{ij}, p_c) = \frac{q^2}{M^2} + p(p - p_c) = 0$$

and

$$G = G(\sigma_{ij}, q_c) = q - q_c = 0$$

may be considered simultaneously, as shown in Fig. 2.5. By employing a similar formulation as in Sec. 3.2, a general constitutive equation of the form

$$\dot{\sigma}_{ij} = c_{ijkl}\dot{\epsilon}_{kl} - \dot{\sigma}_{ij}^t$$

can again be obtained. Unfortunately, the tensor of moduli c_{ijkl} loses its major symmetry when yield loci F and G are both engaged (refer to Fig. 2.5), leading to a nonsymmetric tangent stiffness matrix.

2. Material anisotropy and overconsolidation have been discussed briefly by Sekiguchi and Ohta [57] and Pender [49], respectively. They have shown that these factors do not only influence the size of the the yield surface but also its shape. Inclusion of these factors would provide a better interpretation of preconsolidation effects for states other than isotropic or K_o -conditions.

3. The underprediction of the rate of secondary compression C_α by the Singh-Mitchell scaling on the creep strain rate tensor in the range where the Singh-Mitchell equation best describes the deviatoric soil behavior ($0.2 \leq \bar{D} \leq 0.8$) is a problem yet to be resolved. Speculations are made that this underprediction of C_α is attributable to either the lack of the relationship between t_v and t_d assumed to justify the simplification made in the development of equation (4.5), or to the existence of a different plastic potential for time-dependent plastic strains. A non-associative flow rule in which the C_α - volumetric contribution is tensorially added to the creep strain rate tensor scaled by the Singh-Mitchell equation is an approach whose validity can be investigated easily, without having to explore the explicit form of the plastic potential for time-dependent plastic strains.

4. More parametric studies and large-scale field test simulations are strongly recommended to verify the validity of the constitutive model.

■ On the finite element program

1. It is recommended that a restart capability be implemented in the program. This will make it possible to continue the incremental solution after the execution is temporarily halted (e.g., to verify convergence) without having to run the problem again from the start.

2. For undrained analyses where discontinuous pore pressure interpolation is employed, it is recommended that the element routines be modified to eliminate the pore pressure degrees of freedom on the element level. This scheme will reduce

the global number of equations by the number of unknown nodal pore pressures, a factor which is considerable in large-scale problems.

3. When using the mixed formulation for consolidation analyses (or undrained analyses when recommendation (2) is not implemented), the pore pressure degrees of freedom may be interspersed with the displacement degrees of freedom (i.e., arrange all unknowns for each node next to each other), as opposed to equation (4.37) which explicitly segregates them. Program implementation is relatively more tedious, but this only requires special book-keeping to classify which displacement nodes are also pore pressure nodes. The extra coding effort needed to account for the ordering of unknown degrees of freedom will result in a more efficient global stiffness matrix formation in which the stiffness elements are more closely banded. The reduction in storage requirement is significant especially in large-scale problems.

4. Currently, SPIN 2D has an expanded element library of eight isoparametric quadrilateral elements and triangular elements to which some of these quadrilateral elements may degenerate. Further investigation is recommended to evaluate the performance of the higher-order triangular elements compared to their quadrilateral counterparts in both compressible and incompressible cases.

REFERENCES

- [1] BATHE, Klaus-Jürgen, and WILSON, Edward L. (1976), *Numerical Methods in Finite Element Analysis*, Prentice-Hall, NJ.
- [2] BECKER, Eric B., CAREY, Graham F., and ODEN, J. Tinsley (1981), *Finite Elements, An Introduction 1*, Prentice-Hall, NJ.
- [3] BERRE, T., and IVERSEN, K. (1972), "Oedometer Tests With Different Specimen Heights on a Clay Exhibiting Large Secondary Compression," *Geotechnique* **22**, No. 1, 53-70.
- [4] BIOT, Maurice A. (1941), "General Theory of Three-dimensional Consolidation," *J. Appl. Phys.* **12**, 155-164.
- [5] BISHOP, A. W., and HENKEL, D. J. (1962), *The Measurement of Soil Properties in the Triaxial Test*, Edward Arnold Ltd., London, 2nd ed.
- [6] BISHOP, Alan, and LOVENBURY, Howard T. (1969), "Creep Characteristics of Two Undisturbed Clays," *Seventh International Conference on Soil Mechanics and Foundation Engineering 1*, Mexico, 29-37.
- [7] BJERRUM, Laurits, and LO, K. Y. (1963), "Effect of Aging on the Shear-Strength Properties of a Normally Consolidated Clay," *Geotechnique* **13**, No. 2, 147-157.
- [8] BJERRUM, Laurits (1967), "Engineering Geology of Normally Consolidated Marine Clays as Related to Settlements of Buildings," *Seventh Rankine Lecture, Geotechnique* **17**, No. 2, 82-118.
- [9] BJERRUM, Laurits (1972), "Embankments on Soft Ground," *Proceedings, ASCE Specialty Conference on Earth and Earth-Supported Structures 1*, Purdue University, West Lafayette, IN, 1-54.
- [10] BONAPARTE, Rudolph, and MITCHELL, James K. (1979), "The Properties of San Francisco Bay Mud at Hamilton Air Force Base, California," *Geotechnical Engineering Report*, University of California, Berkeley.
- [11] BONAPARTE, Rudolph (1981), "A Time-Dependent Constitutive Model for Cohesive Soils," *Ph.D. thesis*, University of California, Berkeley.
- [12] BOOKER, J. R., and SMALL, J. C. (1975), "An Investigation of the Stability of Numerical Solutions of Biot's Equations of Consolidation," *Int. J. Solids Struct.* **11**, Nos. 7/8, 907-917.
- [13] BROMS, B. B., and CASBARIAN, A. O. (1965), "Effects of Rotation of the Principal Stress Axes and of the Intermediate Principal Stress on the Shear Strength," *Proceedings, Sixth International Conference on Soil Mechanics and Foundation Engineering 1*, Montreal, 179-183.
- [14] CAMPANELLA, R. G., and VAID, Y. P. (1974), "Triaxial and Plane Strain Creep Rupture of an Undisturbed Clay," *Canadian Geotechnical Journal* **2**, 1-10.
- [15] CHENEY, J. A., and ARULANANDAN, K. (1977), "Stress Relaxation in Sand and Clay," *Proceedings of Specialty Session 9, Ninth International Conference on Soil Mechanics and Foundation Engineering*, Tokyo, 279-285.

- [16] CHRISTIAN, John T. (1977), "Two- and Three-Dimensional Consolidation," Chapter 12: *Numerical Methods in Geotechnical Engineering*, Desai and Christian, eds., McGraw-Hill, 399-426.
- [17] DUNCAN, J.M. and CHANG, C.Y. (1970), "Nonlinear Analysis of Stress and Strain in Soils," *Journal of the Soil Mechanics and Foundations Division, ASCE* 96, No. SM5, September, 1629-1653.
- [18] DUNCAN, J. M. (1974), "Foundation Deformation Prediction," *Proceedings of the Foundation Deformation Prediction Symposium 2*, Appendix D, Report No. FHWA-RD-75-516, D-1-D-21.
- [19] GARLANGER, John E. (1972), "The Consolidation of Soils Exhibiting Creep Under Constant Effective Stress," *Geotechnique* 22, No. 1, 71-78.
- [20] HAWLEY, L. G. (1977), "The Measurement of Time Within the Soil Mass," Proceedings of Specialty Session 9, *Ninth International Conference on Soil Mechanics and Foundation Engineering*, Tokyo, 83-85.
- [21] HIBBITT, H. D., MARCAL, P. V., and RICE, J. R. (1970), "A Finite Element Formulation for Problems of Large Strain and Large Displacement," *Int. J. Solids Structures* 6, 1069-1086.
- [22] HILL, R. (1950), *The Mathematical Theory of Plasticity*, Oxford University Press, Great Britain.
- [23] HSIEH, Hsii-Sheng (1984), "An Automated Triaxial Device for Measuring the at-Rest Earth Pressure Coefficient," *Engineer's thesis*, Stanford University, Stanford, CA.
- [24] HUGHES, Thomas J.R. and PRÉVOST, Jean-Hervé (1979), *DIRT II-A Nonlinear Quasi-Static Finite Element Analysis Program*, User's Manual.
- [25] HUGHES, Thomas J. R. (1980), "Generalization of Selective Integration Procedures to Anisotropic and Nonlinear Media," Short Communications, *International Journal for Numerical Methods in Engineering* 15, 1395-1418.
- [26] HUGHES, Thomas J. R., and WINGET, James (1980), "Finite Rotation Effects in Numerical Integration of Rate Constitutive Equations Arising in Large-Deformation Analysis," Short Communications, *International Journal for Numerical Methods in Engineering* 15, No. 12, 1862-1867.
- [27] HUGHES, Thomas J.R. (1982), *A Course in the Finite Element Method 1*, Stanford University, class notes.
- [28] JOHNSTON, Paul R. (1981), "Finite Element Consolidation Analyses of Tunnel Behavior on Clay," *Ph.D. thesis*, Stanford University, Stanford, CA
- [29] KARLSUD, K., SOYDEMIR, C., and WOLFSKILL, L.A. (1970), "Performance of an Embankment on Clay, Interstate 95," *Department of Civil Engineering, Research Report No. R69-67*, Massachusetts Institute of Technology, Cambridge, MA.
- [30] KAVAZANJIAN, Jr., Edward (1978), "A Generalized Approach to the Prediction of Stress-Strain-Time Behavior of Soft Clay," *Ph.D. thesis*, University of California, Berkeley.

- [31] KAVAZANJIAN, Jr., Edward, and MITCHELL, James K. (1980), "Time-Dependent Deformation Behavior of Clays," *Journal of the Geotechnical Engineering Division, ASCE*, 611-630.
- [32] KAVAZANJIAN, Edward Jr., BONAPARTE, Rudolph, and MITCHELL, James K. (1984), "Time-Dependent Behavior of Clays: Theoretical Model," submitted for publication, *Geotechnical Engineering Journal, ASCE*.
- [33] KONDNER, R.L. (1963), "Hyperbolic Stress-Strain Response; Cohesive Soils," *Journal of the Soil Mechanics and Foundations Division, ASCE* 89, No. SM1, February, 115-144.
- [34] LACERDA, Willy A. (1976), "Stress-Relaxation and Creep Effects on Soil Deformation," *Ph.D. thesis, University of California, Berkeley*.
- [35] LADD, Charles C., and PRESTON, William B. (1965), "On the Secondary Compression of Saturated Clays," *Research in Earth Physics, Phase Report No. 6, Research Report R-65-59, Massachusetts Institute of Technology*.
- [36] LADD, Charles C., and FOOTT, R. (1974), "New Design Procedure for Stability of Soft Clays," *Journal of the Geotechnical Engineering Division, ASCE* 100, No. GT7, 763-786.
- [37] LADE, P.V., and DUNCAN, J.M. (1975), "Elasto-Plastic Stress-Strain Theory for Cohesionless Soils," *Journal of the Geotechnical Engineering Division, ASCE* 101, No. GT10, 1037-1053.
- [38] LEONARDS, G. A., and RAMIAH, B. K. (1960), "Time Effects in the Consolidation of Clays," *ASTM Special Technical Publication* 254, 116-130.
- [39] MALVERN, Lawrence E. (1969), *Introduction to the Mechanics of a Continuous Medium*, Prentice-Hall, NJ.
- [40] Massachusetts Institute of Technology, *Proceedings of the Foundation Deformation Prediction Symposium 1: Symposium Summary, Report No. FHWA-RD-75-515, November 13-15, 1974*, 1-18.
- [41] MATSUI, T., and ITO, T. (1977), "Flow Mechanism of Clay-Water System and Microscopic Meaning of Shear Parameters of Soils," *Proceedings of Specialty Session 9, Ninth International Conference on Soil Mechanics and Foundation Engineering, Tokyo*, 143-152.
- [42] MATTHIES, Hermann, and STRANG, Gilbert (1979), "The Solution of Nonlinear Finite Element Equations," *International Journal for Numerical Methods in Engineering* 14, 1613-1629.
- [43] McMEEKING, R. M., and RICE, J. R. (1975), "Finite-Element Formulations for Problems of Large Elastic-Plastic Deformations," *Int. J. Solids Structures* 11, 601-616.
- [44] MESRI, Gholamreza, and GODLEWSKI, Paul M. (1977), "Time-and-Stress-Compressibility Relationship," *Journal of the Geotechnical Engineering Division, ASCE*, 417-430.
- [45] MESRI, G., FEBRES-CORDERO, E., SHIELDS, D. R., and CASTRO, A. (1981), "Shear Stress-Strain-Time Behavior of Clays," *Geotechnique* 31, No. 4, 537-552.

- [46] MITCHELL, James K. (1976), *Fundamentals of Soil Behavior*, John Wiley and Sons, New York.
- [47] NEWMARK, N.M. (1960), "Failure Hypotheses for Soils," *Proc. ASCE Res. Conf. on Shear Strength of Cohesive Soils*, University of Colorado, 17-32.
- [48] OWEN, D.R.J., and HINTON, E. (1980), *Finite Elements in Plasticity: Theory and Practice*, Pineridge Press Limited, Swansea, U.K.
- [49] PENDER, M. J. (1977), "A Unified Model for Soil Stress-Strain Behavior," *Proceedings of Specialty Session 9, Ninth International Conference on Soil Mechanics and Foundation Engineering*, Tokyo, 213-222.
- [50] POEPSEL, Patrick (1984), "Finite Element Analysis of Embankment Construction and Foundation Consolidation: Two Case Histories," *Engineer's thesis*, Stanford University, Stanford, CA.
- [51] ROSCOE, K. H., SCHOFIELD, A. N., and THURAIRAJAH, A. (1963), "Yielding of Clays in States Wetter Than Critical," *Geotechnique*, 13, No. 2, 211-240.
- [52] ROSCOE, K. H., and BURLAND, J. B. (1968), "On the Generalized Stress-Strain Behavior of 'Wet' Clay," *Engineering Plasticity*, Cambridge, 535-609.
- [53] SANDHU, Ranbir (1968), "Fluid Flow in Saturated Porous Elastic Media," *Ph.D. thesis*, University of California, Berkeley.
- [54] SCHOFIELD, Andrew, and WROTH, Peter (1968), *Critical State Soil Mechanics*, McGraw-Hill Book Co., Great Britain.
- [55] SCHOFIELD, A. (1980), "Cambridge Geotechnical Centrifuge Operations," Twentieth Rankine Lecture, *Geotechnique* 3, No. 3, 225-268.
- [56] SCOTT, Ronald F. (1963), *Principles of Soil Mechanics*, Addison-Wesley Publishing Co. Inc., U.S.A.
- [57] SEKIGUCHI, H., and OHTA, H. (1977), "Induced Anisotropy and Time Dependency in Clays," *Proceedings of Specialty Session 9, Ninth International Conference on Soil Mechanics and Foundation Engineering*, Tokyo, 239-244.
- [58] SHACKEL, B. (1977), "Problems of Defining Constitutive Relationships for Soils," *Proceedings of Specialty Session 9, Ninth International Conference on Soil Mechanics and Foundation Engineering*, Tokyo, 229-238.
- [59] SINGH, Awtar, and MITCHELL, James K. (1968), "General Stress-Strain-Time Functions for Soils," *Journal of the Soil Mechanics and Foundation Division, ASCE*, 21-46.
- [60] SINRAM, Arno (1984), *Engineer's thesis*, Stanford University, in preparation.
- [61] SMALL, J. C., BOOKER, J. R., and DAVIS, E. H. (1976), "Elasto-Plastic Consolidation of Soil," *Int. J. Solids Structures* 12, 431-448.
- [62] TAVENAS, F. and LEROUEIL, S. (1977), "Effects of Stresses and Time on Yielding of Clays," *Proceedings of the Ninth International Conference on Soil Mechanics and Foundation Engineering*, Tokyo, 319-326.
- [63] TAVENAS, F., MIEUSSENS, C., and BOURGES, F. (1979), "Lateral Displacements in Clay Foundations Under Embankments," *Canadian Geotechnical Journal* 16, 532-550.

- [64] TAYLOR, D.W. (1948), *Fundamentals of Soil Mechanics*, John Wiley and Sons, New York.
- [65] TAYLOR, R. L. (1977), "Computer Procedures for Finite Element Analysis," Chap. 24: *The Finite Element Method* by O. C. Zienkiewicz, 3rd ed., McGraw-Hill, London.
- [66] TIMOSHENKO, S.P. and GOODIER, J.N. (1970), *Theory of Elasticity*, McGraw-Hill, 3rd ed., New York.
- [67] VAID, Y. P., and CAMPANELLA, R. G. (1977), "Time-Dependent Behavior of Undisturbed Clay," *Journal of the Geotechnical Engineering Division, ASCE GT7*, 693-709.
- [68] WROTH, C. P., THOMPSON, S. A., and HUGHES, J. M. O. (1974), "MIT Foundation Prediction Symposium", *Proceedings of the Foundation Deformation Prediction Symposium 2*, Report No. FHWA-RD-75-516, Appendix G, G-1-G-12.

APPENDIX 1

1.1 DEVELOPMENT OF WEAK FORM

BACKGROUND

The *strong form* (S) is given by (4.2)–(4.4). Assuming a constitutive equation of the form

$$\dot{\sigma}_{ij} = c_{ijkl}\dot{\epsilon}_{ij} - \dot{\sigma}_{ij}^t, \quad (A 1.1)$$

and that Darcy's law given by

$$\dot{u}_i = -k_{ij}\rho_{,j}/\gamma_w \quad (A 1.2)$$

is valid, then develop the statement of the weak form (W).

FORMULATION

Rewriting (4.2a, b),

$$\int_{\Omega} w_i \cdot (\dot{\sigma}_{ij,j} + \dot{f}_i) d\Omega + \int_{\Omega} q \cdot (\dot{u}_{i,i} - \dot{\epsilon}_v) d\Omega = 0, \quad (A 1.3)$$

which can be verified by observing that the quantities inside the parentheses are zero pointwise.

Expanding (A 1.3),

$$\int_{\Omega} w_i \dot{\sigma}_{ij,j} d\Omega + \int_{\Omega} w_i \dot{f}_i d\Omega + \int_{\Omega} q \dot{u}_{i,i} d\Omega - \int_{\Omega} q \dot{\epsilon}_v d\Omega = 0. \quad (A 1.4)$$

Using the divergence theorem and integrating by parts,

$$\begin{aligned} \int_{\Omega} w_i \dot{\sigma}_{ij,j} d\Omega &= - \int_{\Omega} w_{i,j} \dot{\sigma}_{ij} d\Omega + \int_{\Gamma} w_i \dot{\sigma}_{ij} n_j d\Gamma \\ &= - \int_{\Omega} w_{(i,j)} \cdot (c_{ijkl}\dot{\epsilon}_{ij} - \dot{\sigma}_{ij}^t) d\Omega + \sum_{n=1}^{n_{sd}} \left(\int_{\Gamma_{h_n}} w_i \dot{h}_i d\Gamma_{h_n} \right) \end{aligned} \quad (A 1.5)$$

where $w_{(i,j)} \leftarrow w_{i,j}$ since the Cauchy stress rate $\dot{\sigma}_{ij}$ is symmetric, while $\dot{\sigma}_{ij} n_j = \dot{h}_i$ from traction boundary condition (4.3b);

$$\begin{aligned} \int_{\Omega} q \dot{u}_{i,i} d\Omega &= - \int_{\Omega} q_{,i} \dot{u}_i d\Omega + \int_{\Gamma} q \dot{u}_i n_i d\Gamma \\ &= - \int_{\Omega} q_{,i} \frac{-k_{ij}}{\gamma_w} \rho_{,j} d\Omega + \int_{\Gamma_s} q s d\Gamma_s. \end{aligned} \quad (A 1.6)$$

upon substitution of $\dot{u}_i n_i = s$ from flow velocity boundary condition (4.4b).

Substituting (A 1.5), (A 1.6), and $\dot{\epsilon}_v \leftarrow \dot{u}_{i,i}$ in (A 1.4), the equation of the weak form is obtained as follows:

$$\begin{aligned} \int_{\Omega} w_{(i,j)} c_{ijkl} \dot{u}_{(k,l)} d\Omega + \int_{\Omega} w_{i,j} \dot{\rho} d\Omega - \int_{\Omega} q_{,i} \frac{k_{ij}}{\gamma_w} \rho_{,j} d\Omega + \int_{\Omega} q \dot{u}_{i,i} d\Omega \\ = \int_{\Omega} w_i \dot{f}_i d\Omega + \int_{\Omega} w_{i,j} \dot{\sigma}_{ij}^t d\Omega + \int_{\Gamma_s} q s d\Gamma_s + \sum_{n=1}^{n_{sd}} \left(\int_{\Gamma_{h_n}} w_i \dot{h}_i d\Gamma_{h_n} \right). \end{aligned} \quad (A 1.7)$$

* * *

1.2 MODIFIED CONSTITUTIVE EQUATION ACCOUNTING FOR FINITE DEFORMATION

BACKGROUND

Consider a class of rate constitutive equations of the form

$$-(\dot{\sigma}_{ij} + \dot{\sigma}_{ij}^t) = \bar{c}_{ijkl} v_{(k,l)} + s_{ijkl} v_{[k,l]} \quad (A 1.8)$$

in which

$$\bar{c}_{ijkl} = c_{ijkl} + c_{ijkl}^* \quad (A 1.9)$$

is the material response tensor and

$$s_{ijkl} = \frac{1}{2}(\sigma_{ik}\delta_{jl} + \sigma_{jk}\delta_{il} - \sigma_{il}\delta_{jk} - \sigma_{jl}\delta_{ik}) \quad (A 1.10)$$

is the tensor uniquely specified by objectivity requiring that $(\dot{\sigma}_{ij} + \dot{\sigma}_{ij}^t)$ transform properly under rigid-body rotations. Defining

$$c_{ijkl}^* = \sigma_{ij}\delta_{kl}, \quad (A 1.11)$$

develop the modified constitutive equation accounting for finite deformation.

FORMULATION

Development of the linearized variational equation

Using the domain Ω in the current configuration, the nonlinear variational equation is written as follows:

$$-\underbrace{\int_{\Omega} w_{(i,j)} \sigma_{ij} d\Omega}_{F_{INT}} = \underbrace{\int_{\Omega} w_i f_i d\Omega + \int_{\Gamma_h} w_i h_i d\Gamma}_{F_{EXT}}, \quad (A 1.12)$$

which simply states that "the internal force is equal to the external force."

Since the Cauchy stress tensor σ_{ij} is symmetric, $w_{(i,j)} \rightarrow w_{i,j}$, i.e., the parentheses in the internal force term w can be removed. Using chain rule on $w_{i,j}$ and referencing the variables with respect to the initial (undeformed) configuration,

$$F_{INT} = \mathcal{F}(\sigma_{ij}, \mathbf{u}) = - \int_{\Omega} w_{i,j} \sigma_{ij} d\Omega \quad (A 1.13a)$$

$$= \int_{\Omega_0} (w_{i,A} F_{A,j}^{-1}) \sigma_{ij} (J d\Omega_0), \quad (A 1.13b)$$

where

$$F_{A,j}^{-1} = \frac{\partial X_A}{\partial x_j} = \delta_{Aj} - \frac{\partial u_A}{\partial x_j} \quad (A 1.14)$$

is the inverse of the deformation gradient tensor and

$$J = \frac{d\Omega}{d\Omega_0} = \det \mathbf{F} = \det \left(\frac{\partial \mathbf{x}}{\partial \mathbf{X}} \right) = \det \left[\frac{\partial (\mathbf{X} + \mathbf{u})}{\partial \mathbf{X}} \right] \quad (A 1.15)$$

is the determinant of the deformation gradient tensor.

The linearized variational equation can be obtained by evaluating the directional derivative of \mathcal{F} in the direction $(\Delta\sigma_{ij}, \Delta\mathbf{u})$ as follows:

$$\begin{aligned} \frac{d}{d\epsilon} \mathcal{F}(\sigma_{ij} + \epsilon \Delta\sigma_{ij}, \mathbf{u} + \epsilon \Delta\mathbf{u}) \Big|_{\epsilon=0} = & - \int_{\Omega_o} w_{i,A} F_{A_j}^{-1} \Delta\sigma_{ij} J d\Omega_o \\ & - \int_{\Omega_o} w_{i,A} F_{A_j}^{-1} \sigma_{ij} \Delta u_{k,k} J d\Omega_o \\ & + \int_{\Omega_o} w_{i,A} \Delta u_{A,j} \sigma_{ij} J d\Omega_o, \quad (A 1.16) \end{aligned}$$

where ϵ is a real parameter.

Transforming back with respect to the current configuration,

$$- \int_{\Omega} w_{i,j} \cdot (\Delta\sigma_{ij} + \sigma_{ij} \Delta u_{k,k} - \sigma_{k,l} \Delta u_{j,k}) d\Omega = F_{EXT} - F_{INT}, \quad (A 1.17)$$

in which F_{INT} is the current value of the internal force and F_{EXT} is the value of the external force a period of time Δt later. Equation (A 1.17) is the linearized variational equation deduced from (A 1.12). An incremental constitutive equation is necessary because of the incremental stress $\Delta\sigma_{ij}$ which appears in (A 1.17).

Development of the modified constitutive equation

Rewriting (A 1.8) in incremental form,

$$-(\Delta\sigma_{ij} + \Delta\sigma_{ij}^t) = \bar{c}_{ijkl} \Delta u_{(k,l)} + s_{ijkl} \Delta u_{[k,l]}, \quad (A 1.18)$$

where $\Delta u_{(k,l)}$ and $\Delta u_{[k,l]}$ are the symmetric and the skew-symmetric parts of the incremental displacement gradient $\Delta u_{k,l}$, respectively.

Substituting (A 1.9) and (A 1.10) in (A 1.18),

$$\begin{aligned} -(\Delta\sigma_{ij} + \Delta\sigma_{ij}^t) &= (c_{ijkl} + \sigma_{ij}\delta_{kl}) \cdot \Delta u_{(k,l)} \\ &\quad + \frac{1}{2}(\sigma_{ik}\delta_{jl} + \sigma_{jk}\delta_{il} - \sigma_{il}\delta_{jk} - \sigma_{jl}\delta_{ik}) \cdot \Delta u_{[k,l]} \quad (A 1.19a) \end{aligned}$$

$$= c_{ijkl} \Delta u_{(k,l)} + \sigma_{ij} \Delta u_{k,k} + \sigma_{ik} \Delta u_{[k,j]} + \sigma_{jk} \Delta u_{[k,i]}. \quad (A 1.19b)$$

Defining

$$-c_{ijkl} \Delta u_{(k,l)} = \Delta\sigma_{ij}^* + \sigma_{ij} \Delta u_{k,k} \quad (A 1.20a)$$

or

$$-c_{ijkl} v_{(k,l)} = \sigma_{ij}^* + \sigma_{ij} v_{k,k}, \quad (A 1.20b)$$

the Jaumann derivative σ_{ij}^* is obtained thus:

$$\Delta\sigma_{ij}^* = (\Delta\sigma_{ij} + \Delta\sigma_{ij}^t) + \sigma_{ik} u_{[k,j]} + \sigma_{jk} \Delta u_{[k,i]} \quad (A 1.21a)$$

or

$$\sigma_{ij}^* = (\dot{\sigma}_{ij} + \dot{\sigma}_{ij}^t) + \sigma_{ik} v_{[k,j]} + \sigma_{jk} v_{[k,i]}. \quad (A 1.21b)$$

Equations (A 1.20b) and (A 1.21b) also appear as (4.53) and (4.54), respectively, in Section 4.4.

Substituting (A 1.19b) in the linearized equation (A 1.17),

$$\int_{\Omega} w_{i,j} \cdot (c_{ijkl} \Delta u_{(k,l)} + \sigma_{ik} \Delta u_{[k,j]} + \sigma_{jk} \Delta u_{[k,i]} + \sigma_{kl} \Delta u_{j,k}) d\Omega = F_{EXT} - F_{INT} . \quad (A 1.22)$$

If creep effects are included, the term $\int_{\Omega} w_{i,j} \Delta \sigma_{ij}^t d\Omega$ goes to the right-hand side of (A 1.22).

Noting that

$$\begin{cases} \Delta u_{(k,l)} = \frac{1}{2}(\Delta u_{k,l} + \Delta u_{l,k}) \\ \Delta u_{[k,l]} = \frac{1}{2}(\Delta u_{k,l} - \Delta u_{l,k}) \end{cases} , \quad (A 1.23)$$

the linearized equation (A 1.22) is expanded as follows:

$$F_{EXT} - F_{INT} = \int_{\Omega} w_{i,j} [c_{ijkl} + \frac{1}{2}(\sigma_{il}\delta_{jk} + \sigma_{ik}\delta_{jl} + \sigma_{jk}\delta_{il} - \sigma_{jl}\delta_{ik})] \cdot \Delta u_{k,l} d\Omega \quad (A 1.24a)$$

$$= \int_{\Omega} w_{i,j} d_{ijkl} \Delta u_{k,l} d\Omega . \quad (A 1.24b)$$

Thus, the stress-strain tensor in the linearized variational equation can be written in any of the following forms:

$$d_{ijkl} = \begin{cases} c_{ijkl}, & \text{small deformations;} \\ c_{ijkl} + \frac{1}{2}(\sigma_{il}\delta_{jk} + \sigma_{ik}\delta_{jl} + \sigma_{jk}\delta_{il} - \sigma_{jl}\delta_{ik}), & \text{finite deformations.} \end{cases} \quad (A 1.25)$$

The tensor d_{ijkl} possesses the major symmetry (i.e., $d_{ijkl} = d_{klji}$) if and only if c_{ijkl} possesses the major symmetry, which would lead to a symmetric tangent stiffness.

* * *

APPENDIX 2

2.1 FLOW CHARTS OF CLAY-CONSTITUTIVE ROUTINES

This section is to be compared with Appendix 2.2 which shows the actual subroutines in their FORTRAN-code forms.

SUBROUTINE AGE(TV,TD,AV,AD,DT)

program to compute volumetric and deviatoric
ages (t_v, t_d) and creep factors (AV,AD)

Volumetric age and creep factor:

- VRI $\leftarrow e_2 = e_a + (\lambda - \kappa) \ln p_o - \kappa \ln p$ (equation (3.51))
- TV $\leftarrow (t_v)_i \exp \left(\frac{e_2 - e}{\psi} \right)$
- AV $\leftarrow \frac{\psi}{1+e} \ln \left(1 + \frac{\Delta t}{t_v} \right)$

Deviatoric age and creep factor

- DBAR $\leftarrow \bar{D} = 2^{(1-\kappa/\lambda)} \frac{q}{Mpc}$ (Deviatoric stress level)
- E1 $\leftarrow \gamma_2 = \sqrt{\frac{4}{3} \Pi_{e_d}}$ (cf. equation (3.4))
- EI $\leftarrow \gamma_1 = \frac{qa}{R_f p_c - qb}$ (cf. equation (3.64))
- EA $\leftarrow \gamma_1 - \gamma_2$
- TD $\leftarrow (t_d)_i$ (default deviatoric age)
- if ($m \neq 1$) go to 10 (note numerical tolerance used in code)

Singh-Mitchell parameter m = 1

- TD $\leftarrow (t_d)_i \exp \left(\frac{\gamma_1 - \gamma_2}{A e^{\bar{D}}} \right)$
- AD $\leftarrow A e^{\bar{D}} (t_d)_i \ln \left(1 + \frac{\Delta t}{t_d} \right)$

- return

Singh-Mitchell parameter m $\neq 1$

10 if (EA < 10^{-5}) go to 11 (check if point is on the hyperbola)

$$- TD \leftarrow \left[\frac{(\gamma_2 - \gamma_1)(1-m)}{A e^{\bar{D}} (t_d)_i^m} \right]^{\frac{1}{1-m}}$$

$$11 AD \leftarrow A e^{\bar{D}} (t_d)_i^m \frac{[(t_d + \Delta t)^{1-m} - t_d^{1-m}]}{1-m}$$

- return

• end

SUBROUTINE CREEP(EPSI,AV,AD)

program to compute creep strain increment EPSI(I) = $\Delta\epsilon_I^t$;
 creep factors AV = $\int_t^{t+\Delta t} \frac{\psi}{(1+\epsilon)t_0} dt$; AD = $\int_t^{t+\Delta t} A e^{\alpha D} \left(\frac{t}{t_0}\right)^m dt$.

— if (ICR ≠ 1) go to 2

Non-associative creep

— THETA ← $\theta = \tan^{-1} \frac{2\sigma_{12}}{\sigma_{11} - \sigma_{22}}$

— EPSI ← $\begin{Bmatrix} \Delta\epsilon_{11}^t \\ \Delta\epsilon_{22}^t \\ \Delta\epsilon_{33}^t \\ \Delta\epsilon_{12}^t \end{Bmatrix} = \begin{Bmatrix} AV/2 + \sqrt{3} AD \cos\theta \\ AV/2 - \sqrt{3} AD \cos\theta \\ 0 \\ \sqrt{3} AD \sin\theta \end{Bmatrix}$

— return

Associative creep strain

2 EPSI(I) ← $\frac{\partial F}{\partial \sigma_I}$

— D1 ← $\frac{\partial F}{\partial \sigma_{kk}} = \frac{\partial F}{\partial p}$

— if (D1 < 1×10^{-3}) go to 3 (avoid vertical normal)

Volumetric scaling:

— FAC ← $\frac{AV}{D1}$ (the scaling factor)

— if (ICR=2) go to 4

Deviatoric scaling:

3 D2 ← $\frac{\partial F}{\partial \sigma_{ij}} \frac{\partial F}{\partial \sigma_{ij}} - \frac{1}{3} \left(\frac{\partial F}{\partial p} \right)^2$

— if (D2 > 1×10^{-3}) FAC ← $\sqrt{\frac{3}{2}} \frac{AD}{\sqrt{D2}}$ (avoid horizontal normal)

4 EPSI(I) ← FAC × EPSI(I) = FAC × $\frac{\partial F}{\partial \sigma_I}$

— return

• end

SUBROUTINE MATRIX (D,DSIG,DT)

program to compute stress-strain matrix
and stress relaxation terms

- clear D(4,4), DSIG(4), DEET(4)
- define P, Q, PO
- if (ICR \neq 0) CALL AGE (*obtain t_d , t_v , and creep factors*)
CALL CREEP (*obtain DEET(J) = $\Delta\epsilon_j^t$*)
- CALL MODULI
- construct elastic $D(I,J) \leftarrow C_{IJ}^e$
- CALL TRIAL (*if elastic, TRIAL returns IFLAG=0*
(if plastic, TRIAL returns IFLAG=1))
- if (IFLAG=0) go to 10
- construct C_{IJ}^p
- if (ICR=0) go to 4
- evaluate $DSIG(I) = \chi p_e \frac{\partial F}{\partial p_e} \frac{\psi}{\lambda - \kappa} \sum_{J=1}^4 C_{IJ}^e \frac{\partial F}{\partial \sigma_J} \ln \left(1 + \frac{\Delta t}{t_v} \right)$
- 4 compute elasto-plastic $D(I,J) \leftarrow C_{IJ} = C_{IJ}^e - C_{IJ}^p$
- 10 if (ICR=0) return
- compute $DSIG(I) \leftarrow DSIG(I) + \sum_{J=1}^4 C_{IJ} \Delta\epsilon_J^t$
- return
- end

SUBROUTINE MODULI(BMOD,SMOD)

program to compute elastic bulk and shear moduli

Elastic bulk modulus:

$$- BMOD \leftarrow \frac{1+e}{\kappa} p$$

Elastic shear modulus:

$$- SMOD \leftarrow \frac{R_f p_e}{3a}$$

- return

• end

SUBROUTINE TRIAL(D,T,DEE,DEET,PC,DM,IFLAG)

program to compute and locate trial stresses
program returns IFLAG=0 if behavior is elastic,
IFLAG=1 if behavior is plastic.

– IFLAG=0

$$-\sigma_1^{tr} \leftarrow \sigma_1 + \sum_{j=1}^4 C_{ij}^e \cdot (\Delta\epsilon_j^{tr} - \Delta\epsilon_j^t)$$

– define trial quantities P^{tr}, Q^{tr}, PO^{tr}
– if (PO^{tr} < PC) return
– IFLAG ← 1
– return
• end

SUBROUTINE UPDATE(S2,S1,VOID,D,DSIG)

program to update stresses, preconsolidation pressure
and void ratio

– CALL MATRIX (evaluate C_{ij} and DSIG(I) = Δσ_i^t)

$$- DSIG(I) \leftarrow \sum_{j=1}^4 C_{ij} \Delta\epsilon_j - DSIG(I) \quad (\text{evaluate incremental stress vector})$$

– if (IFD=0) go to 30

$$- DSIG(I) \leftarrow DSIG(I) - σ_1 \Delta\epsilon_v - \sum_{j=1}^4 S_{ij} \Delta\theta_j \quad (\text{correct for rigid body rotations})$$

30 S2(I) ← S1(I) + DSIG(I), I=1,...,4 (update stresses)

Update preconsolidation and void ratio

– define updated P, Q, PO, PC

Time-independent strain-hardening:

– e ← ε_a - κ ln p - (λ - κ) ln p_c

$$- p_c \leftarrow \frac{\partial p_c}{\partial \epsilon_v^P} \Delta\epsilon_v^P$$

– if (ICR=0) return

Time-dependent strain hardening:

$$- e \leftarrow e - \psi \ln \left(1 + \frac{dt}{t_v} \right)$$

$$- p_c \leftarrow p_c + p_c \frac{\psi}{\lambda - \kappa} \ln \left(1 + \frac{dt}{t_v} \right)$$

– return

• end

2.2 PROGRAM LISTING

```

C SUBROUTINE AGE (TV,TD,AV,AD,DT) AGE 1
C =====
C C.... PROGRAM TO COMPUTE VOLUMETRIC/DEVIATORIC AGES AGE 2
C C..... VOLUMETRIC/DEVIATORIC CREEP FACTORS AGE 3
C C IMPLICIT REAL*8 (A-H,O-Z) AGE 4
C C.... REMOVE ABOVE CARD FOR SINGLE PRECISION OPERATION AGE 5
C C COMMON/FSTRES/AL,C(36),T(6),EE(9),DEE(9) AGE 6
C COMMON/VALUES/SPAR(16),PC,P,Q,PO,VR,ICR AGE 7
C DATA HALF,ONE,TWO,THREE,SIX/ AGE 8
C S 0.5D0,1.0D0,2.0D0,3.0D0,6.0D0/ AGE 9
C C.... MODIFY ABOVE CARD(S) FOR SINGLE PRECISION OPERATION AGE 10
C CR = SPAR(1) AGE 11
C CC = SPAR(2) AGE 12
C HA = SPAR(3) AGE 13
C HB = SPAR(4) AGE 14
C HRF= SPAR(5) AGE 15
C CA = SPAR(6) AGE 16
C SA = SPAR(7) AGE 17
C SM = SPAR(8) AGE 18
C SAL= SPAR(9) AGE 19
C TDI=.SPAR(10) AGE 20
C TVI= SPAR(11) AGE 21
C DM = SPAR(12) AGE 22
C VR1= SPAR(13) AGE 23
C C.... COMPUTE VOLUMETRIC AGE AND CREEP FACTOR AGE 24
C C VRI= VR1 - (CC-CR)*DLOG (PO) - CR*DLOG (P) AGE 25
C TEMP = (VRI-VR)/CA AGE 26
C IF (TEMP.GT.150.D0) TEMP=150.D0 AGE 27
C TV = TVI*DEXP(TEMP) AGE 28
C AV = CA*DLOG(ONE+DT/TV)/(ONE+VR) AGE 29
C C.... COMPUTE DEVIATORIC AGE AND CREEP FACTOR AGE 30
C C TEMP = HALF** (ONE-CR/CC) AGE 31
C QF = TEMP*DM*PC AGE 32
C DBAR = Q/QF AGE 33
C ETA = Q/PC AGE 34
C E1 = DSQRT(((EE(1)-EE(2))**2+(EE(2)-EE(3))**2+(EE(3)-EE(1))**2 AGE 35
C * + SIX*(HALF*EE(4))**2)*TWO)/THREE AGE 36
C E1 = ETA*HA/(HRF-ETA*HB) AGE 37
C EA = E1 - E1 AGE 38
C DBAR = SA*DEXP(SAL*DBAR) AGE 39
C TD = TDI AGE 40
C TEMP = ONE - SM AGE 41
C IF (DABS(TEMP).GT.1.0D-3) GOTO 10 AGE 42

```

```

C
C.... SM.EQ.1: AGE 55
C AGE 56
C AGE 57
C     IF (EA.GT.1.0D-5) TD=TD1*DEXP (EA/DBAR) AGE 58
C     AD = DBAR*TD1*DLOG (ONE+DT/TD) AGE 59
C     RETURN AGE 60
C
C.... SM.NE.1: AGE 61
C AGE 62
C AGE 63
C     10 IF (EA.LT.1.0D-5) GOTO 11 AGE 64
C     TD = EA*TEMP/(DBAR*TD1**SM) AGE 65
C     TD = TD** (ONE/TEMP) AGE 66
C     IF (TD.LT.TD1) TD=TD1 AGE 67
C     11 AD = (TD+DT)**TEMP - TD**TEMP AGE 68
C     AD = DBAR*AD*TD1**SM/TEMP AGE 69
C     RETURN AGE 70
C     END AGE 71
C -----
C     SUBROUTINE CREEP(EPSI,AV,AD) CREE 1
C -----
C
C.... PROGRAM TO COMPUTE CREEP STRAIN RATE VECTOR CREE 2
C CREE 3
C     IMPLICIT REAL*8(A-H,O-Z) CREE 4
C
C.... REMOVE ABOVE CARD FOR SINGLE PRECISION OPERATION CREE 5
C CREE 6
C
C     COMMON/FSTRES/AL,C(36),T(6),EE(9),DEE(9) CREE 7
C     COMMON/VALUES/SPAR(16),PC,P,Q,PO,VR,ICR CREE 8
C     DIMENSION EPSI(1) CREE 9
C     DATA ZERO,ONE,ONEPT5,RT3,TWO,THREE/ CREE 10
C     S    0.000,1.000,1.500,1.732059000,2.000,3.000/ CREE 11
C
C.... MODIFY ABOVE CARD FOR SINGLE PRECISION OPERATION CREE 12
C CREE 13
C     IF (ICR.NE.1) GO TO 2 CREE 14
C CREE 15
C     CREE 16
C     CREE 17
C
C.... NON-ASSOCIATIVE CREEP STRAIN CREE 18
C CREE 19
C     COSINE = ZERO CREE 20
C     SINE = ONE CREE 21
C     TDEL = T(1) - T(2) CREE 22
C     IF (DABS(TDEL).LT.1.0D-5) GO TO 1 CREE 23
C     THETA = DATAN(TWO*T(4)/TDEL) CREE 24
C     COSINE = DCOS(THETA) CREE 25
C     SINE = DSIN(THETA) CREE 26
C     EPSI(1) = AV/TWO + RT3*AD*COSINE CREE 27
C     EPSI(2) = AV/TWO - RT3*AD*COSINE CREE 28
C     EPSI(3) = ZERO CREE 29
C     EPSI(4) = RT3*AD*SINE CREE 30
C     RETURN CREE 31
C
C.... ASSOCIATIVE CREEP STRAIN CREE 32
C CREE 33
C
C     2 PC1= PO CREE 34
C     DM = SPAR(12) CREE 35
C     D1 = (TWO*P-PC1)/THREE CREE 36
C     D2 = THREE/(DM*DM) CREE 37
C     EPSI(1) = D1 + (T(1)-P)*D2 CREE 38
C     EPSI(2) = D1 + (T(2)-P)*D2 CREE 39
C     EPSI(3) = D1 + (T(3)-P)*D2 CREE 40
C     EPSI(4) = TWO*T(4)*D2 CREE 41
C
C

```

```

D1 = TWO*P - PC1          CREE  44
IF(D1.LT.1.0D-3) GOTO 3    CREE  45
C.... VOLUMETRIC SCALING   CREE  46
C
FAC= AV/D1                CREE  47
IF(ICR.EQ.2) GOTO 4        CREE  49
C.... DEVIATORIC SCALING   CREE  50
C
3 D2 = EPSI(1)*EPSI(1) + EPSI(2)*EPSI(2) + EPSI(3)*EPSI(3)  CREE  54
*           + TWO*EPSI(4)*EPSI(4) - D1*D1/THREE               CREE  55
IF(D2.GT.1.0D-3) FAC = AD*DSQRT(ONEPTS/D2)                  CREE  56
C
4 DO 5 I=1,4              CREE  57
5 EPSI(I) = FAC*EPSI(I)    CREE  58
RETURN                      CREE  59
END                         CREE  60
CREE  61
C -----
SUBROUTINE MATRIX(D,DSIG,DT) MATR  1
C -----
C.... PROGRAM TO COMPUTE STRESS-STRAIN MATRIX AND MATR  2
C      STRESS RELAXATION TERMS MATR  3
C
IMPLICIT REAL*8(A-H,O-Z) MATR  4
C.... REMOVE ABOVE CARD FOR SINGLE PRECISION OPERATION MATR  5
C
COMMON/FSTRES/AL,C(36),T(6),EE(9),DEE(9) MATR  6
COMMON/VALUES/SPAR(16),PC,P,Q,PO,VR,ICR MATR  7
COMMON/XDATA/TV MATR  8
DIMENSION D(4,1),DSIG(1),DEET(4),A1(4),A2(4) MATR  9
DATA ZERO,ONE,TWO,THREE,FOUR,SIX/ MATR 10
$     0.0D0,1.0D0,2.0D0,3.0D0,4.0D0,6.0D0/ MATR 11
DATA RT2/1.41421356237309D0/ MATR 12
C
C.... MODIFY ABOVE CARD(S) FOR SINGLE PRECISION OPERATION MATR 13
C
CALL CLEAR(D,16)          MATR 14
CALL CLEAR(DSIG,4)         MATR 15
CALL CLEAR(DEET,4)         MATR 16
C
P = (T(1)+T(2)+T(3))/THREE MATR 17
Q = DSQRT((T(2)-T(3))**2 + (T(3)-T(1))**2 + (T(1)-T(2))**2) MATR 18
*           + SIX*T(4)*T(4))/RT2 MATR 19
DM = SPAR(12)              MATR 20
IF(P.LT.1.0D-3) P=1.0D-3  MATR 21
PO = P + Q*Q/(P*DM*DM)    MATR 22
C
C.... CREEP COMPUTATION MATR 23
C
IF(ICR.NE.0) CALL AGE(TV,TD,AV,AD,DT) MATR 24
IF(ICR.NE.0) CALL CREEP(DEET,AV,AD)    MATR 25
C
CALL MODULI(BMOD,SMOD)      MATR 26
C.... ELASTIC STRESS-STRAIN MATRIX: MATR 27
C

```

```

D(1,1) = (THREE*BMOD + FOUR*SMOD)/THREE
D(2,2) = D(1,1)
D(3,3) = D(1,1)
D(1,2) = (THREE*BMOD-TWO*SMOD)/THREE
D(1,3) = D(1,2)
D(2,1) = D(1,2)
D(2,3) = D(1,2)
D(3,1) = D(1,2)
D(3,2) = D(1,2)
D(4,4) = SMOD

C.... CHECK IF POINT IS ON THE YIELD SURFACE
C
CALL TRIAL(D,T,DEE,DEET,PC,DM,IFLAG)
IF(IFLAG.EQ.0) GOTO 10
C.... ELASTO-PLASTIC STRESS-STRAIN MATRIX:
C
D1 = (TWO*P-PC)/THREE
D2 = THREE/(DM*DM)
A1(1) = D1 + (T(1)-P)*D2
A1(2) = D1 + (T(2)-P)*D2
A1(3) = D1 + (T(3)-P)*D2
A1(4) = TWO*T(4)*D2

C
CR = SPAR(1)
CC = SPAR(2)
CA = SPAR(6)

DO 1 I=1,3
A2(I) = ZERO
DO 1 J=1,3
1 A2(I) = A2(I) + D(I,J)*A1(J)
A2(4) = SMOD*A1(4)
DEN = ZERO
DO 2 I=1,4
2 DEN = DEN + A1(I)*A2(I)
DEN = DEN + P*PC*(ONE+VR)*(TWO*P-PC)/(CC-CR)
IF(ICR.EQ.0) GOTO 4

C
D1 = -P*PC*CA*DLOG(ONE+DT/TV)/(DEN*(CC-CR))
DO 3 I=1,4
3 DSIG(I) = A2(I)*D1

C
4 DO 5 I=1,4
DO 5 J=1,4
5 D(I,J) = D(I,J) - A2(I)*A2(J)/DEN

C
10 IF(ICR.EQ.0) RETURN

C
DO 11 I=1,4
DO 11 J=1,4
11 DSIG(I) = DSIG(I) + D(I,J)*DEET(J)
RETURN
END

```

```

C----- SUBROUTINE MODULI (BMOD,SMOD) MODU 1
C----- C.... PROGRAM TO COMPUTE ELASTIC BULK AND SHEAR MODULI MODU 2
C----- C..... IMPLICIT REAL*8 (A-H,O-Z) MODU 3
C----- C..... REMOVE ABOVE CARD FOR SINGLE PRECISION OPERATION MODU 4
C----- C----- COMMON/VALUES/SPAR(16),PC,P,Q,PD,VR,ICR MODU 5
C----- DATA ONE,THREE/ MODU 6
C----- $ 1.000,3.000/ MODU 7
C----- C.... MODIFY ABOVE CARD FOR SINGLE PRECISION OPERATION MODU 8
C----- C----- CR = SPAR(1) MODU 9
C----- HA = SPAR(3) MODU 10
C----- HB = SPAR(4) MODU 11
C----- HRF = SPAR(5) MODU 12
C----- C.... COMPUTE BULK MODULUS MODU 13
C----- C----- BMOD = (ONE+VR)*P/CR MODU 14
C----- C.... COMPUTE SHEAR MODULUS MODU 15
C----- C----- SMOD = PC*HRF/(THREE*HA) MODU 16
C----- RETURN MODU 17
C----- END MODU 18
C----- C----- SUBROUTINE TRIAL(D,T,DEE,DEET,PC,DM,IFLAG) TRIA 1
C----- C.... PROGRAM TO COMPUTE AND CHECK TRIAL STRESSES TRIA 2
C----- C..... IF WITHIN THE YIELD SURFACE, IFLAG = 0 TRIA 3
C----- C..... IF OUTSIDE THE YIELD SURFACE, IFLAG = 1 TRIA 4
C----- C..... IMPLICIT REAL*8(A-H,O-Z) TRIA 5
C----- C.... REMOVE ABOVE CARD FOR SINGLE PRECISION OPERATION TRIA 6
C----- C----- DIMENSION D(4,1),T(1),DEE(1),DEET(1),S(4) TRIA 7
C----- DATA ZERO,THREE,SIX,RT2/ TRIA 8
C----- $ 0.000,3.000,6.000,1.41421356237309D0/ TRIA 9
C----- C.... MODIFY ABOVE CARD FOR SINGLE PRECISION OPERATION TRIA 10
C----- C..... IFLAG = 0 TRIA 11
C----- DO 20 I=1,4 TRIA 12
C----- TEMP = ZERO TRIA 13
C----- DO 10 J=1,4 TRIA 14
C----- 10 TEMP = TEMP + D(I,J)*(DEE(J)-DEET(J)) TRIA 15
C----- 20 S(I) = T(I) + TEMP TRIA 16
C----- C..... P = (S(1)+S(2)+S(3))/THREE TRIA 17
C----- Q = DSQRT((S(2)-S(3))*#2 + (S(3)-S(1))*#2 + (S(1)-S(2))*#2) TRIA 18
C----- * + SIX*S(4)*S(4)/RT2 TRIA 19
C----- IF(P.LT.1.0D-3) P=1.0D-3 TRIA 20
C----- PO = P + Q*Q/(P*DM*DM) TRIA 21
C----- IF(PO.LT.PC) RETURN TRIA 22
C----- IFLAG = 1 TRIA 23
C----- RETURN TRIA 24
C----- END TRIA 25

```

```

C -----
C   SUBROUTINE UPDATE(S2,S1,VOID,D,DSIG)          UPDA  1
C -----
C
C.... PROGRAM TO UPDATE STRESSES, PRECONSOLIDATION, AND      UPDA  2
C   VOID RATIO                                              UPDA  3
C
C   IMPLICIT REAL*8(A-H,O-Z)                           UPDA  4
C
C.... REMOVE ABOVE CARD FOR SINGLE PRECISION OPERATION      UPDA  5
C
C   DIMENSION S2(1),S1(1),D(4,1),DSIG(1)                 UPDA  6
C   COMMON/FSTRES/AL,C(36),T(6),EE(9),DEE(9)            UPDA  7
C   COMMON/TDATA/IPC,NS,DT,TT,FAC,ALPHA,BETA           UPDA  8
C   COMMON/VALUES/SPAR(16),PC,P,Q,PD,VR,ICR             UPDA  9
C   COMMON/ISTRES/IFD,N,IOPt                            UPDA 10
C   COMMON/XDATA/TV                                     UPDA 11
C   COMMON/TSTEP/DT1                                    UPDA 12
C   DATA ZERO,HALF,ONE,THREE,SIX,RT2/                  UPDA 13
C   $      0.000,0.500,1.000,3.000,6.000,1.41421356237309D0/ UPDA 14
C
C.... MODIFY ABOVE CARD FOR SINGLE PRECISION OPERATION      UPDA 15
C
C
C   CR = SPAR(1)                                         UPDA 16
C   CC = SPAR(2)                                         UPDA 17
C   CA = SPAR(6)                                         UPDA 18
C   DM = SPAR(12)                                        UPDA 19
C   VR1= SPAR(13)                                       UPDA 20
C   VR = VOID                                           UPDA 21
C   PC = T(5)                                            UPDA 22
C   PCI= S1(5)                                         UPDA 23
C
C.... STRESS UPDATE LAGS IPC BY ONE TIME-STEP              UPDA 24
C
C   IF(IPC.EQ.1.AND.ICR.NE.0) CALL EESET(EE,DEE,4,1)       UPDA 25
C   IF(IPC.EQ.2) DT1=ALPHA*DT                           UPDA 26
C   CALL MATRIX(D,DSIG,DT1)                             UPDA 27
C   IF(IPC.EQ.1.AND.ICR.NE.0) CALL EESET(EE,DEE,4,2)       UPDA 28
C
C.... UPDATE STRESSES                                     UPDA 29
C
C   DO 20 I=1,4                                         UPDA 30
C   TEMP = ZERO                                         UPDA 31
C   DO 10 J=1,4                                         UPDA 32
C   10 TEMP = TEMP + D(I,J)*DEE(J)                      UPDA 33
C   20 DSIG(I) = TEMP - DSIG(I)                         UPDA 34
C   IF(IFD.EQ.0) GOTO 30                                UPDA 35
C
C.... CORRECT FOR ROTATION (FINITE DEFORMATION)          UPDA 36
C
C   DEE(5) = -DEE(5)                                     UPDA 37
C   DVOL = DEE(1) + DEE(2) + DEE(3)                      UPDA 38
C   TEMP = DEE(5)*S1(4)                                  UPDA 39
C   DSIG(1) = DSIG(1) + DVOL*S1(1) + TEMP               UPDA 40
C   DSIG(2) = DSIG(2) + DVOL*S1(2) - TEMP               UPDA 41
C   DSIG(3) = DSIG(3) + DVOL*S1(3)                      UPDA 42
C   DSIG(4) = DSIG(4) + DVOL*S1(4) - HALF*DEE(5)*(S1(1)-S1(2)) UPDA 43

```

```

30 DO 40 I=1,4
40 S2(I) = S1(I) + DSIG(I)
      UPDA 57
      UPDA 58
      UPDA 59
      UPDA 60
      UPDA 61
C..... UPDATE PRECONSOLIDATION AND VOID RATIO
C
      P = (S2(1)+S2(2)+S2(3))/THREE
      Q = DSQRT((S2(2)-S2(3))**2+(S2(3)-S2(1))**2+(S2(1)-S2(2))**2
      *           + SIX*S2(4)*S2(4))/RT2
      IF (P.LT.1.0D-3) P=1.0D-3
      PO = P+Q*Q/(P*DM*DM)
      IF (PO.GT.PCI) PC=PO
      VOID = VR1 - CR*DLOG(P) - (CC-CR)*DLOG(PC)
      S2(5) = PC
      IF (ICR.EQ.0) RETURN
      UPDA 62
      UPDA 63
      UPDA 64
      UPDA 65
      UPDA 66
      UPDA 67
      UPDA 68
      UPDA 69
      UPDA 70
C..... TIME-DEPENDENT CONTRIBUTION
C
      TEMP = DLOG(ONE+DT1/TV)
      VOID = VOID - CA*TEMP
      S2(5) = S2(5) + PC*CA*TEMP/(CC-CR)
      UPDA 71
      UPDA 72
      UPDA 73
      UPDA 74
      UPDA 75
      UPDA 76
      UPDA 77
      UPDA 78
      UPDA 79
C
      RETURN
      END

```

APPENDIX 3

3.1 SPIN 2D USER'S MANUAL

1. TITLE CARD (20A4)		
Columns	Variable	Description
1-80	TITLE(20)	Job title for output heading

2. CONTROL CARD (13I5)		
Columns	Variable	Description
1-5	NUMNP	Number of nodal points; if = 0, program stops
6-10	NPPN	Number of pore pressure nodes; if > 0, mixed formulation
11-15	NSD	Number of spatial dimensions; the number 2
16-20	NDOF	Number of degrees of freedom per node; input 2 if NPPN=0, input 3 if NPPN>0
21-25	NUMEG	Number of element groups; ≥ 1
26-30	NTSG	Number of time step groups; ≥ 1
31-35	NLC	Number of load cases; if =0, set internally to 1
36-40	NLS	Number of load steps; ≥ 0
41-45	NSB	Number of time steps between spatial printout; ≥ 1
46-50	NDOUT	Number of displacement/pore pressure output histories; ≥ 0
51-55	MODE	Execution mode; = 0, data check only = 1, execution
56-60	ISYMM	Symmetry parameter; input 0 (symmetric stiffness matrix)
61-65	LABOR	Analysis abort parameter = 0, no abort performed = 1, abort check performed ¹

¹ Computation is terminated if the norm of the incremental solution vector exceeds an internally pre-set tolerance "TOL".

3. CONTROL CARD (2F10.0)

Columns	Variable	Description
1-10	ALPHA	Predictor-corrector parameter α ; $0.0 \leq \alpha \leq 1.0$ ($\alpha = \frac{1}{2}$ recommended)
11-20	BETA	Pore pressure algorithm parameter β ; $0.0 \leq \beta \leq 1.0$ ($\beta = \frac{1}{2}$ recommended)

4. CONTROL CARDS¹ (2I5, F10.0)

Columns	Variable	Description
1-5	N	Time-step group number; $1 \leq N \leq NTSG$
6-10	NTS	Number of time steps for this time-step group; ≥ 1
11-20	DT	Time step for this group > 0.0

¹ Total number of input cards=NTSG.

5. CONTROL CARD (5I5)

Columns	Variable	Description
1-5	IP1	Undeformed mesh plot code = 0, no plot of undeformed mesh = 1, plot undeformed mesh
6-10	IP2	Deformed mesh plot code = 0, no plot of deformed mesh > 0 , plot every IP2 steps
11-15	IP3	Displacement vectors plot code = 0, no plot of displacement vector > 0 , plot every IP3 steps
16-20	IP4	Velocity vectors plot code (with respect to the undeformed mesh) = 0, no plot of velocity vectors > 0 , plot every IP4 steps
21-25	IP5	Velocity vectors plot code (with respect to the deformed mesh) = 0, no plot of velocity vector > 0 , plot every IP5 steps

6. DISPLACEMENT/PORE PRESSURE HISTORY OUTPUT DATA¹ ((1+NDOF) × 15)		
Columns	Variable	Description
1-5	N	Node number; $1 \leq N \leq \text{NUMNP}$
6-10	ITEMP(1) (displacement 1)	Degree of freedom 1 output code = 0, no plot of degree of freedom 1 = 1, plot degree of freedom 1
11-15	ITEMP(2) (displacement 2)	Degree of freedom 2 output code = 0, no plot of degree of freedom 2 = 1, plot degree of freedom 2
16-20	ITEMP(3) (pore pressure)	Degree of freedom 3 output code ² = 0, no plot of degree of freedom 3 = 1, plot degree of freedom 3

¹ Terminate with a blank card.

² If NDOF = 2, this number is ignored.

7.1 COORDINATE DATA FOR DISPLACEMENT/PORE PRESSURE NODES¹ (215, NSD×F10.0)		
Columns	Variable	Description
1-5	N	Node number; $1 \leq N \leq \text{NUMNP}$
6-10	NUMGP ^{2,3}	Number of generation points = 0, no generation > 0, generate coordinate data
11-20	X(1,N)	x_1 -coordinate of node N
21-30	X(2,N)	x_2 -coordinate of node N

¹ Terminate with a blank card.

² If NUMGP=0, employ a three-card sequence (cards 7.1-7.3).

³ See Sec. 4.6 on floating-point data generation.

**7.2 COORDINATE DATA FOR
DISPLACEMENT/PORE PRESSURE NODES (2I5, NSD×F10.0)**

Columns	Variable	Description
1-5	M	Node number
6-10	MGEN	Generation parameter = 0, coordinates of the Jth generation point are input on this card; M is ignored = 1, coordinates of the Jth generation point are set equal to the coordinates of the Mth node which were previously defined; coordinates on this card are ignored
11-20	TEMP(1,J)	x_1 -coordinate of generation point J
21-30	TEMP(2,J)	x_2 -coordinate of generation point J

**7.3 COORDINATE DATA FOR
DISPLACEMENT/PORE PRESSURE NODES (4I5)**

Columns	Variable	Description
1-5	NINC(1)	Number of nodal increments for direction 1; ≥ 0
6-10	INC(1)	Node number increment for direction 1
11-15	NINC(2)	Number of nodal increments for direction 2 ≥ 0
16-20	INC(2)	Node number increment for direction 2;

8. BOUNDARY CONDITION DATA¹ ((2+NDOF)×I5)

Columns	Variable	Description
1-5	N	Node number; $1 \leq N \leq \text{NUMNP}$
6-10	NG	Generation increment ²
11-15	ID(1,N)	Degree of freedom 1 boundary code ³ = 0, unspecified displacement = 1, specified displacement
16-20	ID(2,N)	Degree of freedom 2 boundary code ³ = 0, unspecified displacement = 1, specified displacement
21-25	ID(3,N)	Degree of freedom 3 boundary code ^{3,4} = 0, unspecified pore pressure = 1, specified pore pressure

¹ Terminate with a blank card.

² See Sec. 4.6 on integer-data generation.

³ If N is a displacement node only and not a pore pressure node, input ID(3,N) = 1; if N is a pore pressure node only and not a displacement node, input ID(1,N) = ID(2,N) = 1.

⁴ If NDOF = 2, this number is ignored.

9.1 INITIAL DISPLACEMENT/PORE PRESSURE DATA ¹ (2I5, NDOFxF10.0)		
Columns	Variable	Description
1-5	N	Node number; $1 \leq N \leq \text{NUMNP}$
6-10	NUMGP ^{2,3}	Number of generation points = 0, no generation > 0, generate data
11-20	D(1,N)	Degree of freedom 1 initial displacement
21-30	D(2,N)	Degree of freedom 2 initial displacement
31-40	D(3,N)	Degree of freedom 3 initial pore pressure ⁴

¹ Terminate with a blank card.² If NUMGP > 0, employ a three-card sequence (cards 9.1-9.3).³ See Sec. 4.6 on floating point data generation.⁴ If NDOF = 2, this number is ignored.

9.2 INITIAL DISPLACEMENT/PORE PRESSURE DATA (2I5, NDOFxF10.0)		
Columns	Variable	Description
1-5	M	Node number
6-10	MGEN	Generation parameter = 0, initial displacement/pore pressure of the Jth generation point are input on this card; M is ignored = 1, initial displacement/pore pressure of the Jth generation point are set equal to the initial displacement/pore pressure of the Mth node which were previously defined; remaining data on this card are ignored
11-20	TEMP(1,J)	Initial displacement 1 of generation point J
21-30	TEMP(2,J)	Initial displacement 2 of generation point J
31-40	TEMP(3,J)	Initial pore pressure of generation point J ¹

¹ If NDOF = 2, this number is ignored.

**9.3 INITIAL
DISPLACEMENT/PORE PRESSURE DATA (4I5)**

Columns	Variable	Description
1-5	NINC(1)	Number of nodal increments for direction 1; ≥ 0
6-10	INC(1)	Node number increment for direction 1
11-15	NINC(2)	Number of nodal increments for direction 2; ≥ 0
16-20	INC(2)	Node number increment for direction 2

**10.1 APPLIED NODAL FORCES/SEEPAGE VELOCITY
PRESCRIBED DISPLACEMENTS/PORE PRESSURES¹
(2I5, NDOFxF10.0)**

Columns	Variable	Description
1-5	N	Node number; $1 \leq N \leq \text{NUMNP}$
6-10	NUMGP ^{2,3}	Number of generation points $= 0$, no generation > 0 , generate data
11-20	F(1,N)	Applied force 1 or prescribed displacement 1
21-30	F(2,N)	Applied force 2 or prescribed displacement 2
31-40	F(3,N)	Applied flux velocity or prescribed pore pressure ⁴

¹ Terminate with a blank card.

² If NUMGP > 0, employ a three-card sequence (cards 10.1-10.3).

³ See Sec. 4.6 on floating point data generation.

⁴ If NDOF = 2, this number is ignored.

**10.2 APPLIED NODAL FORCES/SEEPAGE VELOCITY
PRESCRIBED DISPLACEMENTS/PORE PRESSURES
(2I15, NDOFxF10.0)**

Columns	Variable	Description
1-5	M	Node number
6-10	MGEN	Generation parameter = 0, applied forces/prescribed displacements of the Jth generation point are input on this card; M is ignored = 1, applied forces/prescribed displacements of the Jth generation point are set equal to the applied forces/prescribed displacements of the Mth node which were previously defined; remaining data on this card are ignored
11-20	TEMP(1,J)	Applied force 1 or prescribed displacement 1 of generation point J
21-30	TEMP(2,J)	Applied force 2 or prescribed displacement 2 of generation point J
31-40	TEMP(3,J)	Applied flux velocity or prescribed pore pressure of generation point J ¹

¹ If NDOF = 2, this number is ignored.

**10.3 APPLIED NODAL FORCES/SEEPAGE VELOCITY
PRESCRIBED DISPLACEMENTS/PORE PRESSURES (4I15)**

Columns	Variable	Description
1-5	NINC(1)	Number of nodal increments for direction 1; ≥ 0
6-10	INC(1)	Node number increment for direction 1
11-15	NINC(2)	Number of nodal increments for direction 2; ≥ 0
16-20	INC(2)	Node number increment for direction 2

11. LOAD-TIME FUNCTIONS^{1,2,3} (2F10.0)

Columns	Variable	Description
1-10	G(J,1)	Time instant t_j
11-20	G(J,2)	Value of load-time function at time t_j

¹ Consult Sec. 4.6 and Fig. 4.8 on load-time functions.

² Input functions in the order G_1, G_2, \dots, G_{NLC} .

³ Total number of input cards = $(NLS + 1) \times NLC$.

12. ELEMENT GROUP CONTROL CARD (1115)		
Columns	Variable	Description
1-5	NPAR(1) (= NTYPE)	The number 4
6-10	NPAR(2) (= NUMEL)	Number of elements in this group ≥ 1
11-15	NPAR(3) (= NQP)	Element type option = 1, Q4P1 = 5, Q9P4 = 2, Q9P3 = 6, Q4P0 = 3, Q4P4 = 7, Q8P0 = 4, Q8P4 = 8, Q9P0
16-20	NPAR(4) (= IOPT)	Analysis option = 1, plane strain = 2, axisymmetric (torsionless)
21-25	NPAR(5) (= IDR)	Drainage condition code ¹ = 0, undrained condition = 1, consolidation
26-30	NPAR(6) (= IFD)	Finite deformation code = 0, finite deformation effects neglected = 1, finite deformation effects included
31-35	NPAR(7) (= IT)	Initial stress stiffness numerical integration code; set equal to IM
36-40	NPAR(8) (= IL)	Matrix B^{vol} numerical integration code ²
41-45	NPAR(9) (= IM)	Matrix B^{dev} numerical integration code ²
46-50	NPAR(10) (= IP)	Flux matrix M numerical integration code ²
51-55	NPAR(11) (= IC)	Coupling matrices G and G^T numerical integration code ²

¹ Applies only to "mixed" type of formulation; in undrained condition ($IDR = 0$), the matrices $\beta \Delta t M$ and $-\Delta t M p_n$ in equation (4.37) are not evaluated.

² Available integration codes are the following: EQ.1, 1-pt quadrature; EQ.2, 2×2 quadrature; EQ.3, 3×3 quadrature.

13. ELEMENT GROUP CONTROL CARD (6I5)		
Columns	Variable	Description
1-5	NPAR(12) (= INC)	Incompatible modes ¹ = 0, incompatible modes neglected = 1, incompatible modes added
6-10	NPAR(13) (= NUMPR)	Number of element pressure load cards
11-15	NPAR(14) (= NOUT)	Number of stress-strain output histories
16-20	NPAR(15) (= IST)	Spatial stress-strain output code = 0, include spatial stress-strain output for group = 1, omit spatial stress-strain output for group
21-25	NPAR(16) (= LCASP)	Pressure load case number; ≥ 0 ; if = 0, set internally to 1
26-30	NPAR(17) (= LCASG)	gravity load case number; ≥ 0 ; if = 0, set internally to 1

¹ Incompatible modes apply only to quadrilateral elements with four displacement nodes.

- MATERIAL LIBRARY -

MATERIAL 1. LINEAR ELASTIC

14.1 MATERIAL CONTROL CARD (I5)		
Columns	Variable	Description
1~5	MATYP	The number 1

14.2 MATERIAL PROPERTIES CARD (3F10.0)		
Columns	Variable	Description
1-10	SPAR(1) (= E)	Young's modulus E of soil skeleton
11-20	SPAR(2) (= POIS)	Poisson's ratio ν of soil skeleton
21-30	SPAR(3) (= AL)	Penalty parameter $\bar{\gamma}_w$ to model incompressibility ^{1,2}

¹ See Sec. 4.5 on penalty formulation.

² Another way of treating incompressibility is to input $\nu \approx 0.5$ (but not 0.5), representing ν of soil mass.

MATERIAL 2. NOT AVAILABLE

MATERIAL 3. ELASTO-PLASTIC WITH CREEP FOR CLAY

14.1 MATERIAL CONTROL CARD (2I5)		
Columns	Variable	Description
1-5	MATYP	The number 3
6-10	ICR	Creep strain code = 0, creep effects suppressed = 1, non-associative flow rule on $\dot{\epsilon}_{kl}^t$ for plane strain = 2, volumetric (C_α) scaling on $\dot{\epsilon}_{kl}^t$ = 3, deviatoric (Singh-Mitchell) scaling on $\dot{\epsilon}_{kl}^t$

14.2 MATERIAL PROPERTIES CARD (5F10.0)		
Columns	Variable	Description
1-10	SPAR(1) (= CR)	Swelling/recompression index κ
11-20	SPAR(2) (= CC)	Virgin compression index λ
21-30	SPAR(3) (= HA)	Hyperbolic stress-strain parameter a
31-40	SPAR(4) (= HB)	Hyperbolic stress-strain parameter b
41-50	SPAR(5) (= HRF)	Duncan and Chang corrector R_f

14.3 MATERIAL PROPERTIES CARD (6F10.0)		
Columns	Variable	Description
1-10	SPAR(6) (= CA)	Secondary compression coefficient ψ
11-20	SPAR(7) (= SA)	Singh-Mitchell creep parameter A
21-30	SPAR(8) (= SM)	Singh-Mitchell creep parameter m
31-40	SPAR(9) (= SAL)	Singh-Mitchell creep parameter $\bar{\alpha}$
41-50	SPAR(10) (= TDI)	Instant deviatoric time (t_d) _i
51-60	SPAR(11) (= TVI)	Instant volumetric time (t_v) _i

14.4 MATERIAL PROPERTIES CARD (6F10.0)		
Columns	Variable	Description
1-10	SPAR(12) (= DM)	Slope M of the critical state line
11-20	SPAR(13) (= VR1)	Void ratio e_a at unit p_c on the isotropic consolidation line
21-30	SPAR(14) (= PKXX)	Permeability component k_{11}
31-40	SPAR(15) (= PKYY)	Permeability component k_{22}
41-50	SPAR(16) (= PKXY)	Permeability component $k_{12} = k_{21}$
51-60	AL	Penalty parameter $\bar{\gamma}_w$ to model incompressibility ¹

¹ See Sec. 4.5 on penalty formulation.

MATERIAL 4. HYPERBOLIC MODEL FOR SAND

14.1 MATERIAL CONTROL CARD (15)		
Columns	Variable	Description
1-5	MATYP	The number 4

14.2 MATERIAL PROPERTIES CARD ¹ (5F10.0)		
Columns	Variable	Description
1-10	SPAR(1) (= PJK)	Janbu's parameter K
11-20	SPAR(2) (= PJN)	Janbu's parameter n
21-30	SPAR(3) (= PATM)	Atmospheric pressure p_a
31-40	SPAR(4) (= BA)	Bulk modulus parameter A
41-50	SPAR(5) (= BB)	Bulk modulus parameter B

¹ The initial tangent modulus is calculated as $E_i = Kp_a(p/p_a)^n$, where $p = \frac{1}{3}\sigma_{kk}$. The tangential Young's modulus is given by $E_t = E_i[1 - (1 - \sin\phi')qR_f/(2p\sin\phi' + 2c\cos\phi')]$. The bulk modulus K is assumed to vary linearly with p thus: $K = A + Bp$.

14.3 MATERIAL PROPERTIES CARD (4F10.0)		
Columns	Variable	Description
1-10	SPAR(6) (= COH)	Cohesion c
11-20	SPAR(7) (= PHI)	Effective friction angle ϕ'
21-30	SPAR(8) (= RF)	Duncan and Chang corrector R_f
31-40	SPAR(9) (= AL)	Penalty parameter $\bar{\gamma}_w$ to model incompressibility ¹

¹ See Sec. 4.5 on penalty formulation.

- END OF MATERIAL LIBRARY -

15.1 INITIAL STRESSES CARD ¹ (2I5, 5F10.0)		
Columns	Variable	Description
1-5	N	Element number; $1 \leq N \leq \text{NUMEL}$
6-10	NUMGP ²	Number of generation points = 0, no data generation = 1, generate data
11-20	SIG(1,N)	Initial stress σ_{11}
21-30	SIG(2,N)	Initial stress σ_{22}
31-40	SIG(3,N)	Initial stress σ_{33}
41-50	SIG(4,N)	Initial stress $\sigma_{12} = \sigma_{21}$
51-60	SIG(5,N) ³	Initial preconsolidation pressure p_c ⁴

¹ Terminate with a blank card.

² If NUMGP>0, employ a three-card sequence (cards 18.1-18.3).

³ This information is not required for material type 1 (linear elastic).

⁴ If SIG(5,N)=0, the soil is assumed to be normally consolidated; program internally computes p_c as $p_c = p + q^2/(M^2 p)$. Overconsolidation is accounted for by inputting $p_c = OCR \cdot [p + q^2/(M^2 p)]$.

15.2 INITIAL STRESSES CARD (2I5, 5F10.0)		
Columns	Variable	Description
1-5	M	Element number
6-10	MGEN	Generation parameter = 0, stresses in the Jth generation element are input on this card; M is ignored = 1, stresses in the Jth generation element are set equal to the stresses of the Mth element which were previously defined; stress data on this card are ignored
11-20	TEMP(1,J)	Stress σ_{11} in generation element J
21-30	TEMP(2,J)	Stress σ_{22} in generation element J
31-40	TEMP(3,J)	Stress σ_{33} in generation element J
41-50	TEMP(4,J)	Stress σ_{12} in generation element J
51-60	TEMP(5,J)	Preconsolidation p_c in generation element J ¹

¹ This information is not required for material type 1 (linear elastic).

15.3 INITIAL STRESSES CARD (4I5)		
Columns	Variable	Description
1-5	NINC(1)	Number of element increments for direction 1; ≥ 0
6-10	INC(1)	Element number increment for direction 1
11-15	NINC(2)	Number of element increments for direction 2; ≥ 0
16-20	INC(2)	Element number increment for direction 2

16. WEIGHT AND GRAVITY LOAD MULTIPLIER CARD (4F10.0)		
Columns	Variable	Description
1-10	WT	Effective unit weight of the soil γ_s
11-20	GW	Unit weight of water γ_w
21-30	GRAV(1)	Multiplier of gravity load in the x_1 -direction
31-40	GRAV(2)	Multiplier of gravity load in the x_2 -direction

17.1 ELEMENT DATA CARDS ¹ (I5, 5X, (NQ+NP+1)×I5)		
Columns	Variable	Description
1-5	N	Element number; $1 \leq N \leq \text{NUMEL}$
6-10	blank	blank
11-15	IEN(1,N)	Number of first displacement node
16-20	IEN(2,N)	Number of second displacement node
...
*	IEN(NQ,N)	Number of NQ th displacement node ²
*	IEN(NQ+1,N)	Number of first pore pressure node
...
*	IEN(NQ+NP,N)	Number of NP th pore pressure node ²
*	NG	Generation parameter ^{3,4} = 0, no generation = 1, generate data

¹ Terminate with a blank card.

² NQ = number of element displacement nodes; NP = number of element pore pressure nodes. Employ the element node numbering scheme shown in Fig. 4.3.

³ If NG = 1, employ a two-card generation sequence (cards 17.1-17.2).

⁴ Consult Sec. 4.6 and Fig. 4.7 on integer data generation.

17.2 ELEMENT DATA CARDS (6I5)		
Columns	Variable	Description
1-5	NEL(1)	Number of elements in direction 1; ≥ 0 ; if = 0, set internally to 1
6-10	INCEL(1)	Element number increment for direction 1; if = 0, set internally to 1
11-15	INC(1)	Node number increment for direction 1; if = 0, set internally to 1
16-20	NEL(2)	Number of elements in direction 2; ≥ 0 ; if = 0, set internally to 1
21-25	INCEL(2)	Element number increment for direction 2; if = 0, set internally to NEL(1)
26-30	INC(2)	Node number increment for direction 2; if = 0, set internally to $(1+NEL(1)) \times INC(1)$

18. ELEMENT PRESSURE LOAD CARDS^{1,2} (2I5, 10X, F10.0)		
Columns	Variable	Description
1-5	IELNO(I)	Element number; ³ $1 \leq IELNO(I) \leq NUMEL$
6-10	ISIDE(I)	Element side number ⁴ $1 \leq ISIDE(I) \leq 4$
21-30	PRES(I)	Pressure ⁵ (force/unit area)

¹ Terminate with a blank card.² Apply only to quadrilateral elements with four displacement nodes.³ Use one card for each loaded side.⁴ If i , j , k , and l are the element node numbers as read in on the element data card, sides 1, 2, 3, and 4 are the faces $i-j$, $j-k$, $k-l$, and $l-i$, respectively.⁵ Pressures are positive when pointing inward with respect to the element faces.

19. ELEMENT OUTPUT HISTORY CARDS¹ (16I5)		
Columns	Variable	Description
1-5	N	Element number; $1 \leq N \leq NUMEL$
6-10	ITEMP(1)	Stress σ_{11} plot code
11-15	ITEMP(2)	Stress σ_{22} plot code
16-20	ITEMP(3)	Stress σ_{33} plot code
21-25	ITEMP(4)	Stress σ_{12} plot code
26-30	ITEMP(5)	Principal stress σ_1 plot code
31-35	ITEMP(6)	Principal stress σ_2 plot code
36-40	ITEMP(7)	Maximum shear stress τ_{12} plot code
41-45	ITEMP(8)	Strain ϵ_{11} plot code
46-50	ITEMP(9)	Strain ϵ_{22} plot code
51-55	ITEMP(10)	Strain ϵ_{33} plot code
56-60	ITEMP(11)	Strain ϵ_{12} plot code
61-65	ITEMP(12)	Principal strain ϵ_1 plot code
66-70	ITEMP(13)	Principal strain ϵ_2 plot code
71-75	ITEMP(14)	Maximum shear strain γ_{12} plot code ²
76-80	ITEMP(15)	Pore pressure u plot code

¹ Input the following plot codes: EQ. 0, no plot; EQ. 1, plot.² Shear strains are engineering strains.

3.2 SOLVED PROBLEM

INPUT DECK:

TYPICAL PRINTOUT:

UNDRAINED 'TRIAXIAL' TEST ON UNDISTURBED BAY MUD, NO CREEP (SEE EX.3, SEC.4.7)

CONTROL INFORMATION

```

NUMBER OF NODAL POINTS . . . . . (NUMNP) = 12
NUMBER OF PORE PRESSURE NODES . . . . . (NPPN) = 3
NUMBER OF SPACE DIMENSIONS . . . . . (NSD) = 2
NUMBER OF DEGREES OF FREEDOM PER NODE . . . . (NDDF) = 2
NUMBER OF ELEMENT GROUPS . . . . . (NUMEG) = 1
NUMBER OF TIME STEP GROUPS . . . . . (NTSG) = 2
NUMBER OF LOAD CASES . . . . . (NLC) = 1
NUMBER OF LOAD STEPS . . . . . (NLS) = 2
NUMBER OF STEPS BETWEEN SPATIAL OUTPUT . . . . (NSB) = 20
NUMBER OF DISPLACEMENT OUTPUT HISTORIES . . . . (INDOUT) = 0
SOLUTION MODE . . . . . . . . . . . (IMODE) = 1
  EQ.0, DATA CHECK
  EQ.1, EXECUTION

SYMMETRIC / NONSYMMETRIC OPTION . . . . . (ISYMM) = 0
  EQ.0, SYMMETRIC MATRIX
  EQ.1, NONSYMMETRIC MATRIX

ABORT OPTION . . . . . . . . . . . (IABORT) = 1
  EQ.0, ABORT CHECK IGNORED
  EQ.1, PERFORM ABORT CHECK

PREDICTOR/CORRECTOR ALGORITHM PARAMETER (ALPHA) = 0.0
PORE PRESSURE ALGORITHM PARAMETER . . . . (BETA) = 0.5000+00

TIME STEP GROUP      NUMBER OF TIME STEPS      TIME STEP
  1                  20                  0.2000-02
  2                  20                  0.1000-02

TOTAL NUMBER OF TIME STEPS . . . . . (INTS) = 40

```

UNDRAINED 'TRIAXIAL' TEST ON UNDISTURBED BAY MUD, NO CREEP (SEE EX.3, SEC.4.7)

PLOTTING INFORMATION

```

UNDEFORMED MESH PLOT . . . . . . . . . . (IP1) = 0
  EQ.0, NO PLOT OF UNDEFORMED MESH
  EQ.1, PLOT UNDEFORMED MESH

DEFORMED MESH PLOTS . . . . . . . . . . (IP2) = 0
  EQ.0, NO PLOTS
  EQ.1, PLOT EVERY IP2 STEPS

DISPLACEMENT VECTOR PLOTS . . . . . . . . (IP3) = 0
  EQ.0, NO PLOTS
  EQ.1, PLOT EVERY IP3 STEPS

VELOCITY VECTOR PLOTS WRT UNDEFORMED MESH . . (IP4) = 0
  EQ.0, NO PLOTS
  EQ.1, PLOT EVERY IP4 STEPS

VELOCITY VECTOR PLOTS WRT DEFORMED MESH . . . (IP5) = 0
  EQ.0, NO PLOTS
  EQ.1, PLOT EVERY IP5 STEPS

```

DISPLACEMENT OUTPUT HISTORY INFORMATION

NODE NUMBER	DOP1	DOP2	DOP3
-------------	------	------	------

NODAL COORDINATE DATA

NODE NUMBER	X1	X2
1	1.75000000D-02	4.45000000D-02
2	8.90000000D-03	4.45000000D-02
3	0.0	4.45000000D-02
4	1.75000000D-02	2.12500000D-02
5	8.90000000D-03	2.12500000D-02
6	0.0	2.12500000D-02
7	1.75000000D-02	0.0
8	8.90000000D-03	0.0
9	0.0	0.0
10	4.45000000D-02	1.11250000D-02
11	1.22500000D-02	2.25000000D-02
12	4.45000000D-02	3.37500000D-02

NODAL BOUNDARY CONDITION CODES

NODE NUMBER	DOF1	DOF2	DOF3
1	0	1	
2	0	1	
3		1	
4	0	0	1
5	0	0	1
6	1	0	1
7	0	1	1
8	0	1	1
9	1	1	1
10	1	1	0
11	1	1	0
12	1	1	0

THERE ARE NO NONZERO INITIAL DISPLACEMENTS/PORE PRESSURES

NODAL FORCES AND DISPLACEMENTS 1

NODE NUMBER	DOF1	DOF2	DOF3
1	0.0	-2.00000000D-02	0.0
2	0.0	-2.00000000D-02	0.0
3	0.0	-2.00000000D-02	0.0

LOAD-TIME FUNCTION 1

TIME	LOAD MULTIPLIER
0.0	0.0
1.00000000D+00	7.00000000D-01
4.00000000D+00	1.00000000D+00

*

ELEMENT GROUP DATA

ELEMENT GROUP NUMBER . . . (NEG) = 1
 2 D ELEMENTS

ELEMENT TYPE NUMBER (ETYPE) = 4

NUMBER OF ELEMENTS (NUMEL) = 1

ON - OFF OPTION (OOF) = 0

EQ.1, Q4-P1 EQ.3, Q4-P4 EQ.5, Q4-P9
 EQ.2, Q8-P2 EQ.4, Q8-P4 EQ.6, Q8-P9
 EQ.5, Q8-P4 EQ.6, Q8-P9

ANALYSIS OPTION (AOP) = 2

EQ.1, PLANE STRAIN
 EQ.3, AXISYMMETRIC

DRAINAGE CONDITION CODE (DRD) = 0

EQ.0, UNDRAINED CONDITION ANALYSIS
 EQ.1, CONSOLIDATION ANALYSIS

FINITE DEFORMATION CODE (FDF) = 0

EQ.0, FINITE DEF. EFFECTS NEGLECTED
 EQ.1, FINITE DEF. EFFECTS INCLUDED

4 5 6 7 8 9 10 11 12 13 14 15 16 17 18 19 20 21 22 23 24 25 26 27 28 29 30 31 32 33 34 35 36 37 38 39 40 41 42 43 44 45 46 47 48 49 50 51 52 53 54 55 56 57 58 59 60 61 62 63 64 65 66 67 68 69 70 71 72 73 74 75 76 77 78 79 80 81 82 83 84 85 86 87 88 89 90 91 92 93 94 95 96 97 98 99 100

GRAVITY LOAD DATA

WEIGHT DENSITY OF SOIL	0.0
WEIGHT DENSITY OF WATER	0.0
X1-DIRECTION MULTIPLIER	0.0
X2-DIRECTION MULTIPLIER	0.0

ELEMENT DATA

ELEMENT NUMBER	NODE 1	NODE 2	NODE 3	NODE 4	NODE 5	NODE 6	NODE 7	NODE 8	NODE 9	NODE 10	NODE 11	NODE 12
1	1	3	9	7	2	8	0	4	5	10	11	12

UNDRAINED 'TRIAXIAL' TEST ON UNDISTURBED BAY MUD, NO CREEP (SEE EX.2, SEC.4.7)

EQUATION SYSTEM DATA

NUMBER OF EQUATIONS	(NEQ) =	12
NUMBER OF TERMS IN STIFFNESS	(NA) =	78
MEAN HALF BANDWIDTH	(NB) =	6
TOTAL LENGTH OF BLANK COMMON REQUIRED	(NLB) =	995

SOLUTION PHASE:

STEP NUMBER = 20
NUMBER OF ITERATIONS = 1

TIME = .4000-01

DISPLACEMENTS

NODE NUMBER	DDF1	DDF2	DDF3
1	1.12000000D-04	-5.60000000D-04	0.0
2	5.00000000D-05	-5.00000000D-04	0.0
3	0.0	-5.00000000D-04	0.0
4	1.12000000D-04	-5.00000000D-04	0.0
5	5.00000000D-05	-5.00000000D-04	0.0
6	0.0	-5.00000000D-04	0.0
7	1.12000000D-04	0.0	0.0
8	5.00000000D-05	0.0	0.0
9	0.0	0.0	0.0
10	0.0	0.0	1.03250157D+02
11	0.0	0.0	1.03250157D+02
12	0.0	0.0	1.03250157D+02

STEP NUMBER = 20
NUMBER OF ITERATIONS = 1

TIME = .4000-01

DISPLACEMENT INCREMENTS

NODE NUMBER	DDF1	DDF2	DDF3
1	5.00000000D-05	-3.00000000D-05	0.0
2	2.00000000D-06	-2.00000000D-05	0.0
3	0.0	-2.00000000D-05	0.0
4	5.00000000D-05	-1.40000000D-05	0.0
5	2.00000000D-06	-1.40000000D-05	0.0
6	0.0	-1.40000000D-05	0.0
7	5.00000000D-05	0.0	0.0
8	2.00000000D-06	0.0	0.0
9	0.0	0.0	0.0
10	0.0	0.0	3.13226002D+00
11	0.0	0.0	3.13226002D+00
12	0.0	0.0	3.13226002D+00

Appendix 3.2 Solved problem

218

ELEMENT STRESSES AND STRAINS

ELEMENT GROUP NUMBER (SEG) * 1											
ELEMENT NUMBER	COORD. X1	COORD. X2	STRESS	STRESS	STRESS	STRESS	PRINC.	PRINC.	SHEAR	VOL.	DEV.
			11	22	33	12	STRESS 1	STRESS 2	STRESS	VOL.	STRESS Q
			STRAIN	STRAIN	STRAIN	STRAIN	PRINC.	PRINC.	STRAIN	VOL.	DEV.
11	22	33	12	STRAIN 1	STRAIN 2	STRAIN	STRAIN	STRAIN	STRAIN	STRAIN	STRAIN
STRESS	STRAIN	PORE	VOID	VOL.	PRECON.	DCR	VOL.	DEV.	AGE TV	AGE TD	DEV.
ANGLE	ANGLE	PRESSURE	RATIO	STR. PD	PC	PC	AGE	AGE	AGE	AGE	AGE
1	8.000-03	2.22D-02	2.28D+02	4.54D+02	2.28D+02	-2.28D-12	4.54D+02	2.28D+02	1.13D+02	3.04D+02	2.28D+02
			-8.28D-03	1.28D-02	-6.28D-03	-2.44D-16	1.28D-02	-1.28D-03	8.44D-03	3.56D-17	1.28D-02
			-8.000+01	-8.000+01	1.63D+02	3.02D-01	4.28D+02	4.28D+02	1.000+00	0.0	0.0

STEP NUMBER = 40
NUMBER OF ITERATIONS = 1
TIME = + .800D-01

DISPLACEMENTS

NODE NUMBER	DDF1	DDF2	DDF3
1	1.000000000D-04	-8.000000000D-04	0.0
2	8.400000000D-05	-8.400000000D-04	0.0
3	0.0	-8.400000000D-04	0.0
4	1.000000000D-04	-4.390000000D-04	0.0
5	8.400000000D-05	-4.390000000D-04	0.0
6	0.0	-4.390000000D-04	0.0
7	1.000000000D-04	0.0	0.0
8	8.400000000D-05	0.0	0.0
9	0.0	0.0	0.0
10	0.0	0.0	1.000000000D+02
11	0.0	0.0	1.000000000D+02
12	0.0	0.0	1.000000000D+02

STEP NUMBER = 40
NUMBER OF ITERATIONS = 1
TIME = + .800D-01

DISPLACEMENT INCREMENTS

NODE NUMBER	DDF1	DDF2	DDF3
1	8.000000000D-05	-1.400000000D-05	0.0
2	1.400000000D-05	-1.400000000D-05	0.0
3	0.0	-1.400000000D-05	0.0
4	8.000000000D-05	-7.000000000D-05	0.0
5	1.400000000D-05	-7.000000000D-05	0.0
6	0.0	-7.000000000D-05	0.0
7	8.000000000D-05	0.0	0.0
8	1.400000000D-05	0.0	0.0
9	0.0	0.0	0.0
10	0.0	0.0	1.07110273D+00
11	0.0	0.0	1.07110273D+00
12	0.0	0.0	1.07110273D+00

Appendix 3.2 Solved problem

ELEMENT STRESSES AND STRAINS

ELEMENT GROUP NUMBER (REG) = 1															
ELEMENT NUMBER	COORD. X1	COORD. X2	STRESS 11	STRESS 22	STRESS 33	STRESS 12	PRINC. STRESS 1	PRINC. STRESS 2	SHEAR STRESS	VOL. STRESS P	DEV. STRESS Q				
	STRAIN 11	STRAIN 22	STRAIN 33	STRAIN 12	PRINC. STRAIN 1	PRINC. STRAIN 2	SHEAR STRAIN	VOL. STRAIN	DEV. STRAIN						
	STRESS ANGLE	STRAIN ANGLE	PORE PRESSURE	VOID RATIO	VOL. STR. PD	PRECON. PC	OCR	VOL. AGE TV	DEV. AGE TD						
1	8.88D-03	2.88D-02	2.88D+02	4.43D+02	2.88D+02	-4.14D-12	4.43D+02	3.88D+02	1.21D+02	2.88D+02	2.41D+02				
			-9.44D-03	1.88D-02	-9.44D-03	-8.70D-16	1.88D-02	-9.44D-03	1.42D+02	8.30D-17	1.88D-02				
			-9.00D+01	-9.00D+01	1.000+02	3.02D+01	4.26D+02	4.26D+02	1.00D+00	0.0	0.0				

UNDRAINED 'TRIAXIAL' TEST ON UNDISTURBED BAY MUD, NO CREEP (SEE EX.2, SEC.4.7)

SOLUTION TIME LOG IN SECONDS

INPUT PHASE	0.03
FORMULATION OF STIFFNESS AND LOAD VECTOR	0.59
FACTORIZATION AND CHECK ON PIVOTS	0.01
BACK-SUBSTITUTION	0.00
DISPLACEMENT UPDATE AND STRESS CALCULATIONS	0.03
PRINTING AND PLOTTING	0.01
TOTAL SOLUTION TIME	0.67

APPENDIX 4

NOTATIONS

- a, a' = hyperbolic stress-strain parameters
 a_p = hyperbolic pore pressure-strain parameter
 A = Singh-Mitchell creep parameter
 $\mathbf{A}, \bar{\mathbf{A}}$ = symmetric bilinear operators
 b, b' = hyperbolic stress-strain parameters
 b_p = hyperbolic pore pressure-strain parameter
 \mathbf{B} = strain-displacement matrix
 $\bar{\mathbf{B}}$ = 'improved' \mathbf{B}
 \mathbf{B}^e = deformation part of \mathbf{B}
 \mathbf{B}^θ = spin part of \mathbf{B}
 $B_i = \partial N_a / \partial x_i$
 c_{ijkl} = stress-strain tensor
 \tilde{c}_{ijkl} = material response tensor = $c_{ijkl} + c_{ijkl}^*$
 c_{ijkl}^* = $\sigma_{ij} \delta_{kl}$ using the Jaumann rate of the Kirchhoff stress
 \mathbf{C} = stress-strain matrix (matrix form of c_{ijkl})
 $\bar{\mathbf{C}}$ = matrix form of \tilde{c}_{ijkl}
 \mathbf{C}^* = matrix form of c_{ijkl}^*
 C_c = virgin compression index, \log_{10} -scale
 C_r = swelling/recompression index, \log_{10} -scale
 C_α = secondary compression coefficient, \log_{10} -scale
 \bar{D} = deviator stress level
 \mathbf{d} = nodal displacement vector
 d_{ijkl} = modified stress-strain tensor accounting for finite deformation
 D = superscript for "delayed"
 \mathbf{D} = material + initial stress stiffness matrix
 e, e_{vr} = void ratio
 $e_a = e|_{p_e=1}$ on the isotropic consolidation curve
 $e_c = e|_{p=1}$ on the critical state line
 e_o = initial void ratio
 \mathbf{E} = pore pressure gradient matrix operator
 E_i = initial tangent modulus
 f_i = i th (Cartesian) component of \mathbf{f}
 \mathbf{f} = effective body force vector
 \mathcal{F} = any function
 F = elliptical yield surface
 $F_{ij} = (i, j)$ -component of the deformation gradient tensor \mathbf{F}
 F_{ijkl} = (i, j, k, l) -general nonlinear constitutive function

- F** = deformation gradient tensor; nodal force vector
 g_i = i th (Cartesian) component of **g**
g = prescribed displacement field
G = horizontal deviatoric yield surface; shear modulus; load-time function
G = coupling matrix
 h = Planck's constant (6.624×10^{-27} erg/sec)
 h_i = i th (Cartesian) component of **h**
h = prescribed traction field
 H = height
 H^n = set of functions with square-integrable n th derivatives
H = force vector
 I = superscript for "instant"
 I_0 = first invariant of ()
 Π_0 = second invariant of ()
 III_0 = third invariant of ()
 k = permeability; Boltzmann's constant (1.38×10^{-6} erg/ $^{\circ}\text{K}$)
 k_{ij} = (i, j) -component of **k**
k = permeability tensor
 K = bulk modulus
 K_o = geostatic lateral earth pressure coefficient
K = tangent stiffness matrix
L = velocity gradient tensor
 L_{ij} = (i, j) -component of **L** ($= v_{i,j}$)
 m = Singh-Mitchell creep parameter
 M = slope of the critical state line
M = flux matrix
 n = shear stress ratio
 n_d = number of element displacement nodes
 n_{dof} = number of degrees of freedom
 n_{ed} = number of element displacement components
 n_{en} = number of element nodes
 n_{eq} = global number of equations
 n_i = direction cosine of the angle between axis i
 and the surface normal
 n_{int} = number of integration points in the normal rule
 \bar{n}_{int} = number of integration points in the reduced rule
 n_p = number of element pore pressure nodes
 n_{sd} = number of spatial dimensions
 N = Avogadro number (6.602×10^{23})

- N_a = displacement shape function
 \hat{N}_a = pore pressure shape function
 \bar{N}_l = special shape function
 p = excess pore pressure; volumetric stress $\frac{1}{3}\sigma_{kk}$
 p^* = volumetric stress corresponding to q on the yield surface
 p_c = preconsolidation pressure
 p_o = preconsolidation pressure corresponding to stress state (p, q) ($p_o \leq p_c$)
 \mathbf{p} = nodal pore pressure vector
 P = superscript for "primary"
 q = pore pressure weighting function ($q \in \Psi$); deviatoric stress $\frac{3}{\sqrt{2}}\tau_{oct}$
 q_u, q_{ult} = undrained shear strength
 r = prescribed pressure function
 R = gas constant (1.98 cal/ $^{\circ}$ K-mole), ratio $C_a / (\frac{-\theta_a}{\partial(\log \sigma_v)})$
 R_f = Duncan and Chang corrector parameter
 s = prescribed velocity flux
 s_{ijkl} = tensor specified by objectivity
 S = superscript for "secondary"
 \mathbf{S} = matrix form of s_{ijkl}
 t = time
 t_d = deviatoric age
 $(t_d)_i$ = instant deviatoric time, usually set to unity
 t_p, t_{100} = time for 100 percent consolidation
 t_v = volumetric age
 $(t_v)_i$ = instant volumetric time, usually set to unity
 T = absolute temperature
 T_v = consolidation time factor
 \mathbf{T} = initial stress matrix
 $u, \Delta u$ = excess pore pressure
 $u_f, \Delta u_f$ = excess pore pressure at failure
 u_i = i th (Cartesian) component of \mathbf{u}
 \mathbf{u} = displacement field function
 v_i = i th (Cartesian) component of \mathbf{v}
 \mathbf{v} = velocity vector
 $v_{i,j}$ = (i,j) -component on the velocity gradient tensor
 $v_{(i,j)}$ = symmetric part of the velocity gradient tensor $v_{i,j}$
 $v_{[i,j]}$ = skew-symmetric part of the velocity gradient tensor $v_{i,j}$
 w = water content
 w_i = i th (Cartesian) component of \mathbf{w}
 \mathbf{w} = displacement weighting function vector ($\mathbf{w} \in \Theta$)
 \mathbf{x} = (Cartesian) coordinates in the current configuration

X = (Cartesian) coordinates in the initial configuration

z = depth

Z = normalized depth = z/H

Greek Symbols

α = predictor-corrector algorithm parameter

$\bar{\alpha}$ = Singh-Mitchell creep parameter

β = pore pressure algorithm parameter

γ = unit weight, deviatoric strain

γ_w = unit weight of water

γ_{oct} = octahedral deviatoric strain

Γ = problem boundary

δ_{ij} = Kronecker delta

Δ = increment

ΔF = potential energy barrier

ϵ = strain, compression positive

$\dot{\epsilon}$ = strain rate from theory of rate processes

ϵ_1 = major principal strain

ϵ_2 = intermediate principal strain

ϵ_3 = minor principal strain

ϵ_a = axial strain

$\dot{\epsilon}_a^t$ = axial creep strain rate

ϵ_d = deviatoric strain

ϵ_v = volumetric strain

ϵ_{oct} = octahedral normal strain = $\frac{1}{3}\epsilon_{kk}$

ϵ_{kl} = small strain tensor

ϵ_{kl}^t = creep strain rate tensor

ϵ_{kl}^* = natural or true strain tensor

ε = real parameter

$\varsigma - \varsigma_r$ = node numbers where pore pressures are unknown

η = stress ratio q/p ; natural coordinate

$\eta - \eta_g$ = node numbers where displacements are unknown

η_o = stress ratio at K_o -condition

η^* = stress ratio q/p^*

θ = spin; orientation of the principal stress axes

ϑ = function of stress invariants

Θ = vector set of displacement weighting functions

κ = swelling-recompression index, ln-scale

λ = virgin compression index, ln-scale

$\bar{\lambda}$ = Lamé parameter

$\bar{\lambda}_w$ = Lamé parameter for water

- λ_0 = distance between equilibrium positions (rate process)
 $-A$ = stretch
 μ^e = elastic shear modulus
 $\bar{\mu}$ = Lamé parameter
 $\bar{\mu}_{soil}$ = shear modulus of soil skeleton
 ν = Poisson ratio
 ξ = natural coordinate
 π = 3.14159...
 ρ = pore pressure field function
 σ = stress, compression positive
 σ_1 = major principal stress
 σ_2 = intermediate principal stress
 σ_3 = minor principal stress
 σ_h = horizontal stress
 σ_v = vertical stress
 σ_{oct} = octahedral normal strain
 σ_{ij} = (i,j)-component of the (Cauchy) stress tensor
 $\dot{\sigma}_{ij}^t$ = stress relaxation rate
 σ_{ij}^* = Jaumann derivative of the Kirchhoff stress tensor
 $\tilde{\tau}$ = directional potential
 τ_{oct} = octahedral shear stress
 v = activation frequency
 T = vector set of displacement trial solutions
 ϕ = associative flow rule proportionality factor
 ϕ' = effective friction angle
 φ = function of strain invariants; associative flow rule proportionality factor
 Φ = set of pore pressure trial solutions
 χ = factor
 ψ = secondary compression coefficient, ln-scale
 Ψ = set of pore pressure weighting functions
 ω = angular velocity
 Ω = problem domain
- Set Symbols**
- \emptyset = null set
 \cup = set union
 \cap = set intersection
 \subset = "is a subset of"
 \in = "is an element of"